NASA/TM–97–104606, Vol. 13

Technical Report Series on Global Modeling and Data Assimilation

Max J. Suarez, Editor
Goddard Space Flight Center, Greenbelt, Maryland

Volume 13

Interannual Variability and Potential Predictability in Reanalysis Products

Wei Min, General Sciences Corporation, Laurel, Maryland; and
Siegfried D. Schubert, Goddard Space Flight Center, Greenbelt, Maryland

National Aeronautics and
Space Administration

Goddard Space Flight Center
Greenbelt, Maryland 20771

December 1997

Available from:

NASA Center for AeroSpace Information
800 Elkridge Landing Road
Linthicum Heights, MD 21090-2934
Price Code: A17

National Technical Information Service
5285 Port Royal Road
Springfield, VA 22161
Price Code: A10

Abstract

The Data Assimilation Office (DAO) at Goddard Space Flight Center and the National Center for Environmental Prediction and National Center for Atmospheric Research (NCEP/NCAR) have produced multi-year global assimilations of historical data employing fixed analysis systems. These "reanalysis" products are ideally suited for studying short–term climatic variations. The availability of multiple reanalysis products also provides the opportunity to examine the uncertainty in the reanalysis data.

The purpose of this document is to provide an updated estimate of seasonal and interannual variability based on the DAO and NCEP/NCAR reanalyses for the 15 year period 1980–1995. Intercomparisons of the seasonal means and their interannual variations are presented for a variety of prognostic and diagnostic fields. In addition, atmospheric potential predictability is re-examined employing selected DAO reanalysis variables.

Contents

List of Figures

1 Introduction

Recently, several efforts have been devoted to the reanalysis of historical data with an unvarying assimilation system (Bengtsson and Shukla 1988; Schubert et al. 1993; Gibson et al. 1996). The motivation for these efforts is that operational assimilation systems undergo frequent updates and thus introduce spurious signals in the analysis output that may contaminate the quality of the atmospheric state and its variability particularly at seasonal or longer time scales. Even the dominant climate events (e.g. the El Niño/ Southern Oscillation, ENSO) can be masked by these signals (see, for example, Fig. 10 in Arpe 1990). This makes the analysis output poorly suited for climate studies. While some quantities are not sensitive to system changes, others are more susceptible due to their sensitivity to model formulation, and the weak constraints imposed by limited and/or poor quality observations. This is particularly true for the hydrological cycle (e.g., Mo and Higgins 1996; Wang and Paegle 1996; Min and Schubert 1997). The use of a fixed assimilation system has eliminated some of these problems, however, discontinuities remain in the output as a result of changes to the observing systems. The main purpose of this document is to provide an updated estimate of seasonal and interannual variability based on the NASA/DAO and NCEP/NCAR reanalyses for the 15 year period 1980–1995. Intercomparisons of the seasonal means and their interannual variations are presented for a variety of prognostic and diagnostic fields.

In addition to understanding short term climate variations, one of the major goals of climate research is the capability to provide useful predictions on seasonal and longer time scales. Atmospheric predictability is determined by both internal dynamics and the influence of slowly varying boundary conditions such as sea surface temperature, sea ice, snow cover, and soil moisture. Numerous studies (e.g. Leith 1978, Lorenz 1982) indicate that, in the absence of anomalous boundary forcing, the inherent nonlinearity of the atmosphere results in an rms error-doubling time of about two days, and a current practical limit of useful predictions of about two weeks. On seasonal and longer time scales, however, boundary forcing has a substantial influence on atmospheric variability. Under the assumption that the variability induced by internal dynamics is unpredictable on seasonal and longer time scales, there would still be a potential for predictability of time averages if the variability due to changes in boundary conditions is sufficiently large compared to that induced by internal dynamics. Early studies using the operational analysis data sets to assess this potential predictability (see Section 4 for definitions and discussion of earlier studies) suffered from the spurious signals introduced by changes in the analysis system and the measurement instruments. In this study, we will also re-examine atmospheric potential predictability using the NASA/DAO reanalysis data set.

The document is divided into two parts. The first part is focused on the seasonal means and their interannual variability of selected prognostic and diagnostic fields from both the

NASA/DAO and NCEP/NCAR reanalyses. We note that Higgins et al. (1997) have already presented a rather comprehensive comparison of mean quantities and within season variability from both reanalyses. This is an extension of that work to include more years, the transition seasons, further diagnostic quantities and, in particular, interannual variability. The second part examines atmospheric potential predictability using the NASA/DAO reanalysis. The results are summarized in terms of variances, characteristic time scales and signal-to-noise ratio.

Section 2 gives a brief overview of the NASA/DAO and the NCEP/NCAR assimilation systems. Section 3 compares the seasonal means and its interannual standard deviation of selected quantities from the two reanalyses. The analysis of atmospheric potential predictability is presented in section 4. Section 5 summarizes the results.

2 Data Assimilation Systems

In this section, we will give a brief overview on the NASA/DAO and the NCEP/NCAR data assimilation systems. Detailed descriptions can be found in Schubert et al. (1993) and Kalnay et al. (1996). There are differences between the two systems in many aspects, including the model characteristics, the analysis techniques, and the input data. These differences may at least partially account for the differences in the reanalysis datasets.

2.1 NASA/DAO system

The NASA/DAO dataset (Schubert et. al. 1993) is the multiyear reanalysis produced with version 1 of the Goddard Earth Observing System (GEOS-1). The general circulation model (GCM) is described in Takacs et al. (1994) and the analysis system is described in Pfaendtner et al. (1995). The analysis scheme consists of a 3-dimensional multivariate optimal interpolation (OI) carried out on 14 standard pressure levels extending from 1000 to 20 hPa. The GEOS-1 GCM is a gridpoint model employing the Aries/GEOS dynamical core described in Suarez and Takacs (1995). For the reanalysis the GCM was run at a horizontal resolution of 2° latitude by 2.5° longitude and with 20 sigma levels in the vertical (top at 10 hPa). The assimilation system does not include an initialization scheme and relies on the damping properties of a Matsuno time differencing scheme to control initial imbalances generated by the insertion of observations. However, the initial imbalances and spin-up have been greatly reduced by introducing an incremental analysis update (IAU) procedure (Bloom et al. 1996).

The GEOS-1 model has 4 levels below 850 hPa and 4 levels between 100 and 10 hPa which includes parameterizations of all major physical processes: radiation, convection,

large-scale precipitation, boundary layer physics, and vertical and horizontal diffusion. In the GEOS-1 system, the sea surface temperature (SST) is updated using the monthly mean blended SST analyses (Reynolds and Marsico 1993). The penetrative convection is parameterized using the Relaxed Arakawa-Schubert (RAS) scheme (Moorthi and Suarez 1992). The soil moisture in the NASA/DAO assimilation system is computed off-line based on a simple bucket model using observed monthly mean surface air temperature and precipitation (Schemm et al. 1992).

2.2 NCEP/NCAR system

The NCEP/NCAR reanalysis products were also produced with a fixed assimilation system (Kalnay et. al. 1996) consisting of the NCEP Medium Range Forecast spectral model and the operational NCEP Spectral Statistical Interpolation scheme, a 3-dimensional variational analysis scheme (SSI; Parrish and Derber 1992) with improved error statistics and a divergence tendency constrain. The assimilation was performed at a horizontal resolution of T62 and with 28 sigma levels in the vertical (top at about 3 hPa). The implementation of SSI in the analysis makes it unnecessary to employ an initialization step. The analysis is performed on the model sigma levels employing mandatory pressure level data, and significant level winds. The bogus surface data (POABs) from the Australian Bureau of Meteorology are also assimilated in the NCEP/NCAR system [1].

This version of the NCEP spectral model has 7 levels below 850 hPa and 6levels between 100 and 10 hPa which includes parameterizations of all major physical processes, including radiation (diurnal cycle and interaction with clouds), convection, large-scale precipitation, shallow convection, boundary layer physics, interactive surface hydrology, gravity wave drag, and vertical and horizontal diffusion. Details of this model are described in Kanamitsu (1989). Recent changes are the use of a simplified Arakawa-Schubert convective parameterization scheme (Pan and Wu 1994) and a diagnostic cloud scheme (Campana et al. 1994). The NCEP/NCAR system incorporates the weekly global optimal interpolation SST analyses (Reynolds and Smith 1994) from 1982-present and the UKMO GISST for earlier years. The soil moisture is updated during the analysis cycle with a simple soil model (Pan and Mahrt 1987).

3 Intercomparison

In this section, we compare the seasonal means and their interannual vaiability from the NASA/DAO and NCEP/NCAR (hereafter we use DAO and NCEP for simplicity) reanal-

[1] The bogus data were inadvertently incorporated with a 180° phase shift in the NCEP product.

yses for various quantities. Conventional definitions of seasons are used in this study, *i.e.*, December-January-February (DJF) for northern winter season, March-April-May (MAM) for northern spring season, June-July-August (JJA) for northern summer season, and September-October-November (SON) for northern fall season. Both the seasonal means and their interannual variability (or more specifically the standard deviation) are based on the 15-year time period March 1980 through February 1995, which was the time period common to both reanalyses at the time of this study. The results of the zonally averaged prognostic fields are presented first. Next the global maps are presented for various fields at selected levels, including one level in the lower stratosphere. The intercomparison of selected diagnostic variables is presented in subsection 3.3. We note that this is primarily intended as an atlas of seasonal means and their variability, and as convenient reference for assessing the uncertainties in these quantities based on the differences between the two reanalyses. As such the discussions of the various figures are rather terse and are intended only to highlight some of the salient features.

3.1 Zonal mean fields

Figures 1 – 30 present the seasonal means and the interannual standard deviations of zonally averaged seasonal mean quantities (zonal mean zonal (u) and meridional (v) winds, zonal mean temperature (T), zonal mean specific humidity (q), and mass streamfunction). The seasonal means of u-wind are very similar in the two reanalyses. The difference maps (Fig.3) show, however, that during all four seasons the DAO product has weaker easterlies in tropics, weaker westerlies in the subtropics and stronger westerlies in the middle and high latitudes than the NCEP product. The differences in the middle and high latitudes of the northern hemisphere are smaller than in the southern hemisphere. The seasonal mean v-wind has similar patterns in the two reanalyses (Figs. 4 and 5). However, large differences in the magnitudes are seen in DJF and MAM indicating a considerably weaker Hadley Cell during these months in the DAO product. During JJA and SON the DAO Hadley Cell is somewhat stronger with the upper branch extending further into the middle troposphere just north of the equator.

For the zonal mean temperature profiles (Figs. 7–9), the seasonal means clearly show systematic differences between the DAO and NCEP products; the DAO temperature is warmer in much of the troposphere and colder than NCEP above 100 hPa and in the middle troposphere (300–500 hPa) near the south pole. The large differences near the surface in the southern hemisphere (SH) polar region are likely related to the interpolation and extrapolation in regions of high topography. The zonal mean moisture profiles (Figs. 10–12) show that the DAO product is wetter in the tropical middle troposphere and northern hemisphere (NH) subtropics near the surface, and drier between the surface layer and approximately 850 hPa. In the midlatitudes, the DAO data is consistently drier than the NCEP product

above the surface layer. The JJA moisture differences are somewhat different from other seasons with the DAO wetter in the SH subtropics and substantially drier in the NH middle and high latitudes. The mass streamfunction (Figs. 13–15) shows that the DAO product has a stronger Hadley cell in JJA and weaker Hadley cell in DJF, indicating a stronger annual cycle in the DAO data. This is consistent with the v-wind results shown previously.

The interannual variability of the seasonal mean zonal mean u-wind (Figs. 16–18) is quite similar in the two products, except in the tropical lower stratosphere where the NCEP product shows considerably more variability, and in the SH polar regions (Fig.18), where the DAO product shows more variability. The DAO product shows more variability in the v-wind for all seasons except MAM (Figs. 19–21). During this season the NCEP product exhibits its largest variability, while the DAO product has the smallest variability. The patterns in the temperature variability (Figs. 22–24) are quite similar in the two reanalyses but large differences are observed in the troposphere near the SH polar region, with the DAO product showing greater variability. The DAO product shows consistently larger variability in the moisture profiles (Figs. 25–27) and the mass streamfunction (Figs. 28–30).

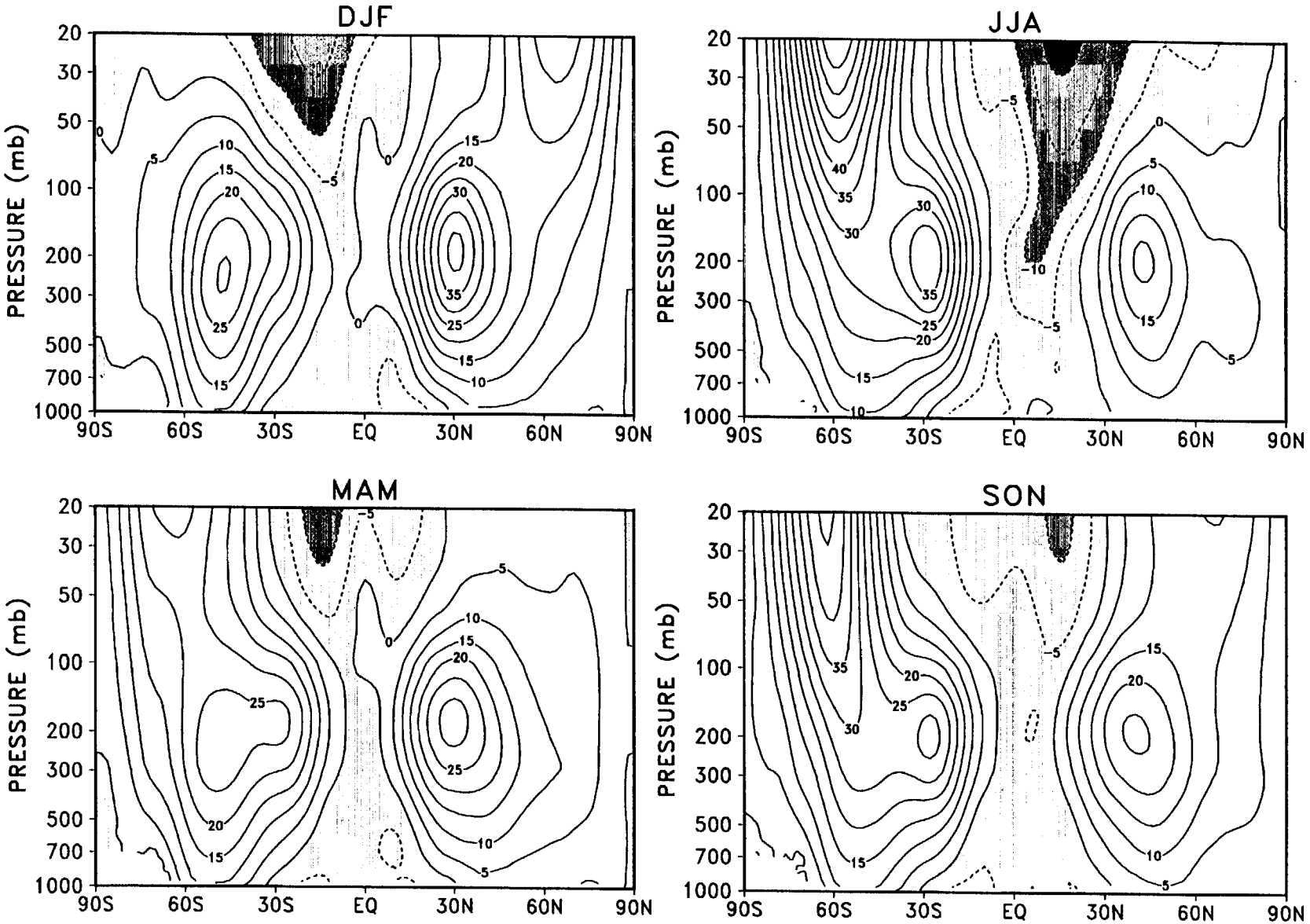

Figure 1: Seasonal means of zonally averaged u-wind for DAO reanalysis during 1980–1995. The contour interval is 5 m s^{-1}. Negative values are shaded.

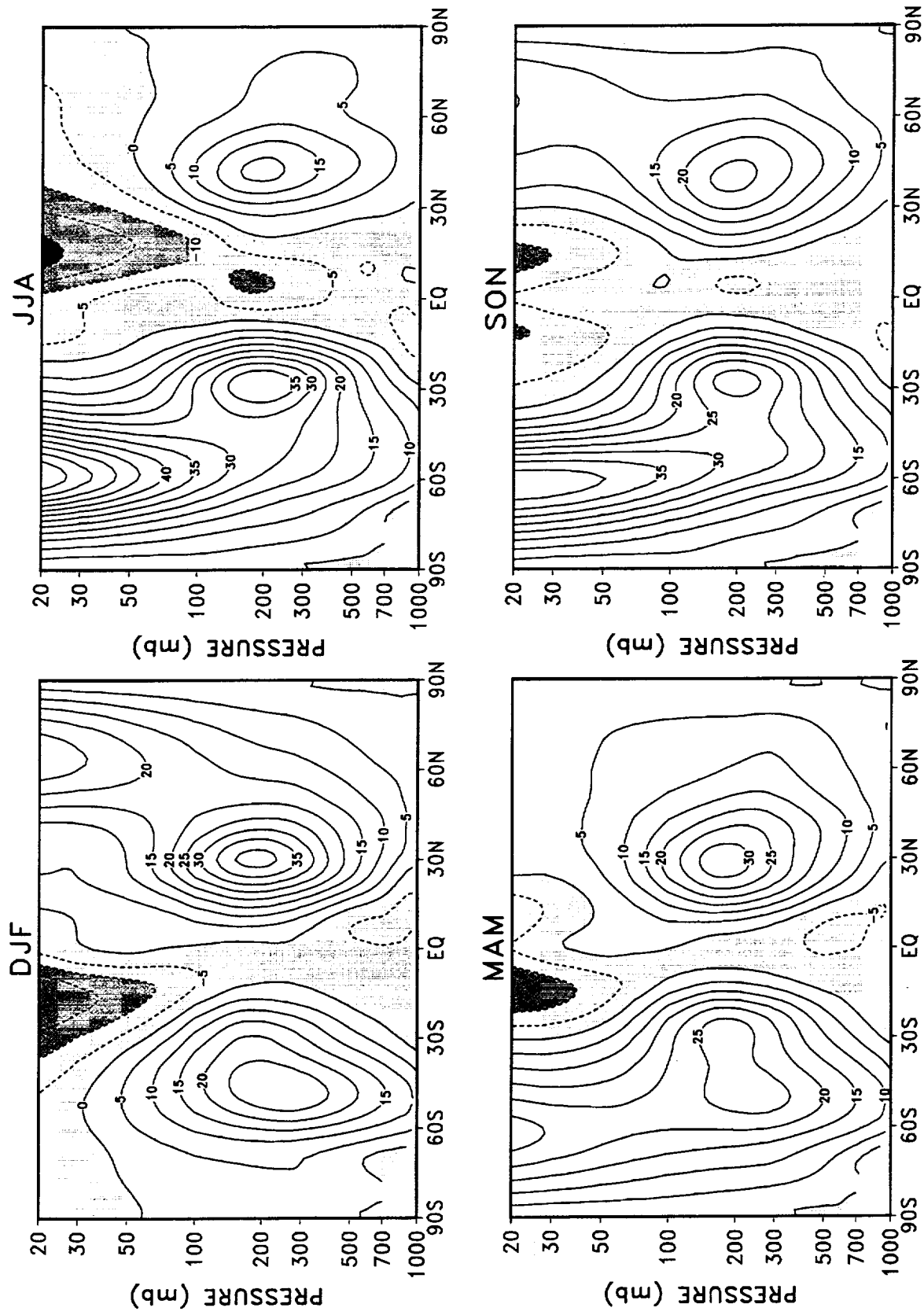

Figure 2: Seasonal means of zonally averaged u-wind for NCEP/NCAR reanalysis during 1980–1995. The contour interval is 5 m s^{-1}. Negative values are shaded.

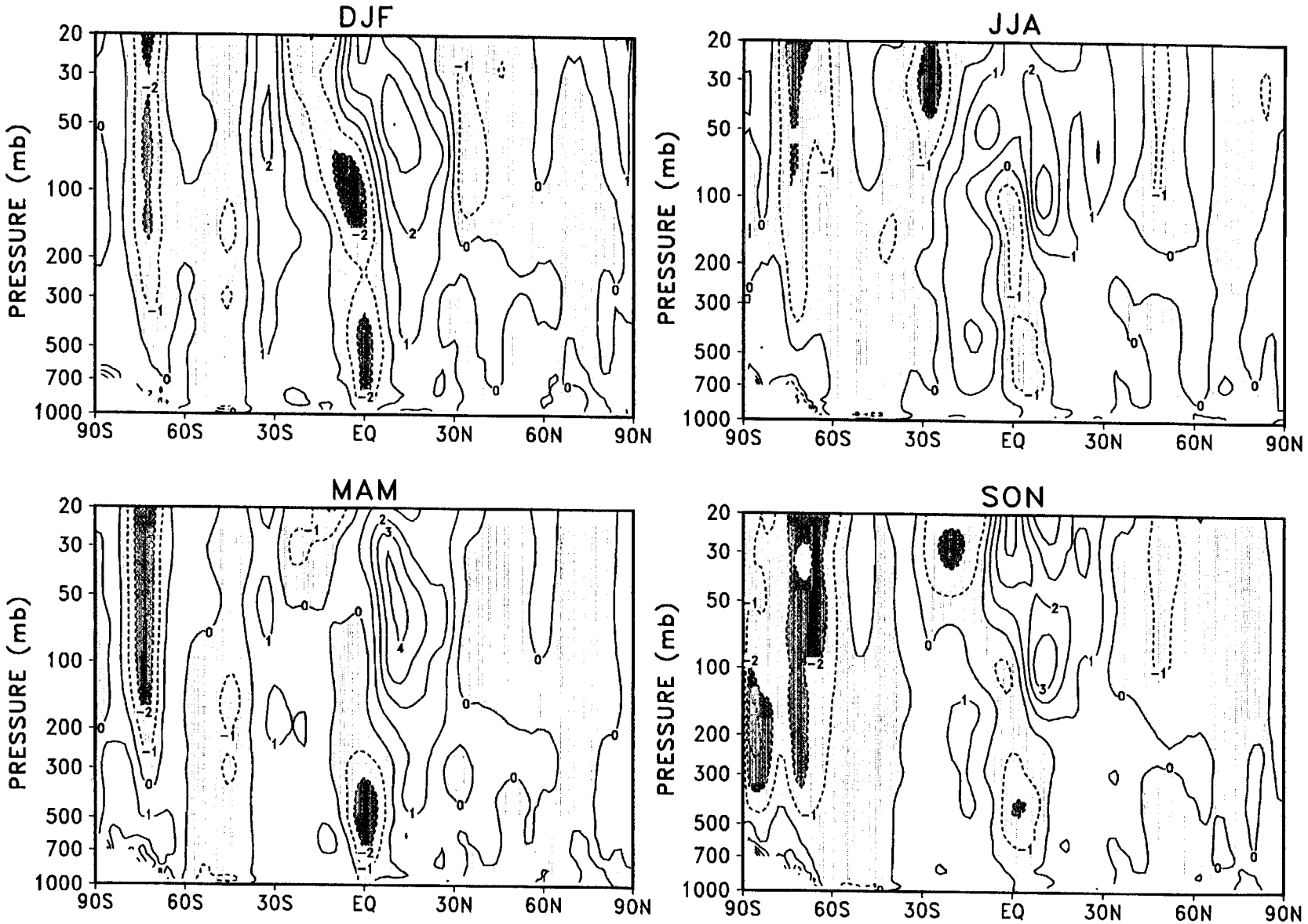

Figure 3: Difference of the seasonal means of zonally averaged u-wind during 1980–1995 (NCEP/NCAR minus DAO). The contour interval is 1 m s^{-1}. Negative values are shaded.

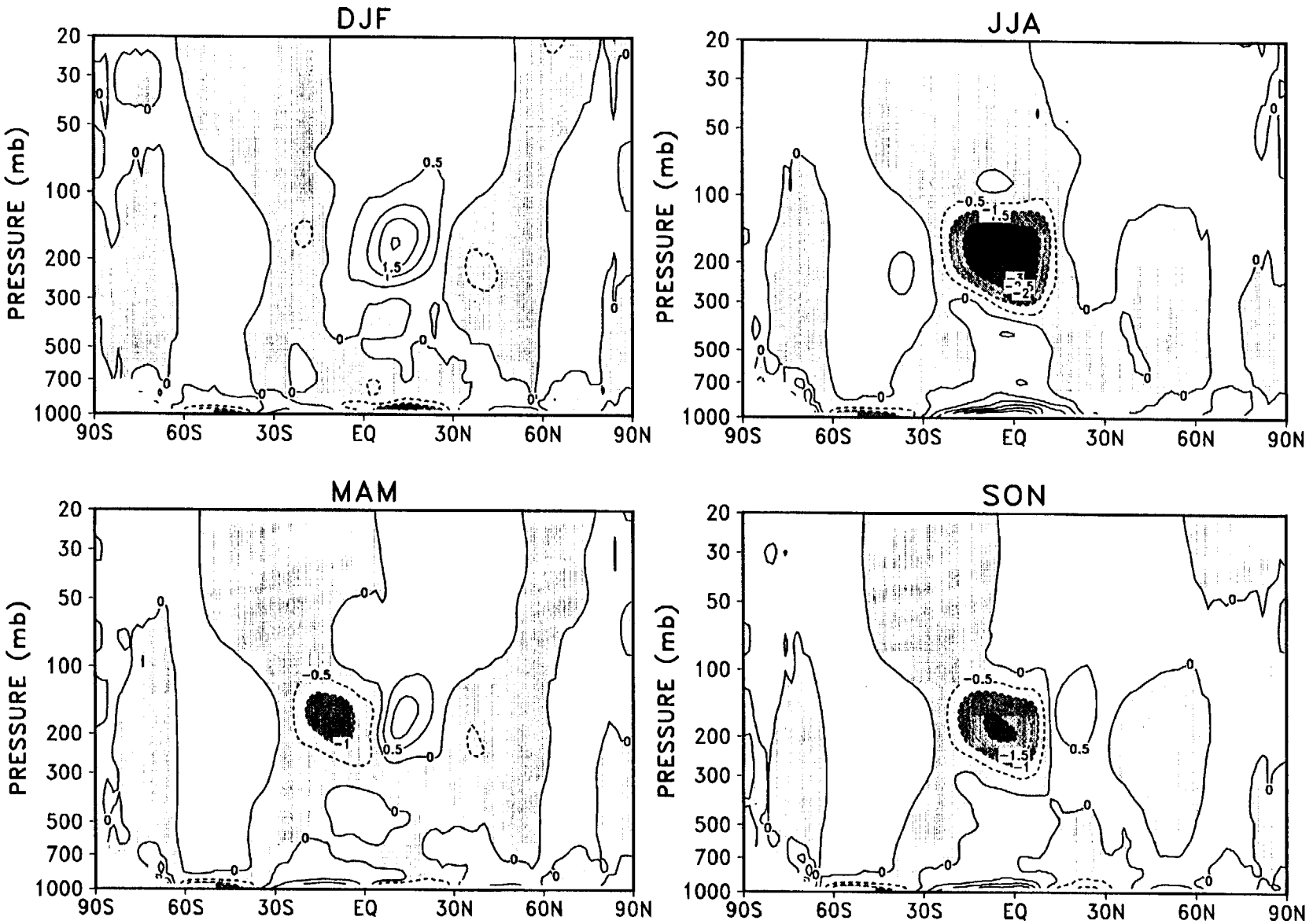

Figure 4: Seasonal means of zonally averaged v-wind for DAO reanalysis during 1980–1995. The contour interval is 0.5 m s^{-1}. Negative values are shaded.

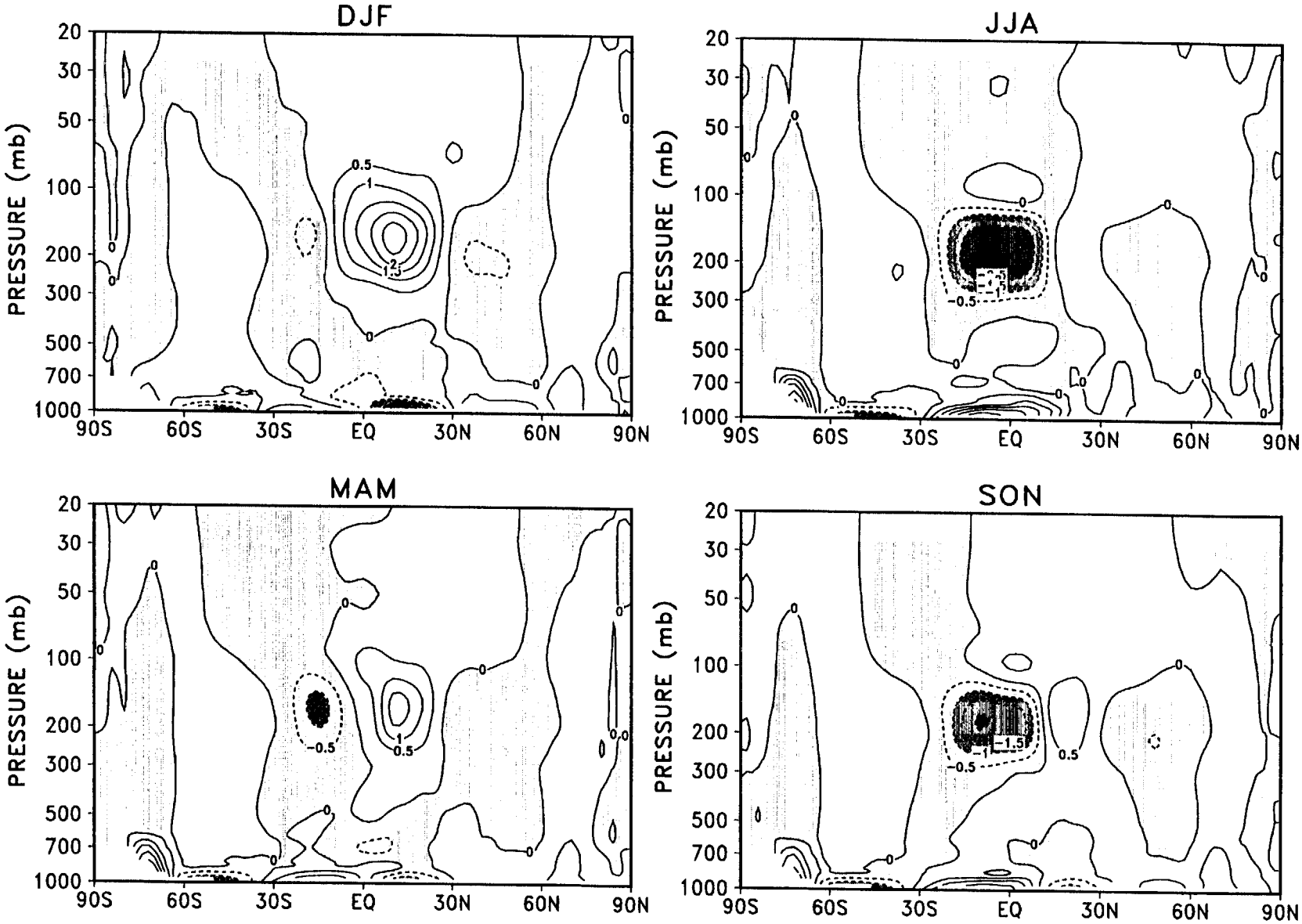

Figure 5: Seasonal means of zonally averaged v-wind for NCEP/NCAR reanalysis during 1980–1995. The contour interval is 0.5 m s^{-1}. Negative values are shaded.

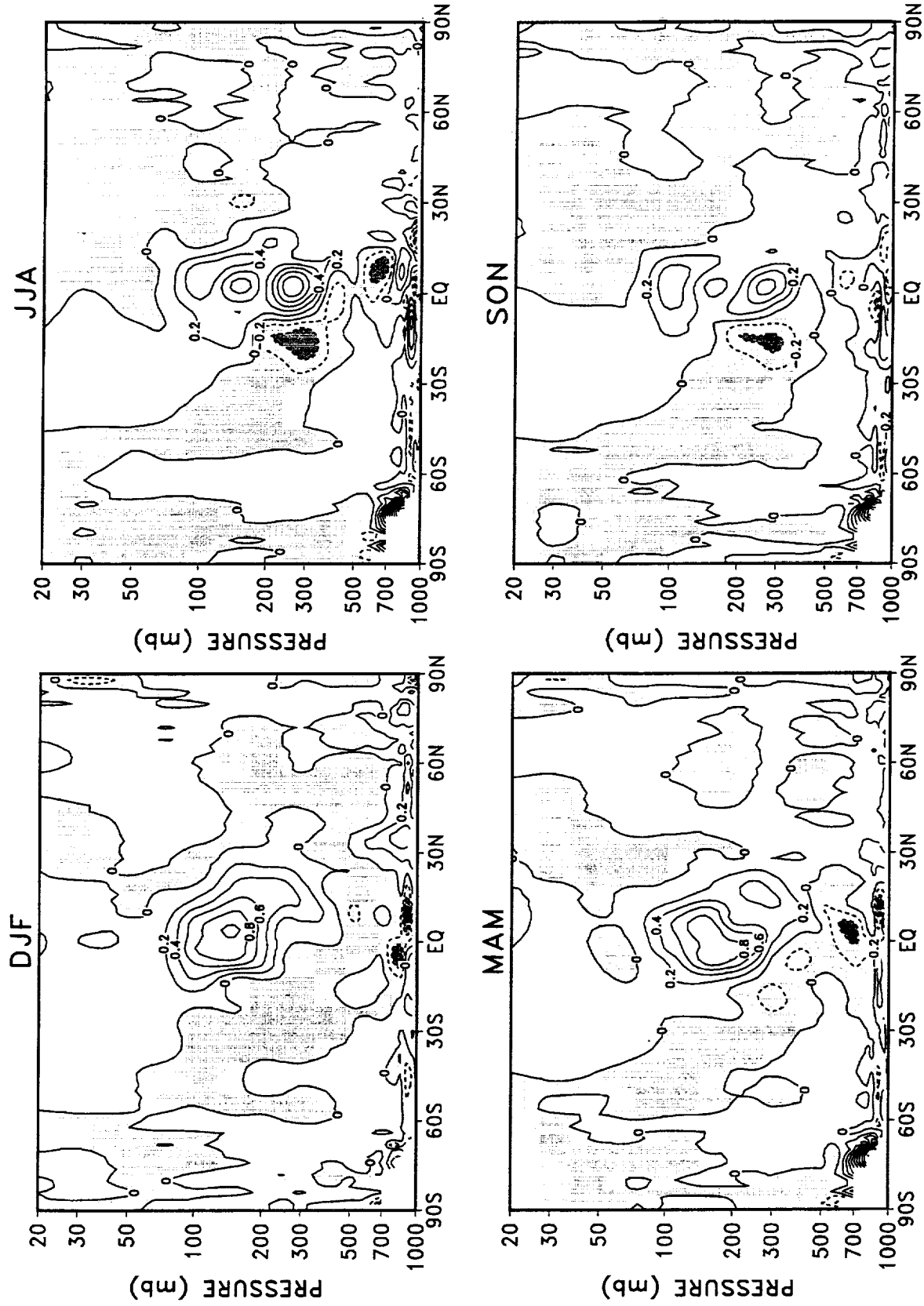

Figure 6: Difference of the seasonal means of zonally averaged v-wind during 1980–1995 (NCEP/NCAR minus DAO). The contour interval is 0.2 m s^{-1}. Negative values are shaded.

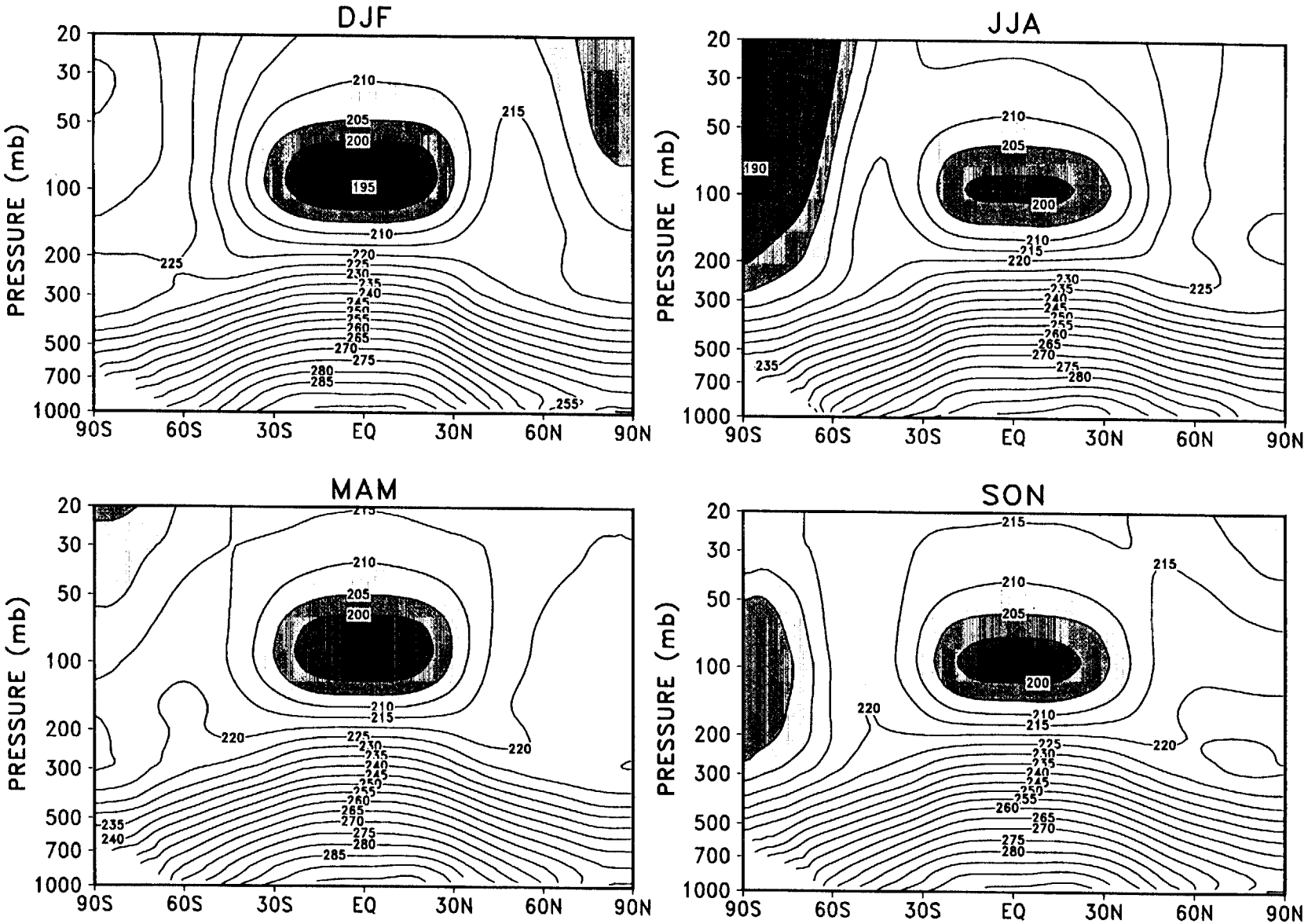

Figure 7: Seasonal means of zonally averaged temperature for DAO reanalysis during 1980–1995. The contour interval is 5°K. Values less than 210°K are shaded.

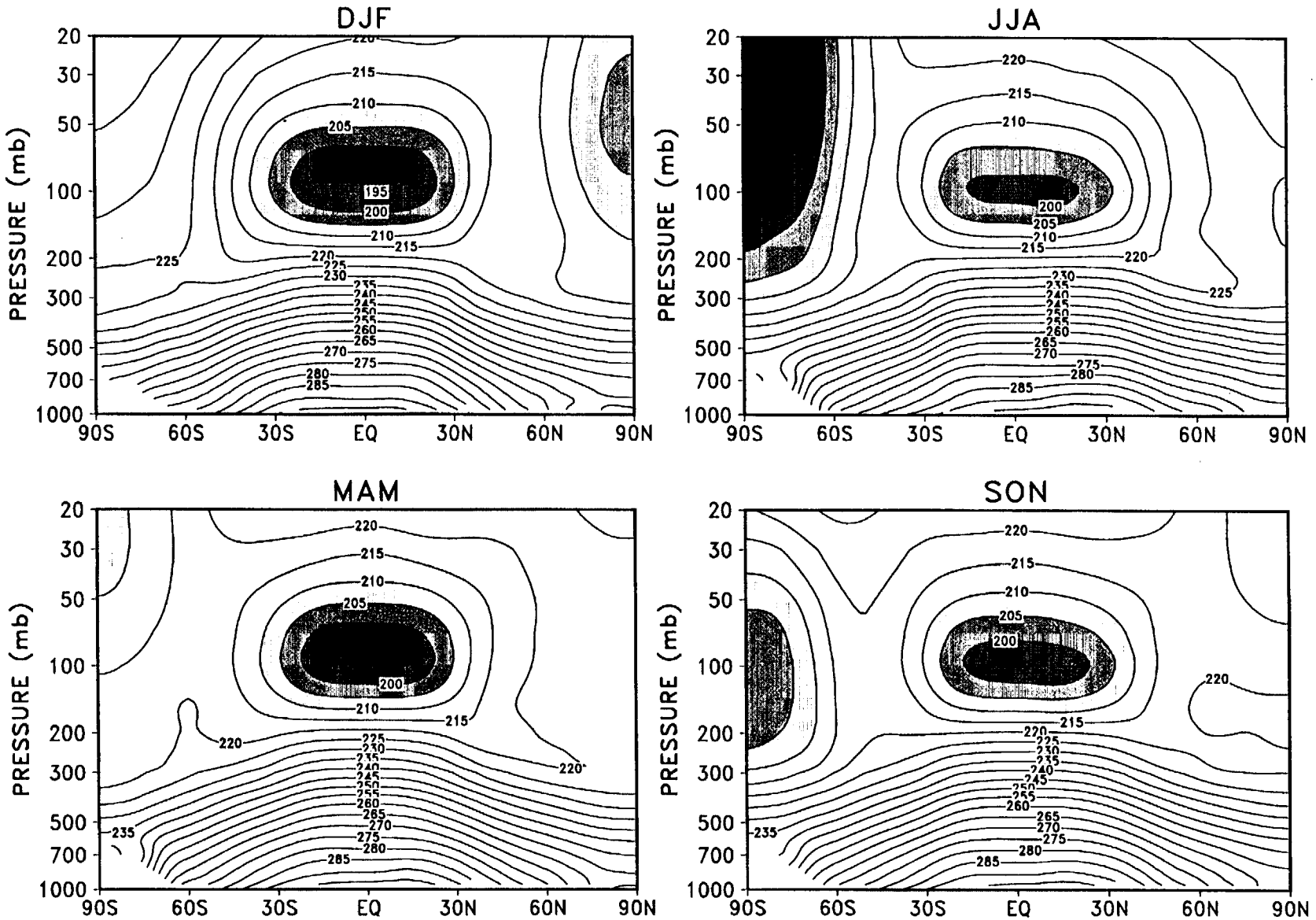

Figure 8: Seasonal means of zonally averaged temperature for NCEP/NCAR reanalysis during 1980–1995. The contour interval is 5°K. Values less than 210°K are shaded.

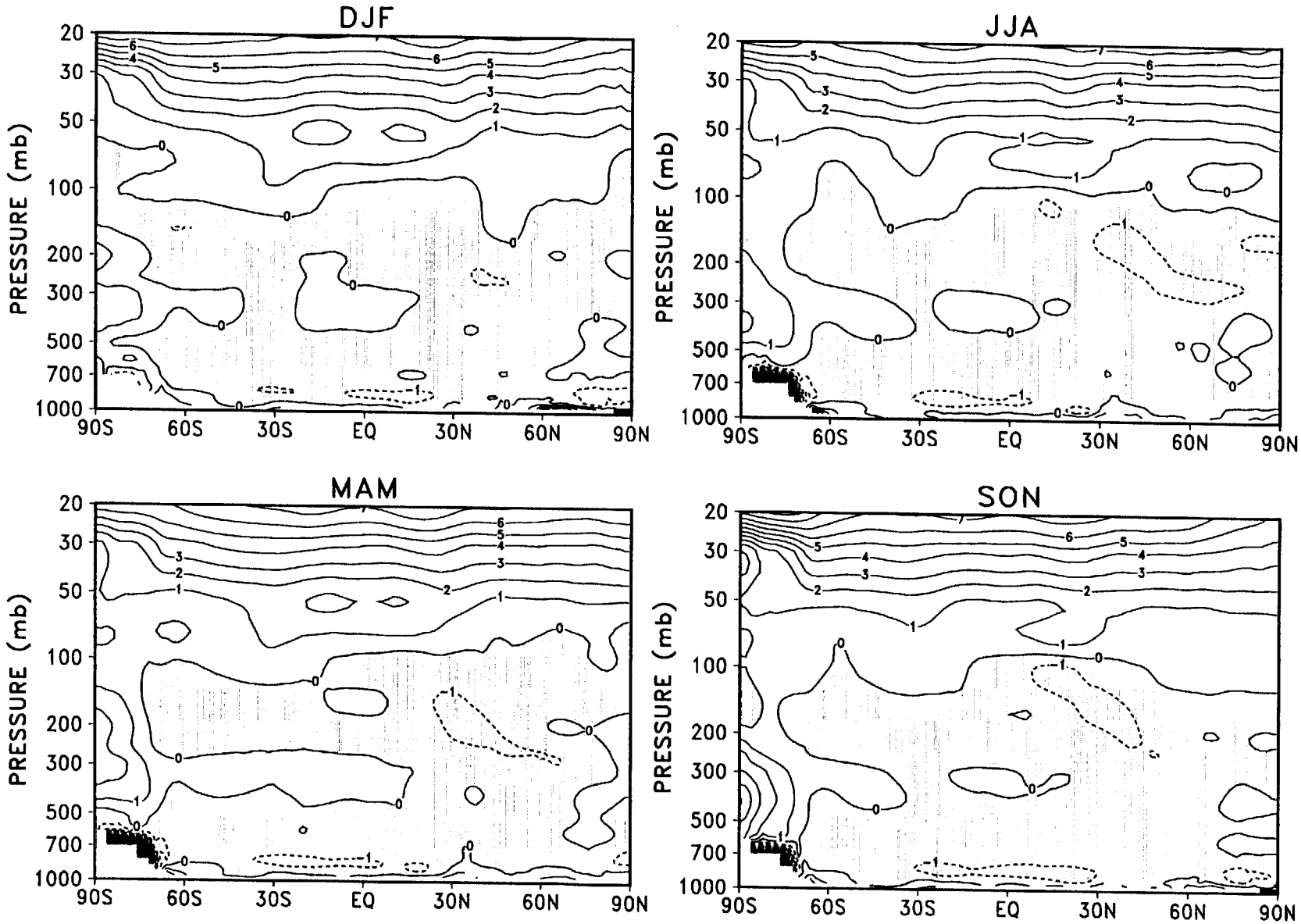

Figure 9: Difference of the seasonal means of zonally averaged temperature during 1980–1995 (NCEP/NCAR minus DAO). The contour interval is 1°K. Negative values are shaded.

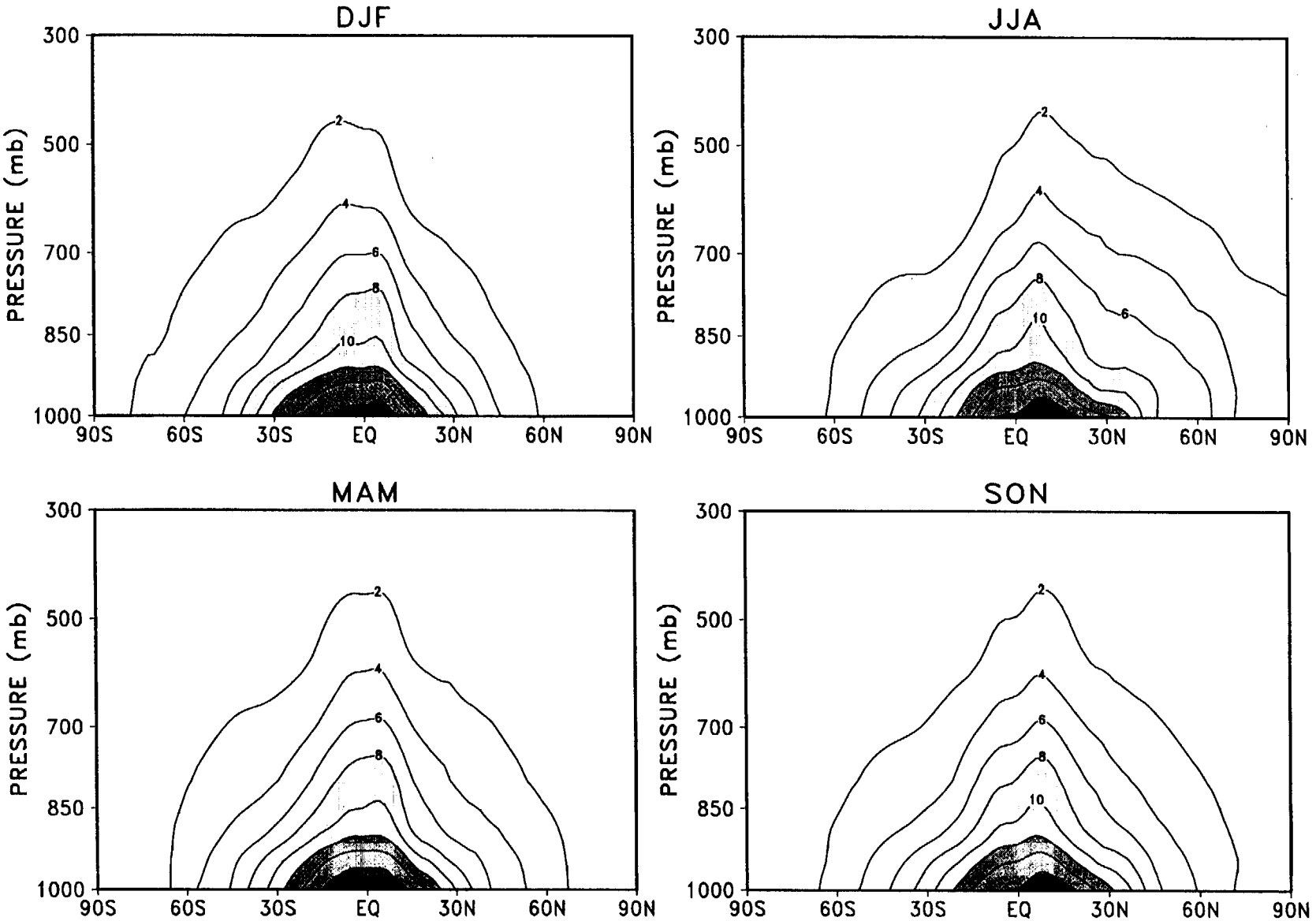

Figure 10: Seasonal means of zonally averaged specific humidity for DAO reanalysis during 1980–1995. The contour interval is 2 g kg^{-1}. Values larger than 8 g kg^{-1} are shaded.

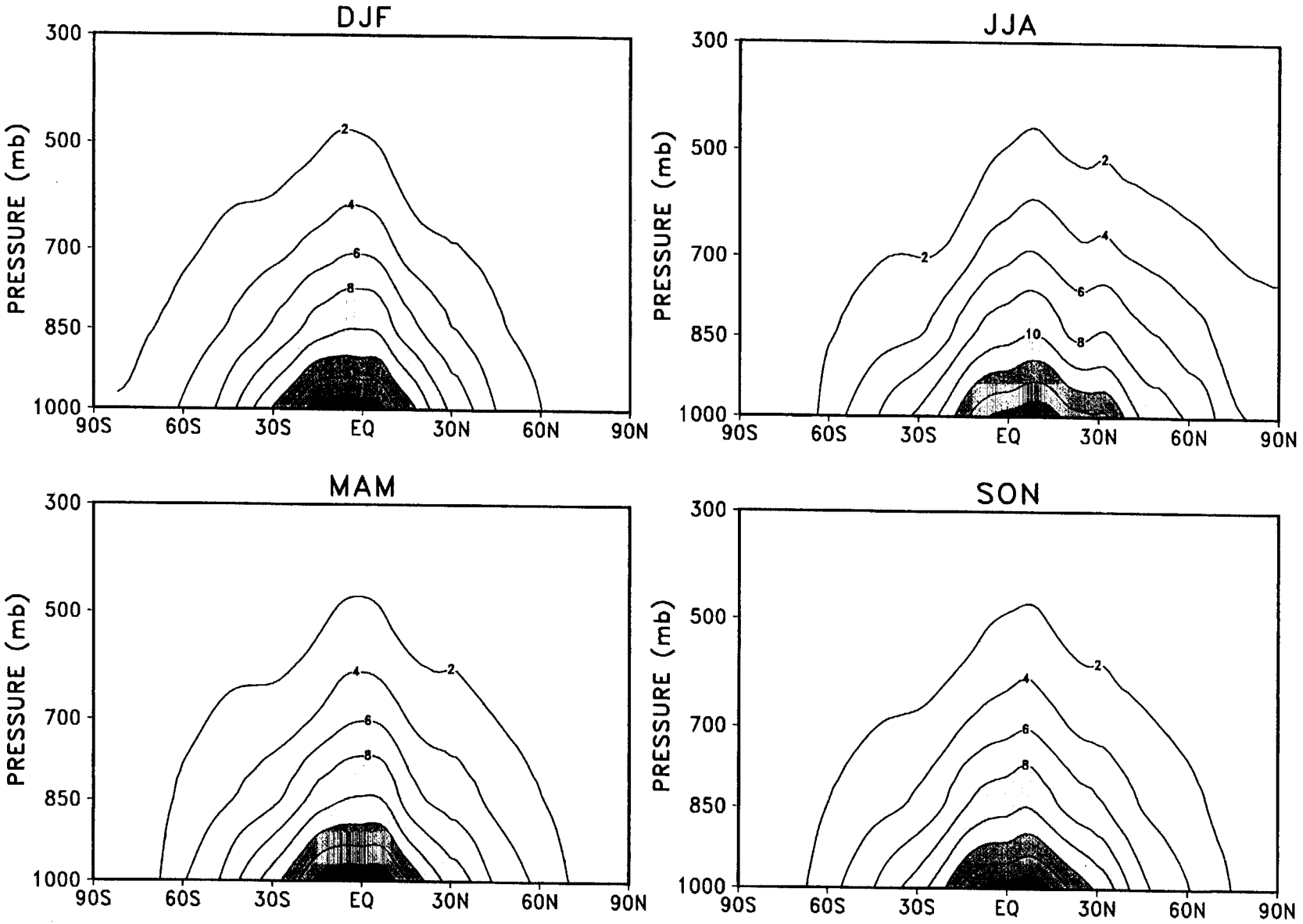

Figure 11: Seasonal means of zonally averaged specific humidity for NCEP/NCAR reanalysis during 1980–1995. The contour interval is 2 g kg^{-1}. Values larger than 8 g kg^{-1} are shaded.

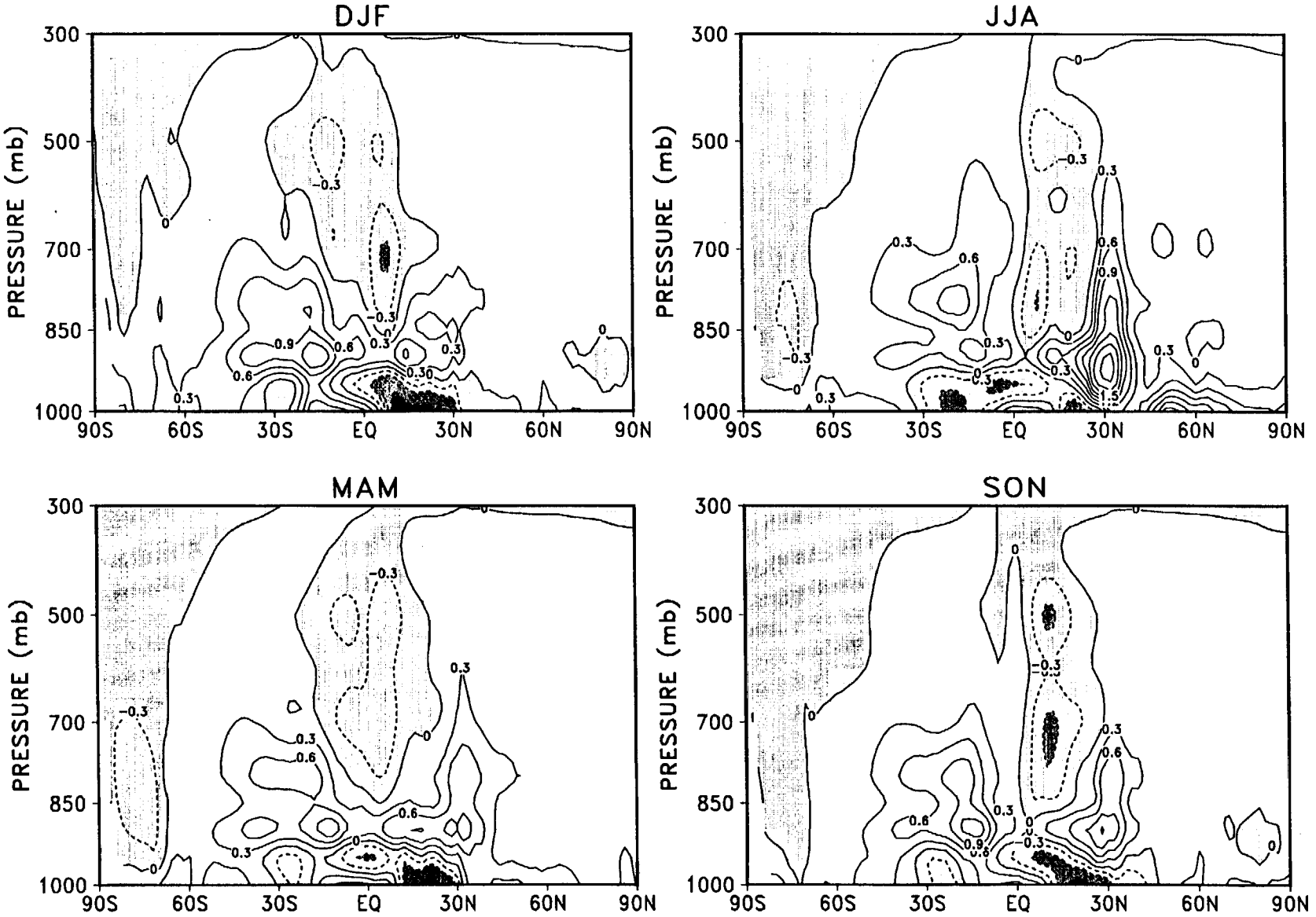

Figure 12: Difference of the seasonal means of zonally averaged specific humidity during 1980–1995 (NCEP/NCAR minus DAO). The contour interval is 0.3 g kg^{-1}. Negative values are shaded.

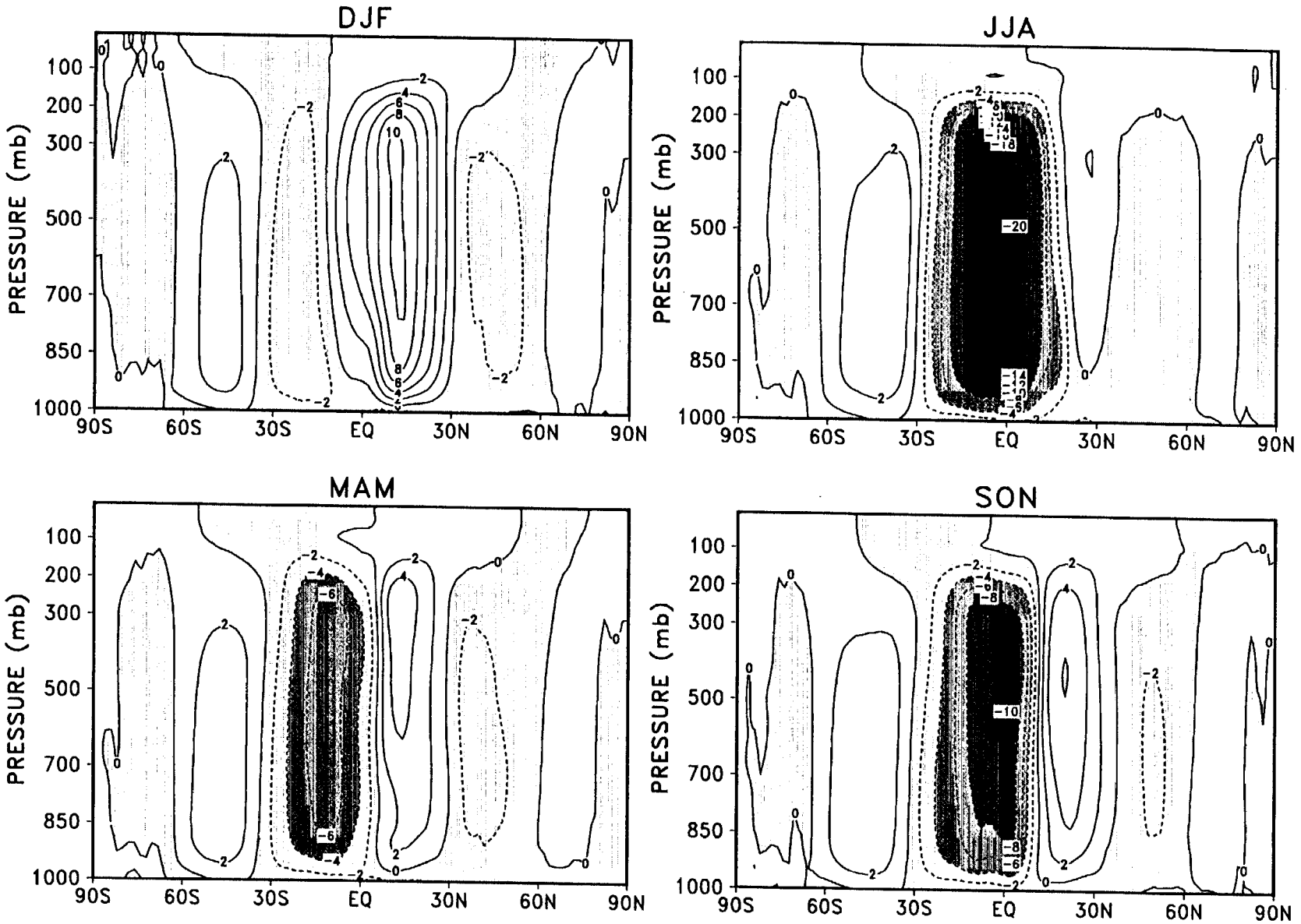

Figure 13: Seasonal means of zonally averaged mass stream function for DAO reanalysis during 1980–1995. The contour interval is 2×10^{10} kg s^{-1}. Negative values are shaded.

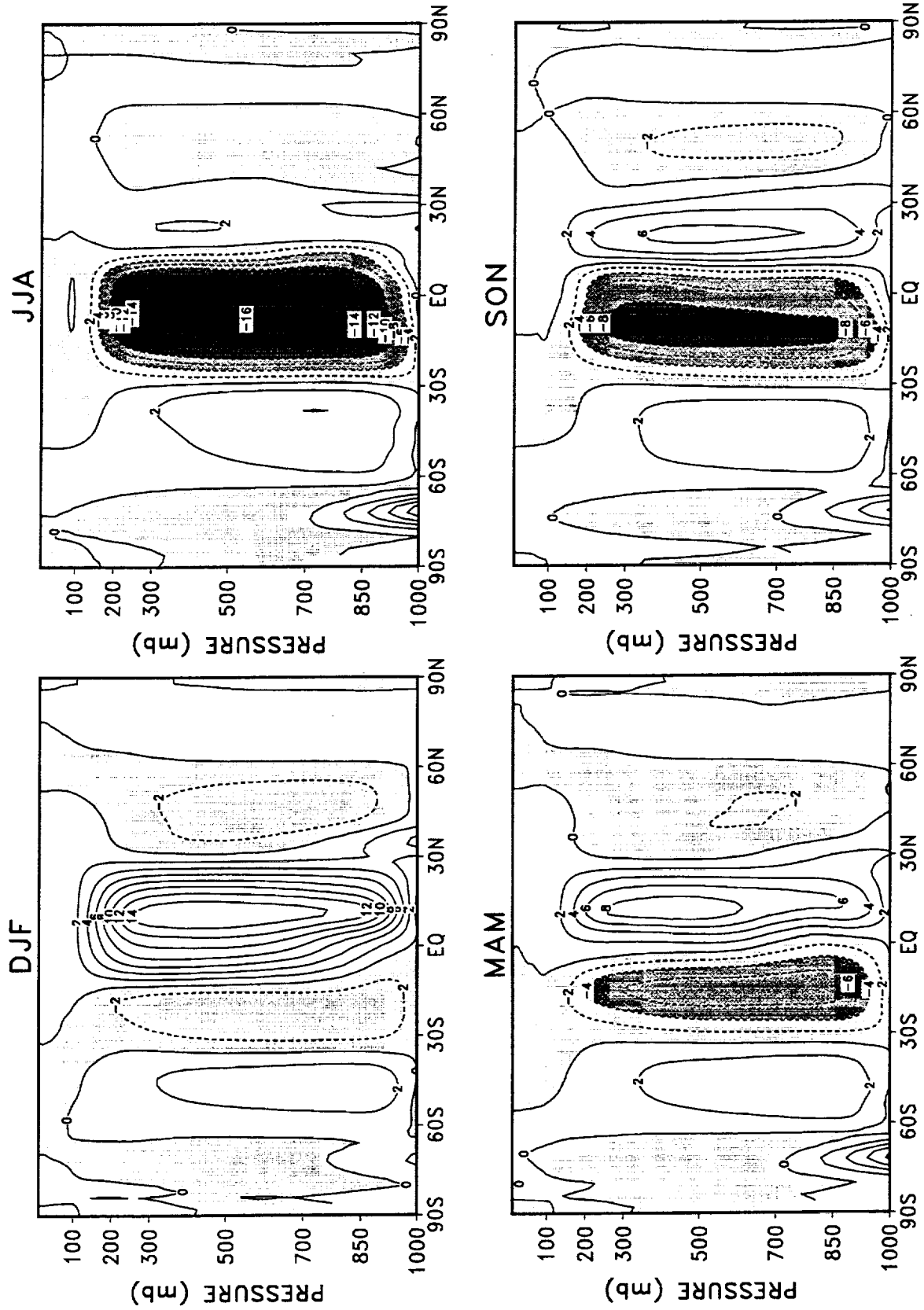

Figure 14: Seasonal means of zonally averaged mass stream function for NCEP/NCAR reanalysis during 1980–1995. The contour interval is 2×10^{10} kg s^{-1}. Negative values are shaded.

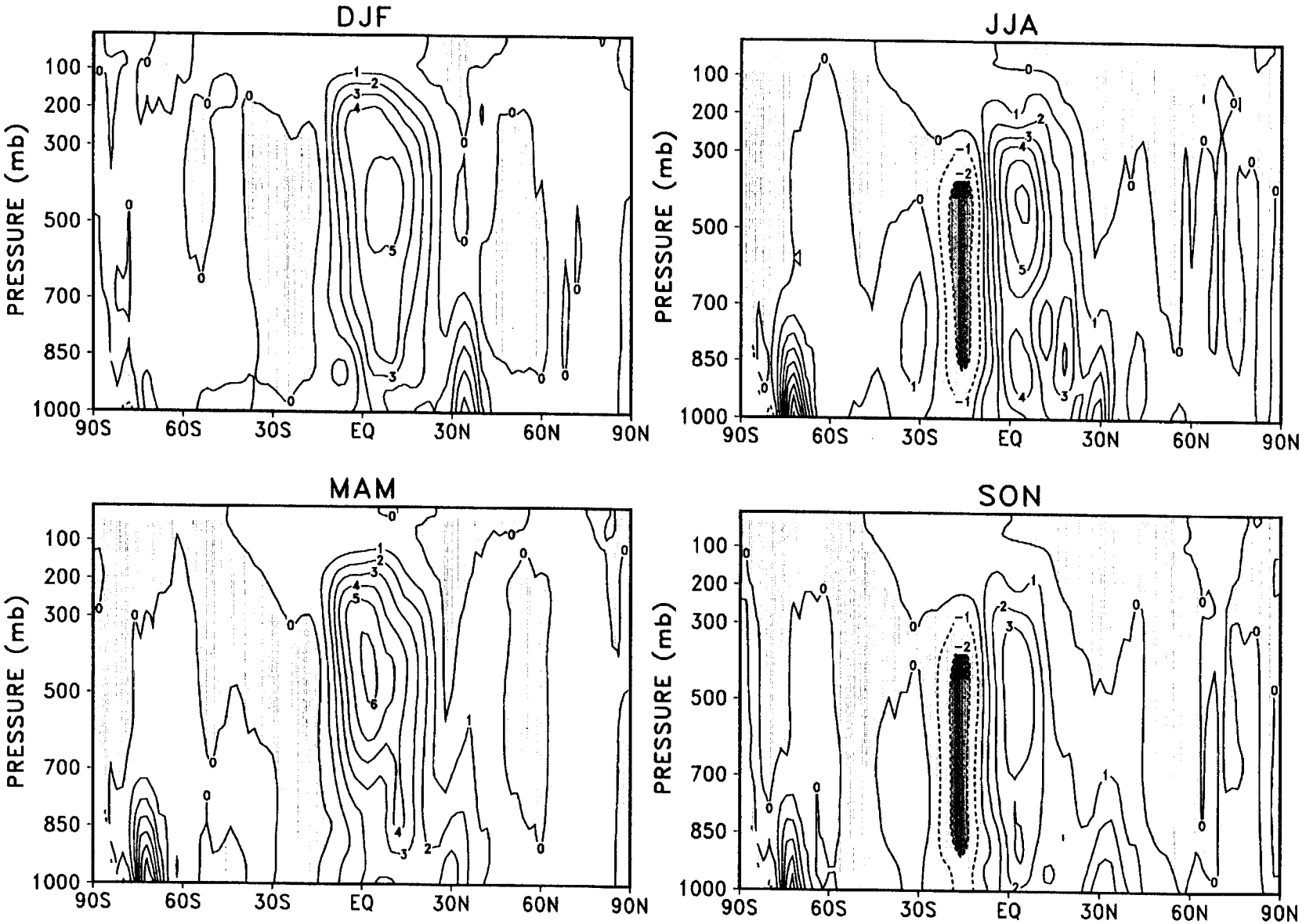

Figure 15: Difference of the seasonal means of zonally averaged mass stream function during 1980–1995 (NCEP/NCAR minus DAO). The contour interval is 1×10^{10} kg s^{-1}. Negative values are shaded.

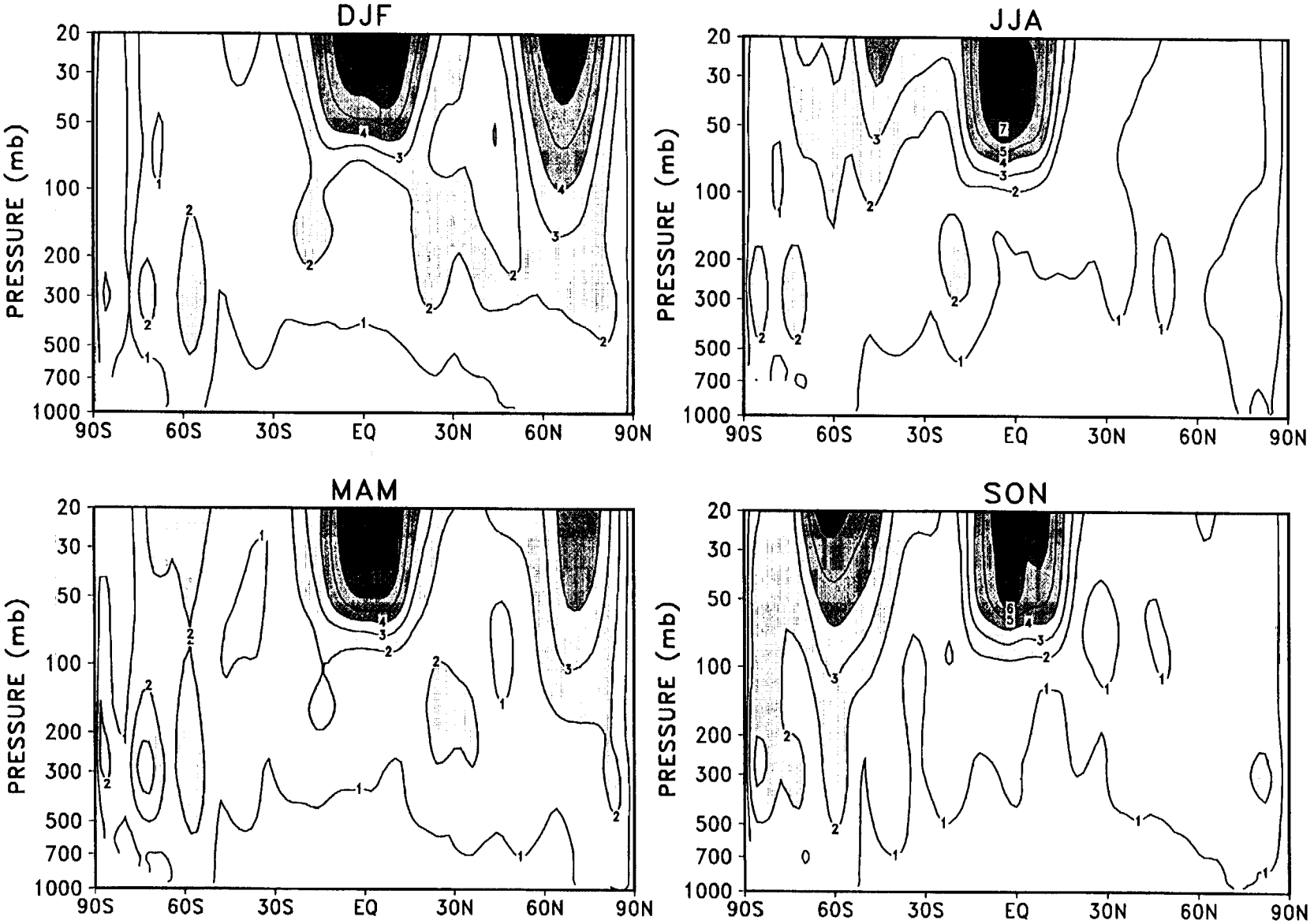

Figure 16: Standard deviations of seasonal mean zonally averaged u-wind for DAO reanalysis during 1980–1995. The contour interval is 1 m s^{-1}. Values larger than 2 m s^{-1} are shaded.

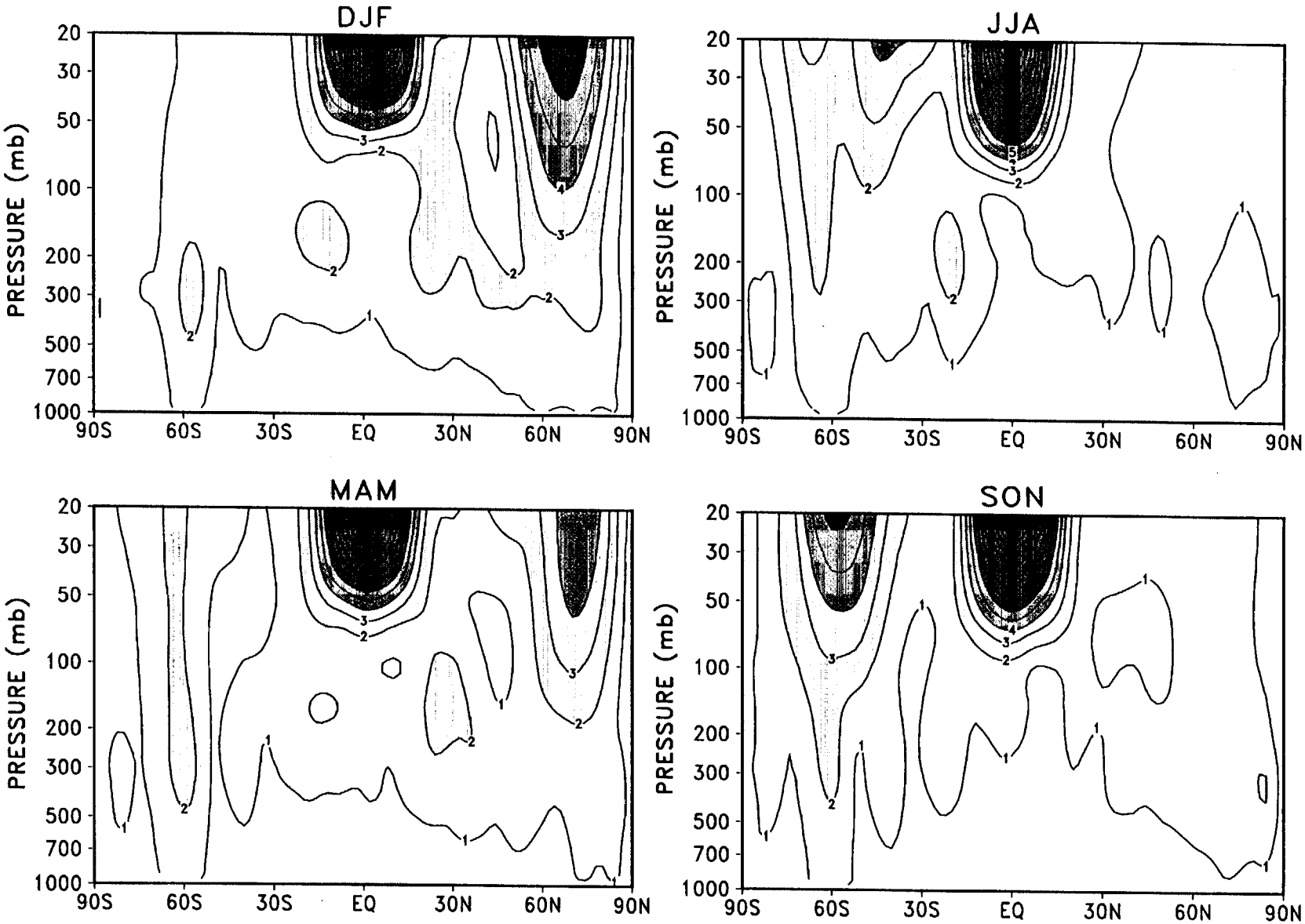

Figure 17: Standard deviations of seasonal mean zonally averaged u-wind for NCEP/NCAR reanalysis during 1980–1995. The contour interval is 1 m s^{-1}. Values larger than 2 m s^{-1} are shaded.

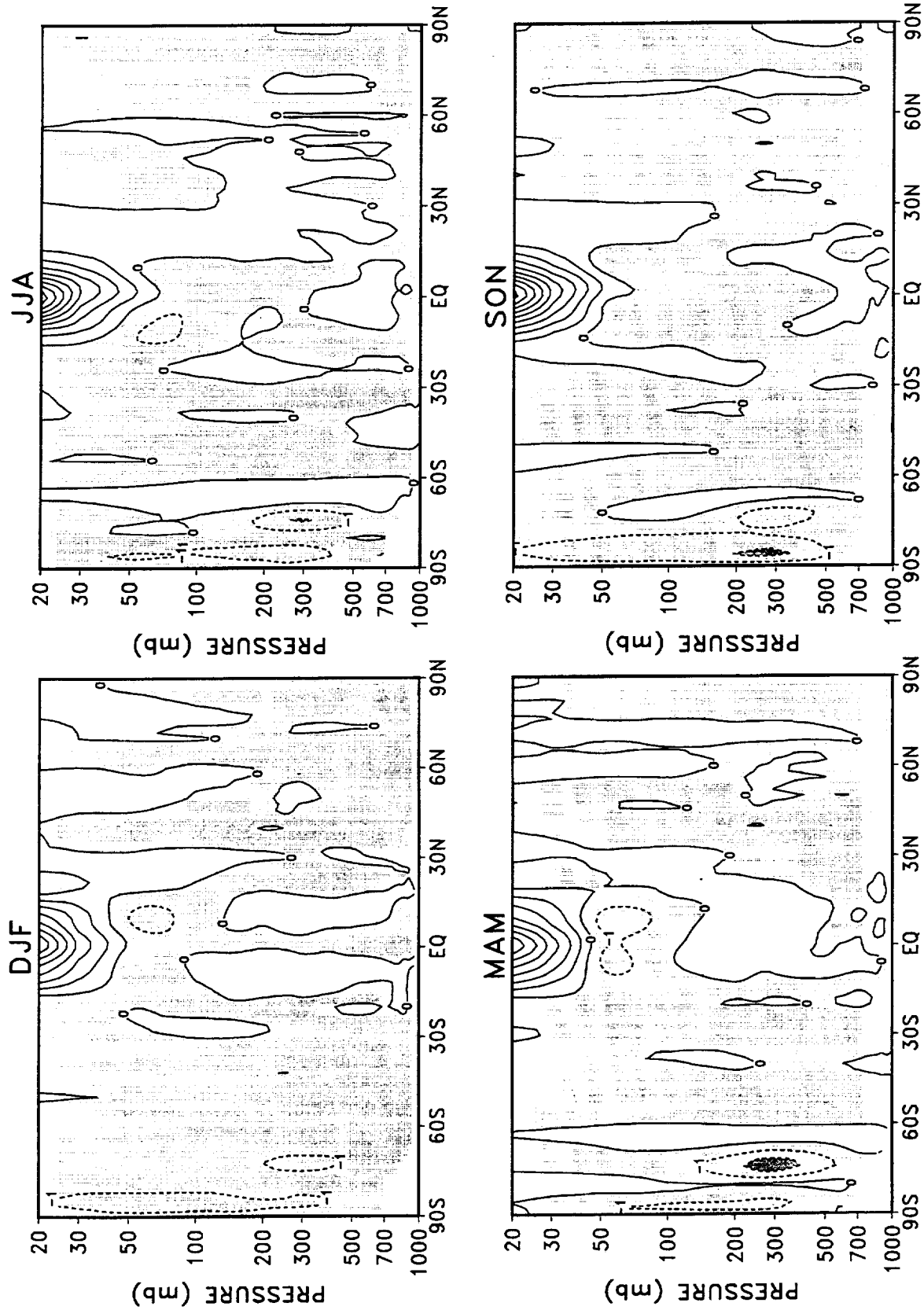

Figure 18: Differences of the standard deviations of seasonal mean zonally averaged u-wind during 1980–1995 (NCEP/NCAR minus DAO). The contour interval is 1 m s^{-1}. Negative values are shaded.

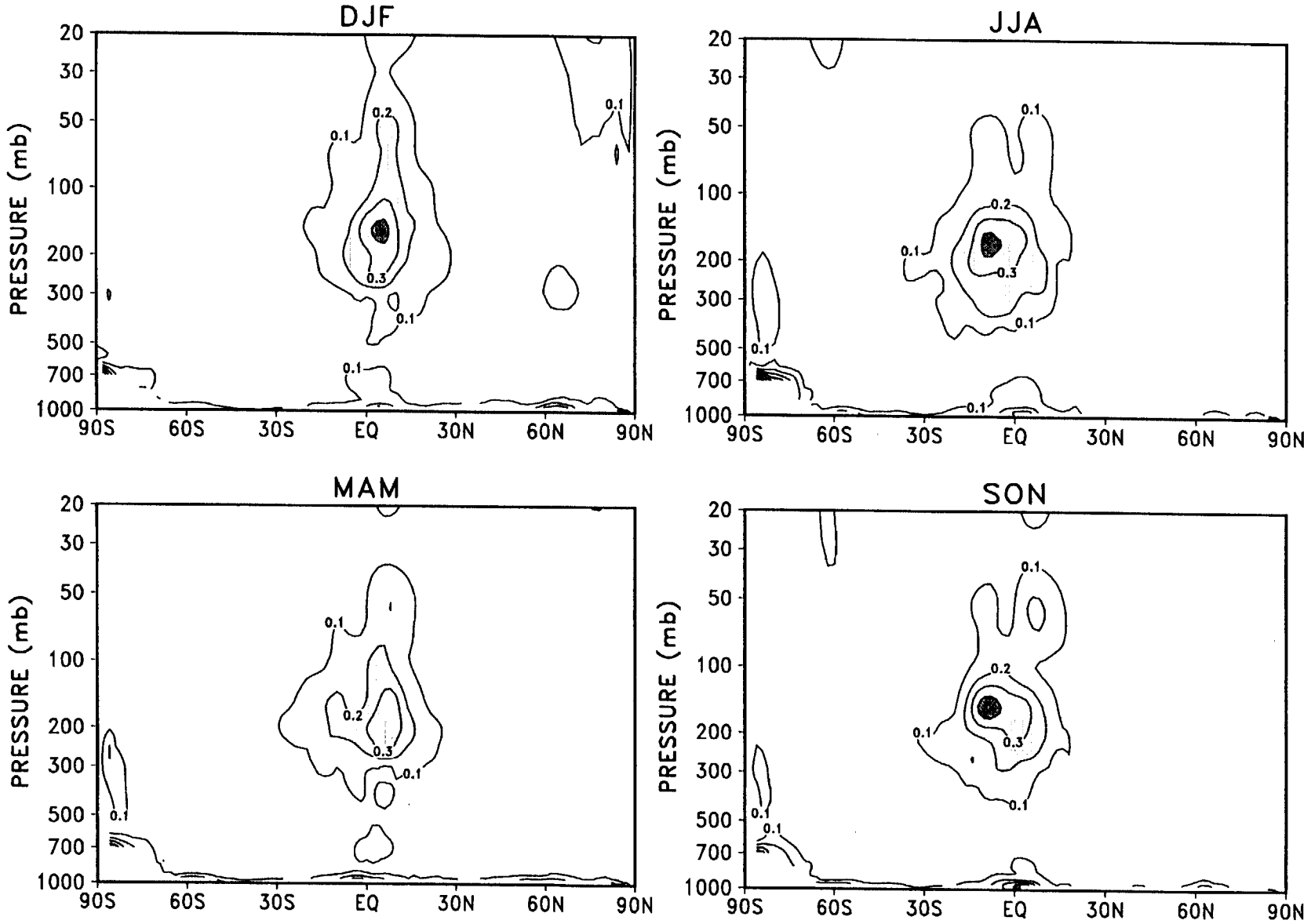

Figure 19: Standard deviations of seasonal mean zonally averaged v-wind for DAO reanalysis during 1980–1995. The contour interval is 0.1 m s^{-1}. Values larger than 0.2 m s^{-1} are shaded.

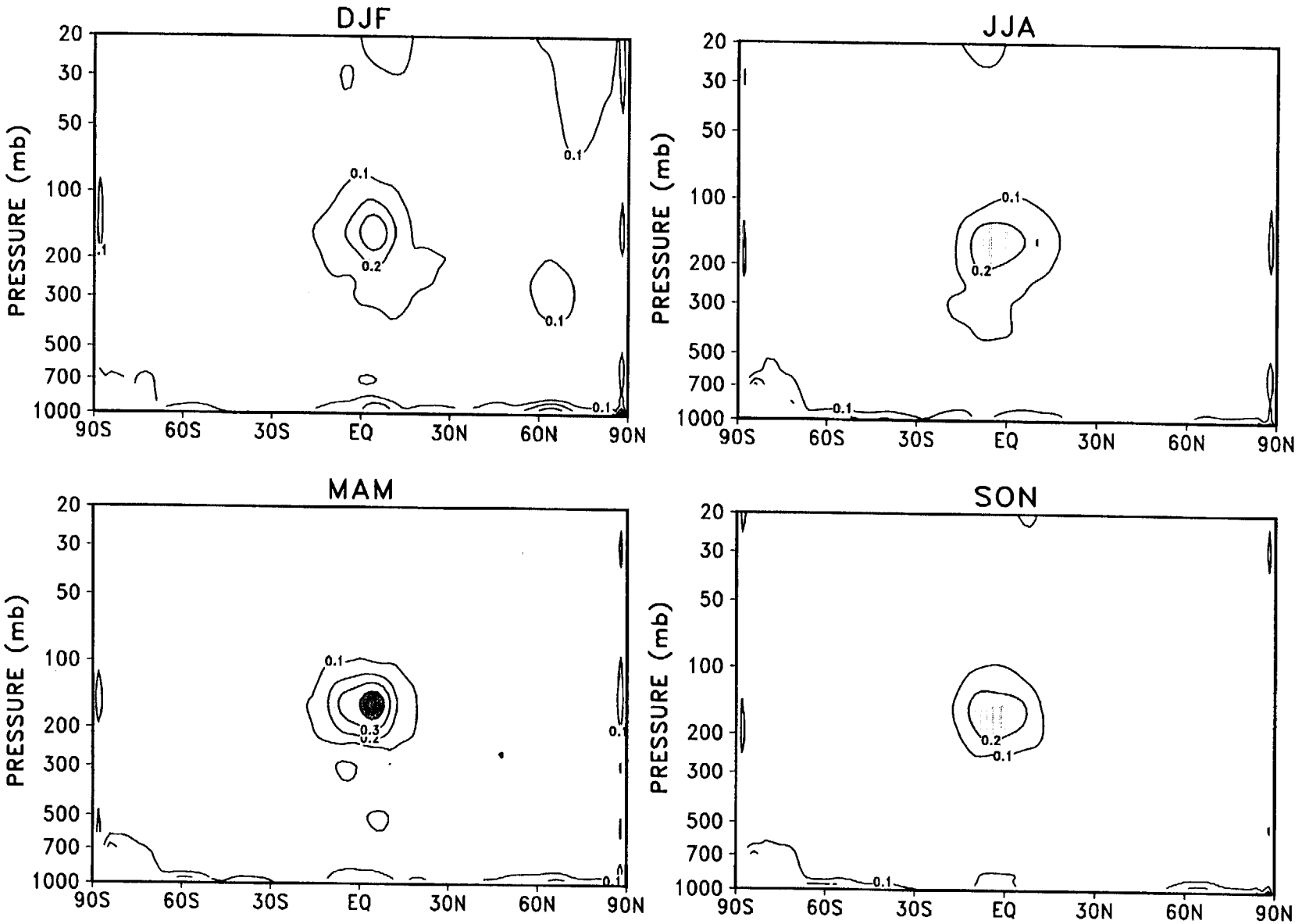

Figure 20: Standard deviations of seasonal mean zonally averaged v-wind for NCEP/NCAR reanalysis during 1980–1995. The contour interval is 0.1 m s^{-1}. Values larger than 0.2 m s^{-1} are shaded.

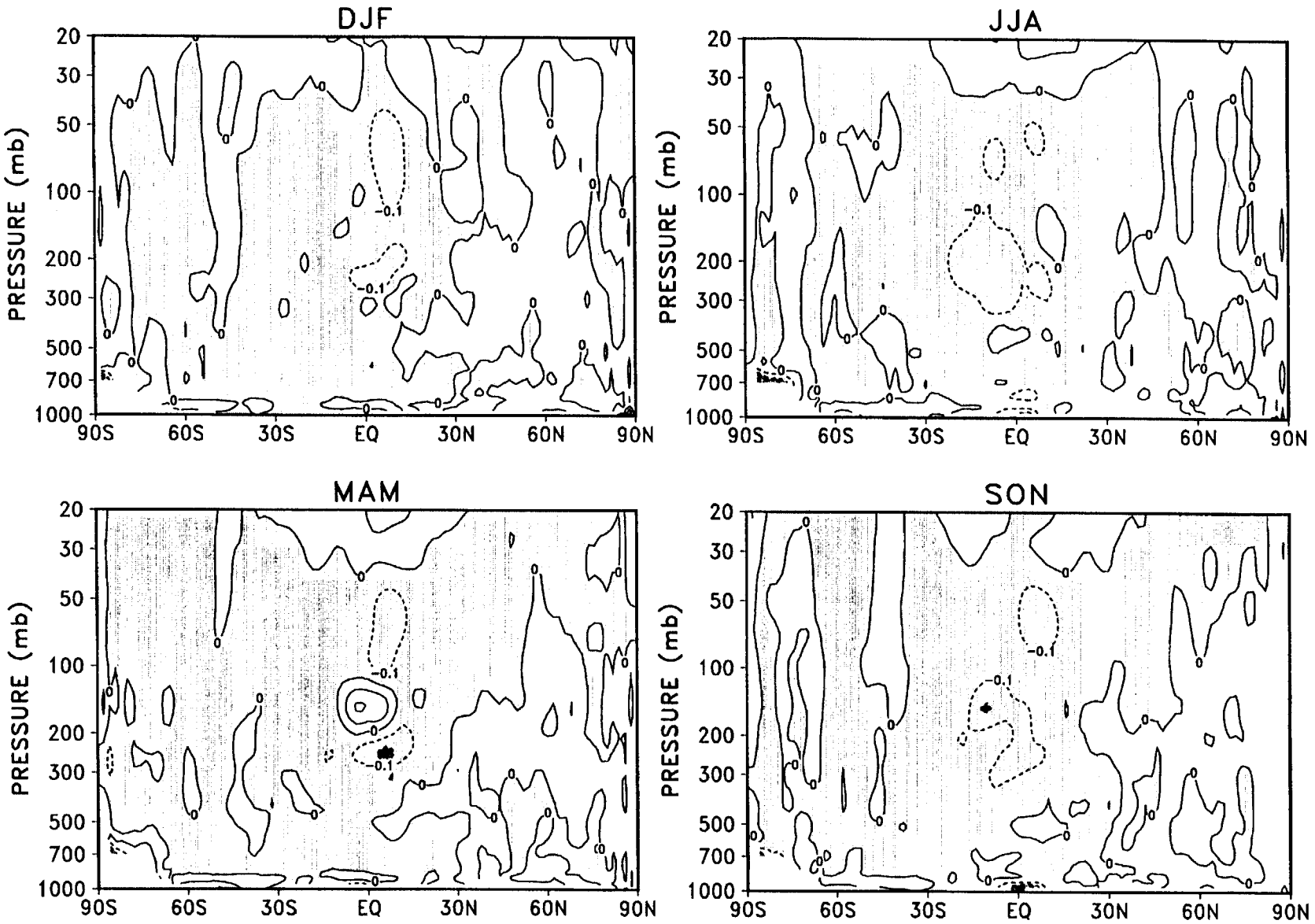

Figure 21: Differences of the standard deviations of seasonal mean zonally averaged v-wind during 1980–1995 (NCEP/NCAR minus DAO). The contour interval is 0.1 m s^{-1}. Negative values are shaded.

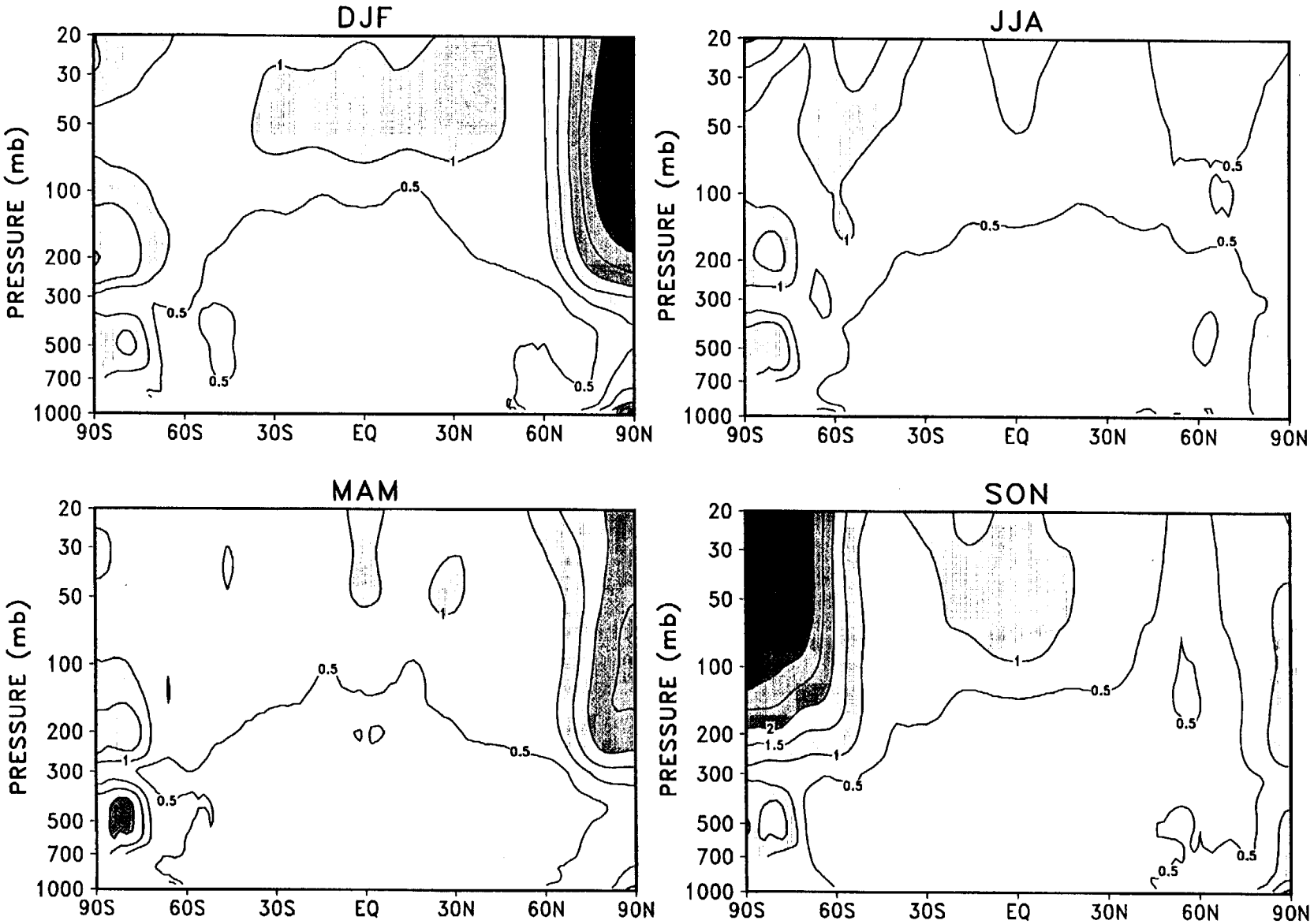

Figure 22: Standard deviations of seasonal mean zonally averaged temperature for DAO reanalysis during 1980–1995. The contour interval is 0.5°K. Values larger than 1°K are shaded.

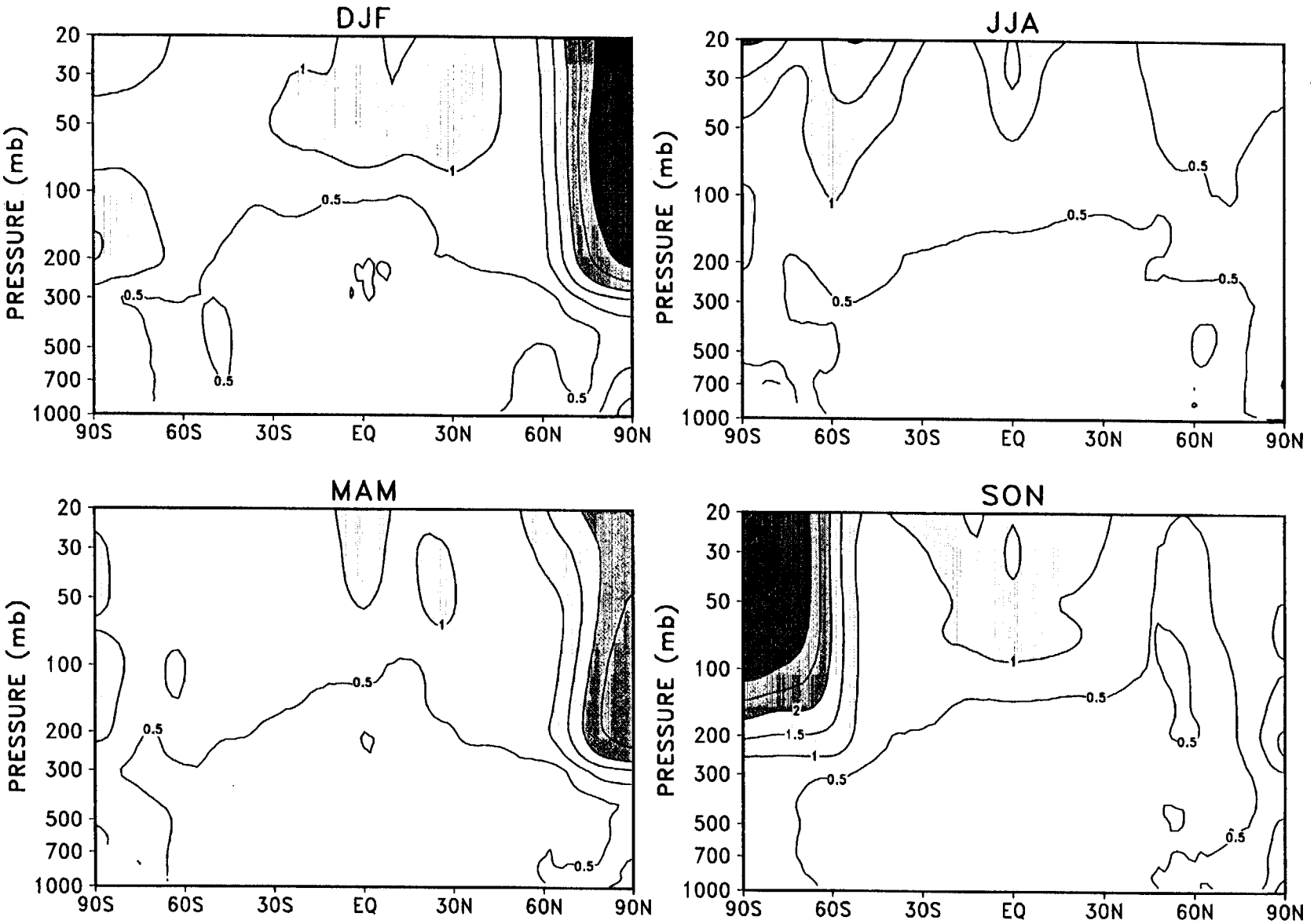

Figure 23: Standard deviations of seasonal mean zonally averaged temperature for NCEP/NCAR reanalysis during 1980–1995. The contour interval is 0.5°K. Values larger than 1°K are shaded.

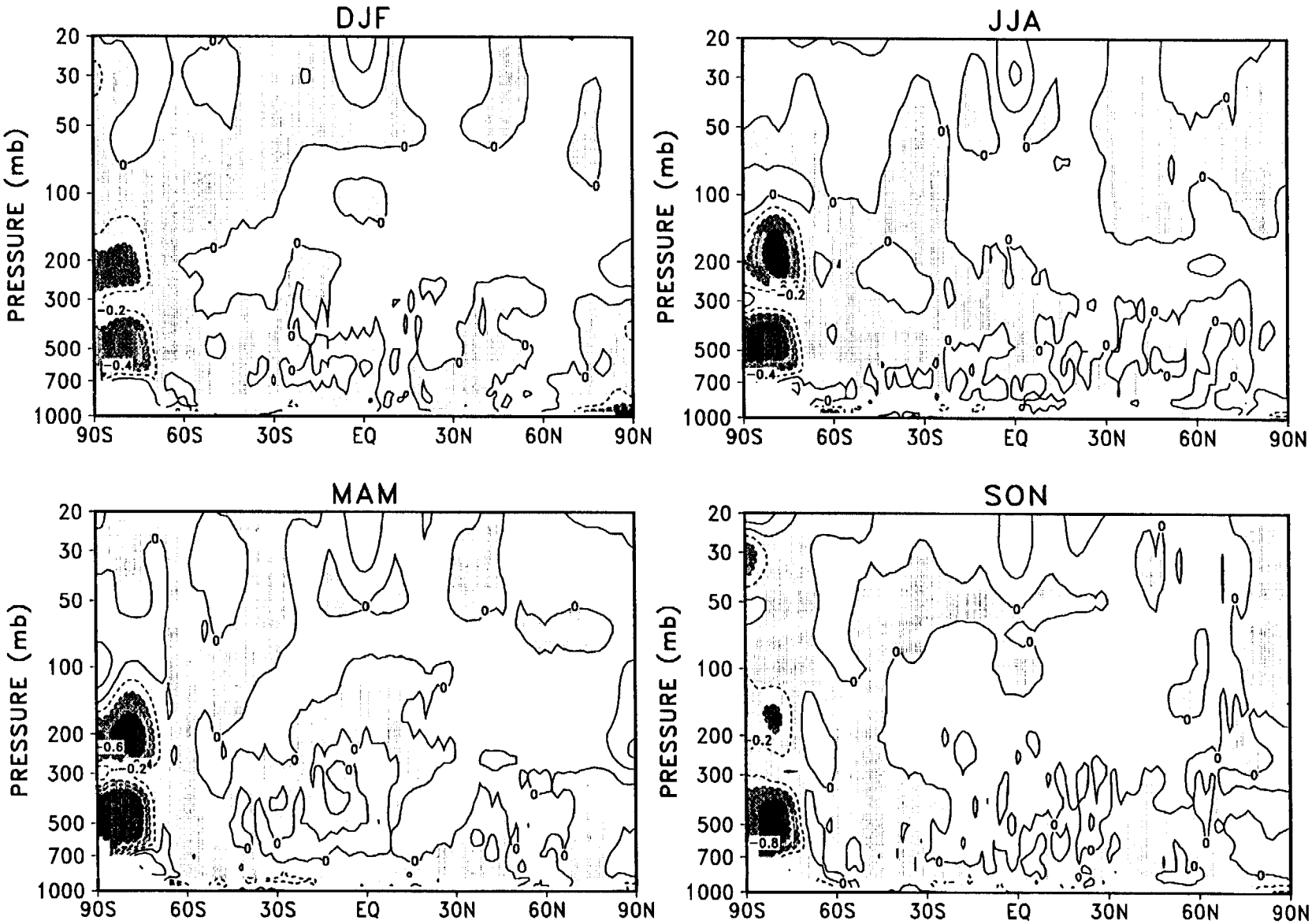

Figure 24: Differences of the standard deviations of seasonal mean zonally averaged temperature during 1980–1995 (NCEP/NCAR minus DAO). The contour interval is 0.2°K. Negative values are shaded.

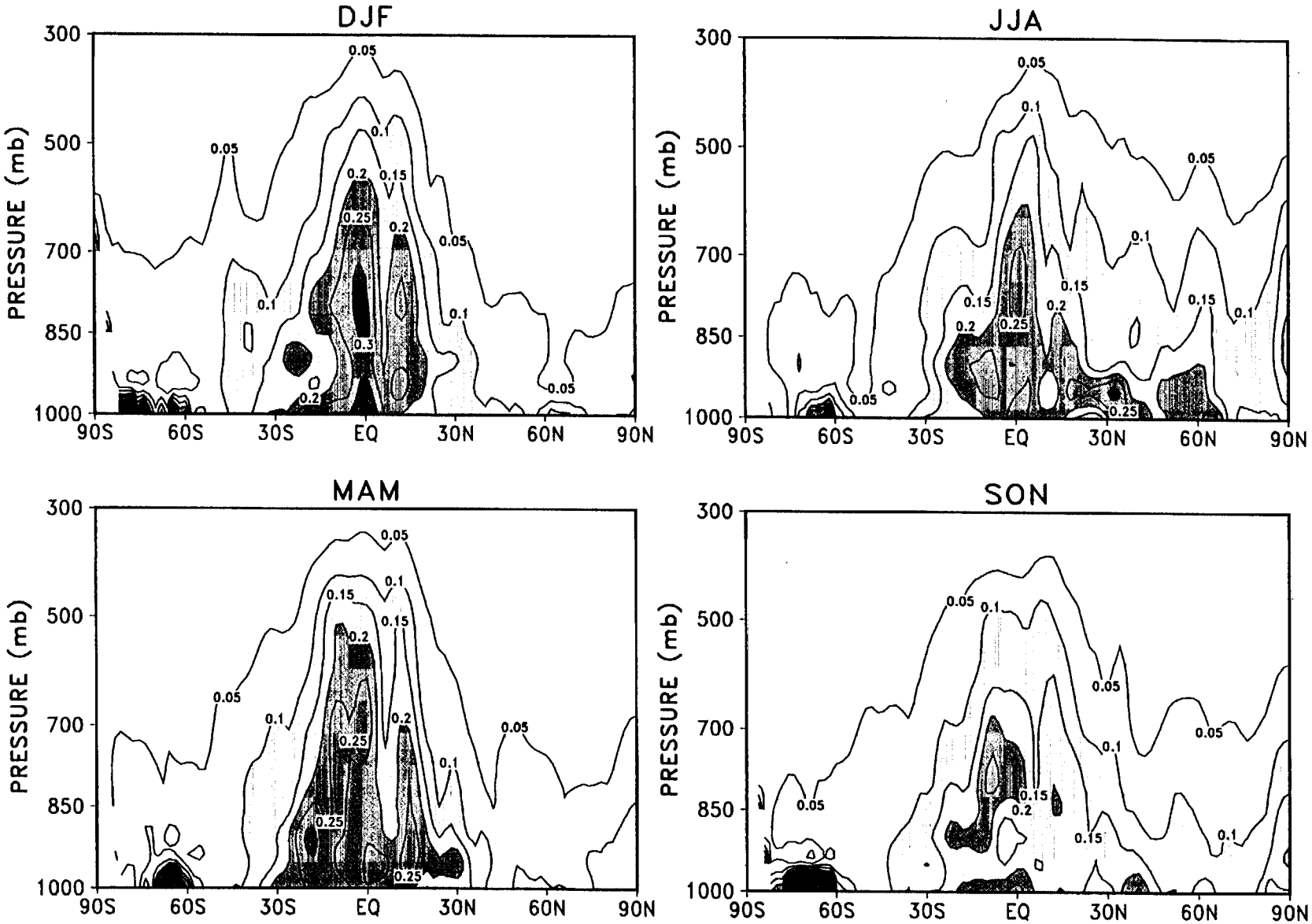

Figure 25: Standard deviations of seasonal mean zonally averaged specific humidity for DAO reanalysis during 1980–1995. The contour interval is 0.05 g kg^{-1}. Values larger than 0.1 g kg^{-1} are shaded.

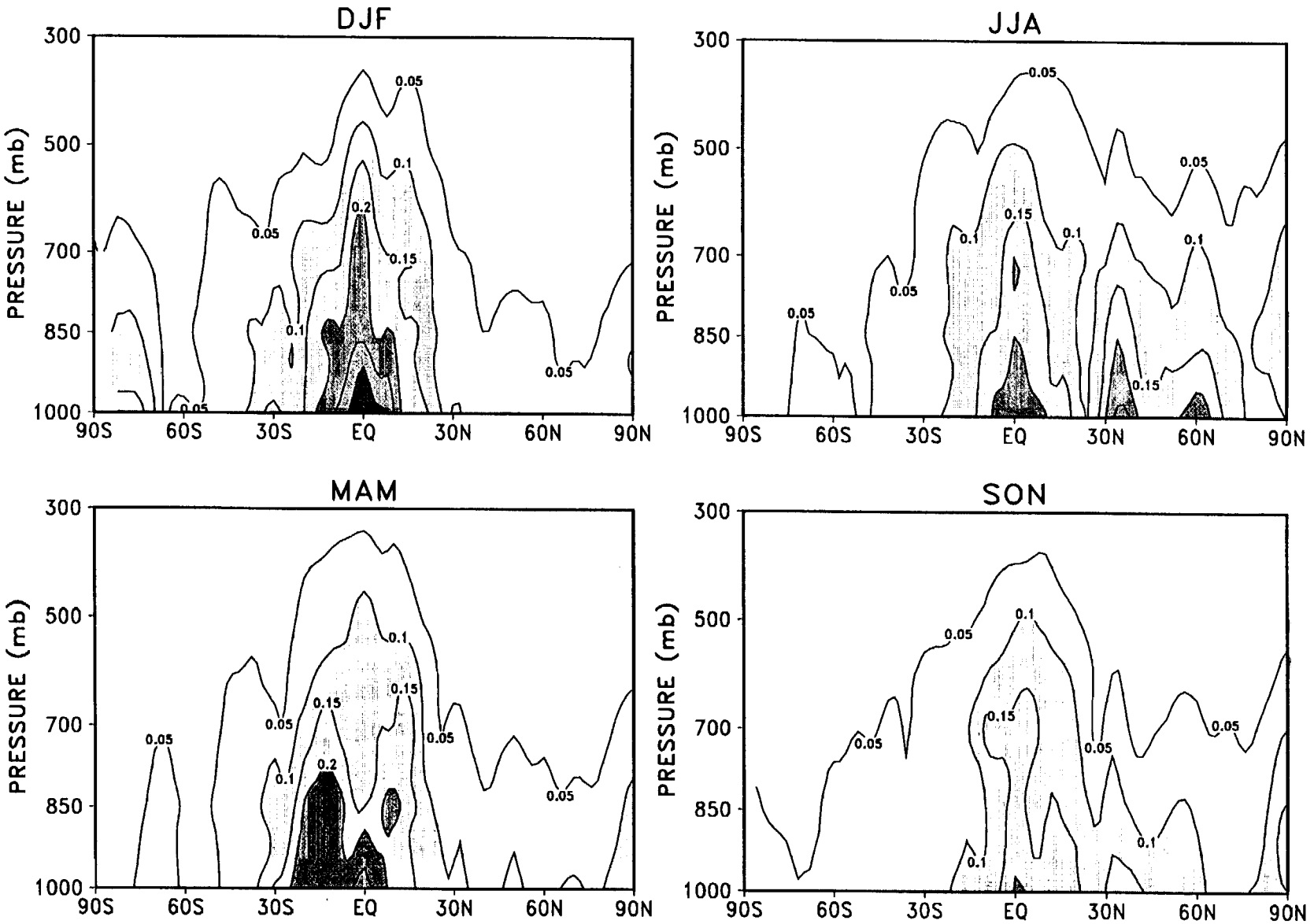

Figure 26: Standard deviations of seasonal mean zonally averaged specific humidity for NCEP/NCAR reanalysis during 1980–1995. The contour interval is 0.05 g kg^{-1}. Values larger than 0.1 g kg^{-1} are shaded.

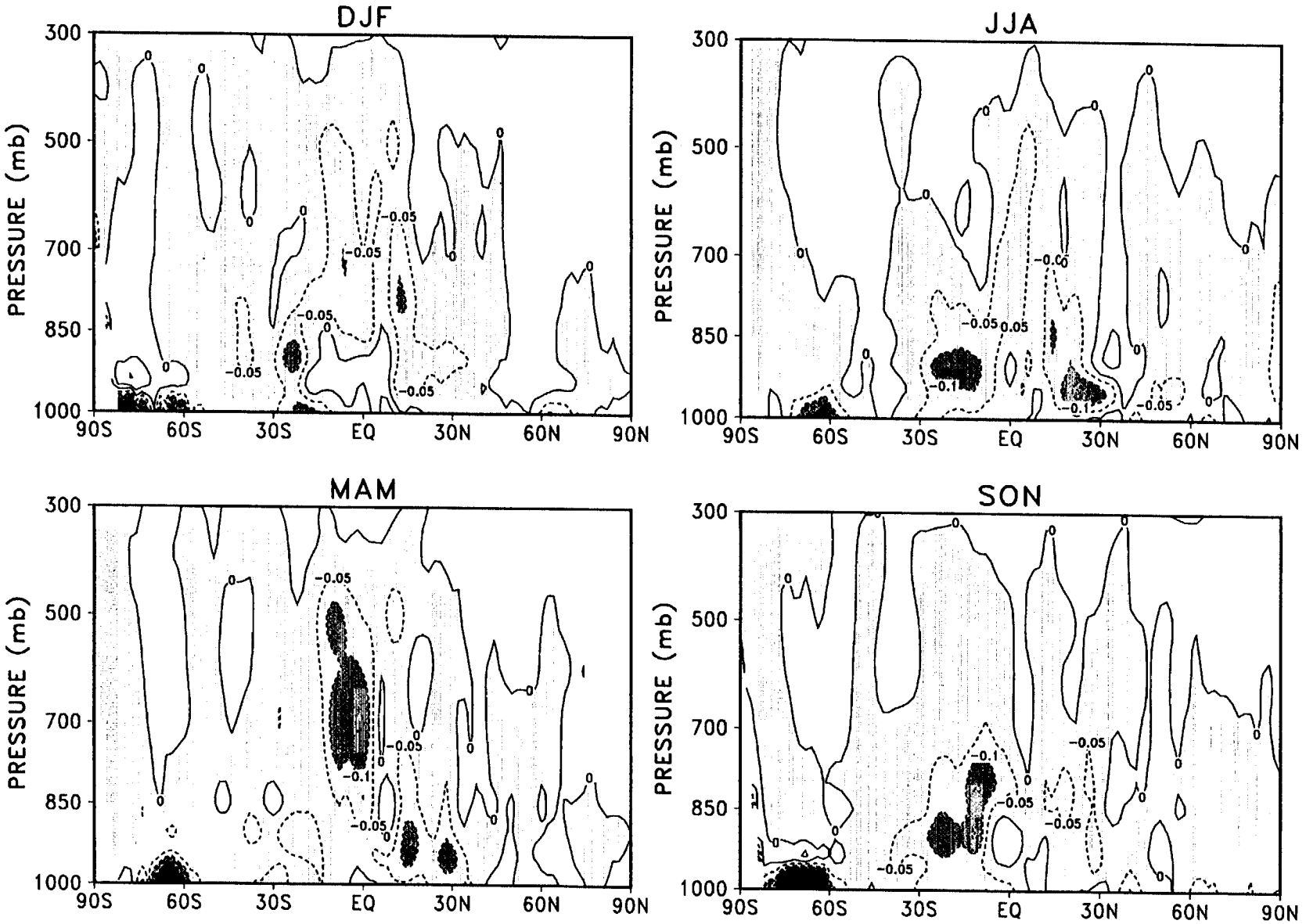

Figure 27: Differences of the standard deviations of seasonal mean zonally averaged specific humidity during 1980–1995 (NCEP/NCAR minus DAO). The contour interval is 0.05 g kg^{-1}. Negative values are shaded.

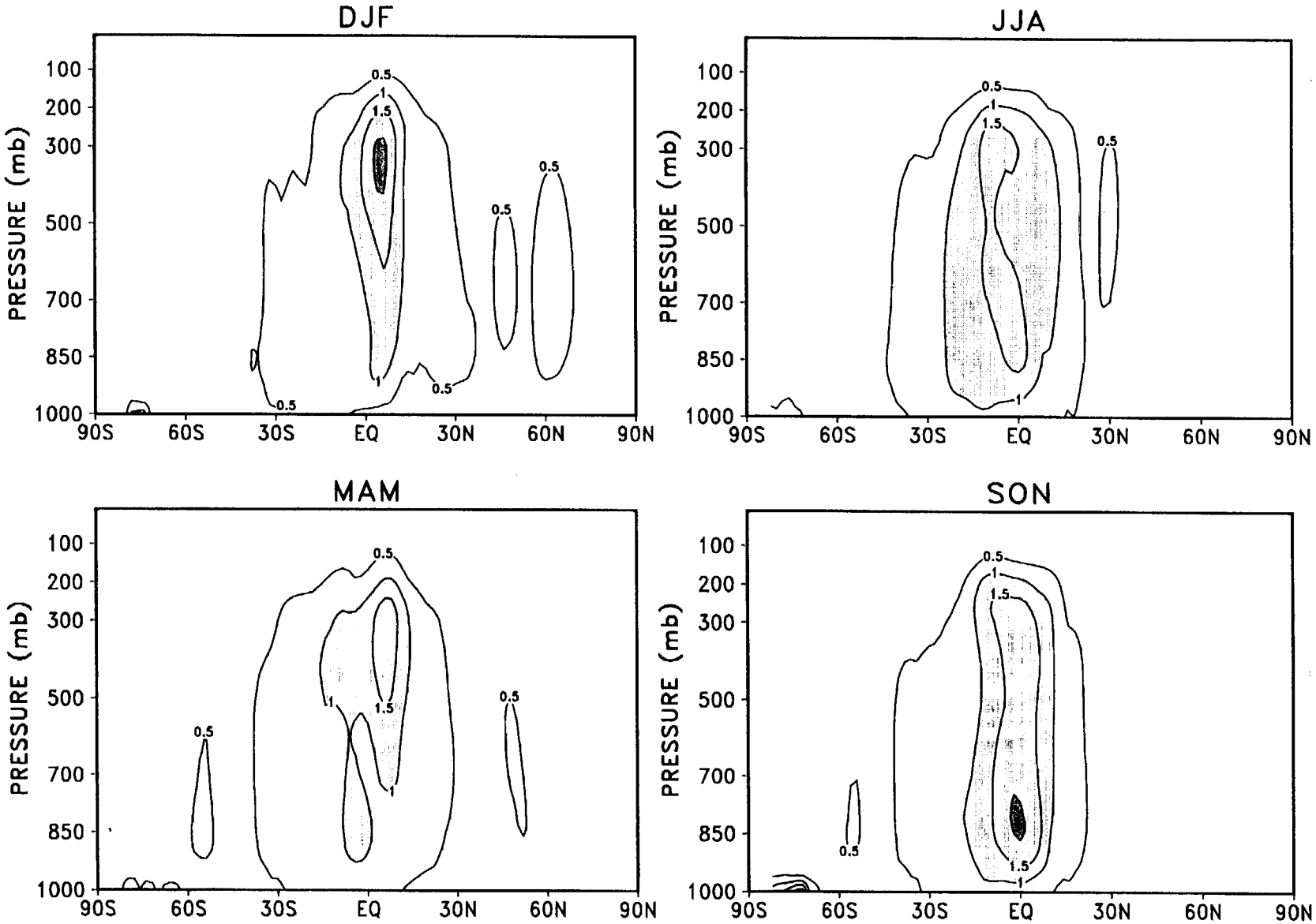

Figure 28: Standard deviations of seasonal mean zonally averaged mass stream function for DAO reanalysis during 1980–1995. The contour interval is 0.5×10^{10} kg s^{-1}. Values larger than 1×10^{10} kg s^{-1} are shaded.

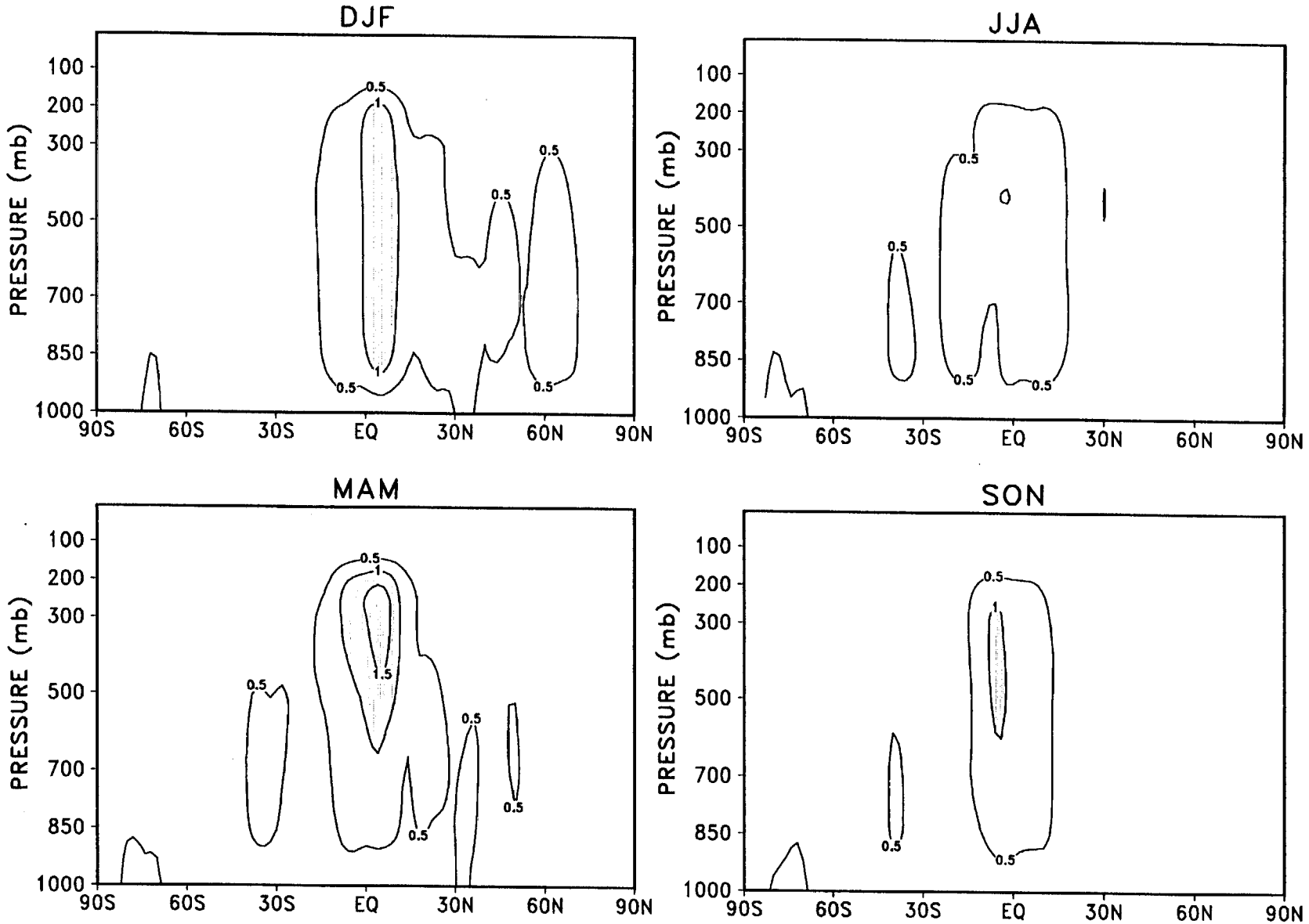

Figure 29: Standard deviations of seasonal mean zonally averaged mass stream function for NCEP/NCAR reanalysis during 1980–1995. The contour interval is 0.5×10^{10} kg s^{-1}. Values larger than 1×10^{10} kg s^{-1} are shaded.

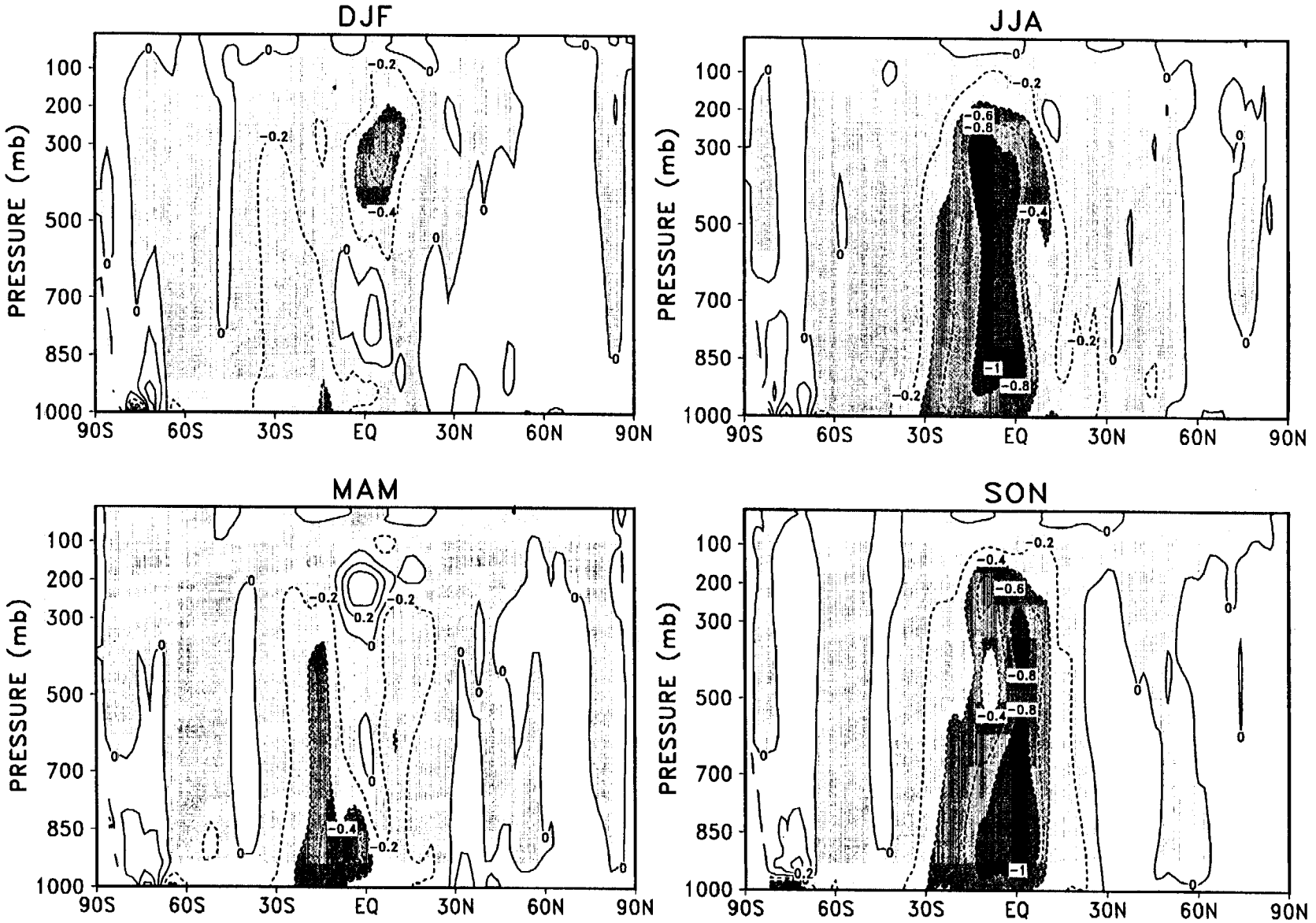

Figure 30: Differences of the standard deviations of seasonal mean zonally averaged mass stream function during 1980–1995 (NCEP/NCAR minus DAO). The contour interval is 0.2×10^{10} kg s^{-1}. Negative values are shaded.

3.2 Global upper-air fields

3.2.1 Troposphere

Figures 31–102 display the global maps of selected quantities from the DAO and the NCEP reanalyses. The seasonal means and the interannual standard deviations are presented.

For the mean zonal wind, the DAO and NCEP products are very similar for all seasons. The largest differences occur near the polar region of the southern hemisphere and in the tropics at both 200 and 850 hPa (Figs.33 and 36). The DAO wind shows weaker easterlies in the tropics and stronger westerlies in the middle and high latitudes of the southern hemisphere. At 200 hPa, both the DAO and the NCEP products show a large seasonal variation in the interannual variability with a maximum during DJF and a minimum during JJA (Figs.37–38). A suggestion of tropical/extratropical coupling is also observed, between the central tropical Pacific and the midlatitudes of both hemispheres, particularly during the DJF. The differences in the standard deviations between the two datasets are generally small (Fig.39). The largest differences occur in the polar region of the southern hemisphere. At 850 hPa, the seasonal variation of the interannual variability of zonal wind is also evident for both the DAO and the NCEP reanalyses (Figs.40–41). The maximum variability occurs over the central and western tropical Pacific. During DJF and MAM seasons, this maximum spreads over the entire tropical Pacific. Large variability is also seen in other regions, such as the Pacific and Atlantic storm track regions. The differences between the DAO and the NCEP indicate that the DAO has substantially larger interannual variability over the tropical Pacific especially during DJF.

Figures 43–51 show the seasonal mean meridional wind and the interannual variability at 200 and 850 hPa. The differences in the seasonal mean reveal rather more complicated patterns than the zonal wind. Systematic differences are observed at 200 hPa in the tropical region (Fig.45). Compared to the NCEP product, the DAO product shows stronger northerlies over Africa, Indian ocean, northern South America and stronger southerlies over the central tropical Pacific. The largest differences are observed in the polar region of the southern hemisphere, which appears to be related to the topography. The differences at 850 hPa are rather noisy, and appear to be associated with topographic features. The meridional wind at both 200 and 850 hPa shows large variability in the middle and high latitudes of both hemispheres. At 200 hPa the variability is particularly large over western North America during DJF and SON, and over Europe and southern Asia during DJF. At 850 hPa the largest variability occurs over the NH polar regions, Europe, and the NH high latitude Pacific and Atlantic oceans during DJF. Large variability also occurs over the SH high latitude Pacific Ocean during JJA. The differences in the interannual variability between the two reanalyses show that the DAO in general has larger variability than the NCEP with the largest differences occurring in the polar region of the southern hemisphere.

In section 3.1, we have shown that the zonal mean temperature profiles have systematic differences between the DAO and the NCEP reanalyses in the troposphere as well as in the lower stratosphere. Here, our focus is on the global distributions of the temperature at 200 and 850 hPa. The comparison for the lower stratosphere will be presented in subsection 3.2.2. The differences in temperature at 200 hPa show that the DAO product is colder than the NCEP product near the pole of both hemispheres, and that the DAO product is warmer than the NCEP product throughout the tropics and midlatitudes (Fig.57). In the midlatitudes of the northern hemisphere, a band of large negative differences (DAO temperatures warmer) is observed for all seasons. At 850 hPa (Fig.60), large negative differences are found in the eastern Pacific near the coast and in the southern Indian Ocean while large positive differences are seen over the continents near high terrain. For the interannual variability, both reanalyses show similar patterns and have large seasonal variations at 200 and 850 hPa. In general, large variability occurs at middle and high latitudes in both hemispheres. At 850 hPa the NCEP temperature tends to have more variability over the tropical oceans and in the subtropics off the west coasts of the continents, while the DAO temperature tends to have more variability over the middle latitude oceans and Africa. At 200 hPa the DAO temperature is less variable than NCEP in the northern hemisphere while it is considerably more variable than NCEP over Antarctica (Figs.63 and 66).

The mean DAO specific humidity at 850 hPa shows a much more concentrated tropical maximum associated with the ITCZ compared with NCEP (Figs.67 and 68). The difference plot (Fig.69) shows that the DAO product is drier just to the west of the continents (just off the equator over the eastern Pacific ocean, the Atlantic ocean, and east of Australia), and it is wetter over the western Pacific, the African continent and the Americas. The largest variability occurs in the tropics and subtropics (Figs.70–72), with the DAO specific humidity showing considerably more variability than NCEP throughout the seasons. The 500 hPa eddy geopotential height shows large ($>$ 10m) differences in the middle and high latitudes of the southern hemisphere and over the midlatitude oceans of the northern hemisphere (Figs.73–75). The interannual variability, in general, shows coherent patterns in the two reanalyses. However, large differences can be found in the polar regions of both hemispheres (Fig.75).

The seasonal means of the 200 hPa eddy streamfunction show substantial differences between the two reanalyses over the subtropics especially during JJA in the southern hemisphere (Fig.81). For the 200 hPa velocity potential, however, the large differences are found in the tropical region (30°S–30°N) where heavy rainfall occurs (Fig.84). The stronger gradients suggest that the NCEP system tends to produce stronger deep convection than DAO over the western Pacific, Indian ocean and the South America continent. Also, NCEP has stronger subsidence over the eastern Pacific ocean, the eastern Atlantic in the tropics and in the northern Africa. This indicates a stronger tropical east-west (Walker) circulation in the NCEP system. For the interannual variability, both reanalyses show large seasonal varia-

tions in the 200 hPa eddy streamfunction with the maximum variability occurring during DJF in both hemispheres (Figs.85–87). This suggests an important role for tropical forcing during this season particularly over the eastern Pacific. The DAO eddy streamfunction has somewhat larger interannual variability during DJF over the eastern subtropical oceans of both hemispheres. Otherwise, the differences are generally larger in the southern hemisphere than in the northern hemisphere. For the 200 hPa velocity potential (Fig.88–90), the largest variability occurs in the tropics with maxima over the western Pacific and the eastern Pacific near the coast of the American continent. The DAO velocity potential has less variability over the southern Indian ocean and the central and eastern Pacific Ocean and more variability over the monsoon region.

The differences in the seasonal means of the mean sea level pressure (Figs.91–93) largely follow the topography, suggesting differences in the model topography and the algorithm used to reduce the surface pressure to the sea level. The interannual variability generally has the same pattern as 500 hPa geopotential height, showing large variability near the preferred regions of persistent atmospheric anomalies. The differences between the two reanalyses indicate larger variability in the DAO sea level pressure, particularly near the polar regions.

The seasonal mean total precipitable water differences (Fig.99) between the two reanalyses are similar to those for the 850 hPa specific humidity (Fig.69). In general, the DAO product shows a more concentrated tropical maximum. The DAO atmosphere is wetter than NCEP over the central and western Pacific, the tropical Indian ocean, Africa, the South American continent, and India and southeastern Asia, and it is drier than NCEP west of Australia, the eastern Pacific ocean and the tropical Atlantic ocean. The largest interannual variability occurs over the ocean with maxima over the central and eastern Pacific (Fig.100 and 101). The differences in the interannual standard deviation indicate that the DAO has substantially larger variability than the NCEP.

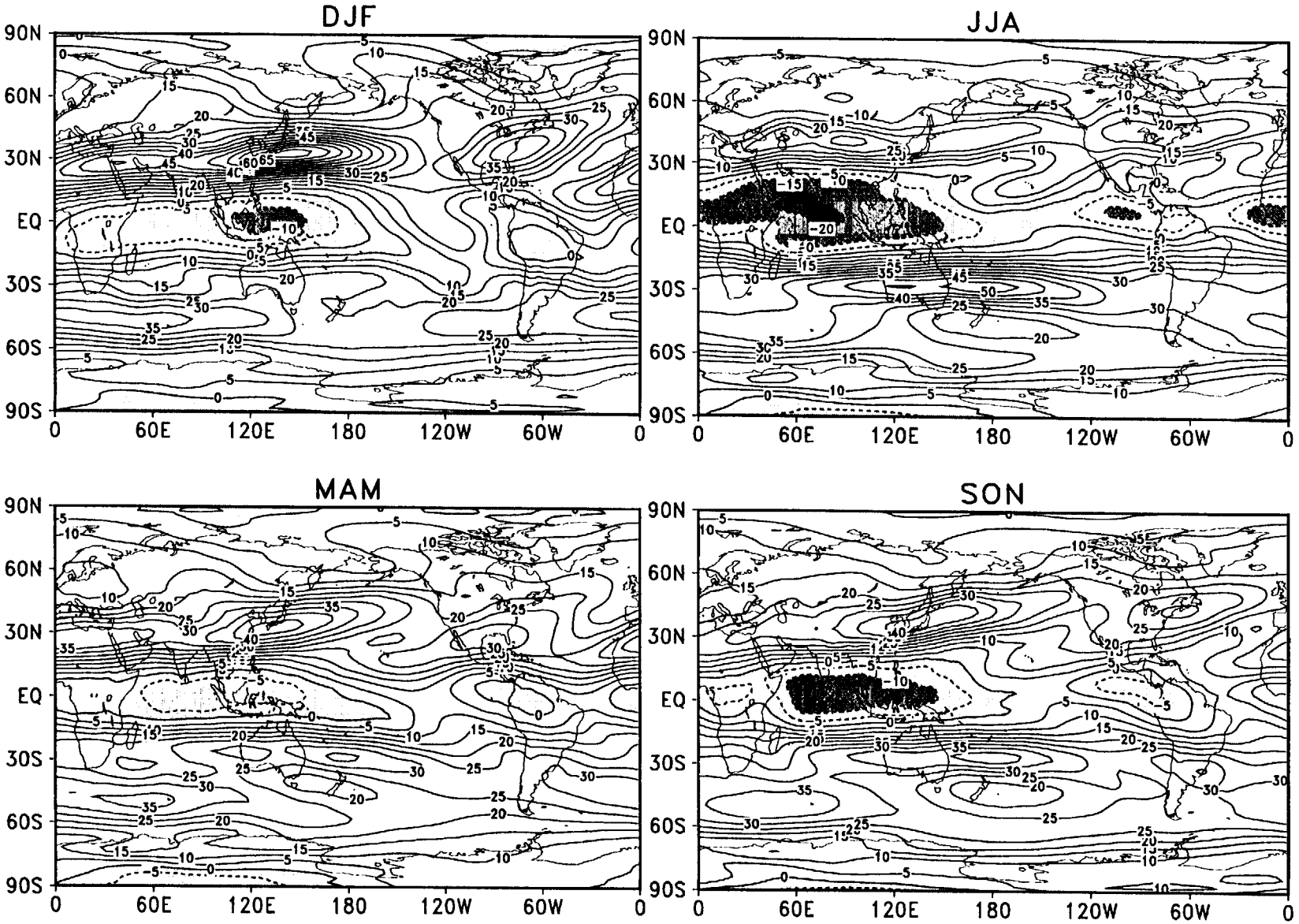

Figure 31: Seasonal means of 200 hPa u-wind for DAO reanalysis during 1980–1995. The contour interval is 5 m s^{-1}. Negative values are shaded.

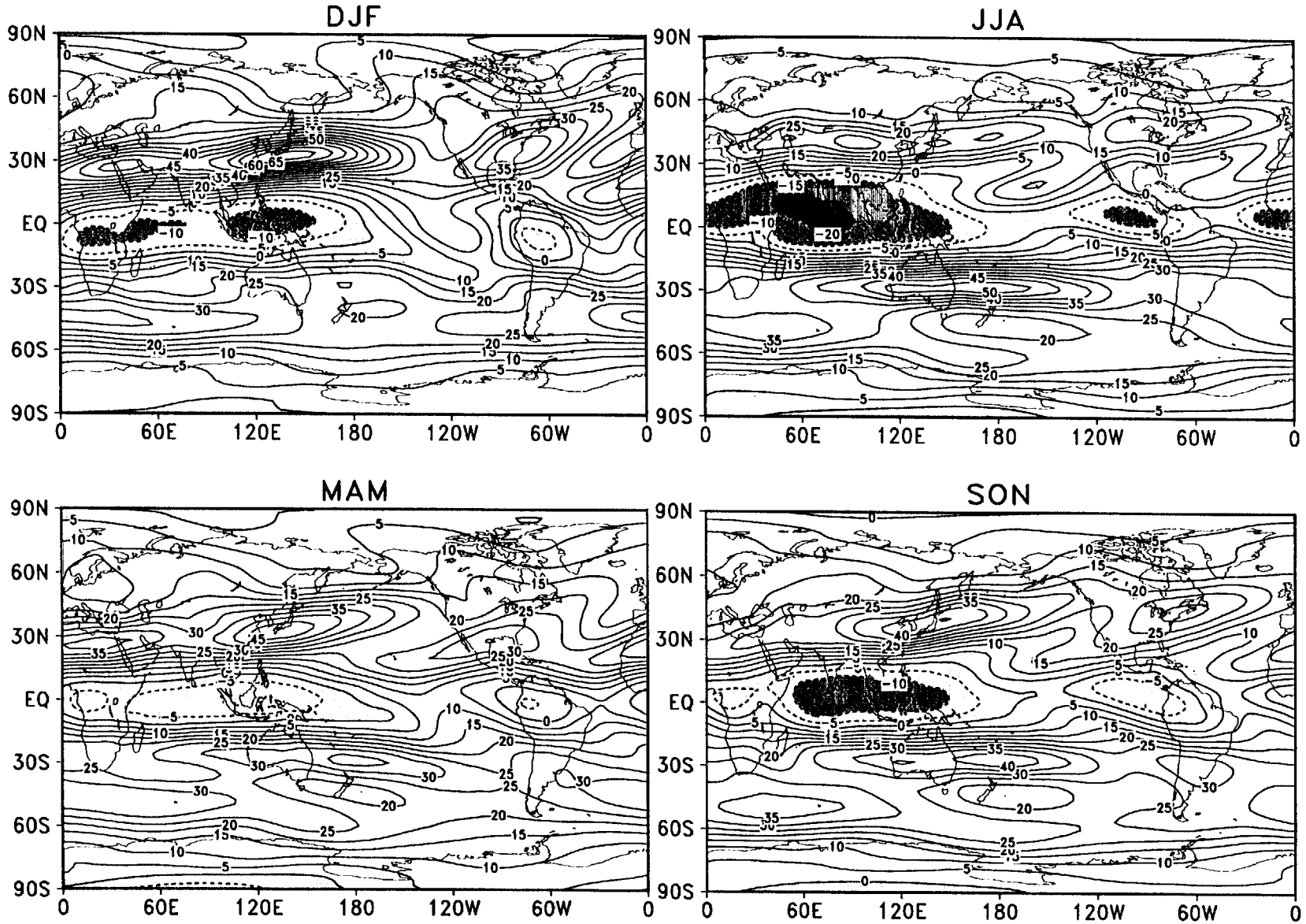

Figure 32: Seasonal means of 200 hPa u-wind for NCEP/NCAR reanalysis during 1980–1995. The contour interval is 5 m s^{-1}. Negative values are shaded.

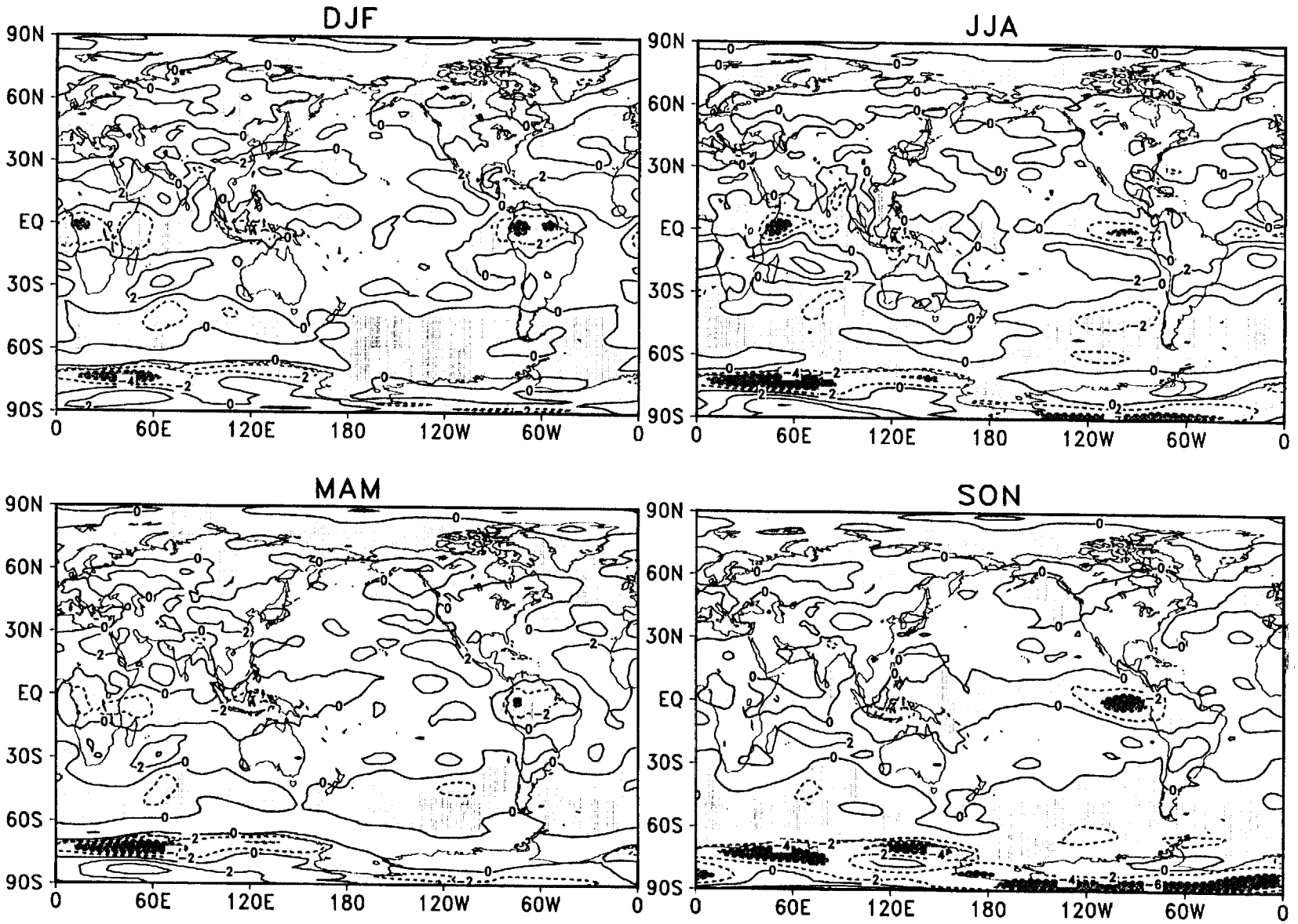

Figure 33: Difference of the seasonal means of 200 hPa u-wind during 1980–1995 (NCEP/NCAR minus DAO). The contour interval is 2 m s^{-1}. Negative values are shaded.

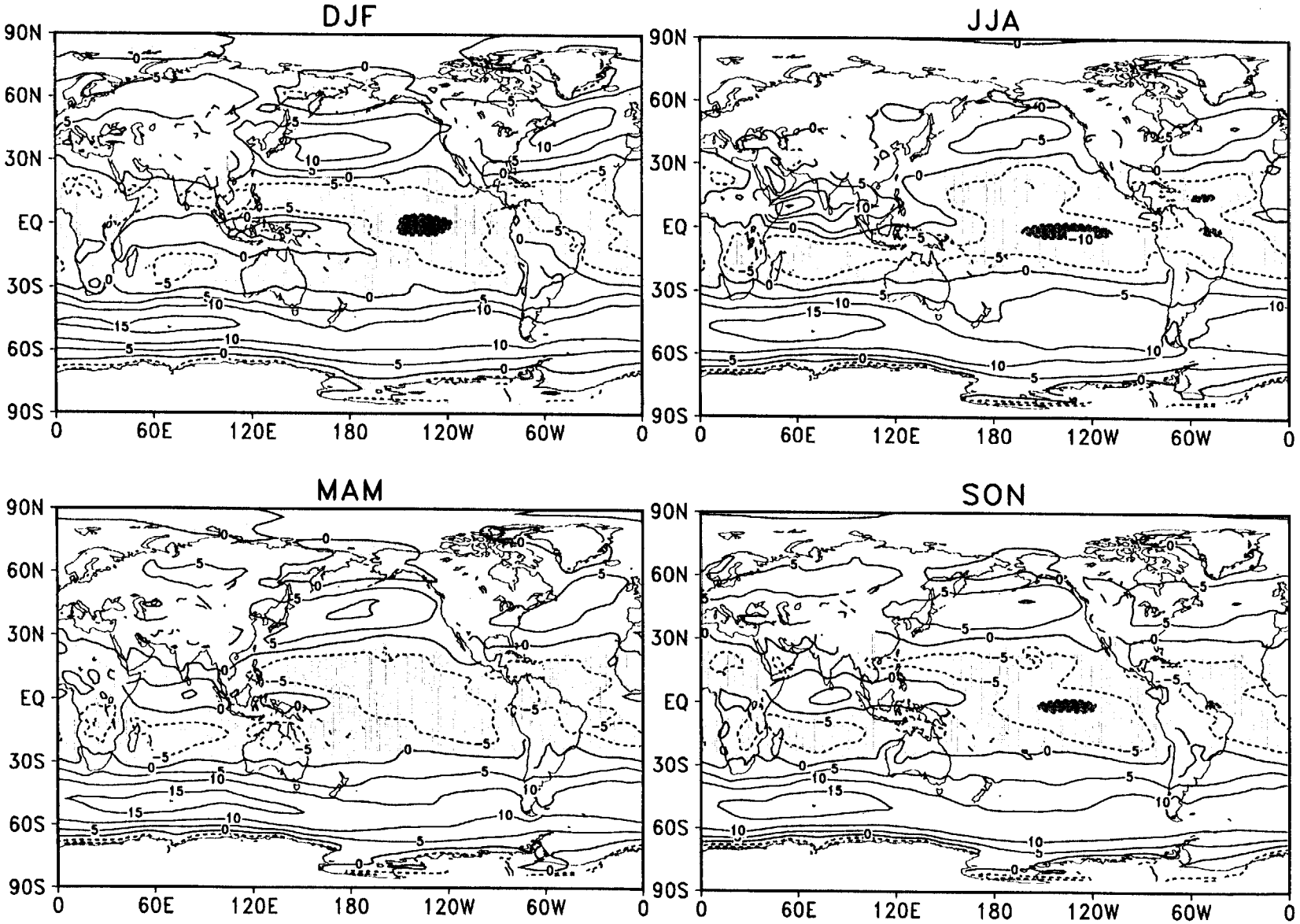

Figure 34: Seasonal means of 850 hPa u-wind for DAO reanalysis during 1980–1995. The contour interval is 5 m s^{-1}. Negative values are shaded.

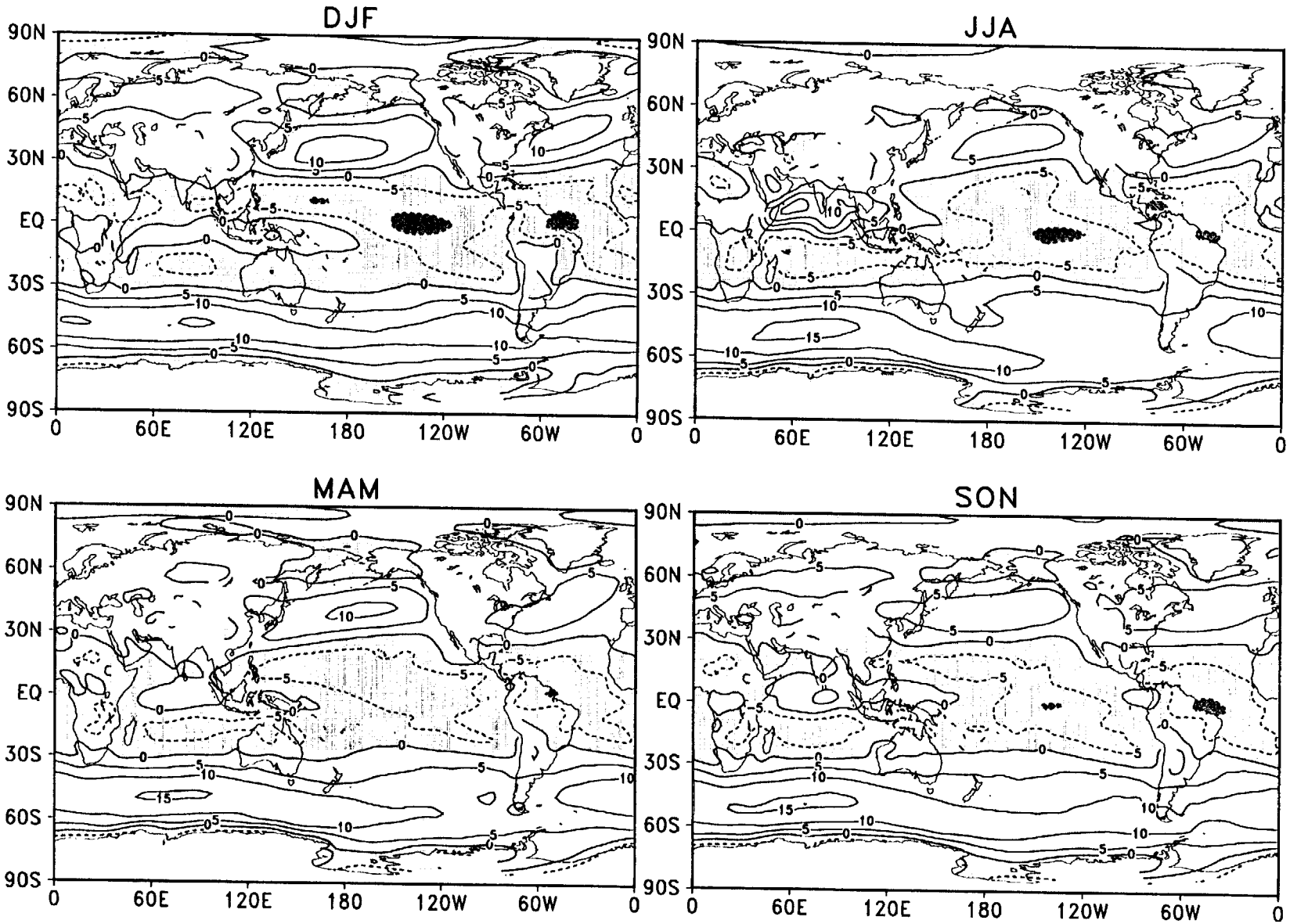

Figure 35: Seasonal means of 850 hPa u-wind for NCEP/NCAR reanalysis during 1980–1995. The contour interval is 5 m s^{-1}. Negative values are shaded.

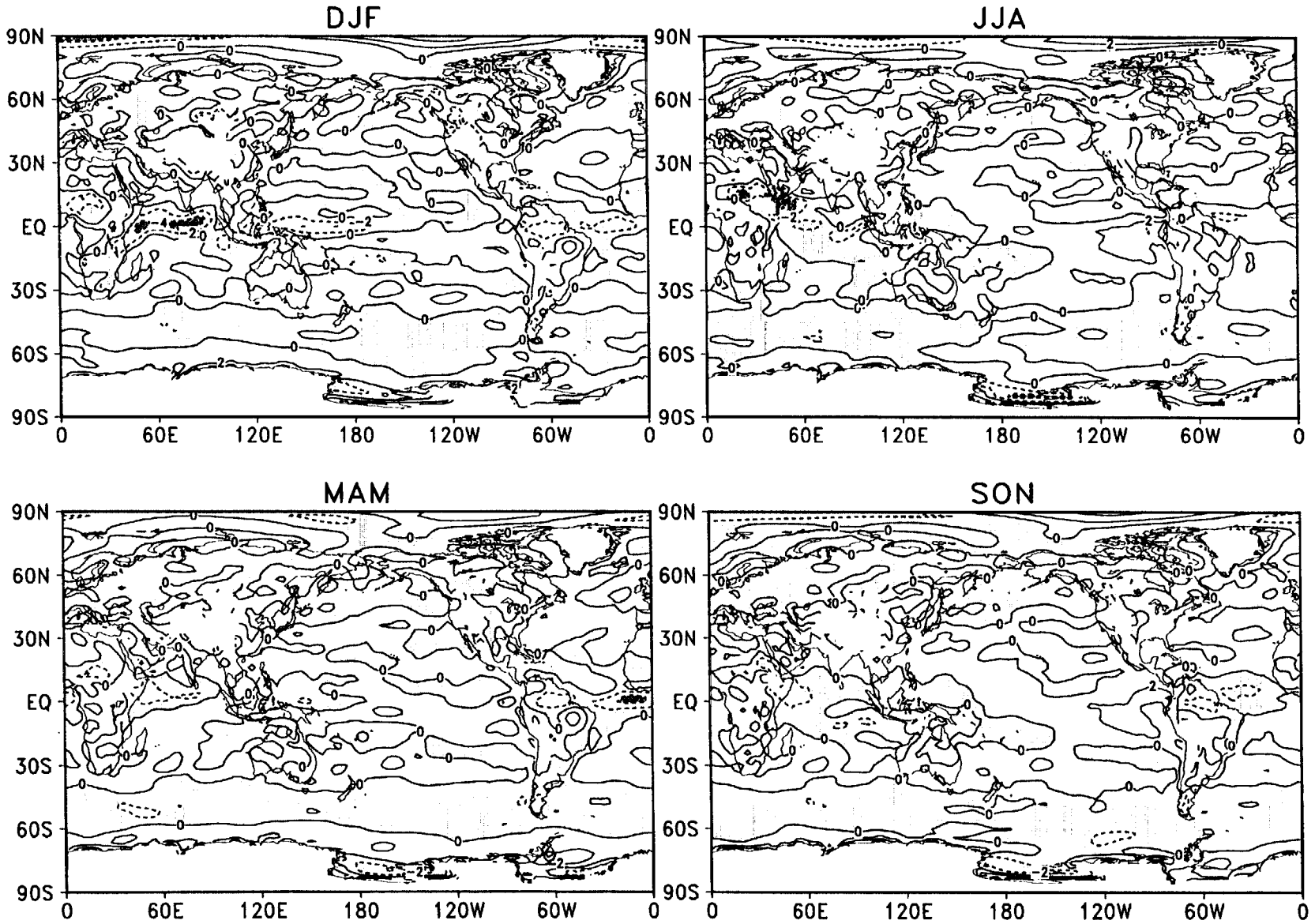

Figure 36: Difference of the seasonal means of 850 hPa u-wind during 1980–1995 (NCEP/NCAR minus DAO). The contour interval is 2 m s^{-1}. Negative values are shaded.

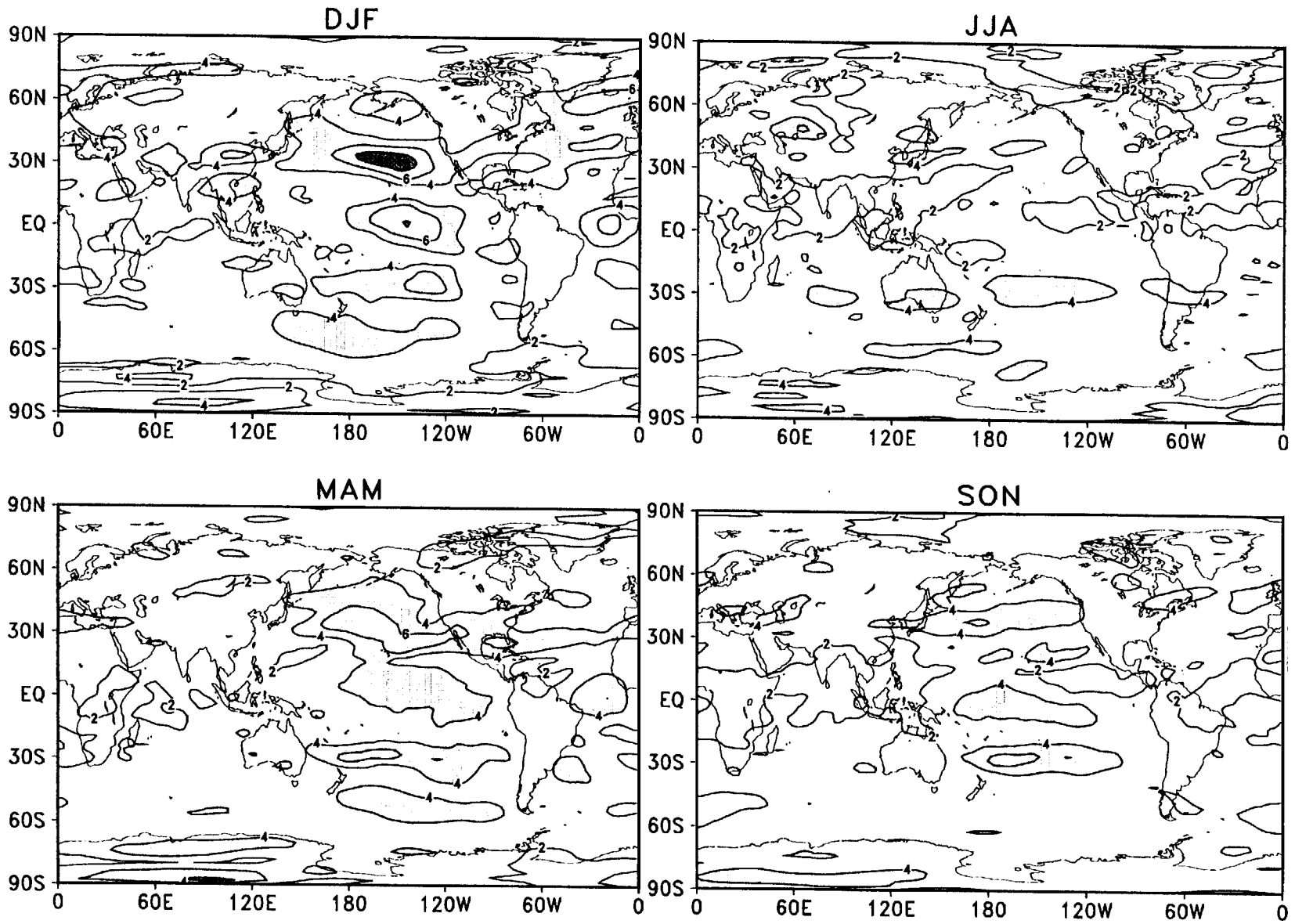

Figure 37: Standard deviations of seasonal mean 200 hPa u-wind for DAO reanalysis during 1980–1995. The contour interval is 2 m s^{-1}. Values larger than 4 m s^{-1} are shaded.

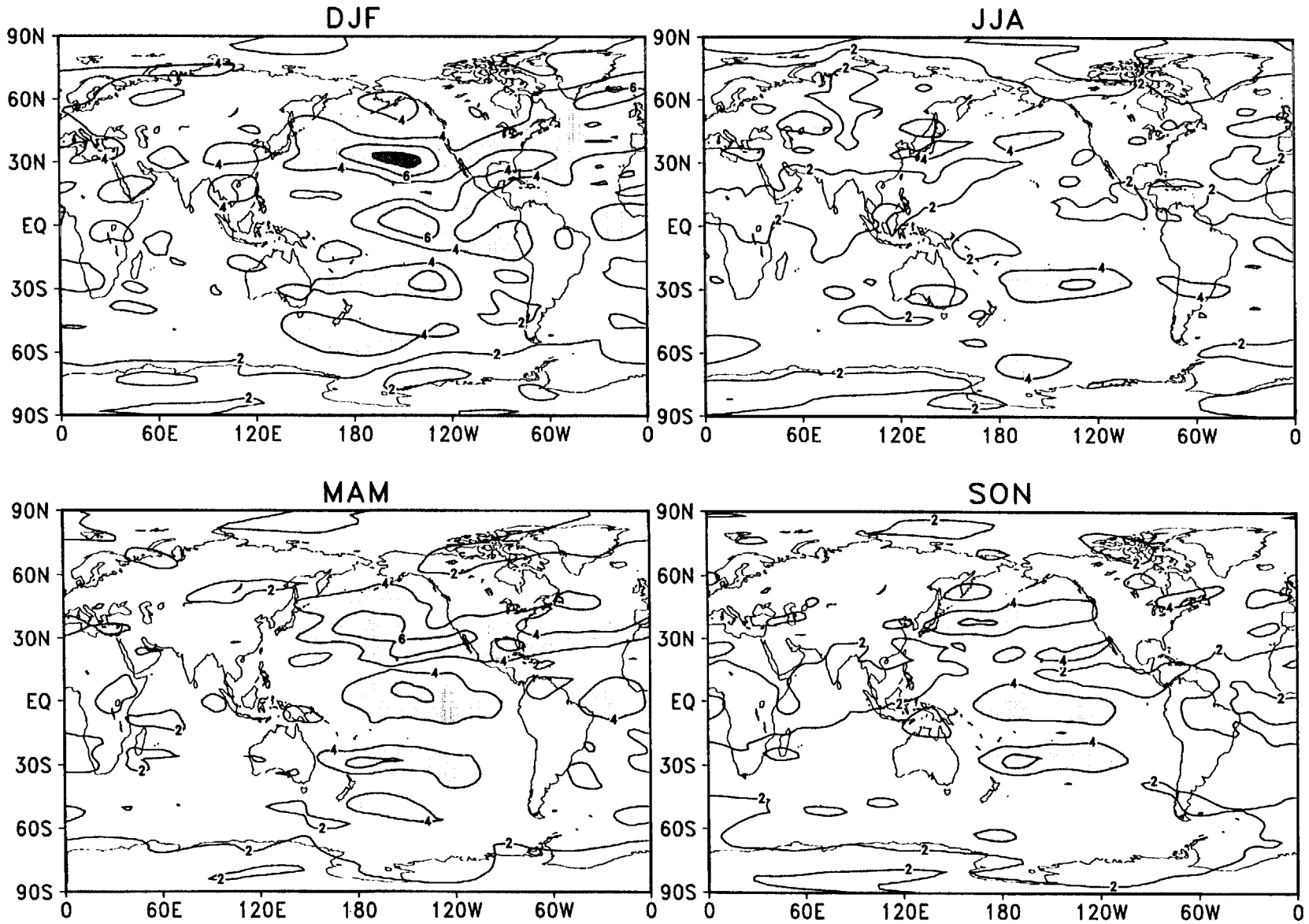

Figure 38: Standard deviations of seasonal mean 200 hPa u-wind for NCEP/NCAR reanalysis during 1980–1995. The contour interval is 2 m s^{-1}. Values larger than 4 m s^{-1} are shaded.

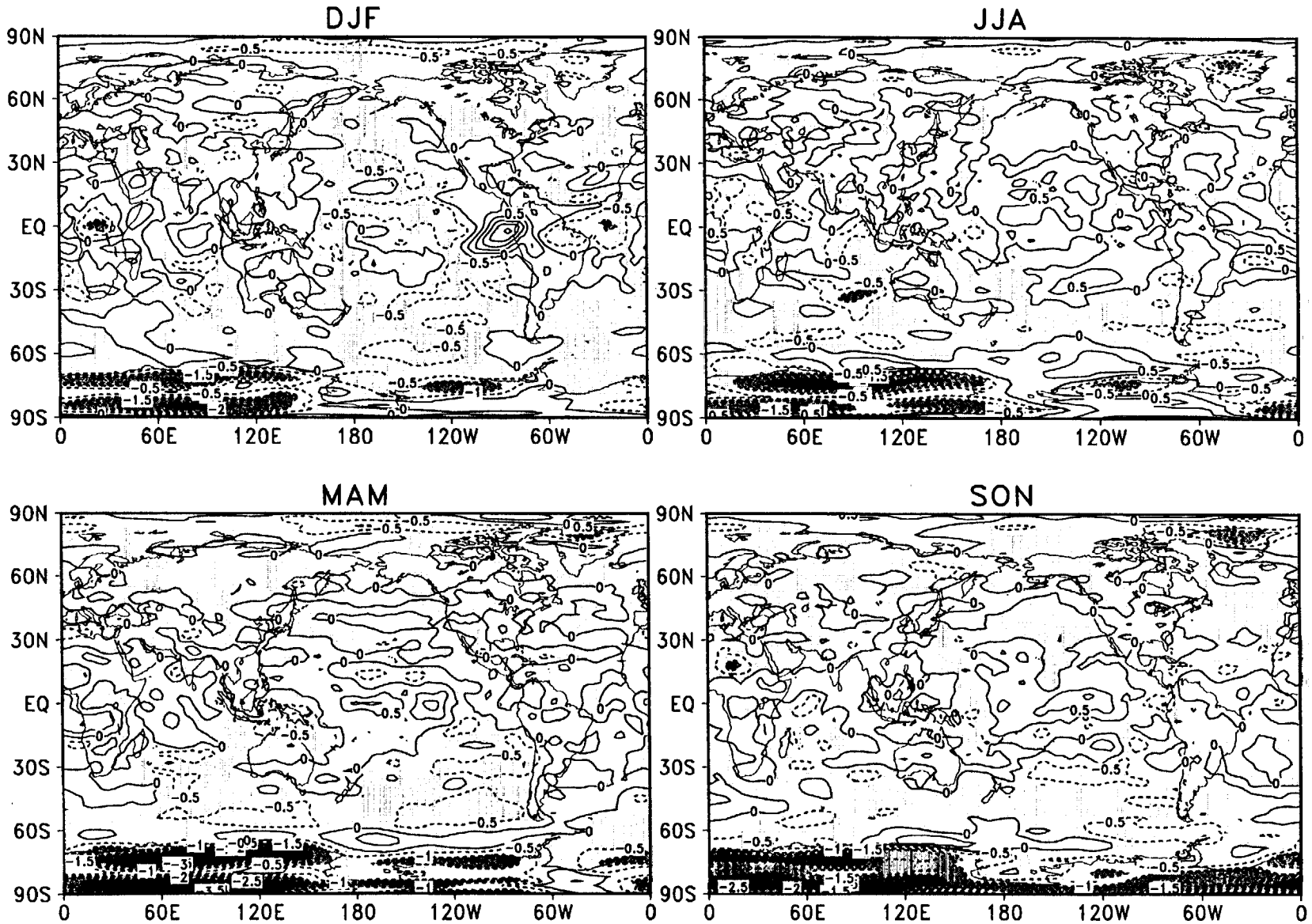

Figure 39: Difference of the standard deviations of seasonal mean 200 hPa u-wind during 1980–1995 (NCEP/NCAR minus DAO). The contour interval is 0.5 m s^{-1}. Negative values are shaded.

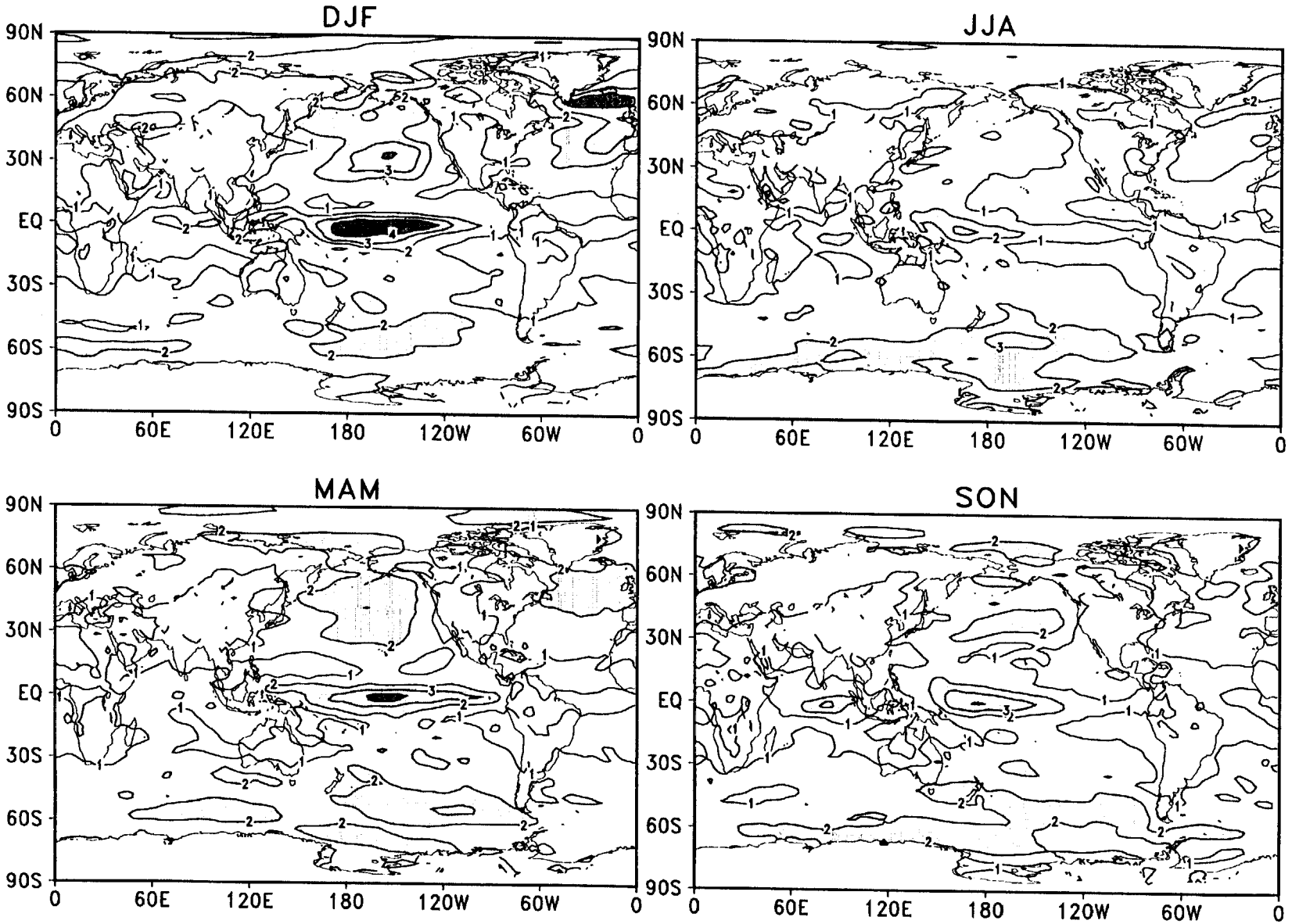

Figure 40: Standard deviations of seasonal mean 850 hPa u-wind for DAO reanalysis during 1980–1995. The contour interval is 1 m s^{-1}. Values larger than 2 m s^{-1} are shaded.

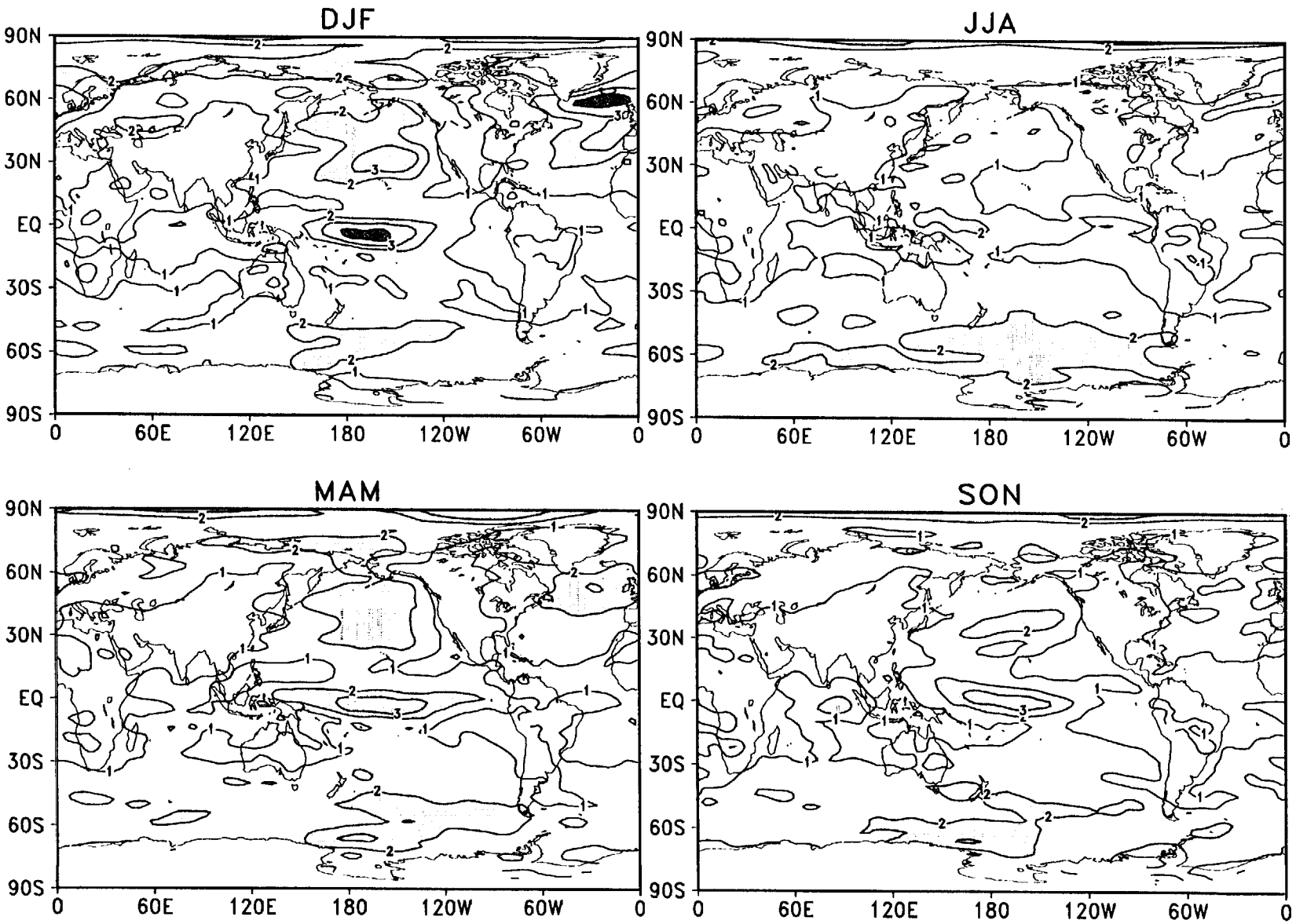

Figure 41: Standard deviations of seasonal mean 850 hPa u-wind for NCEP/NCAR reanalysis during 1980–1995. The contour interval is 1 m s^{-1}. Values larger than 2 m s^{-1} are shaded.

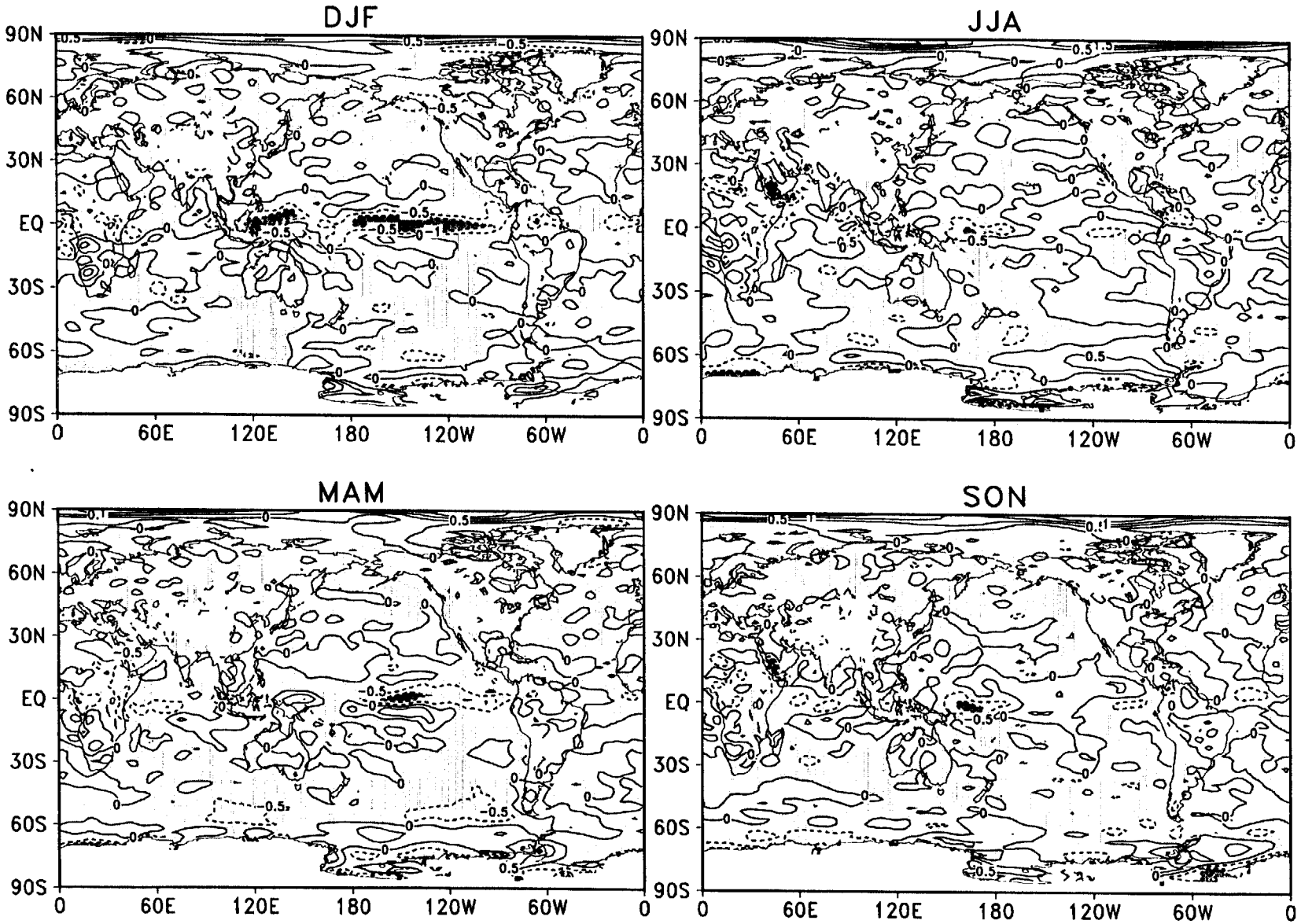

Figure 42: Difference of the standard deviations of seasonal mean 850 hPa u-wind during 1980–1995 (NCEP/NCAR minus DAO). The contour interval is 0.5 m s^{-1}. Negative values are shaded.

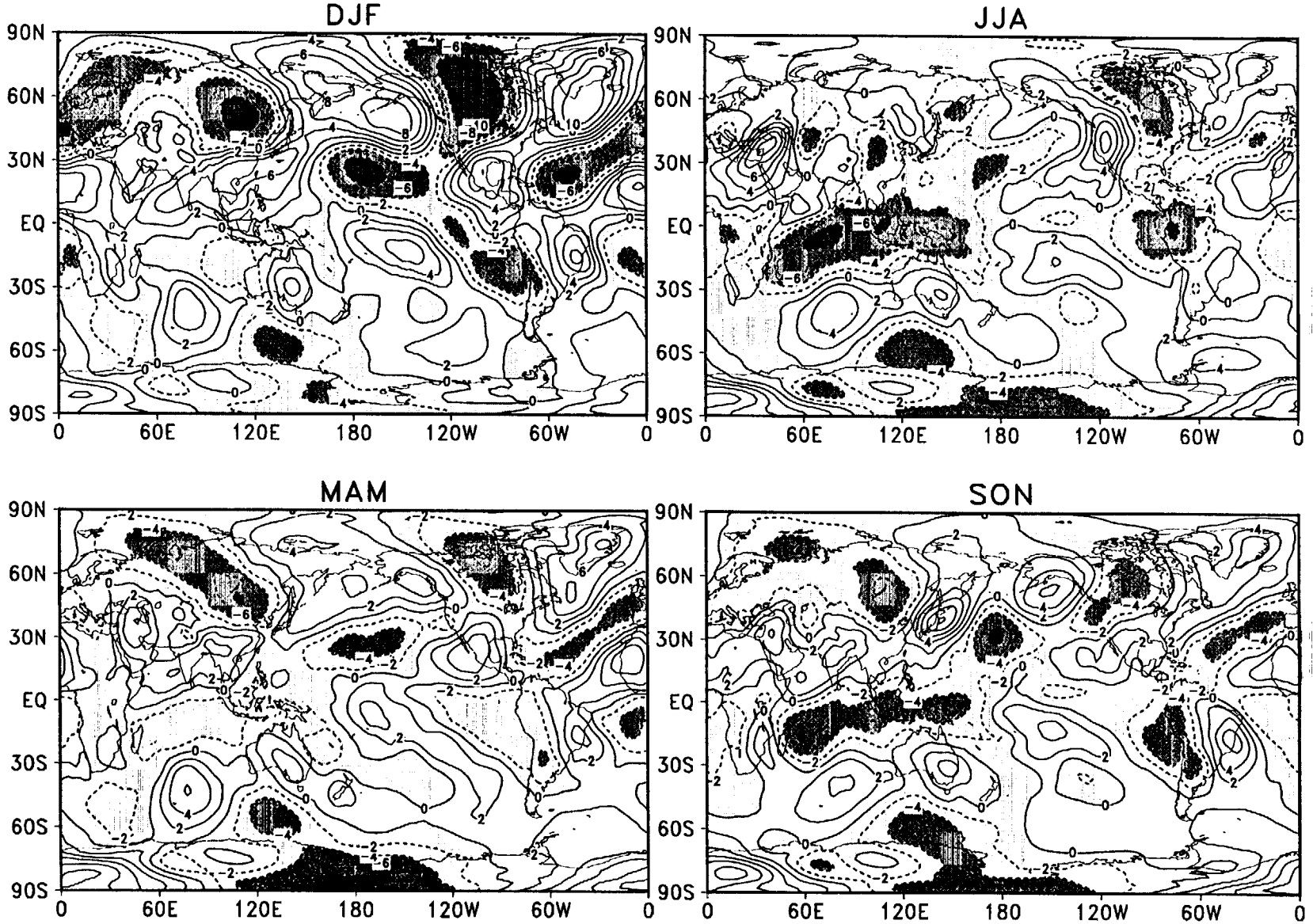

Figure 43: Seasonal means of 200 hPa v-wind for DAO reanalysis during 1980–1995. The contour interval is 2 m s^{-1}. Negative values are shaded.

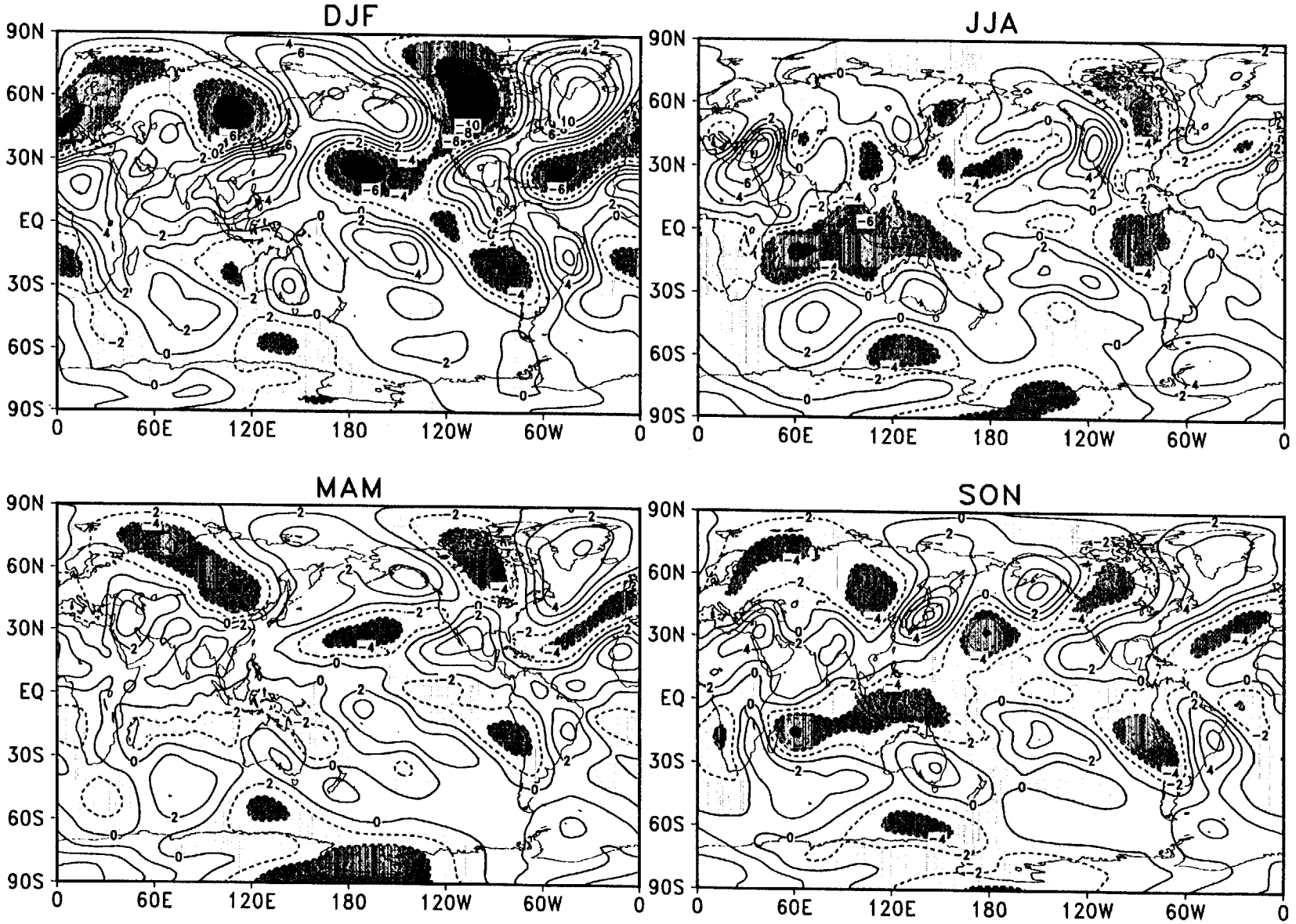

Figure 44: Seasonal means of 200 hPa v-wind for NCEP/NCAR reanalysis during 1980–1995. The contour interval is 2 m s^{-1}. Negative values are shaded.

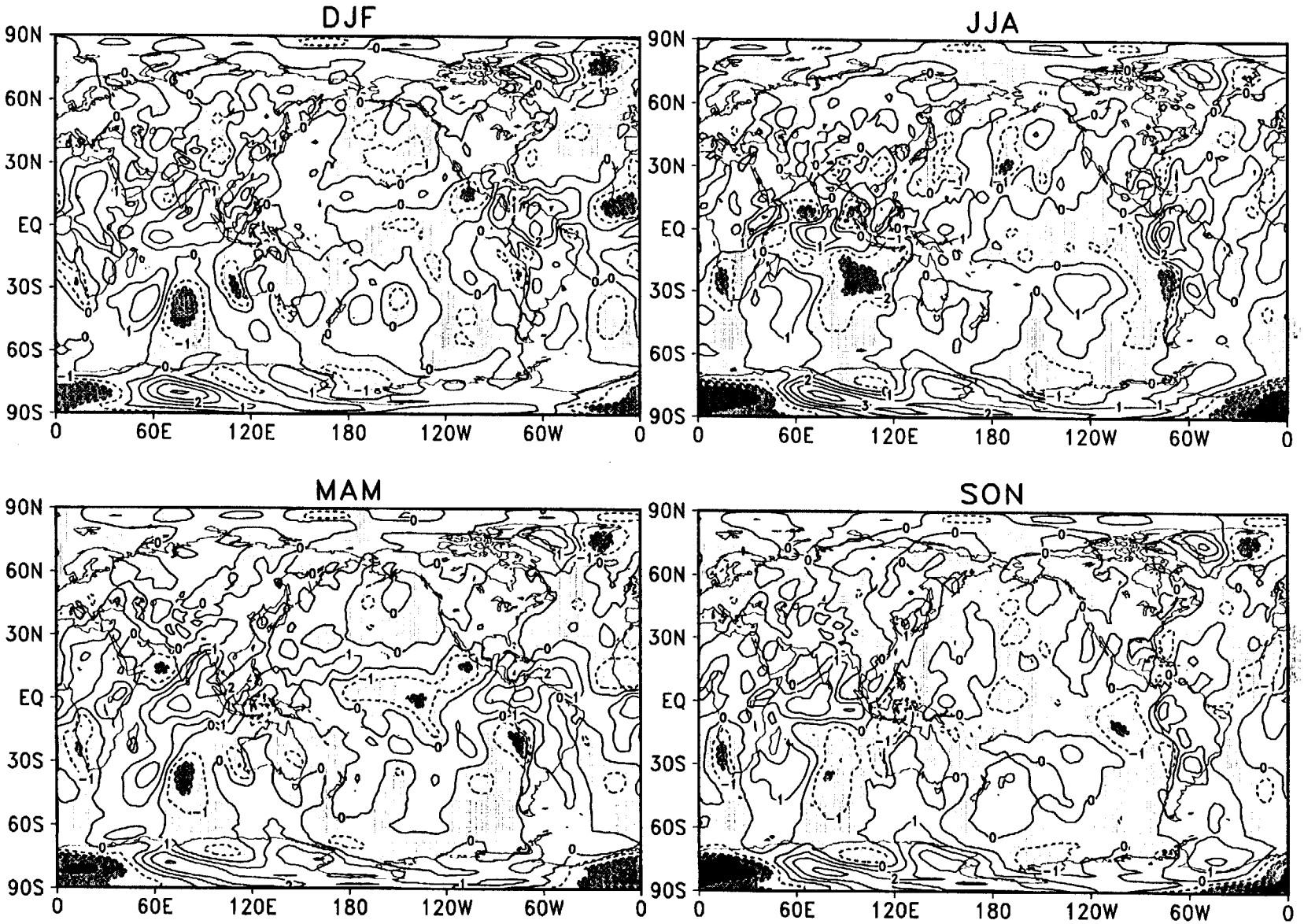

Figure 45: Difference of the seasonal means of 200 hPa v-wind during 1980–1995 (NCEP/NCAR minus DAO). The contour interval is 1 m s^{-1}. Negative values are shaded.

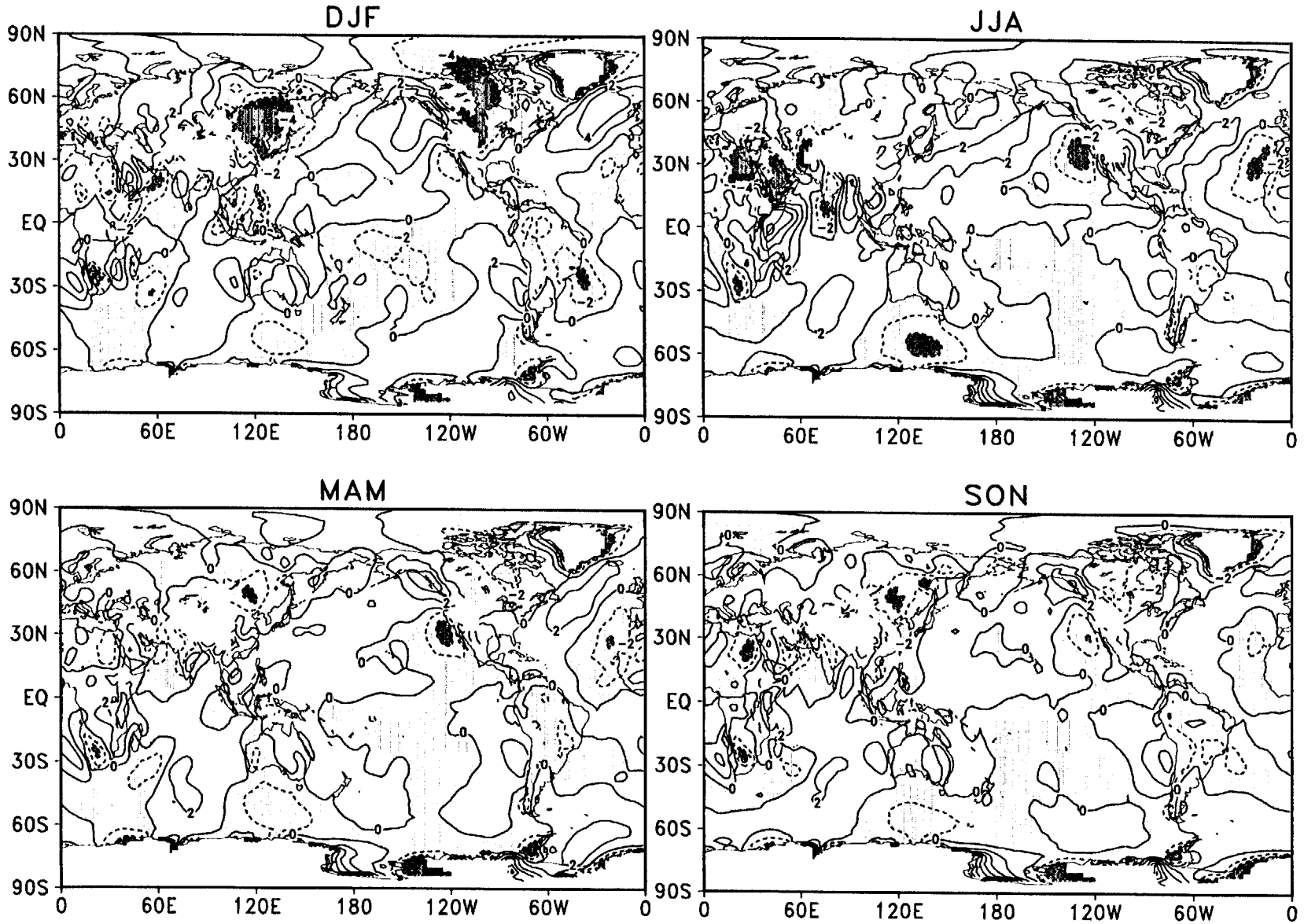

Figure 46: Seasonal means of 850 hPa v-wind for DAO reanalysis during 1980–1995. The contour interval is 2 m s^{-1}. Negative values are shaded.

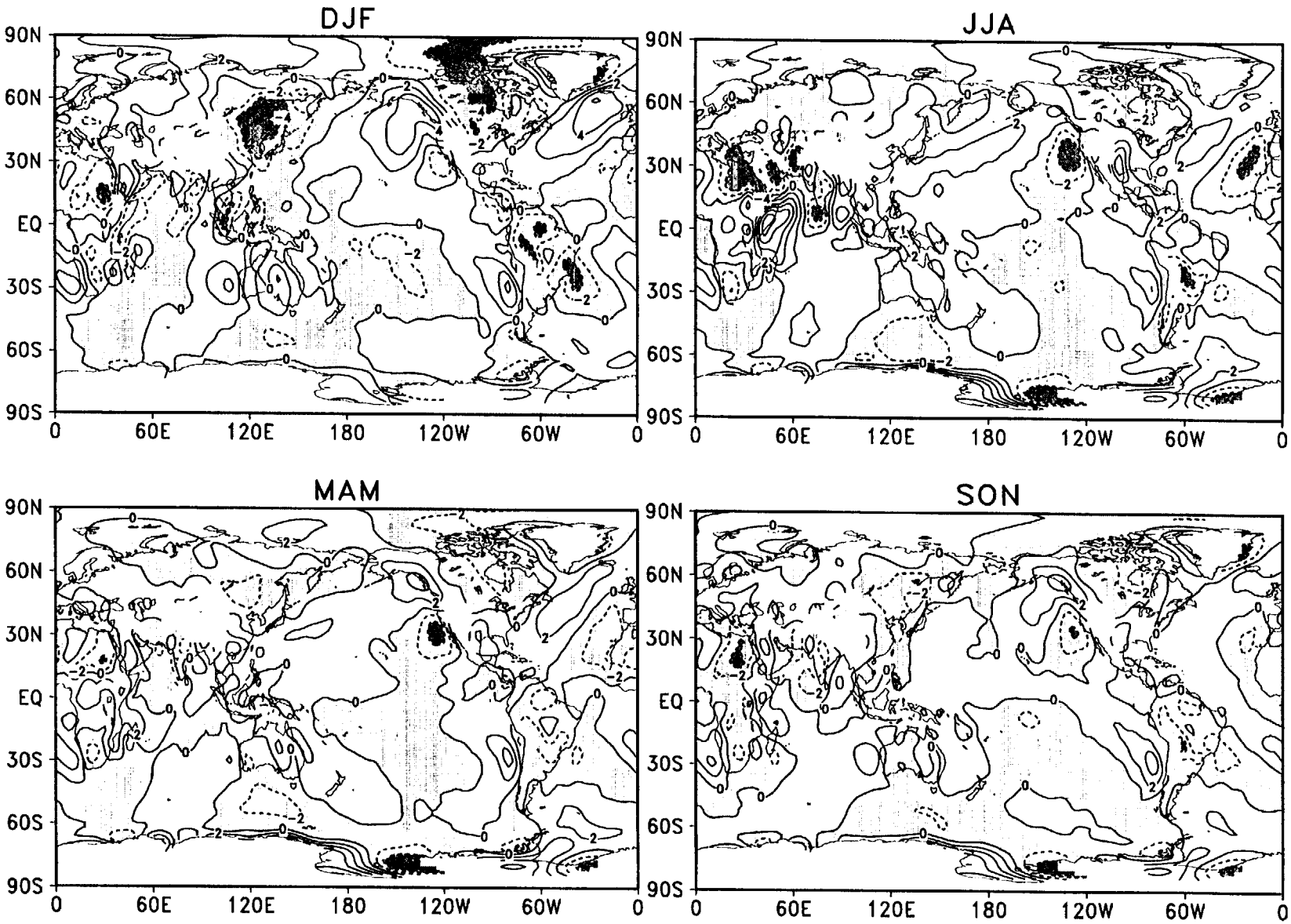

Figure 47: Seasonal means of 850 hPa v-wind for NCEP/NCAR reanalysis during 1980–1995. The contour interval is 2 m s^{-1}. Negative values are shaded.

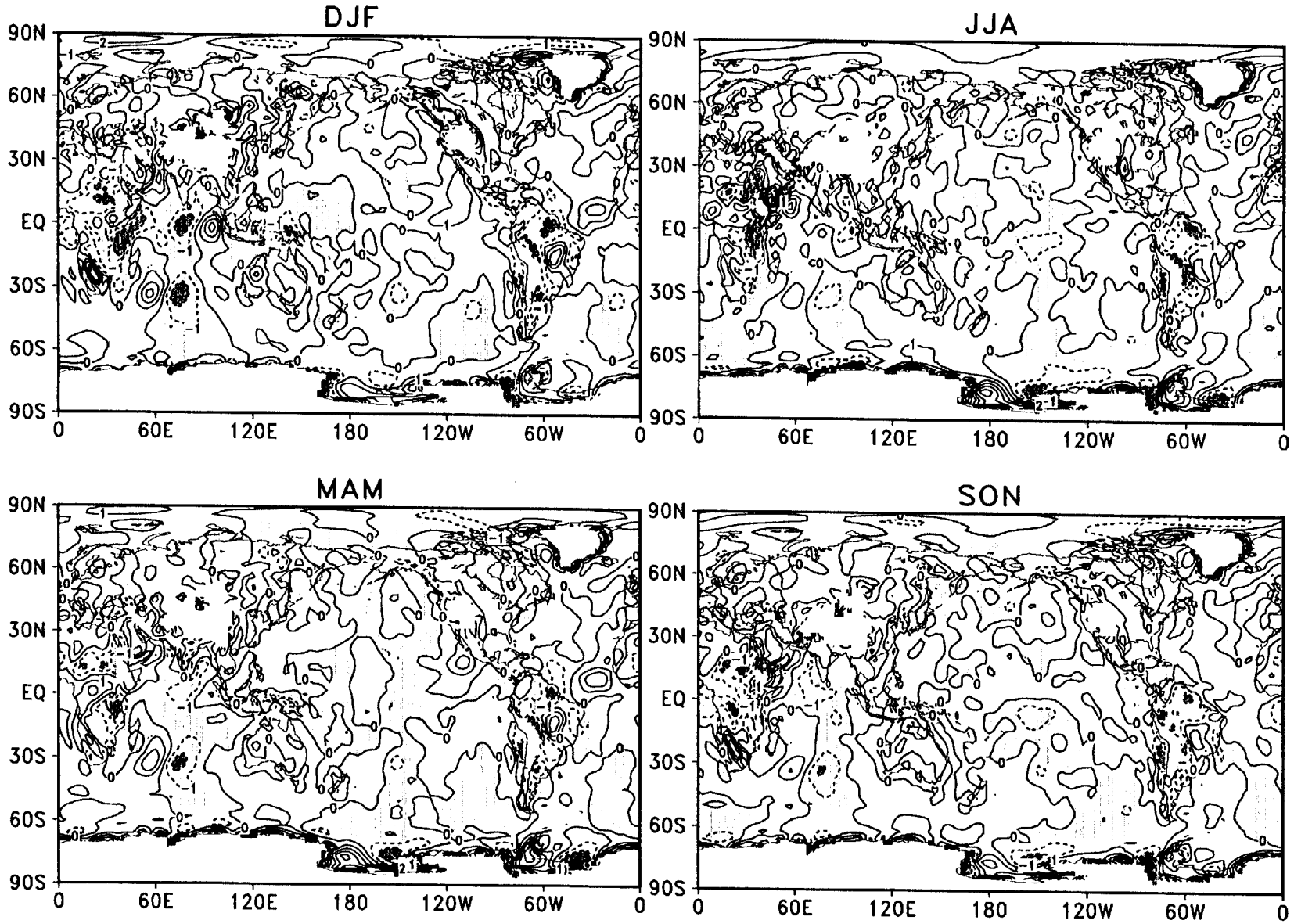

Figure 48: Difference of the seasonal means of 850 hPa v-wind during 1980–1995 (NCEP/NCAR minus DAO). The contour interval is 1 m s^{-1}. Negative values are shaded.

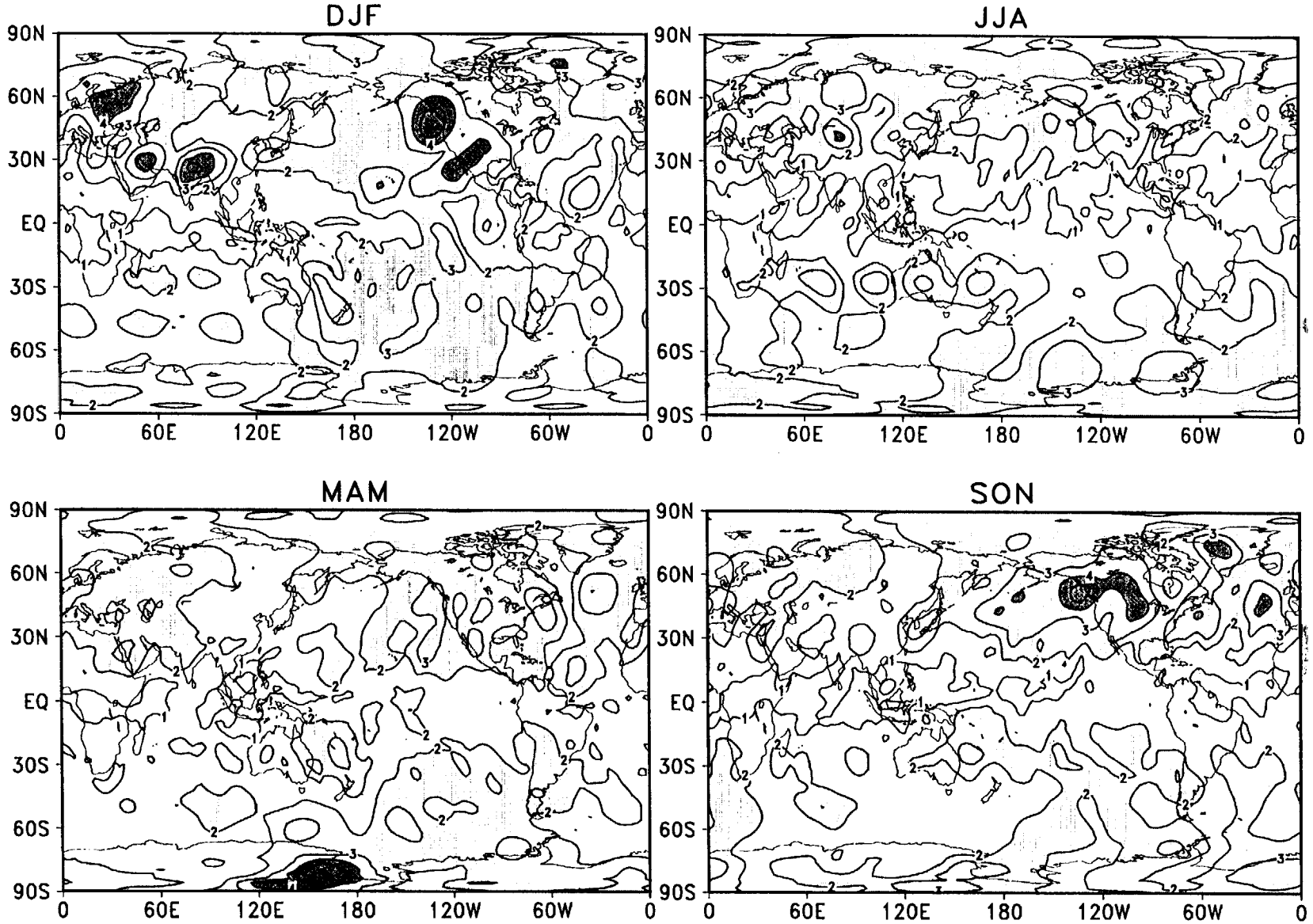

Figure 49: Standard deviations of seasonal mean 200 hPa v-wind for DAO reanalysis during 1980–1995. The contour interval is 1 m s^{-1}. Values larger than 2 m s^{-1} are shaded.

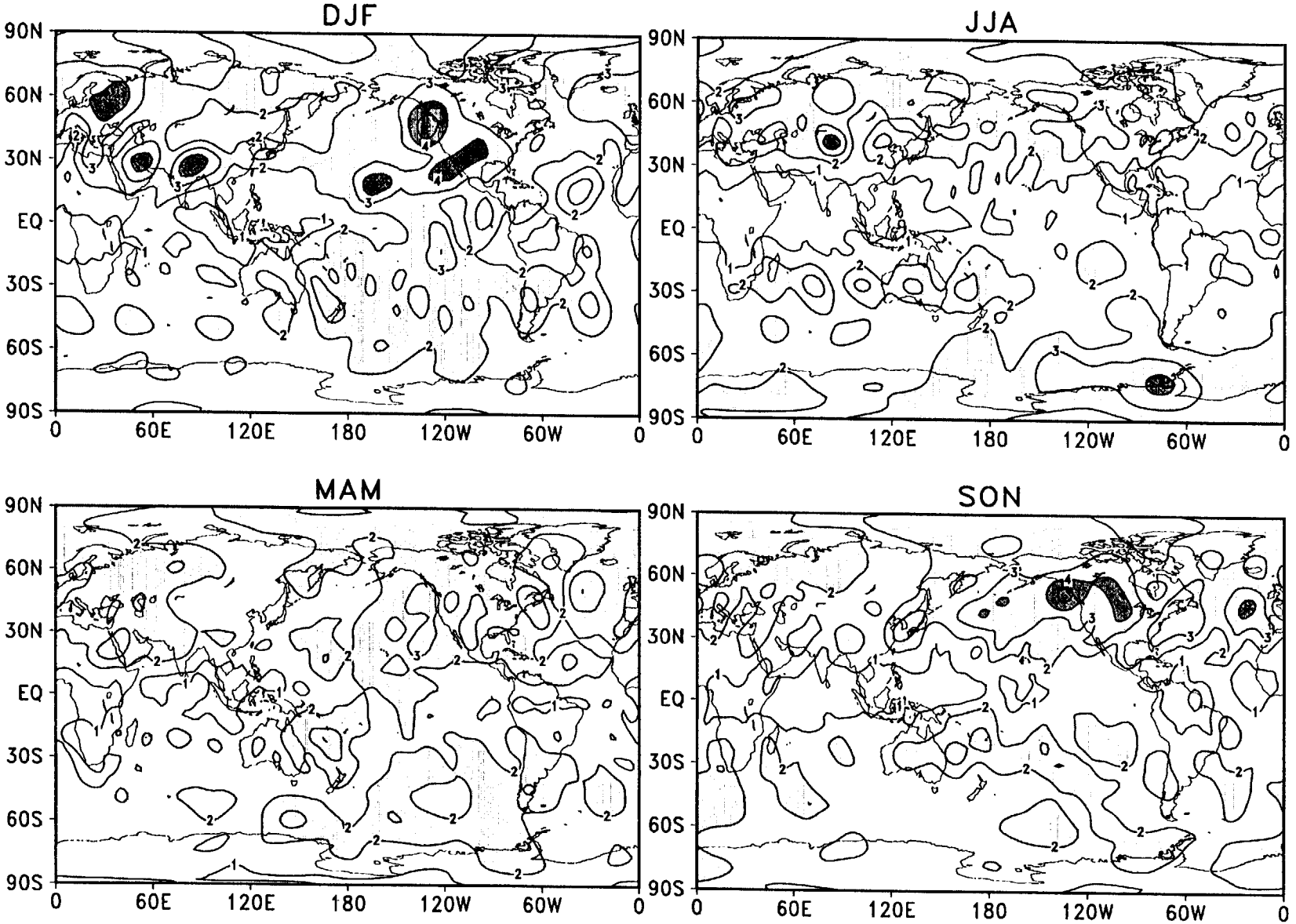

Figure 50: Standard deviations of seasonal mean 200 hPa v-wind for NCEP/NCAR reanalysis during 1980–1995. The contour interval is 1 m s^{-1}. Values larger than 2 m s^{-1} are shaded.

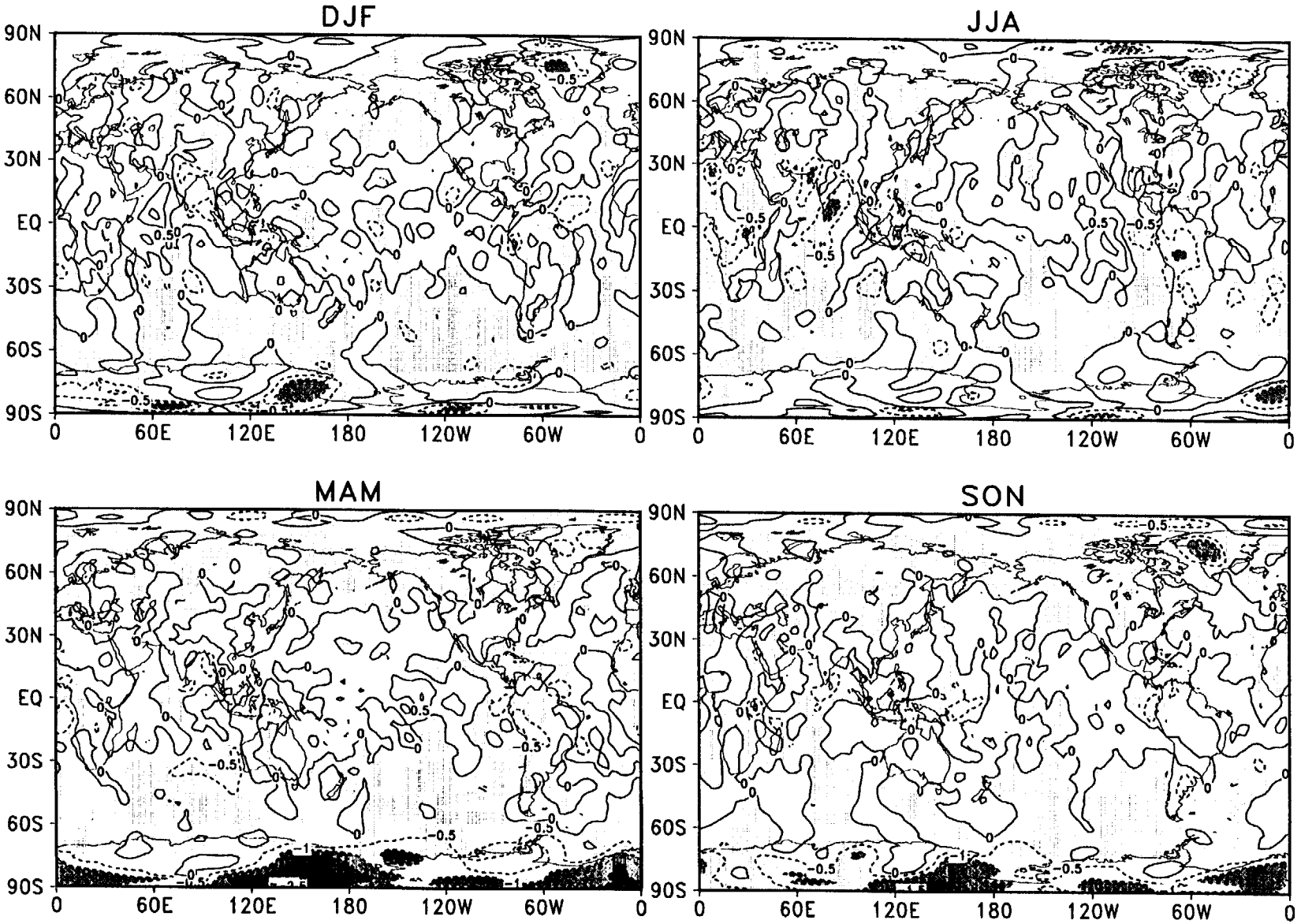

Figure 51: Difference of the standard deviations of seasonal mean 200 hPa v-wind during 1980–1995 (NCEP/NCAR minus DAO). The contour interval is 0.5 m s^{-1}. Negative values are shaded.

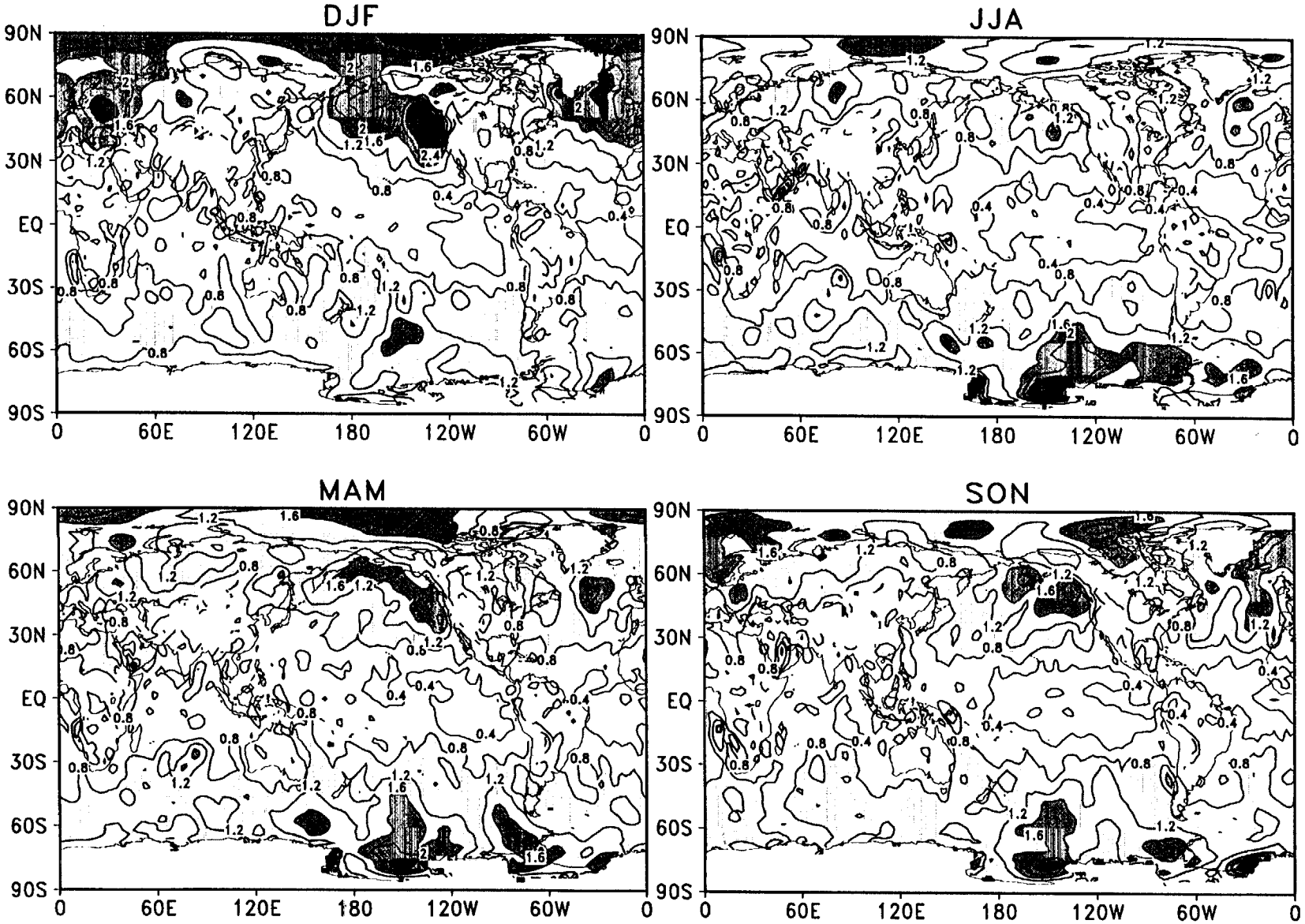

Figure 52: Standard deviations of seasonal mean 850 hPa v-wind for DAO reanalysis during 1980–1995. The contour interval is 0.4 m s^{-1}. Values larger than 0.8 m s^{-1} are shaded.

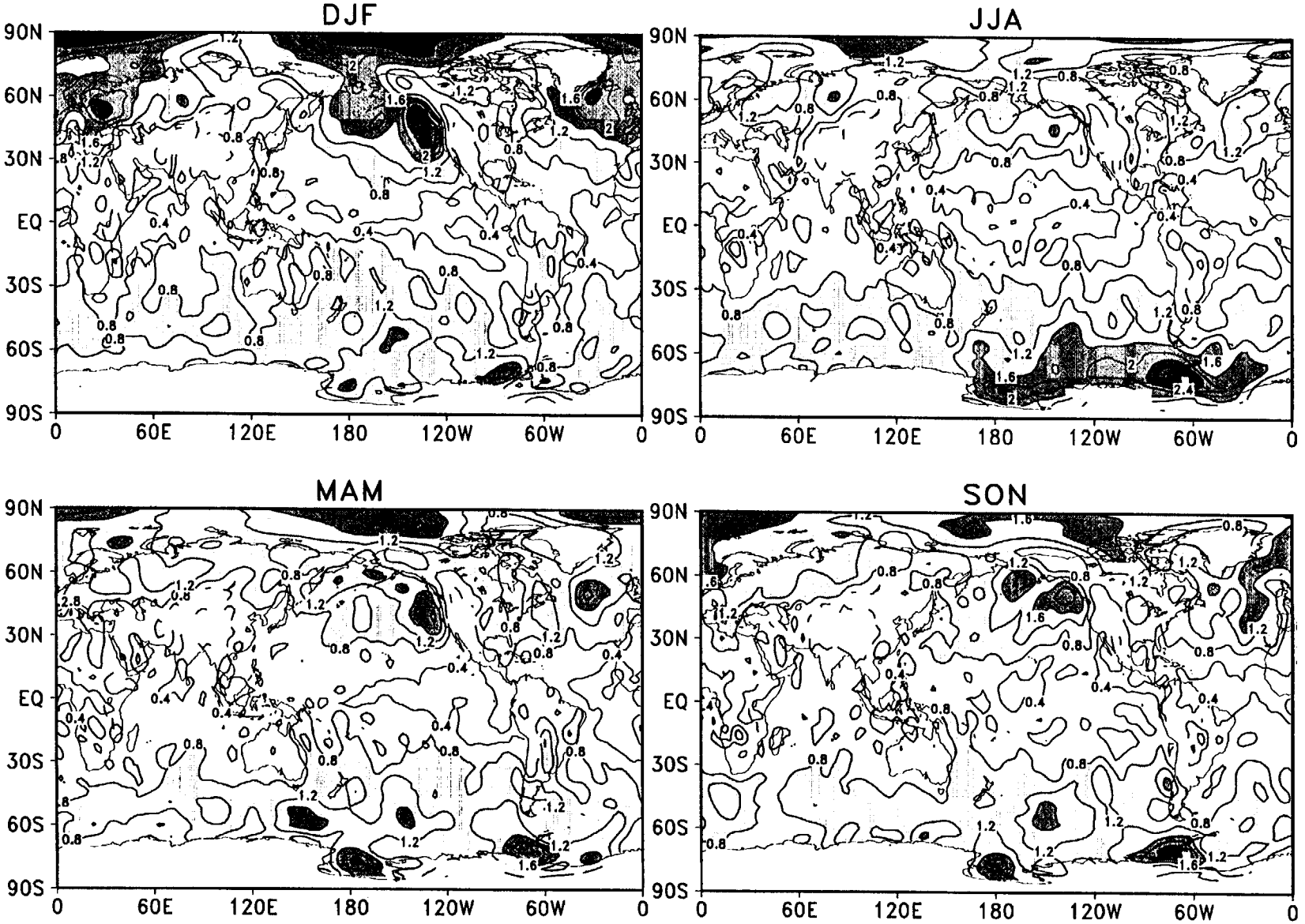

Figure 53: Standard deviations of seasonal mean 850 hPa v-wind for NCEP/NCAR reanalysis during 1980–1995. The contour interval is 0.4 m s^{-1}. Values larger than 0.8 m s^{-1} are shaded.

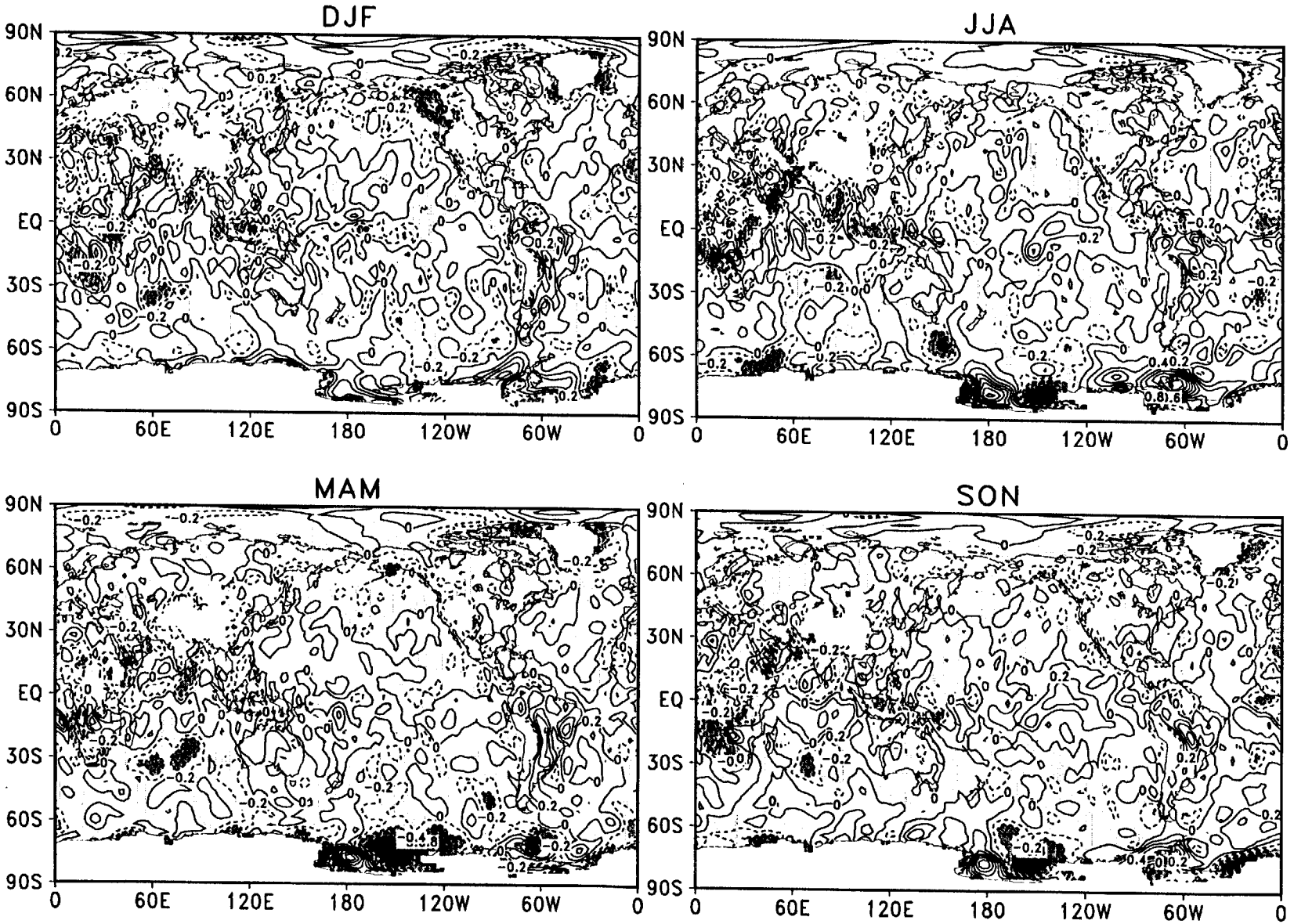

Figure 54: Difference of the standard deviations of seasonal mean 850 hPa v-wind during 1980–1995 (NCEP/NCAR minus DAO). The contour interval is 0.2 m s^{-1}. Negative values are shaded.

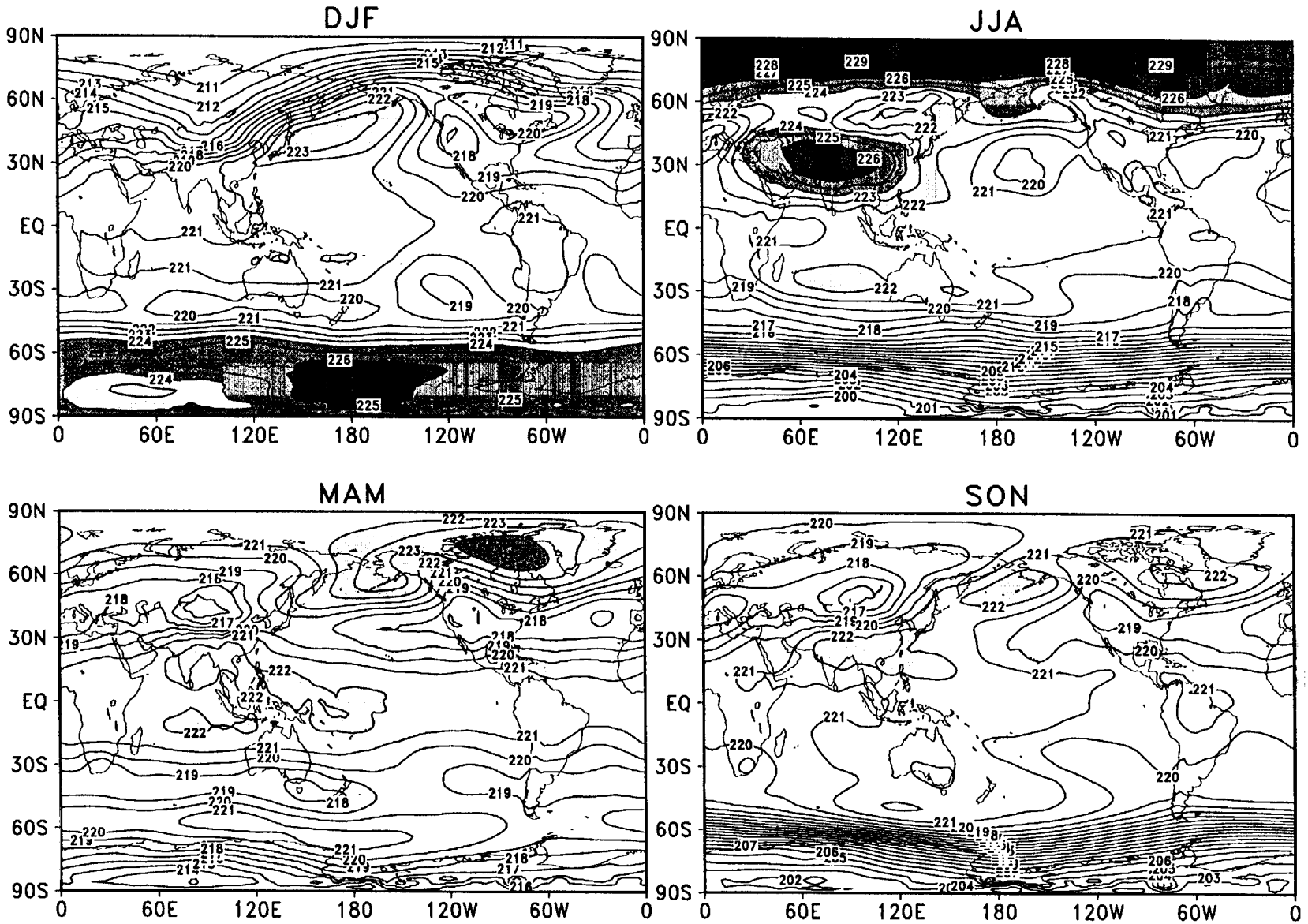

Figure 55: Seasonal means of 200 hPa temperature for DAO reanalysis during 1980–1995. The contour interval is 1°K. Values less than 222°K are shaded.

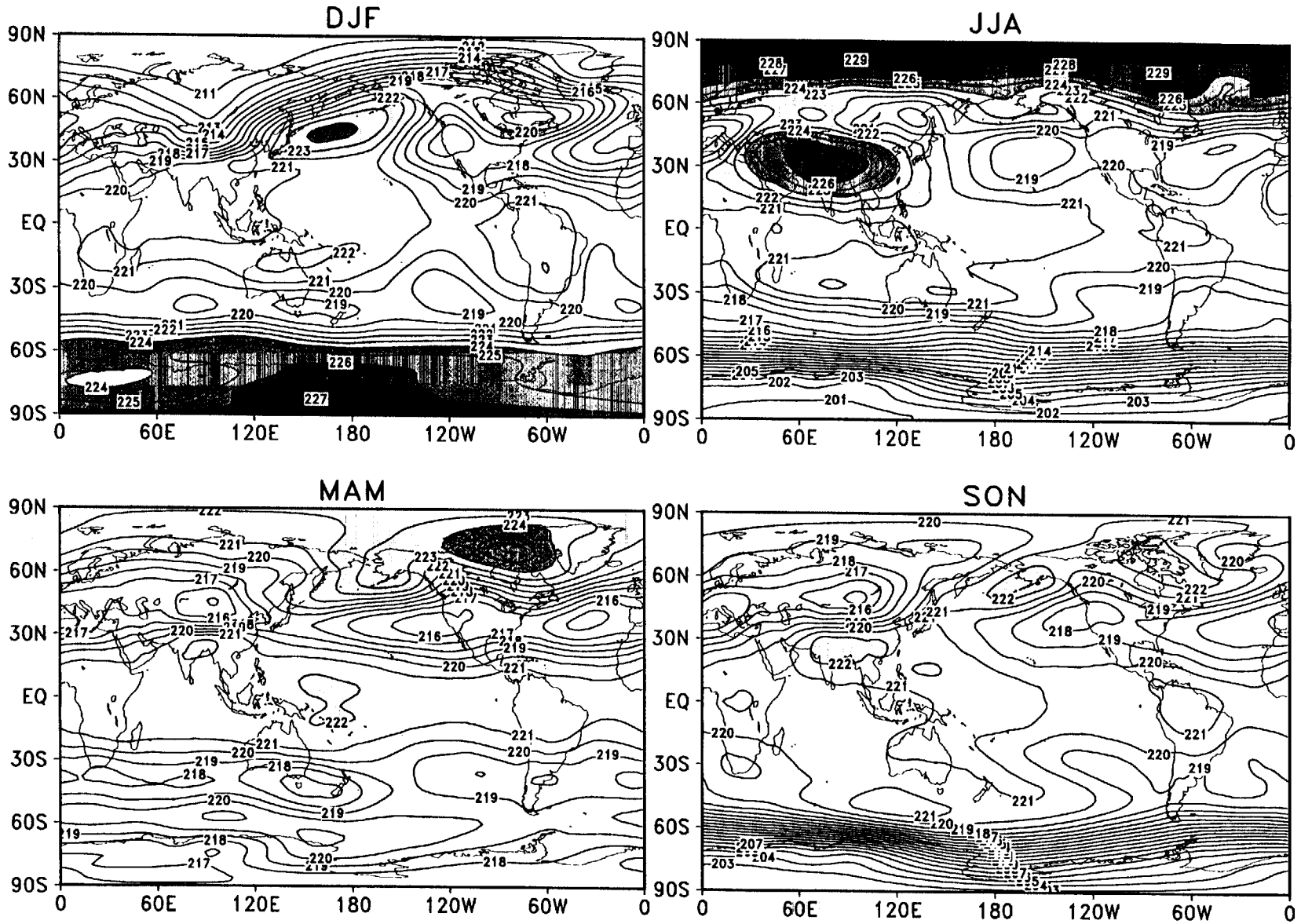

Figure 56: Seasonal means of 200 hPa temperature for NCEP/NCAR reanalysis during 1980–1995. The contour interval is 1°K. Values less than 222°K are shaded.

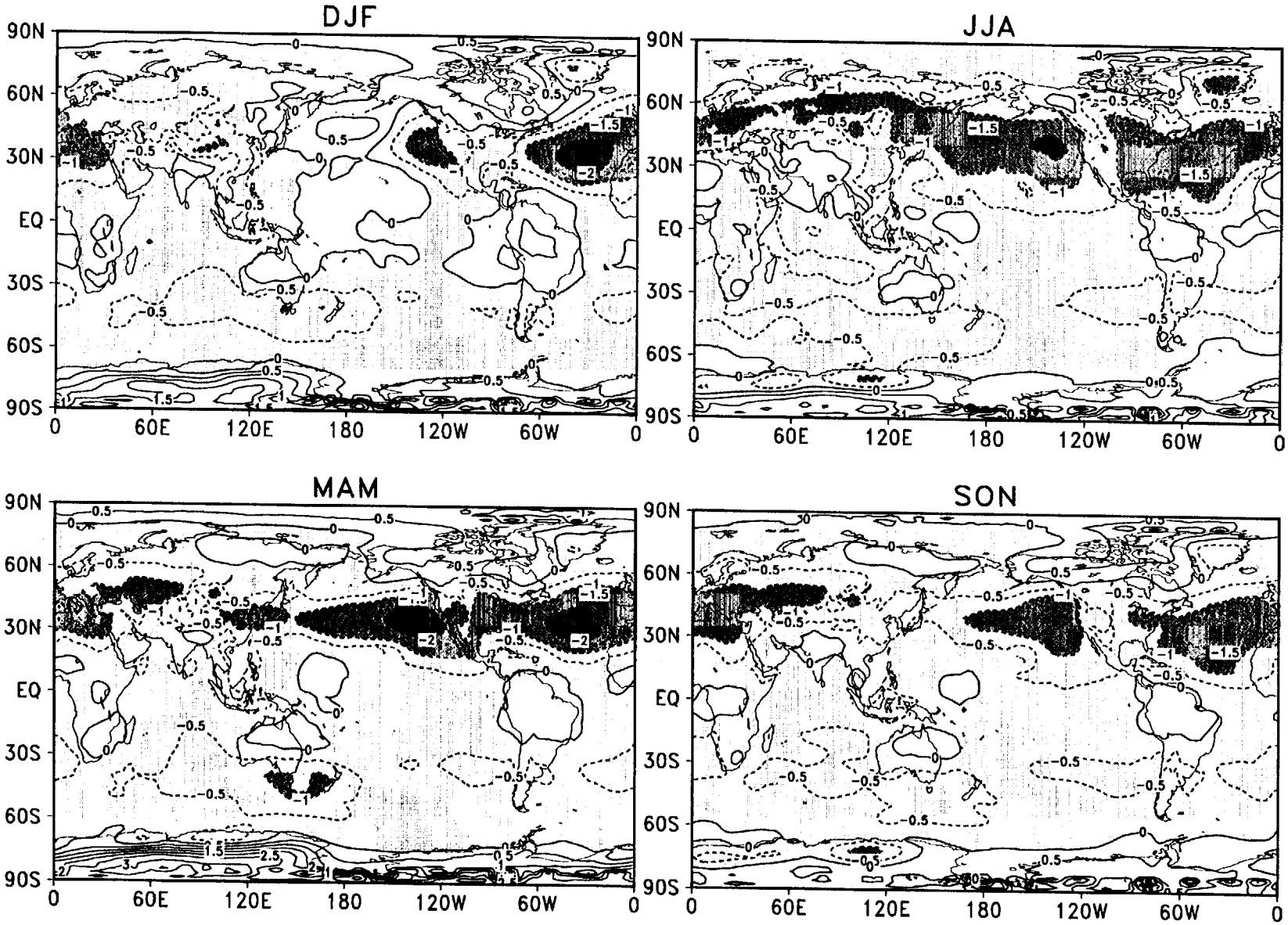

Figure 57: Difference of the seasonal means of 200 hPa temperature during 1980–1995 (NCEP/NCAR minus DAO). The contour interval is 0.5°K. Negative values are shaded.

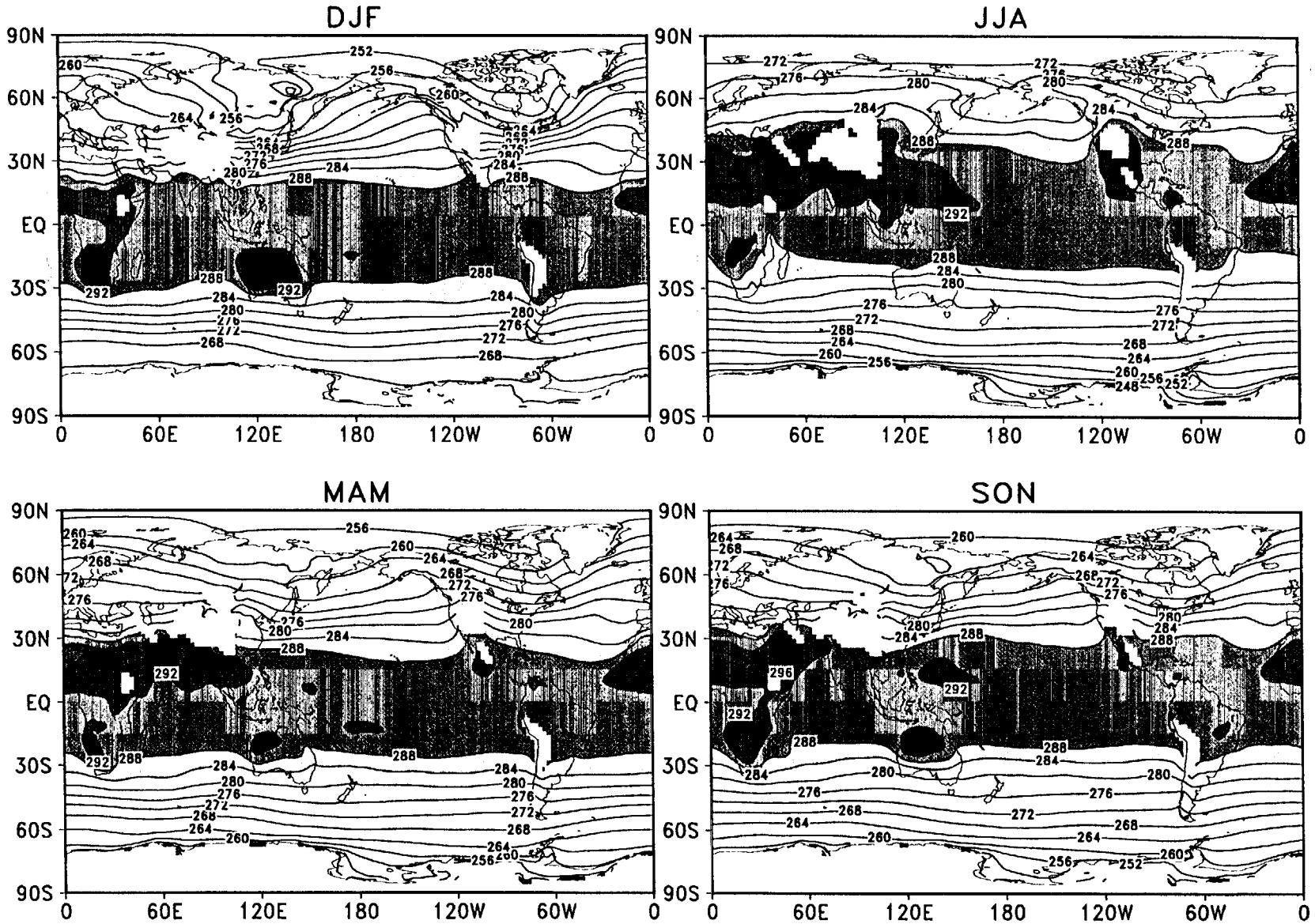

Figure 58: Seasonal means of 850 hPa temperature for DAO reanalysis during 1980–1995. The contour interval is 4°K. Values less than 284°K are shaded.

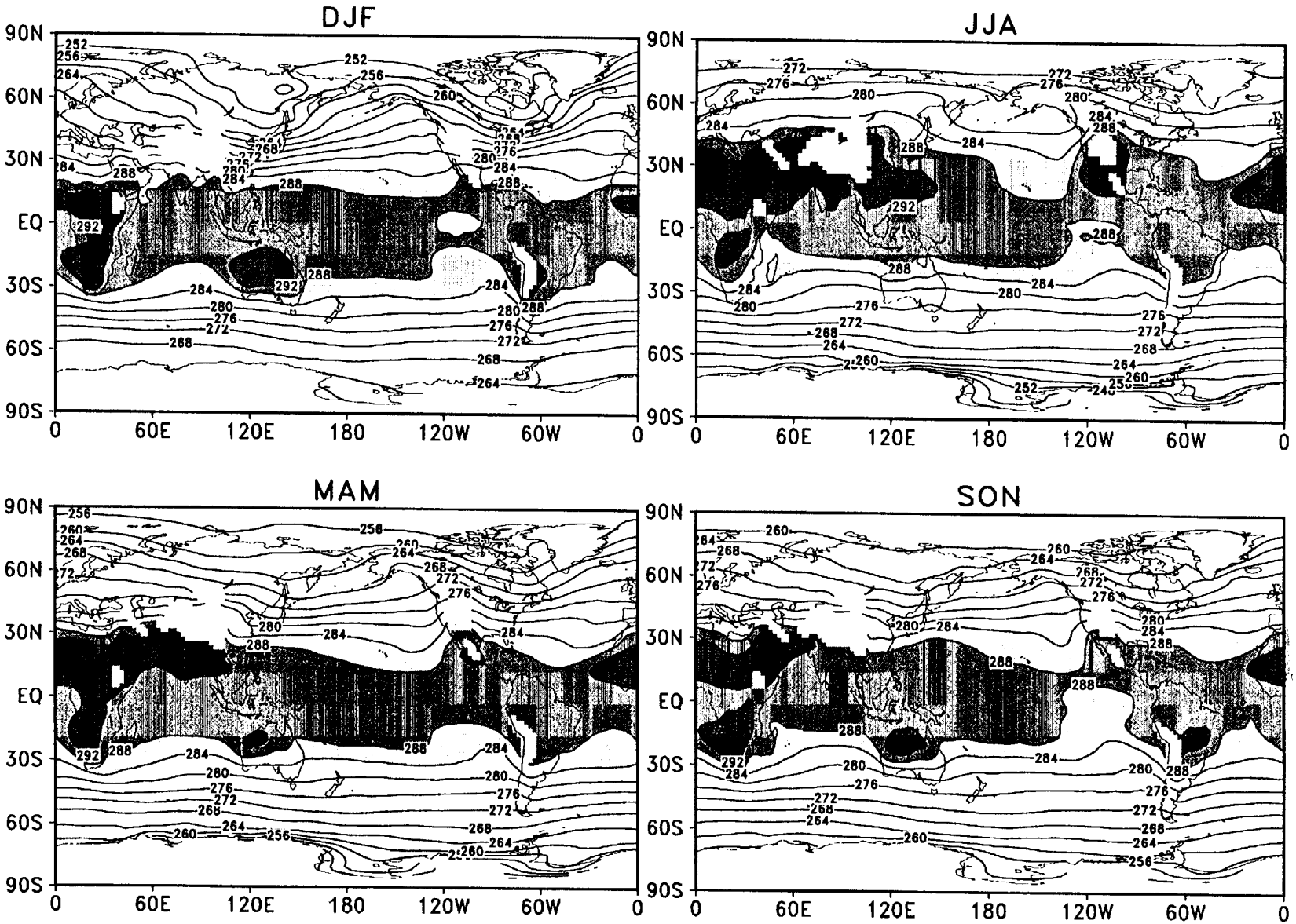

Figure 59: Seasonal means of 850 hPa temperature for NCEP/NCAR reanalysis during 1980–1995. The contour interval is 4°K. Values less than 284°K are shaded.

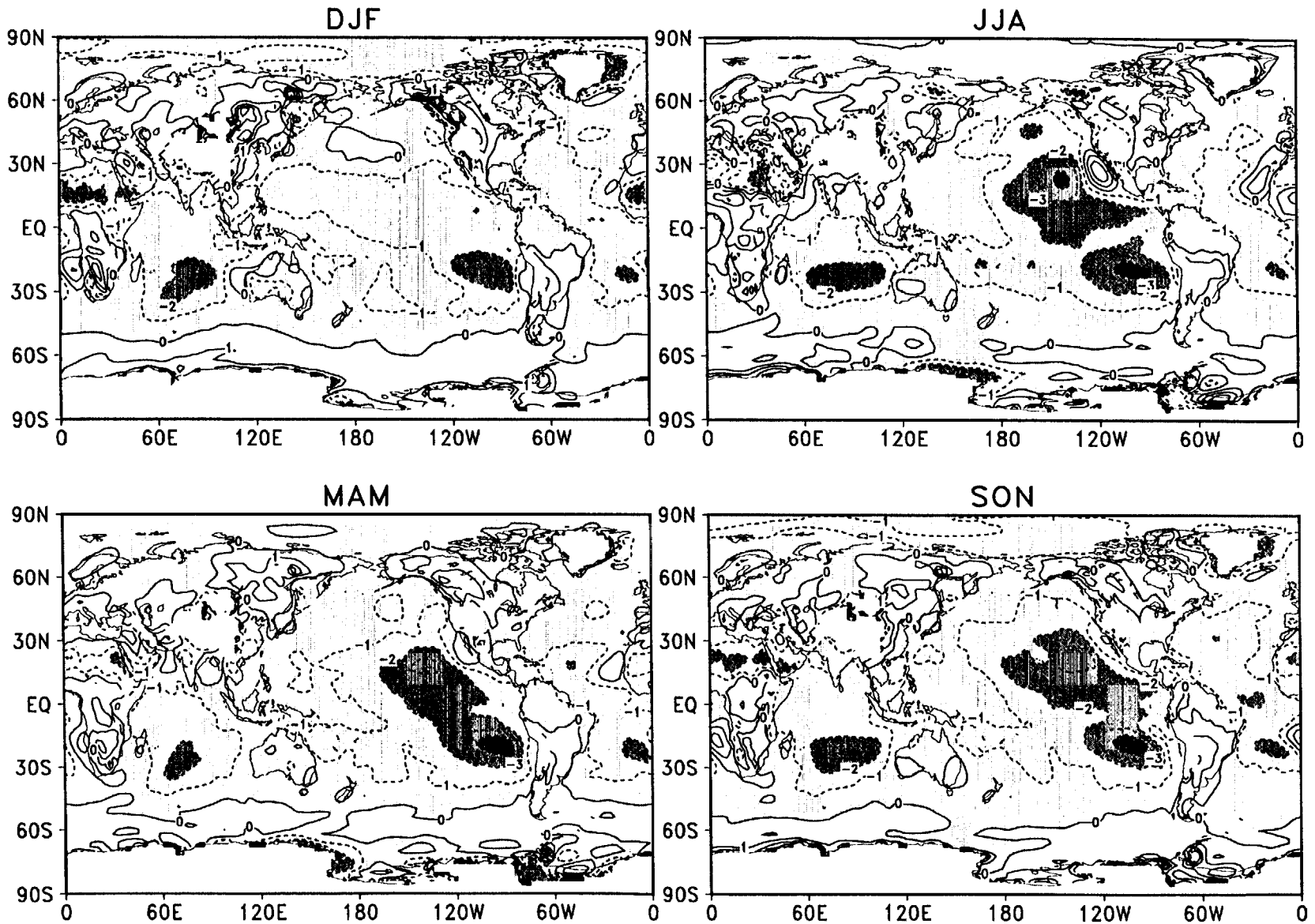

Figure 60: Difference of the seasonal means of 850 hPa temperature during 1980–1995 (NCEP/NCAR minus DAO). The contour interval is 1°K. Negative values are shaded.

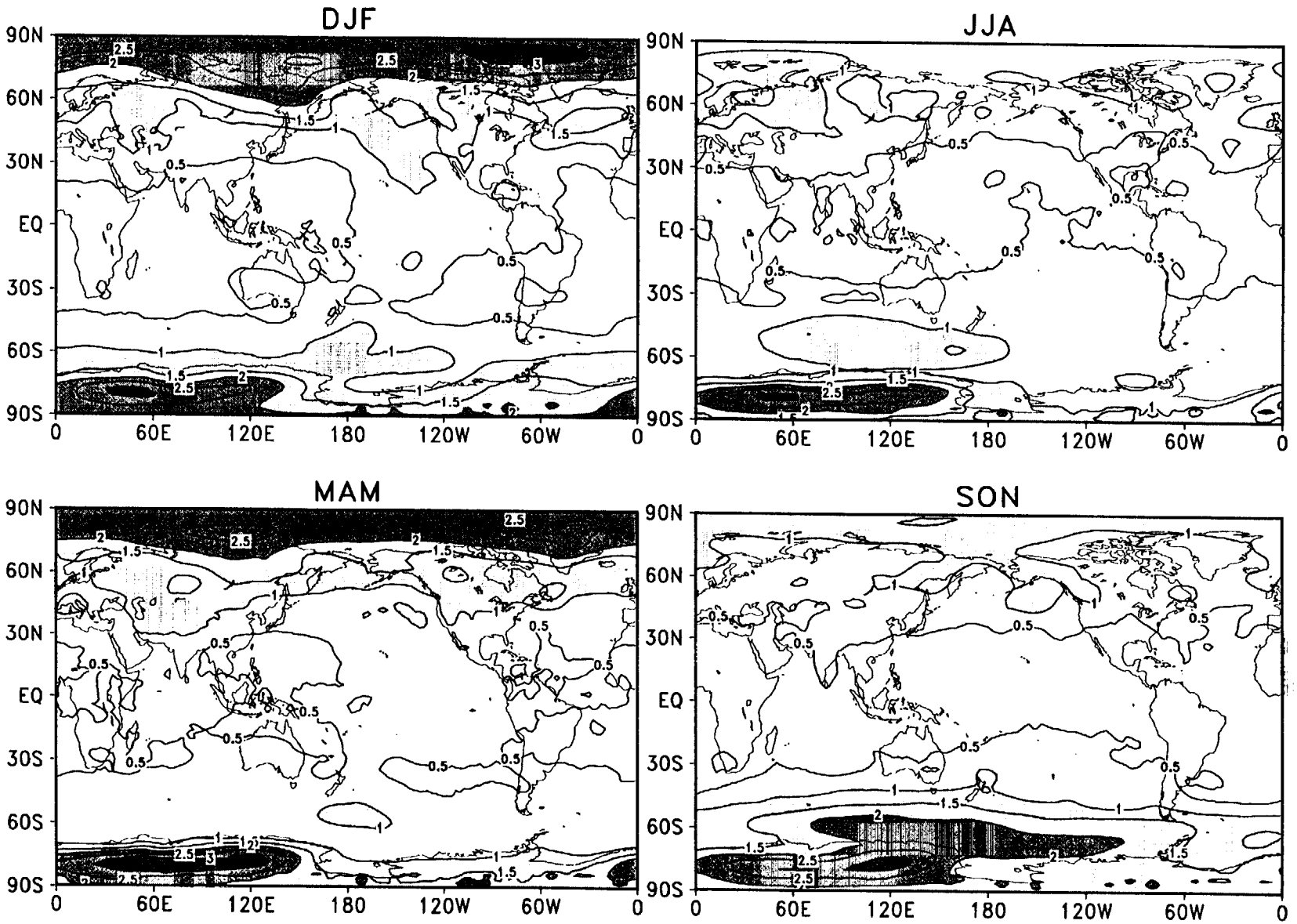

Figure 61: Standard deviations of seasonal mean 200 hPa temperature for DAO reanalysis during 1980–1995. The contour interval is 0.5°K. Values larger than 1°K are shaded.

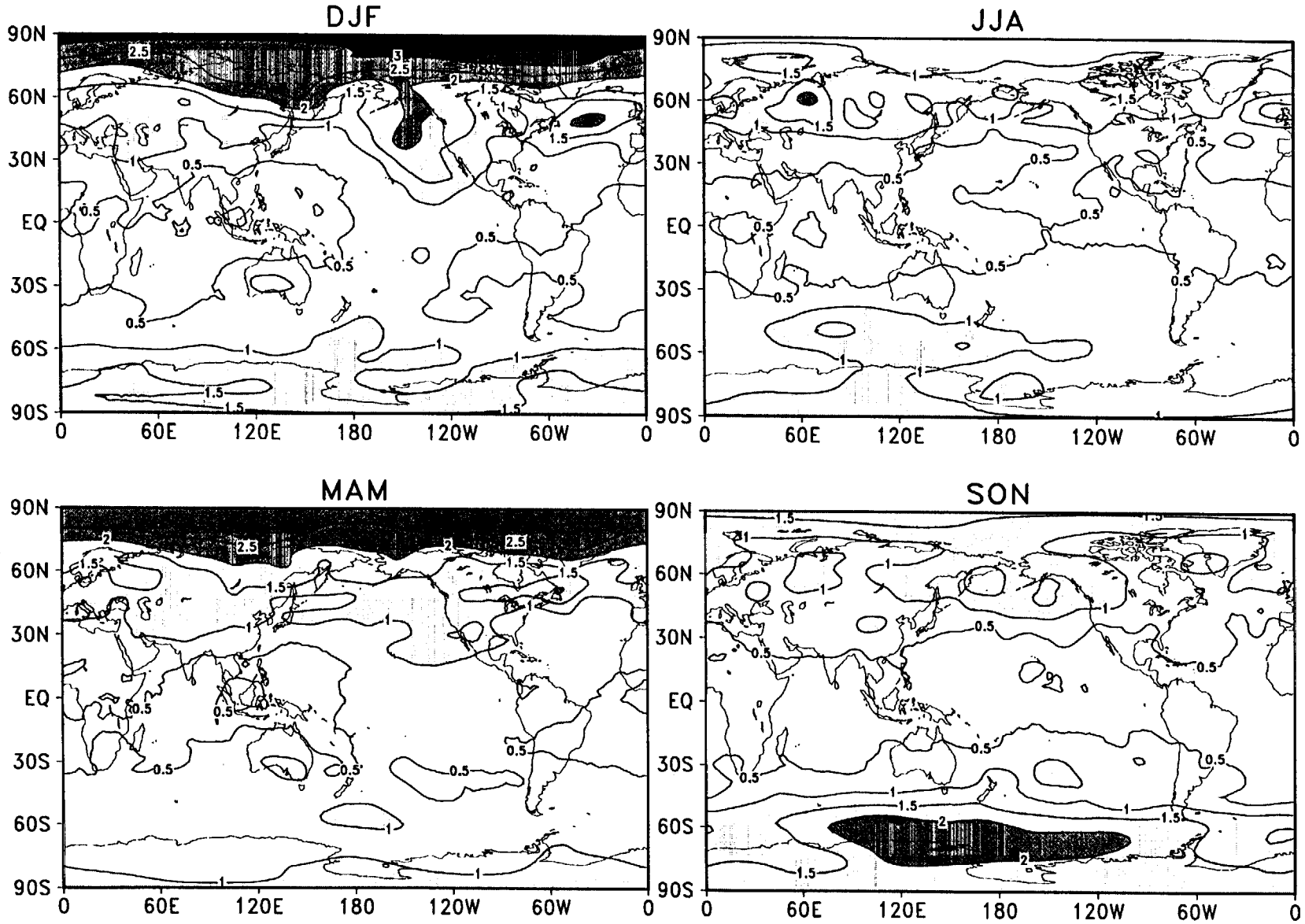

Figure 62: Standard deviations of seasonal mean 200 hPa temperature for NCEP/NCAR reanalysis during 1980–1995. The contour interval is 0.5°K. Values larger than 1°K are shaded.

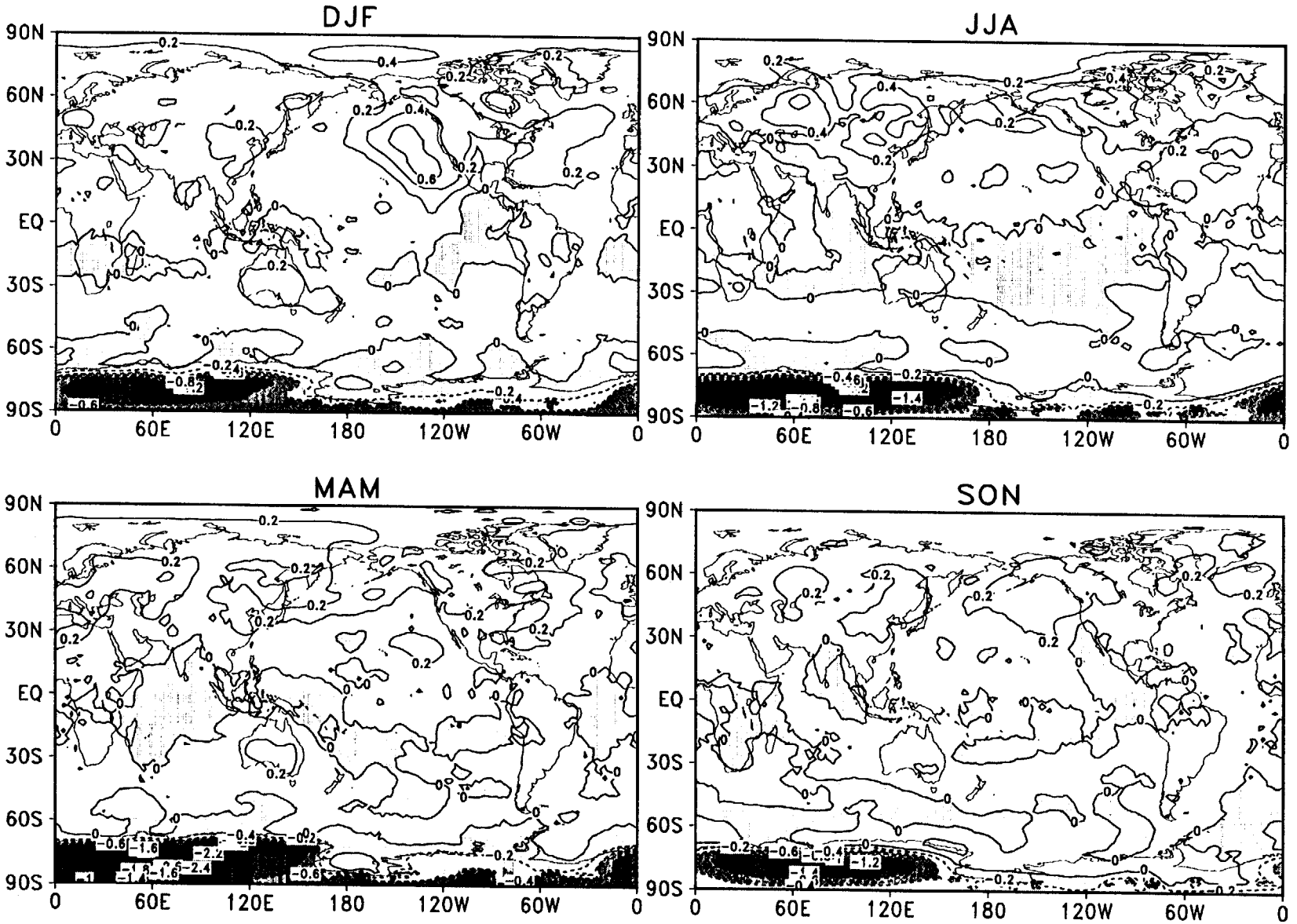

Figure 63: Difference of the standard deviations of seasonal mean 200 hPa temperature during 1980–1995 (NCEP/NCAR minus DAO). The contour interval is 0.2°K. Negative values are shaded.

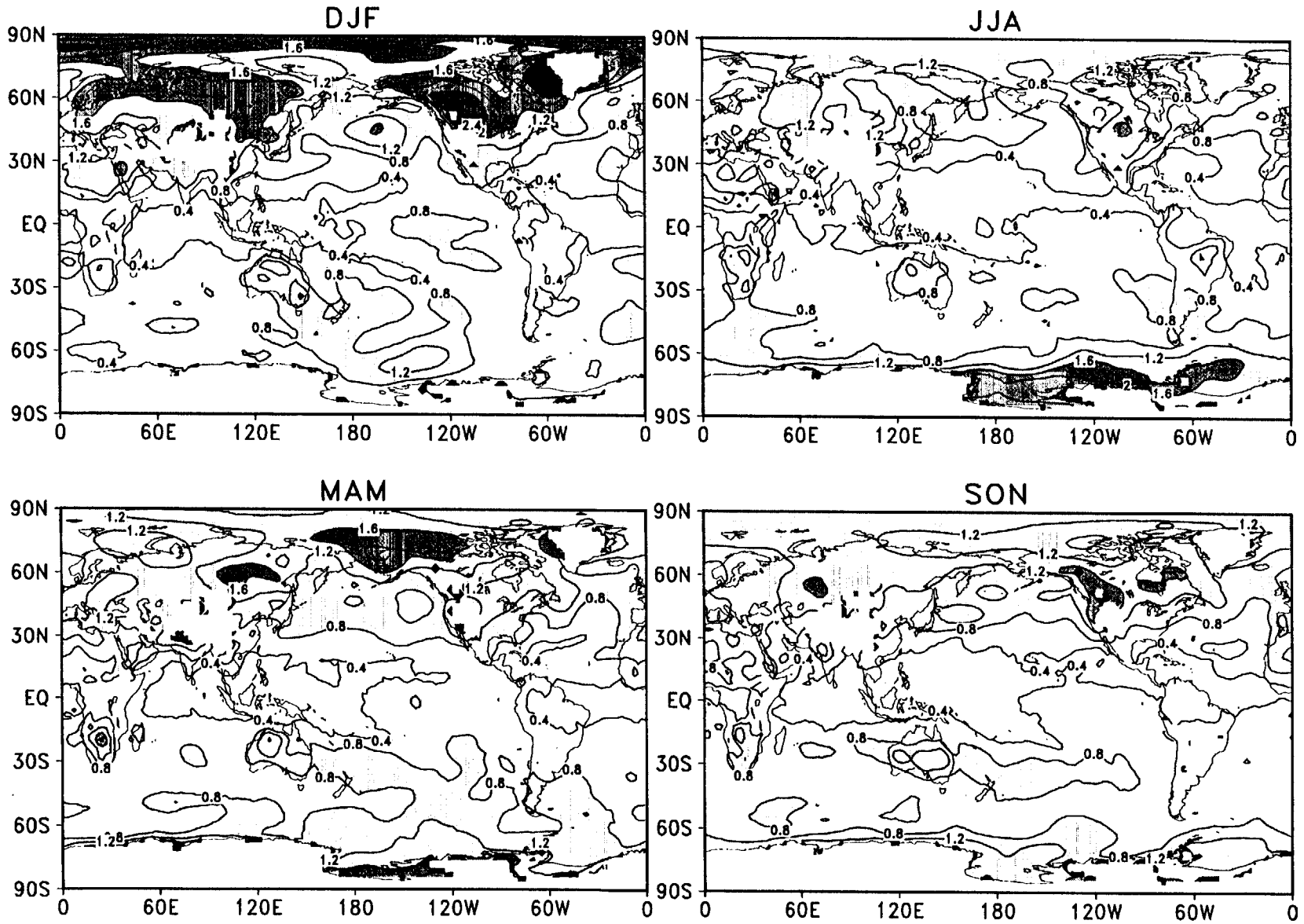

Figure 64: Standard deviations of seasonal mean 850 hPa temperature for DAO reanalysis during 1980–1995. The contour interval is 0.4°K. Values larger than 0.8°K are shaded.

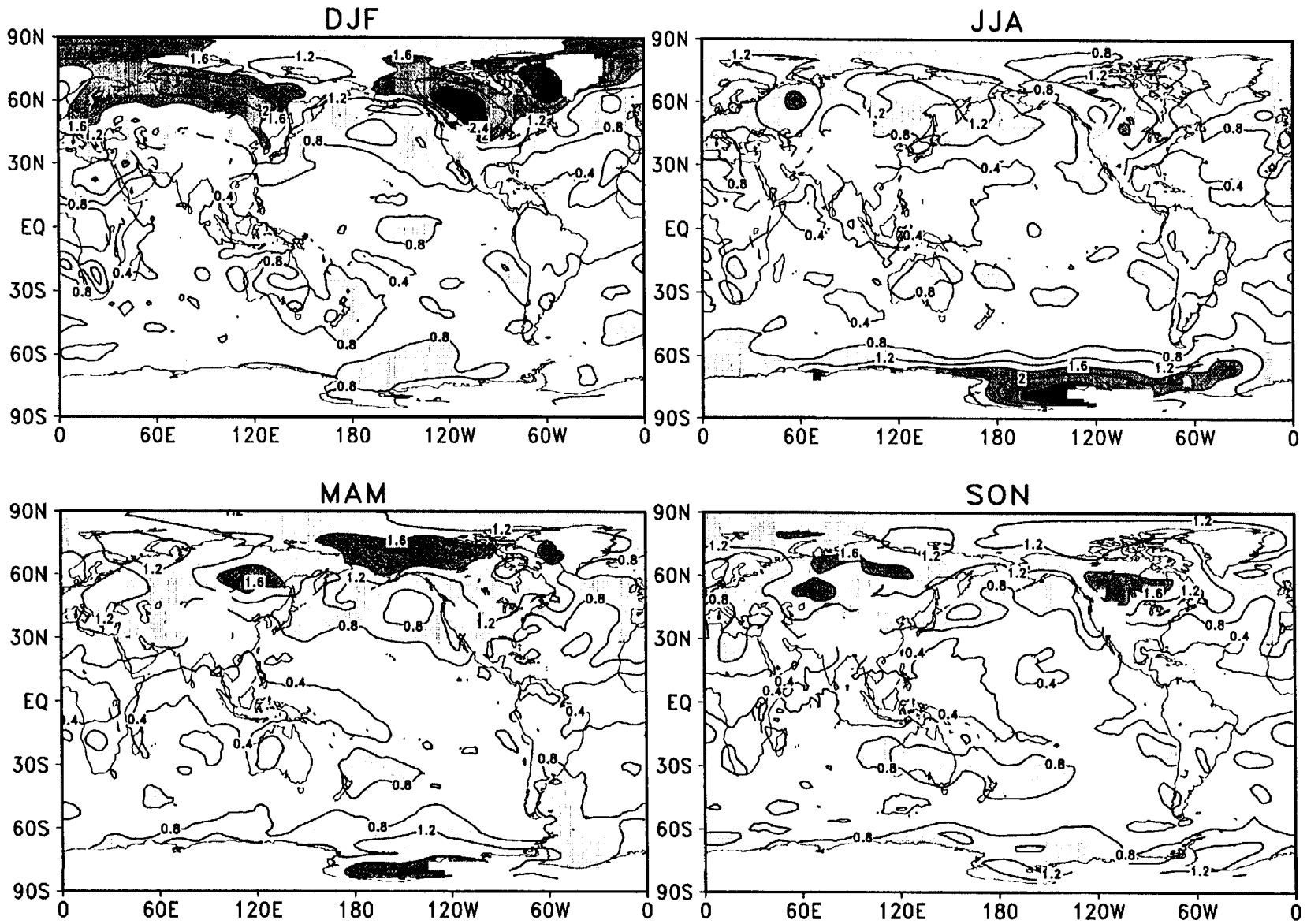

Figure 65: Standard deviations of seasonal mean 850 hPa temperature for NCEP/NCAR reanalysis during 1980–1995. The contour interval is 0.4°K. Values larger than 0.8°K are shaded.

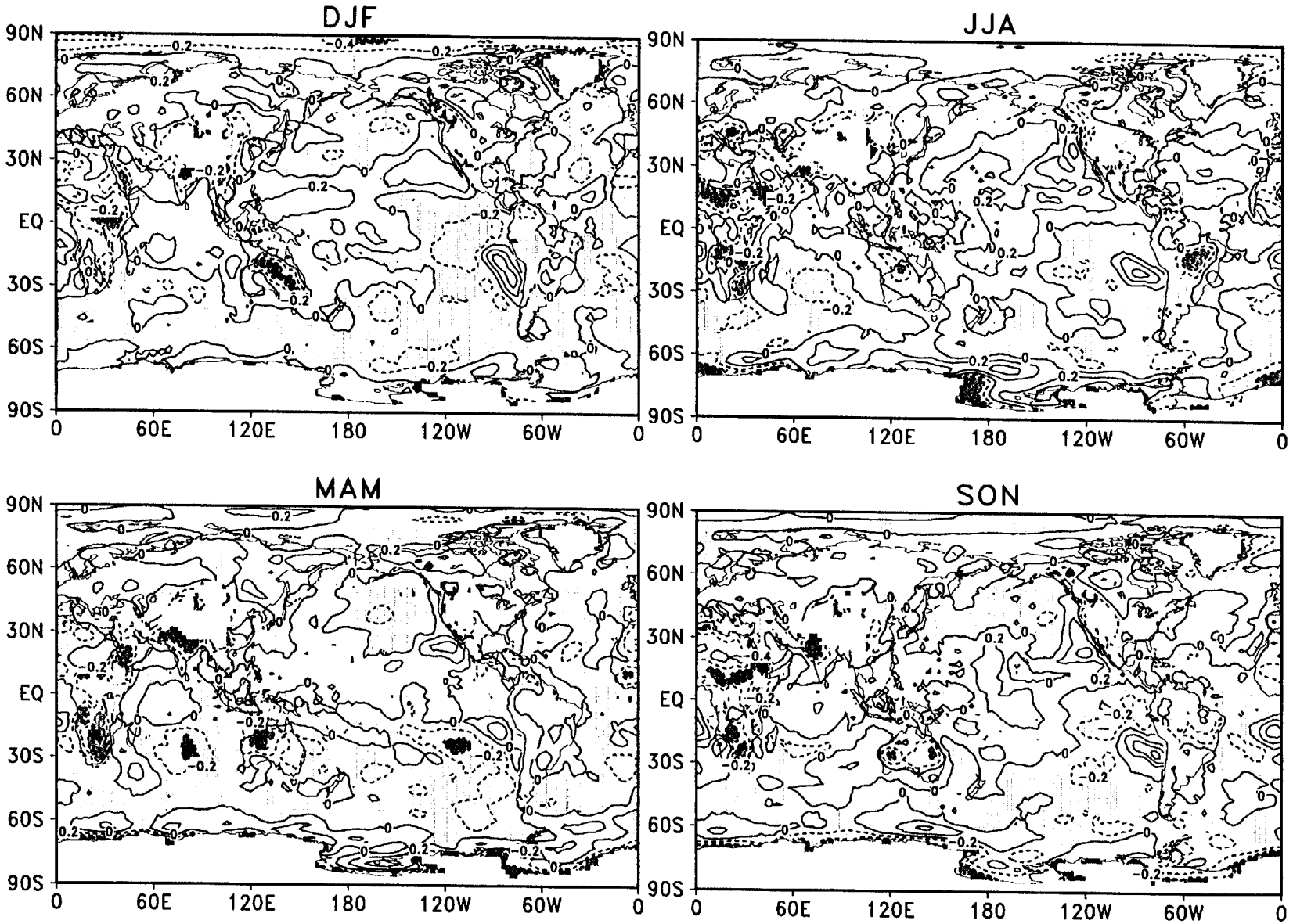

Figure 66: Difference of the standard deviations of seasonal mean 850 hPa temperature during 1980–1995 (NCEP/NCAR minus DAO). The contour interval is 0.2°K. Negative values are shaded.

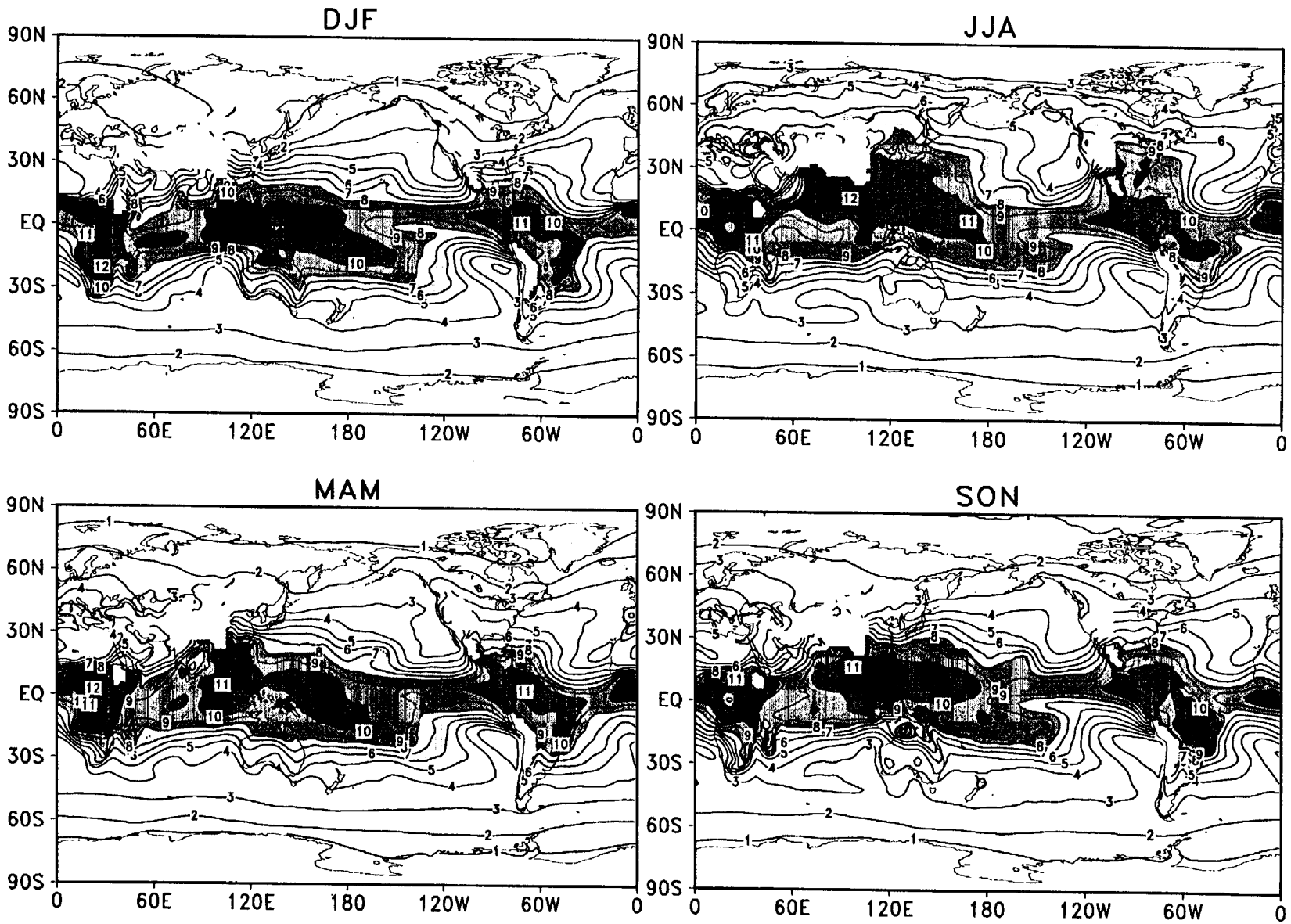

Figure 67: Seasonal means of 850 hPa specific humidity for DAO reanalysis during 1980–1995. The contour interval is 1 g kg^{-1}. Values larger than 6 g kg^{-1} are shaded.

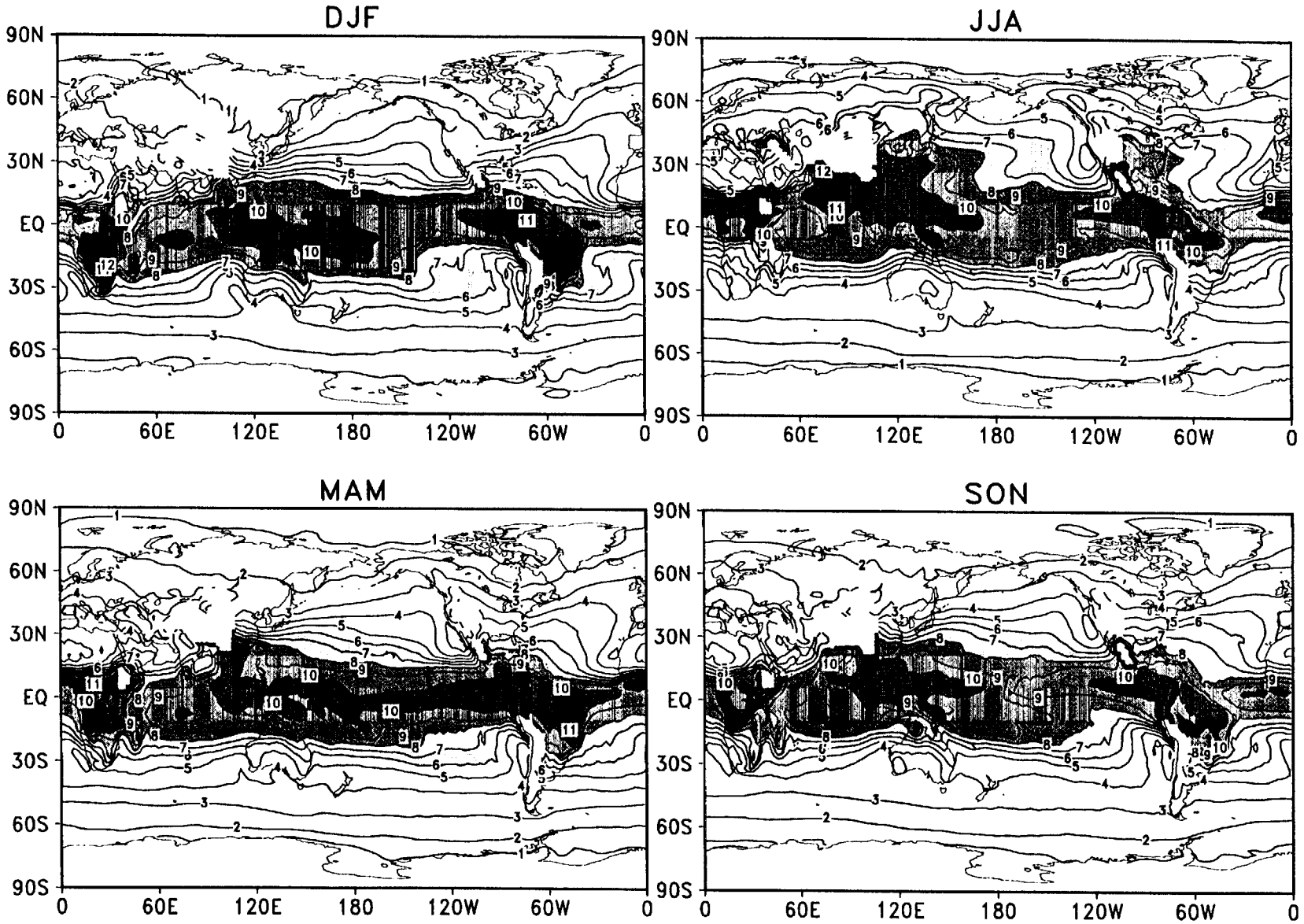

Figure 68: Seasonal means of 850 hPa specific humidity for NCEP/NCAR reanalysis during 1980–1995. The contour interval is 1 g kg^{-1}. Values larger than 6 g kg^{-1} are shaded.

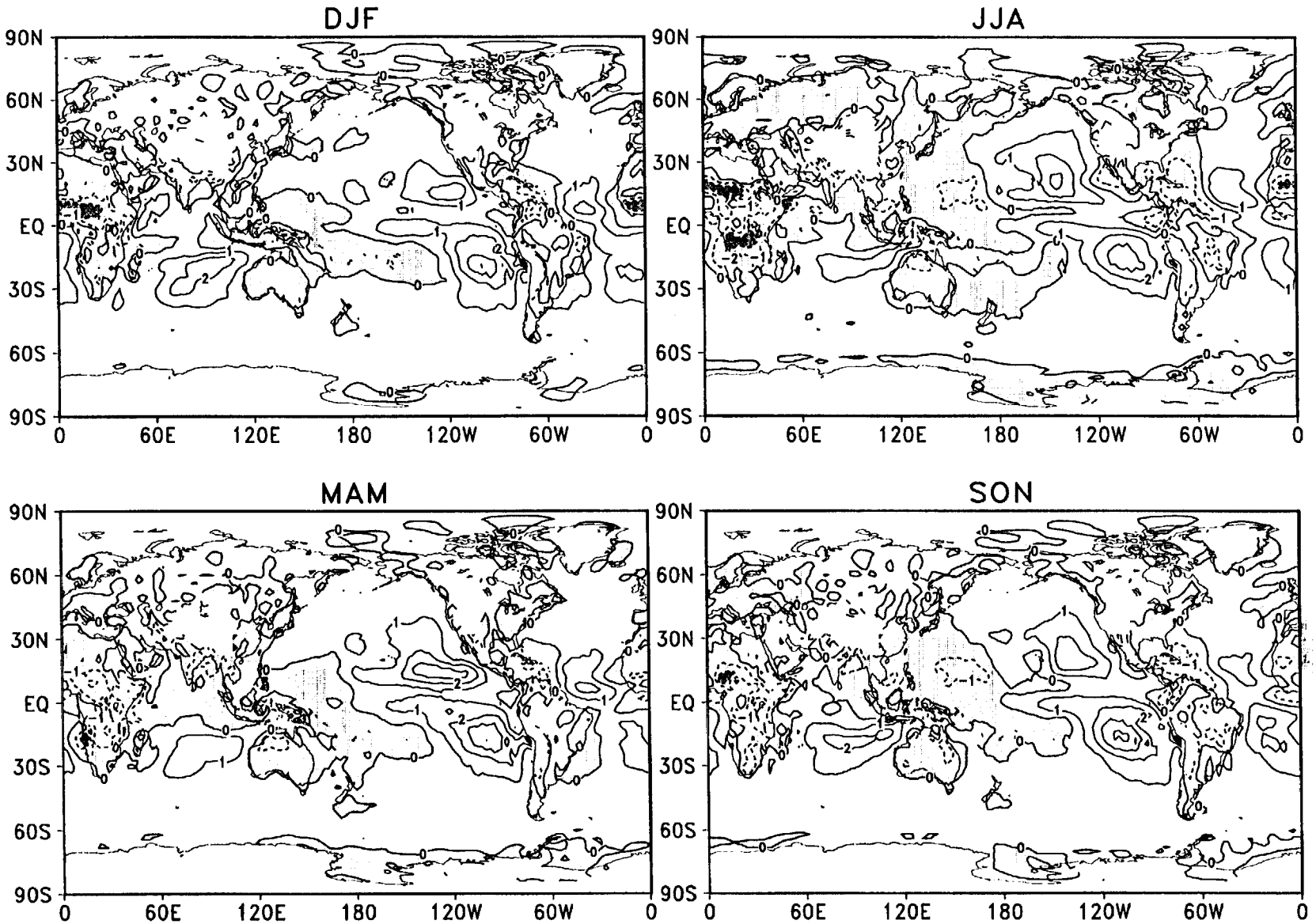

Figure 69: Difference of the seasonal means of 850 hPa specific humidity during 1980–1995 (NCEP/NCAR minus DAO). The contour interval is 1 g kg^{-1}. Negative values are shaded.

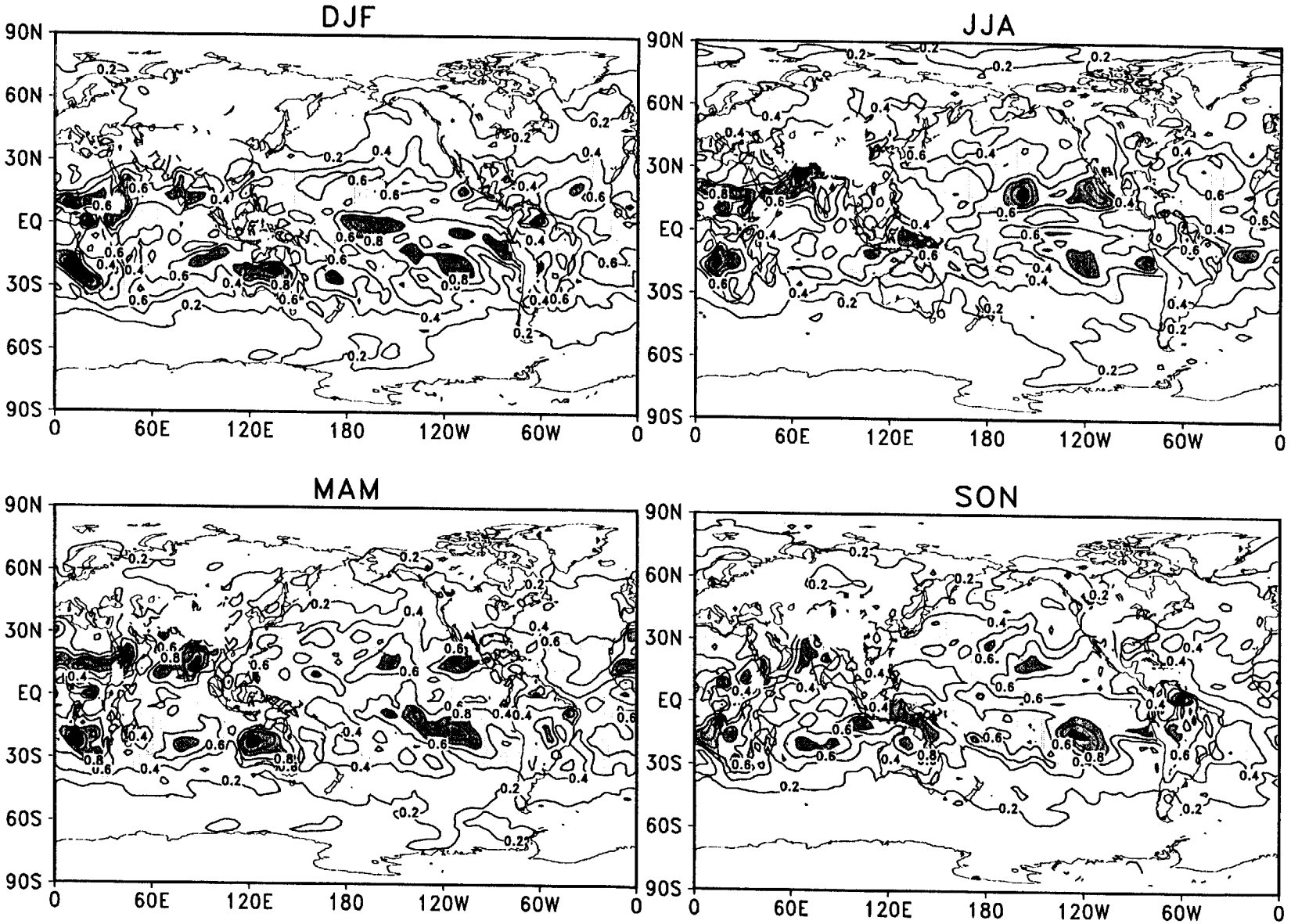

Figure 70: Standard deviations of seasonal mean 850 hPa specific humidity for DAO reanalysis during 1980–1995. The contour interval is 0.2 g kg^{-1}. Values larger than 0.4 g kg^{-1} are shaded.

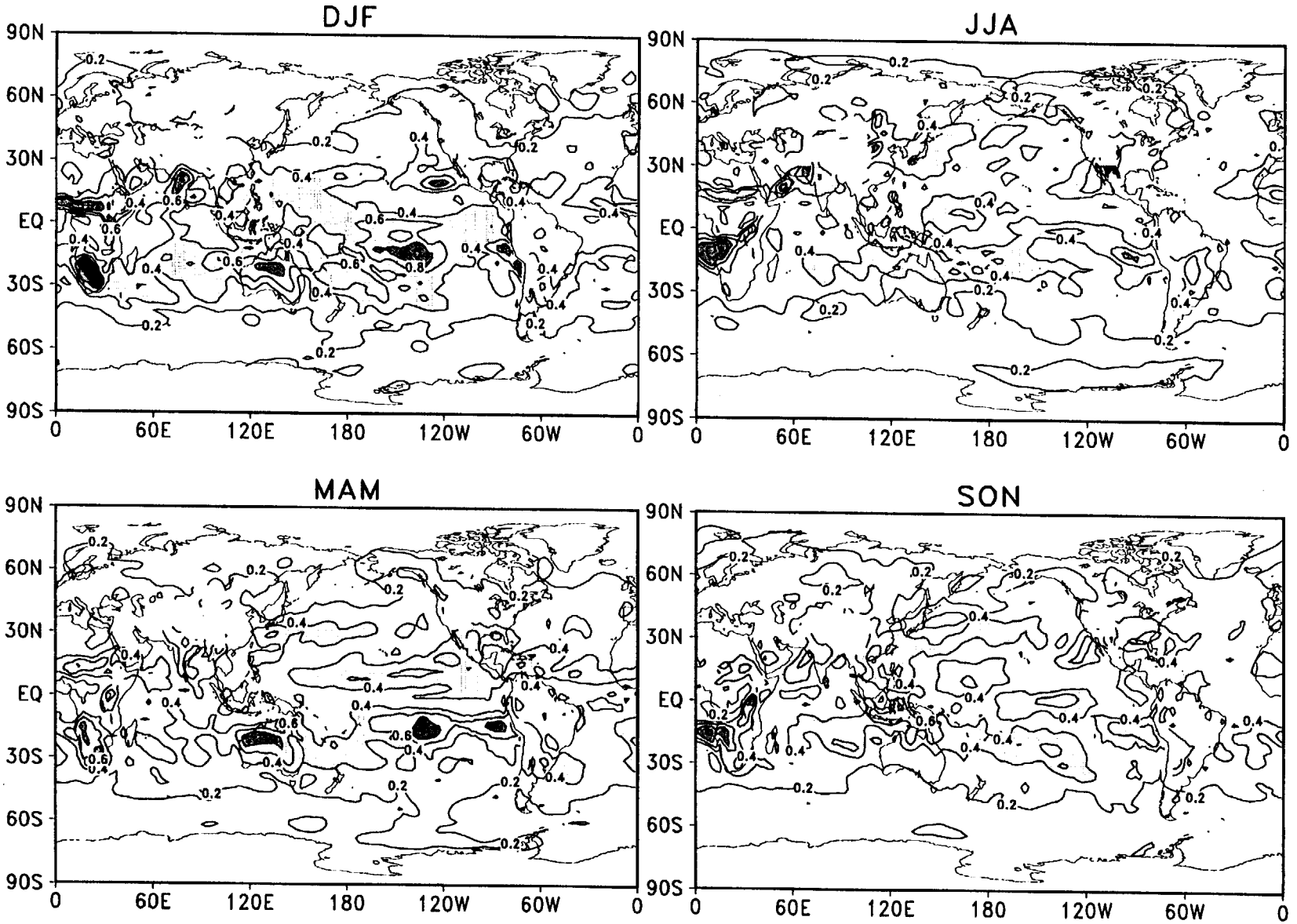

Figure 71: Standard deviations of seasonal mean 850 hPa specific humidity for NCEP/NCAR reanalysis during 1980–1995. The contour interval is 0.2 g kg^{-1}. Values larger than 0.4 g kg^{-1} are shaded.

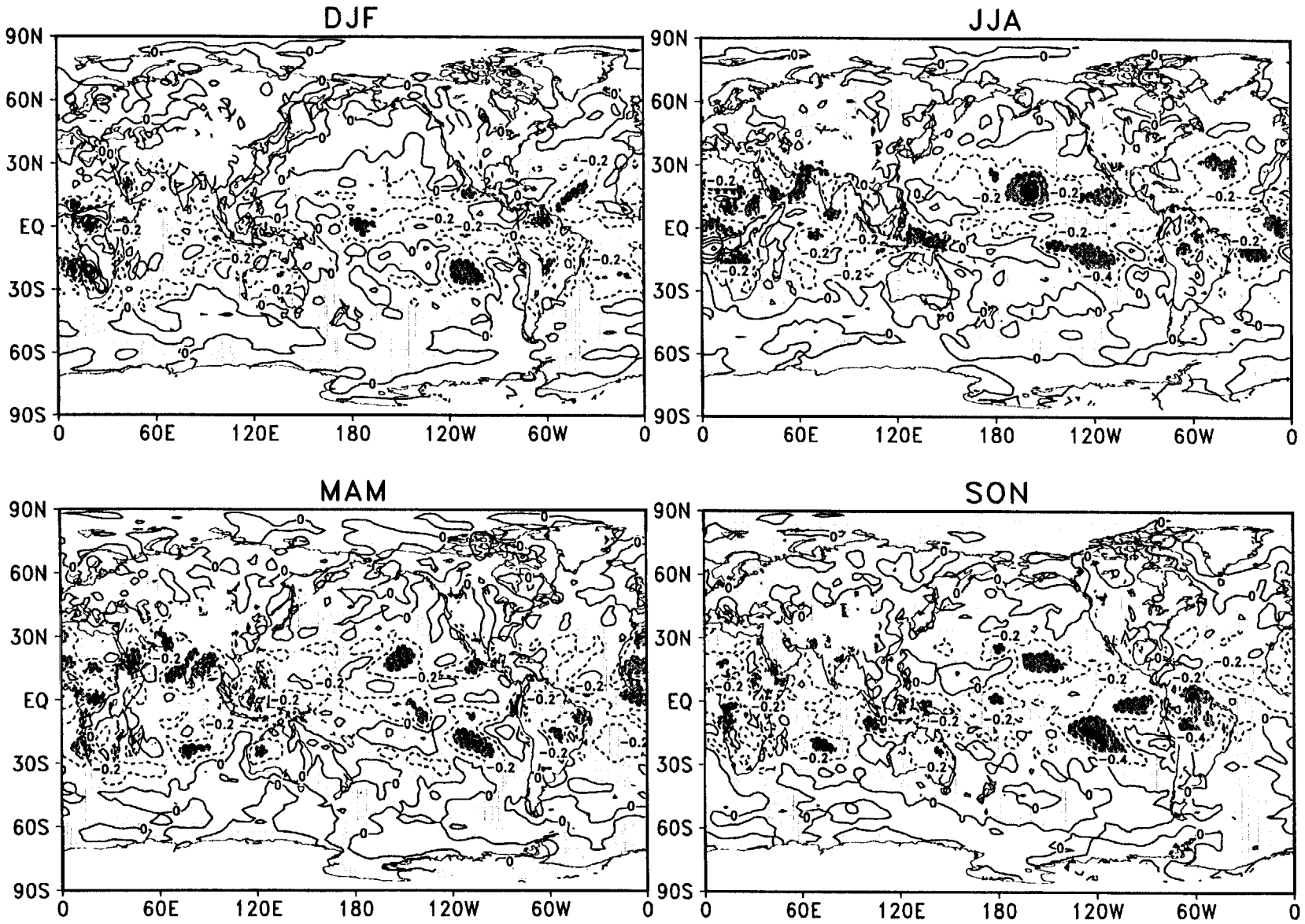

Figure 72: Difference of the standard deviations of seasonal mean 850 hPa specific humidity during 1980–1995 (NCEP/NCAR minus DAO). The contour interval is 0.2 g kg^{-1}. Negative values are shaded.

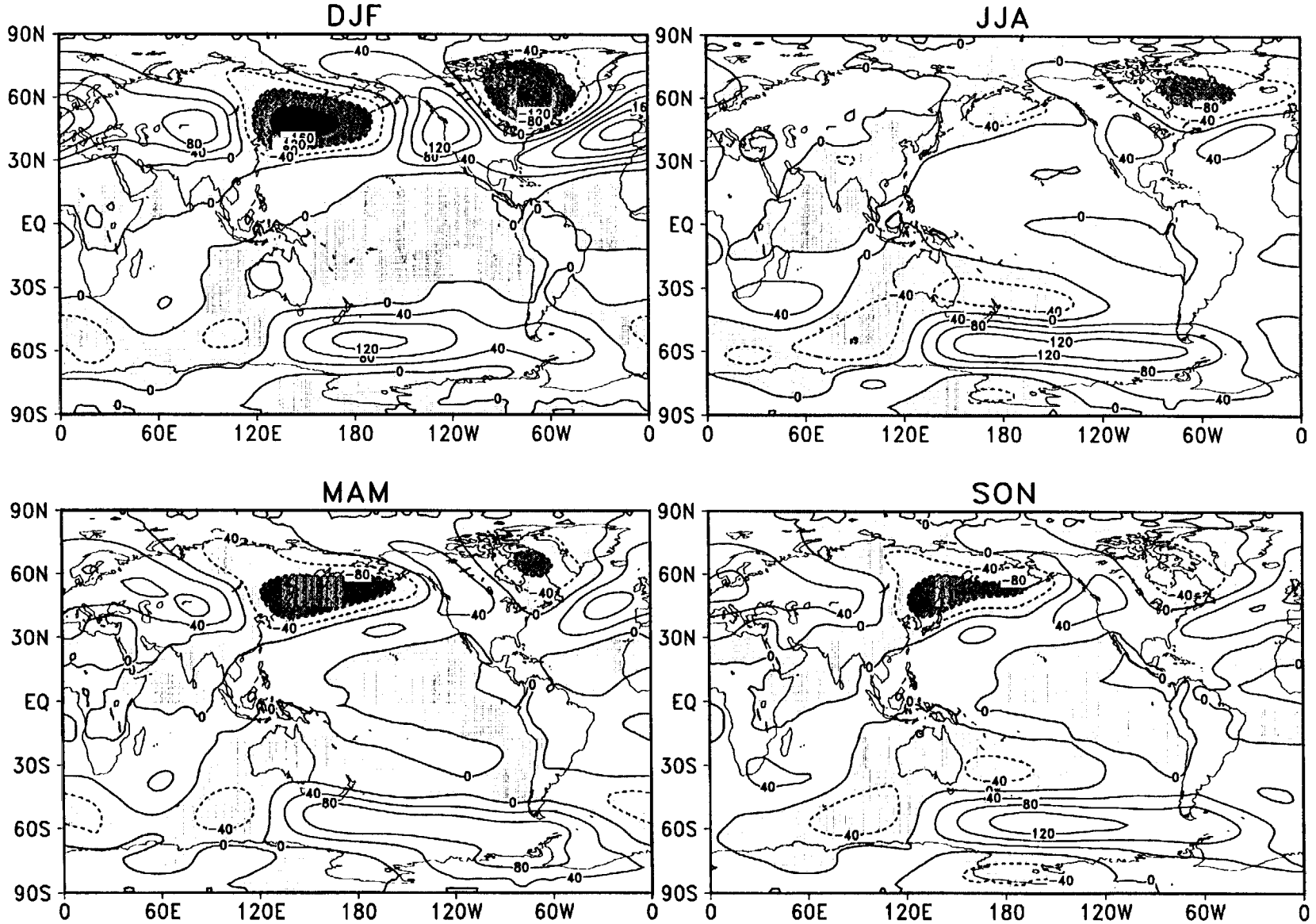

Figure 73: Seasonal means of 500 hPa eddy height for DAO reanalysis during 1980–1995. The contour interval is 40 m. Negative values are shaded.

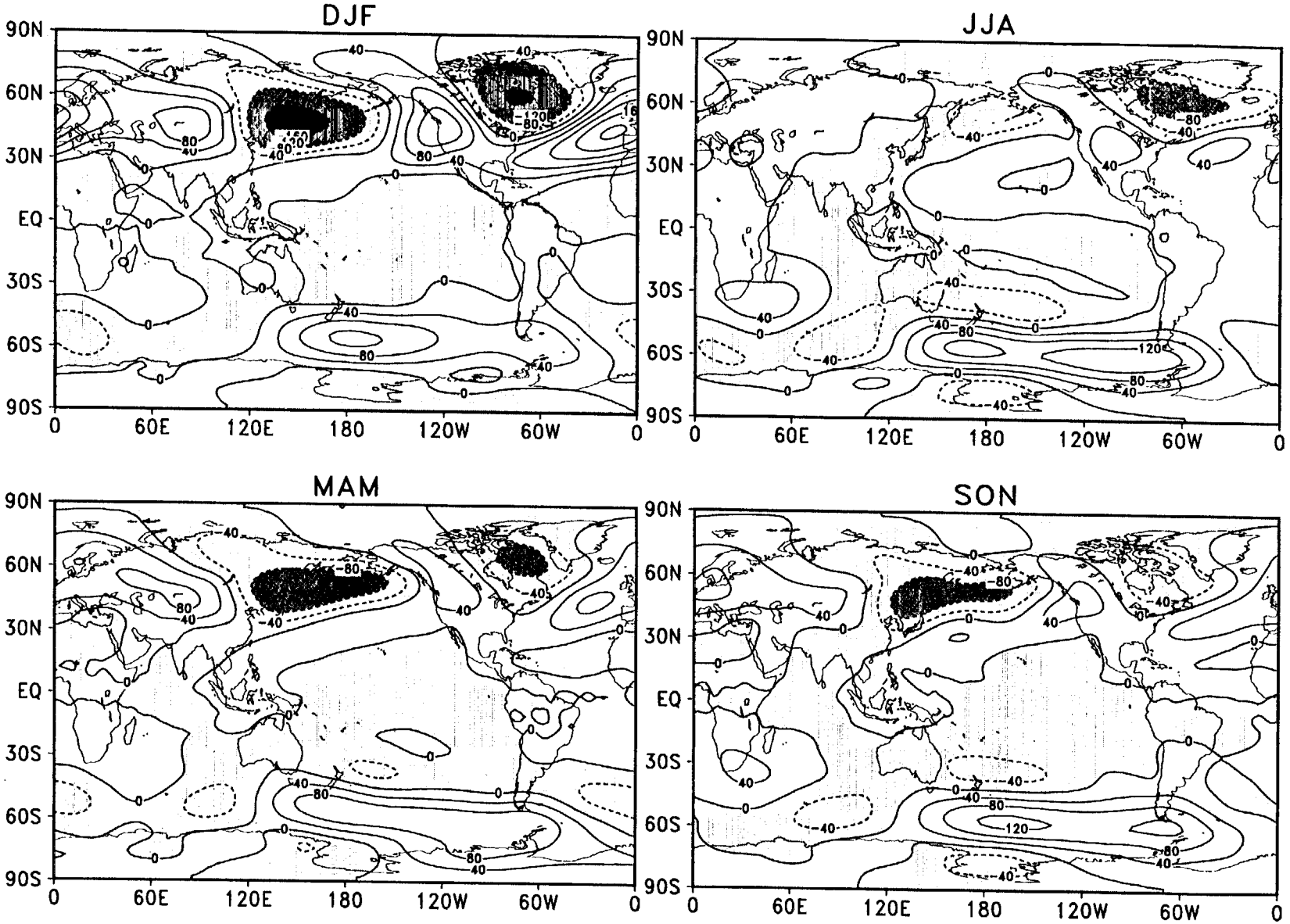

Figure 74: Seasonal means of 500 hPa eddy height for NCEP/NCAR reanalysis during 1980–1995. The contour interval is 40 m. Negative values are shaded.

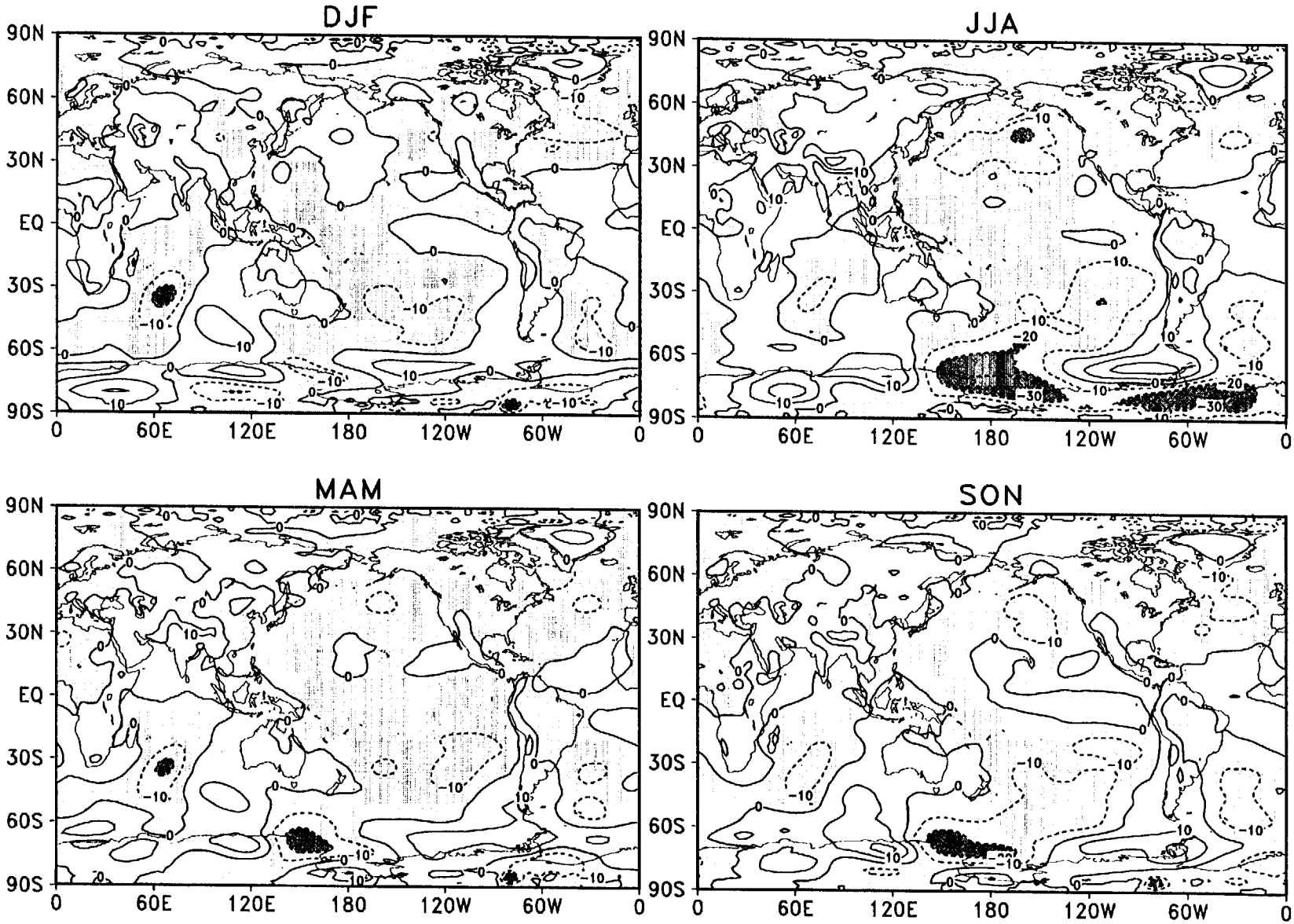

Figure 75: Difference of the seasonal means of 500 hPa eddy height during 1980–1995 (NCEP/NCAR minus DAO). The contour interval is 10 m. Negative values are shaded.

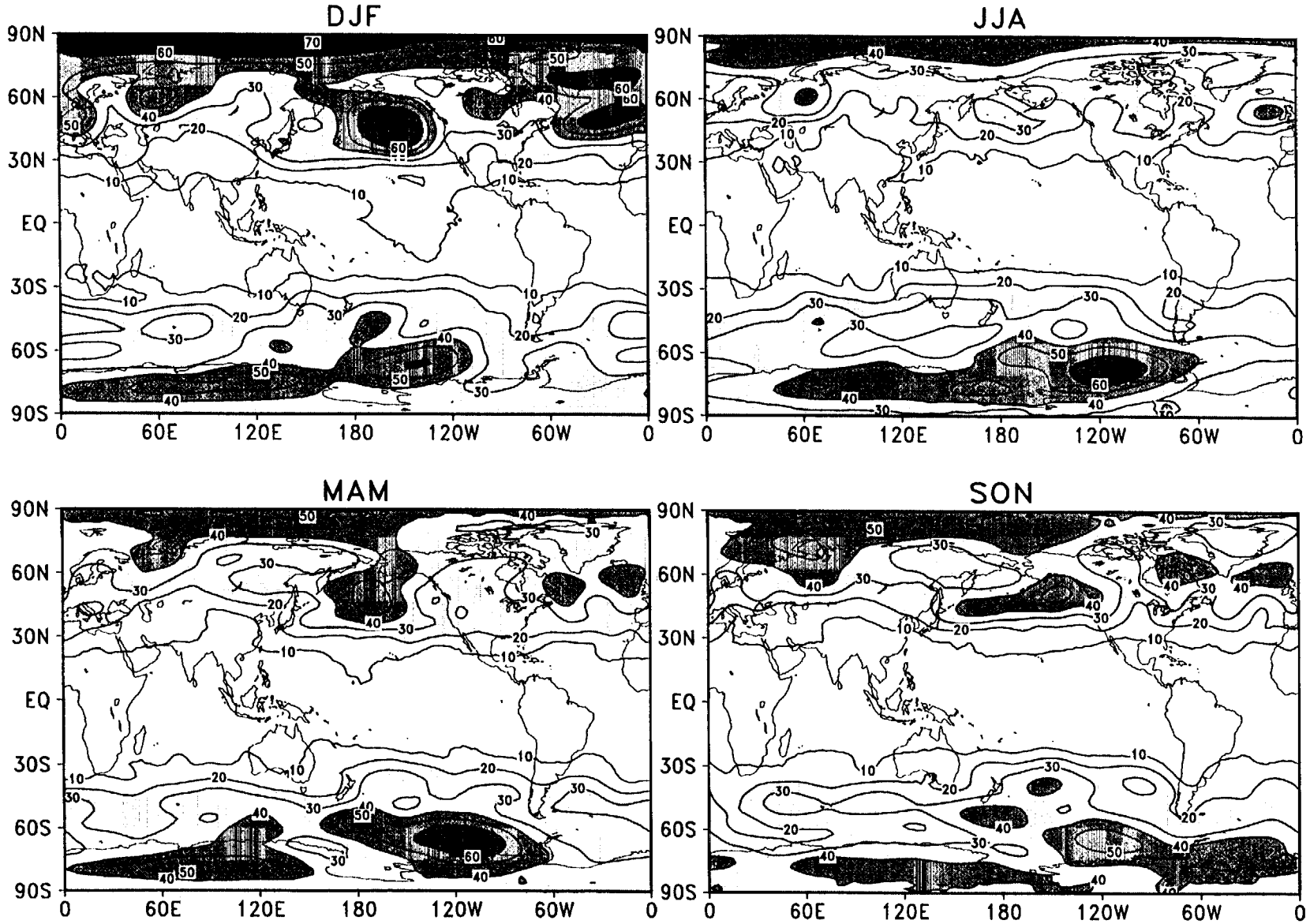

Figure 76: Standard deviations of seasonal mean 500 hPa height for DAO reanalysis during 1980–1995. The contour interval is 10 m. Values larger than 20 m are shaded.

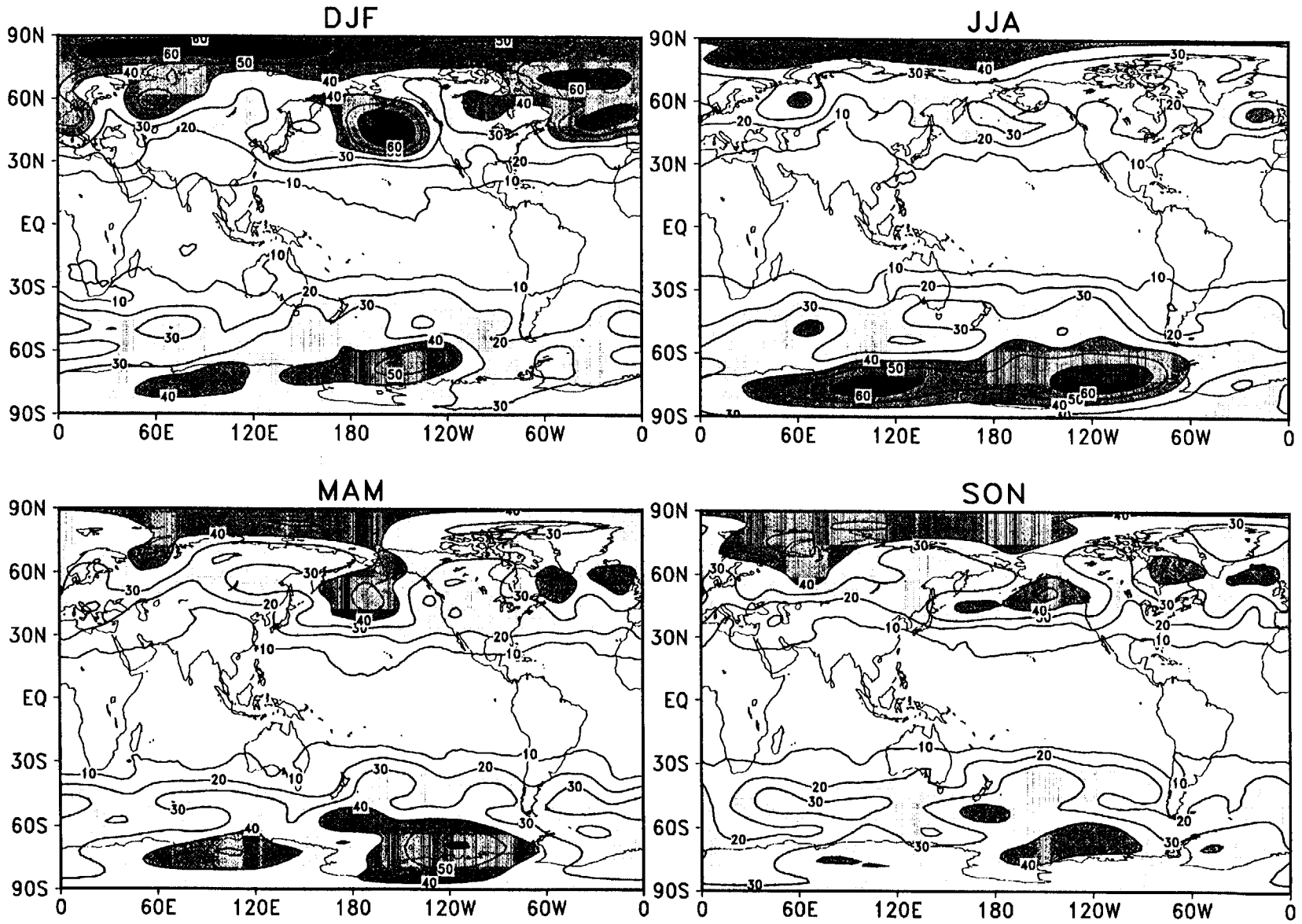

Figure 77: Standard deviations of seasonal mean 500 hPa height for NCEP/NCAR reanalysis during 1980–1995. The contour interval is 10 m. Values larger than 20 m are shaded.

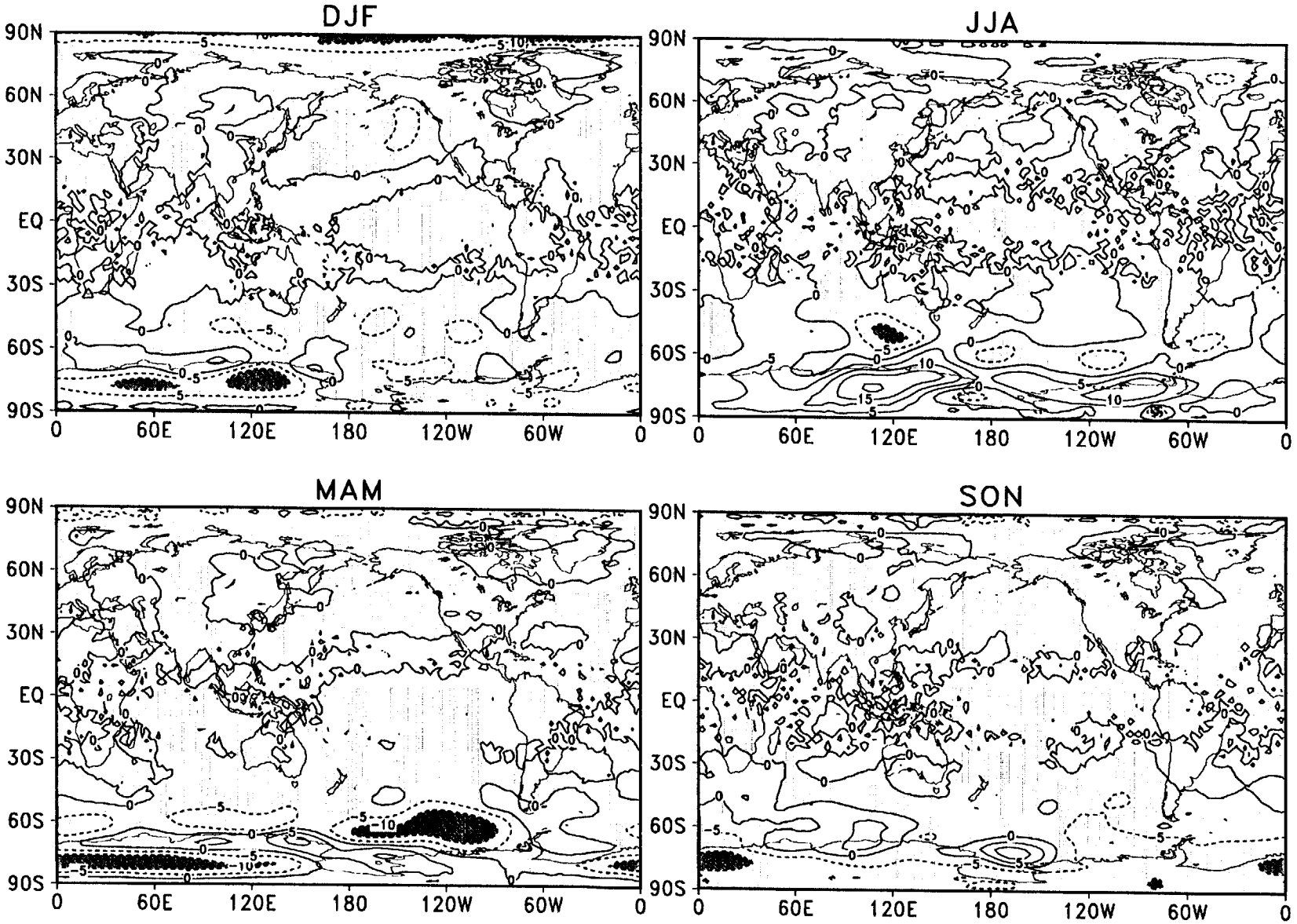

Figure 78: Difference of the standard deviations of seasonal mean 500 hPa height during 1980–1995 (NCEP/NCAR minus DAO). The contour interval is 5 m. Negative values are shaded.

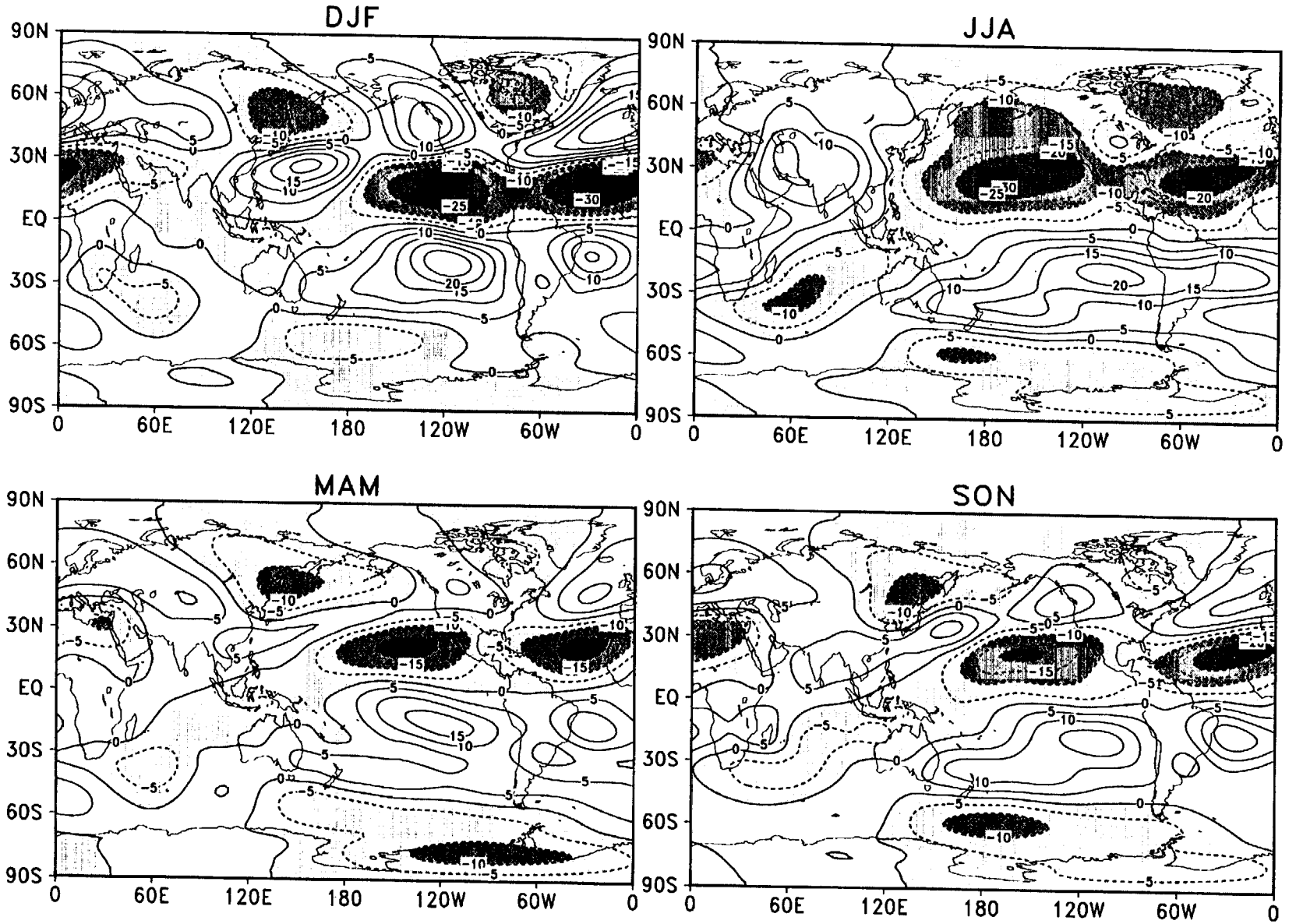

Figure 79: Seasonal means of 200 hPa eddy streamfunction for DAO reanalysis during 1980–1995. The contour interval is 5 $\times 10^{10} m^2 s^{-1}$. Negative values are shaded.

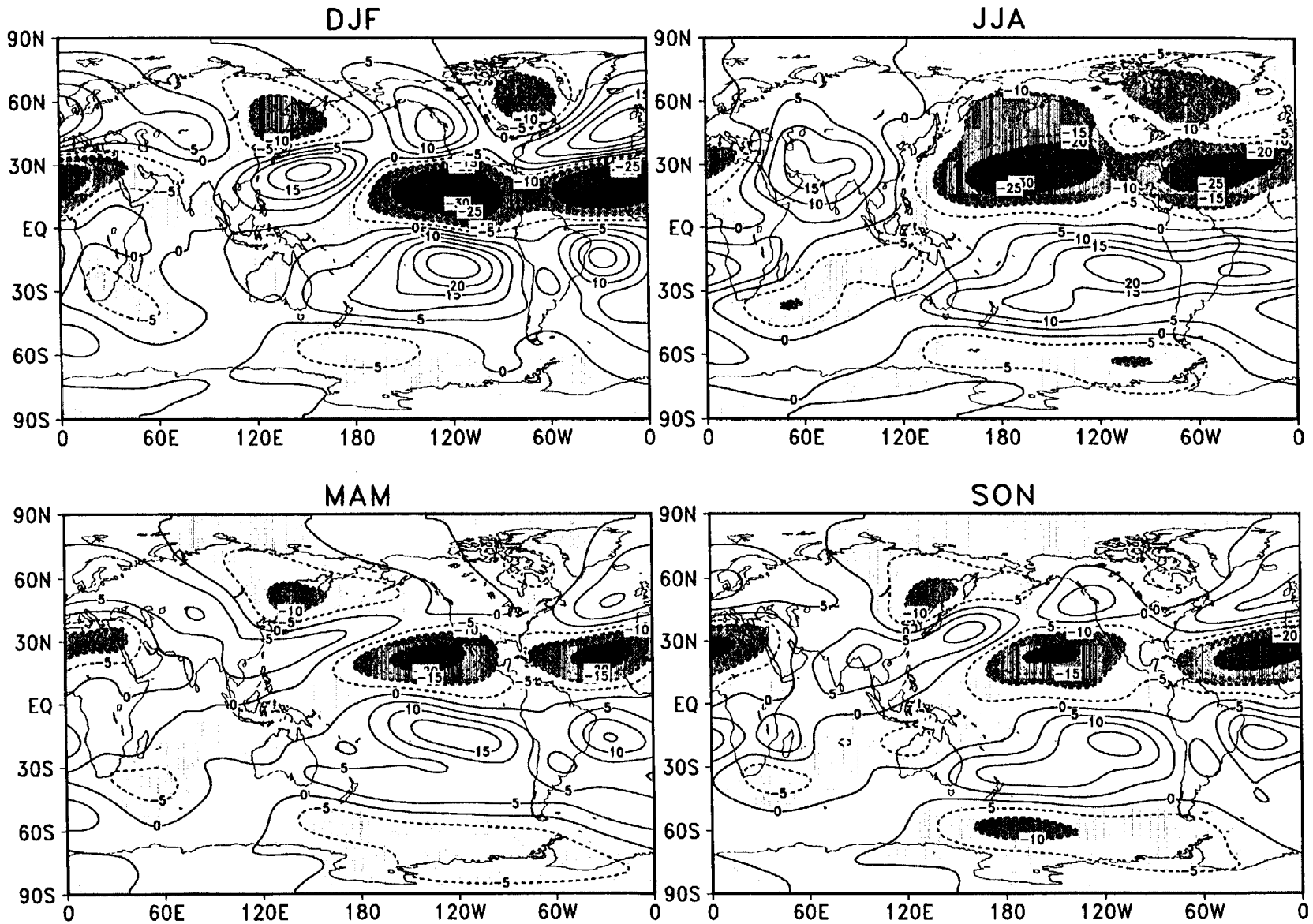

Figure 80: Seasonal means of 200 hPa eddy streamfunction for NCEP/NCAR reanalysis during 1980–1995. The contour interval is 5 $\times 10^{10} m^2 s^{-1}$. Negative values are shaded.

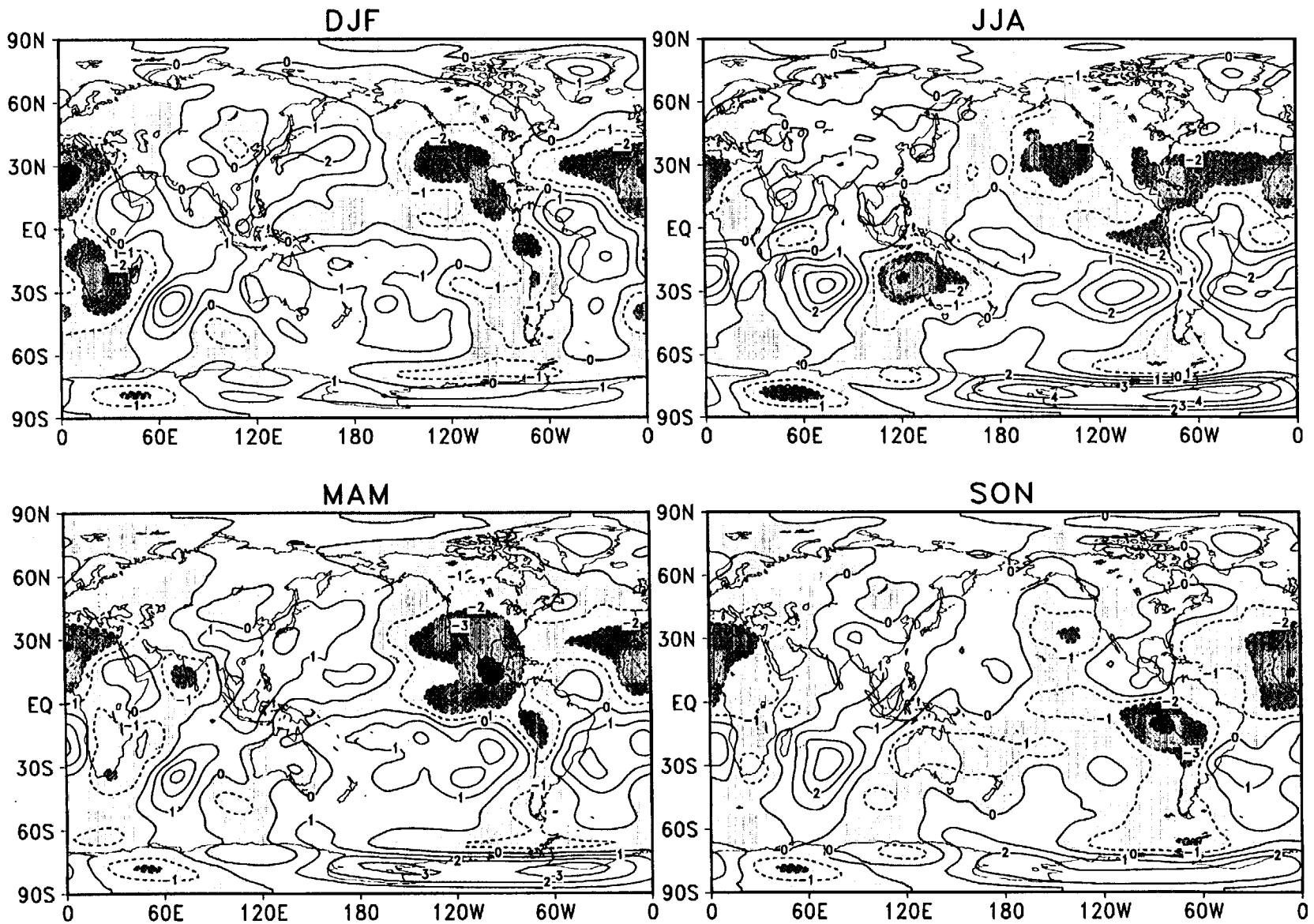

Figure 81: Difference of the seasonal means of 200 hPa eddy streamfunction during 1980–1995 (NCEP/NCAR minus DAO). The contour interval is $1 \times 10^{10} \mathrm{m}^2\mathrm{s}^{-1}$. Negative values are shaded.

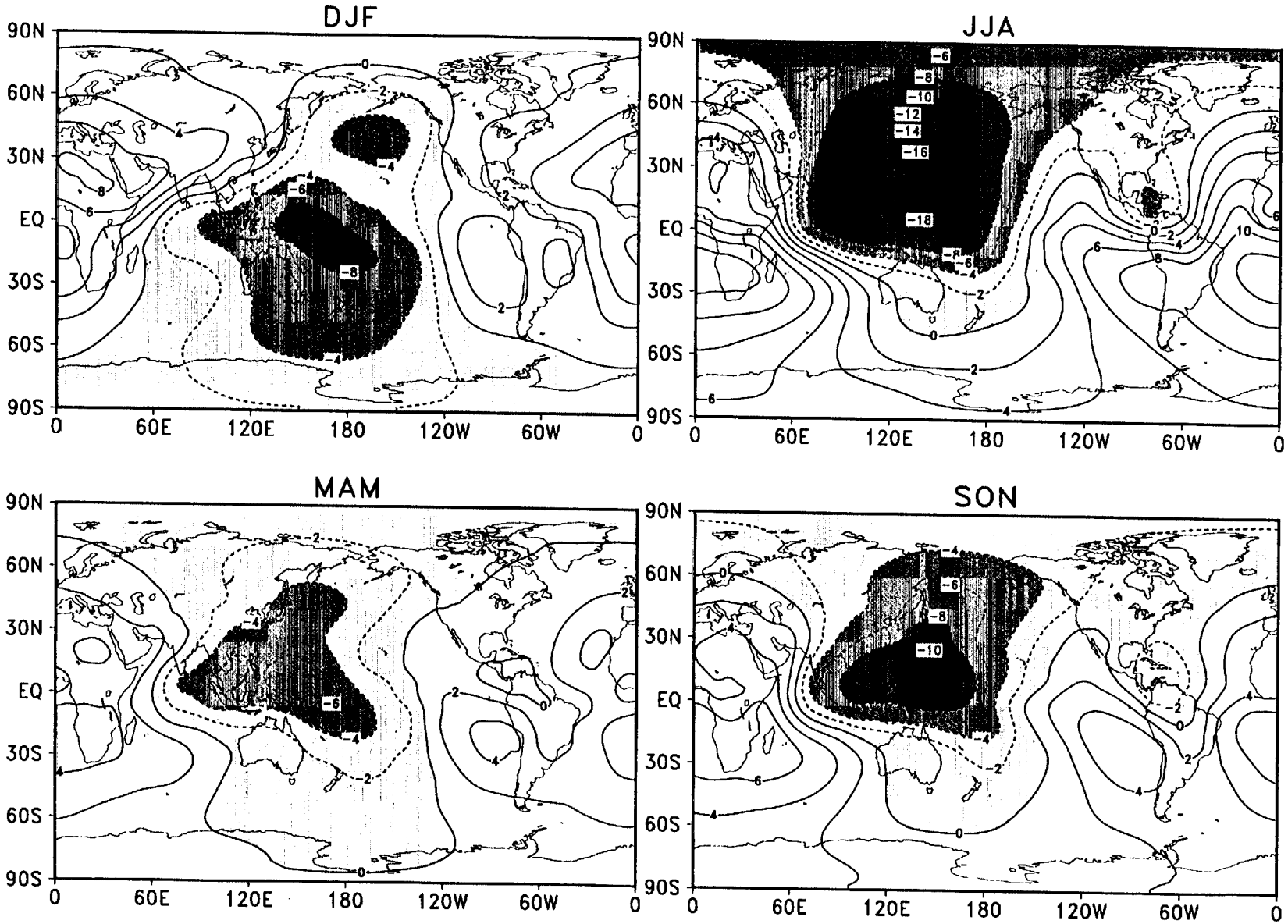

Figure 82: Seasonal means of 200 hPa velocity potential for DAO reanalysis during 1980–1995. The contour interval is 2 $\times 10^{10} m^2 s^{-1}$. Negative values are shaded.

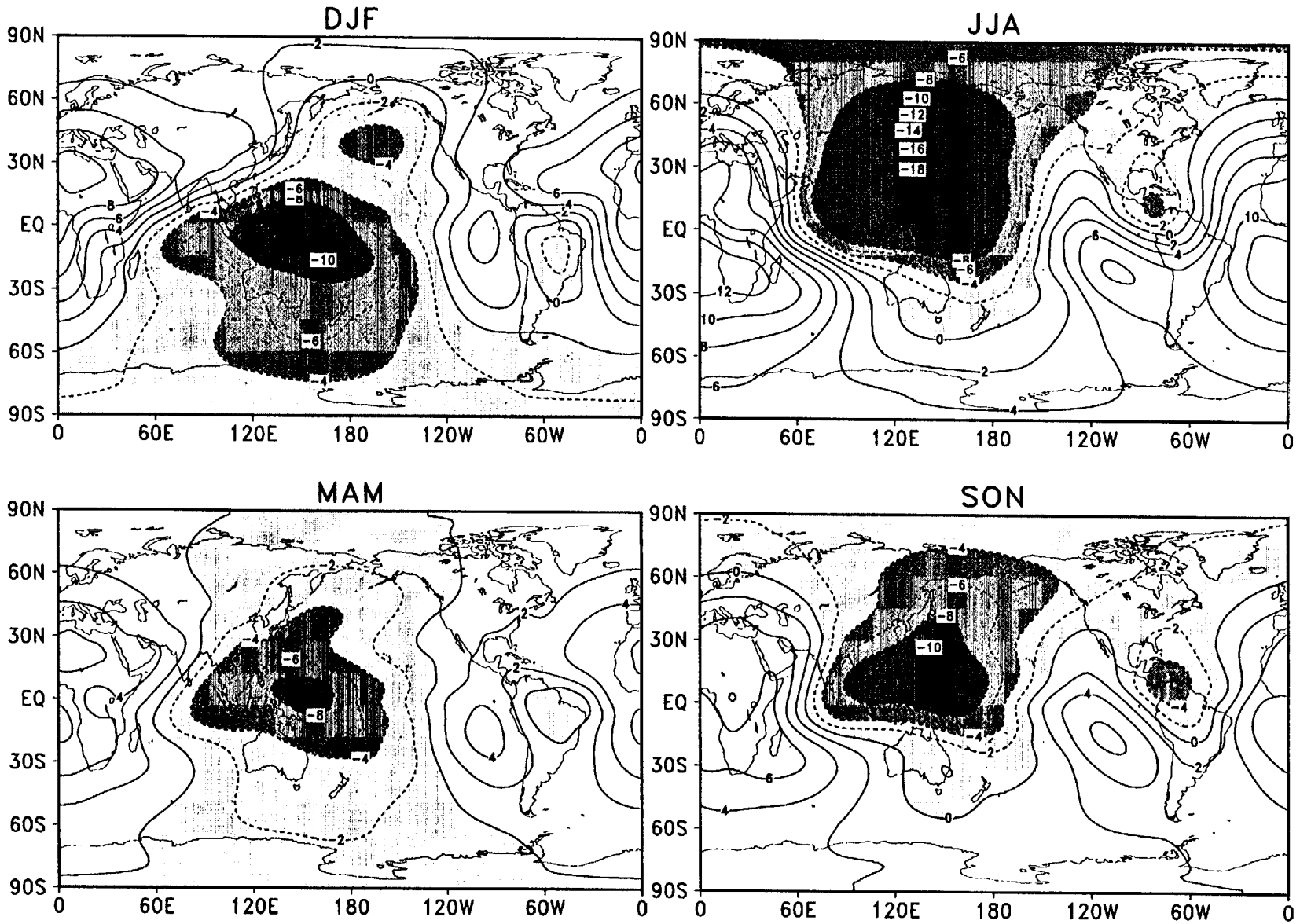

Figure 83: Seasonal means of 200 hPa velocity potential for NCEP/NCAR reanalysis during 1980–1995. The contour interval is $2 \times 10^{10} \mathrm{m}^2 \mathrm{s}^{-1}$. Negative values are shaded.

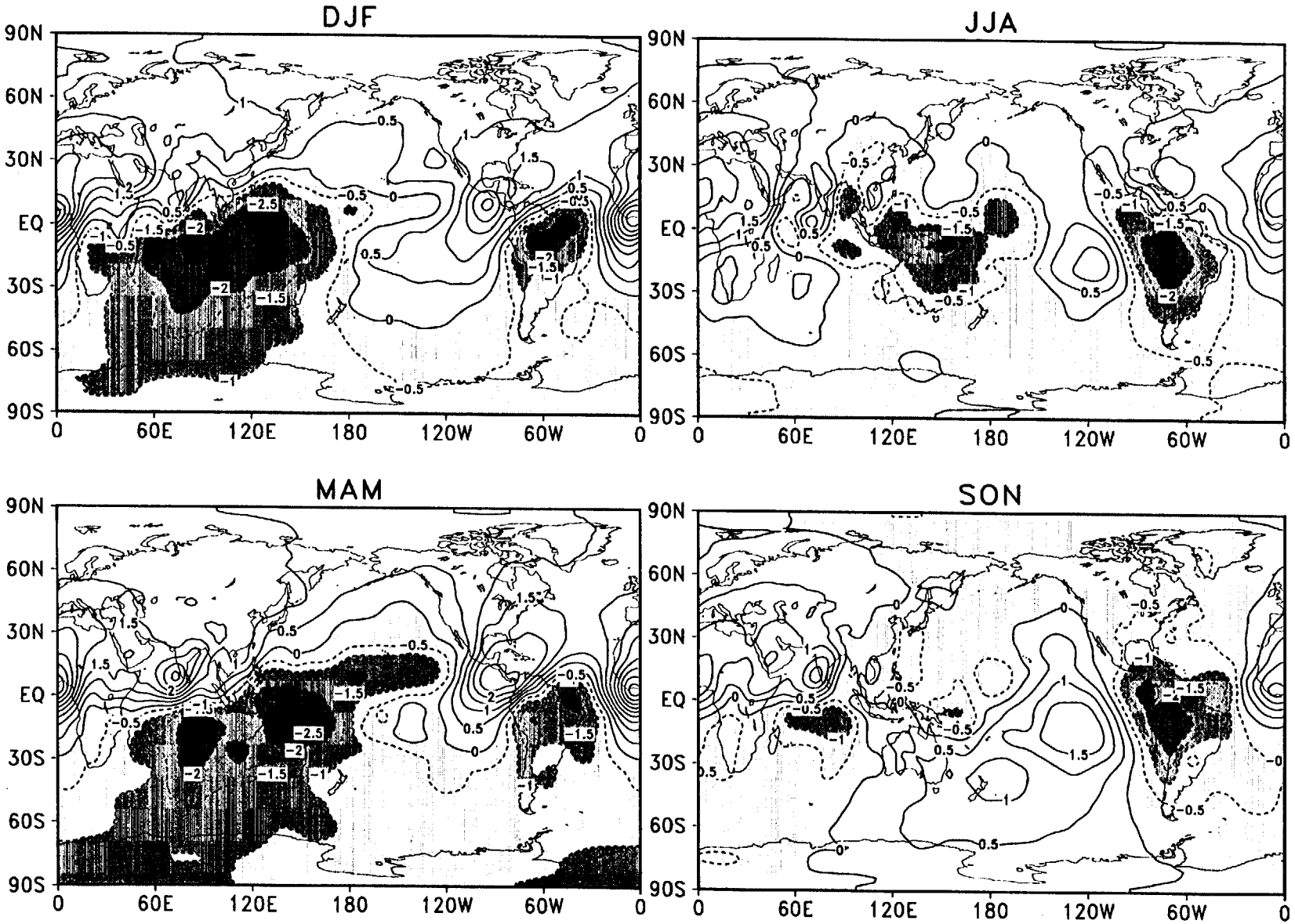

Figure 84: Difference of the seasonal means of 200 hPa velocity potential during 1980–1995 (NCEP/NCAR minus DAO). The contour interval is 0.5 $\times 10^{10} m^2 s^{-1}$. Negative values are shaded.

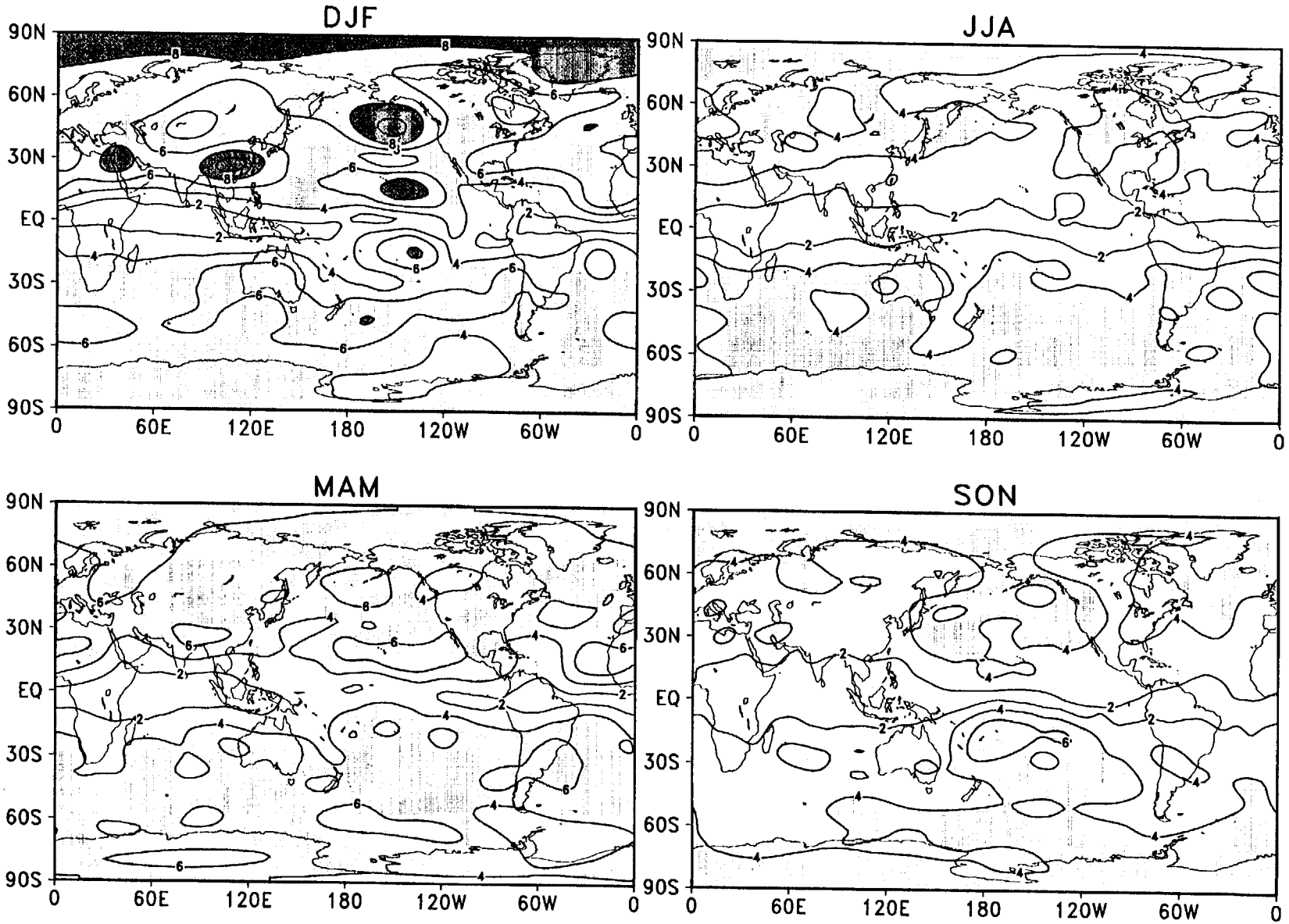

Figure 85: Standard deviations of seasonal mean 200 hPa eddy streamfunction for DAO reanalysis during 1980–1995. The contour interval is 2 $\times 10^{10} m^2 s^{-1}$. Values larger than 4 $\times 10^{10} m^2 s^{-1}$ are shaded.

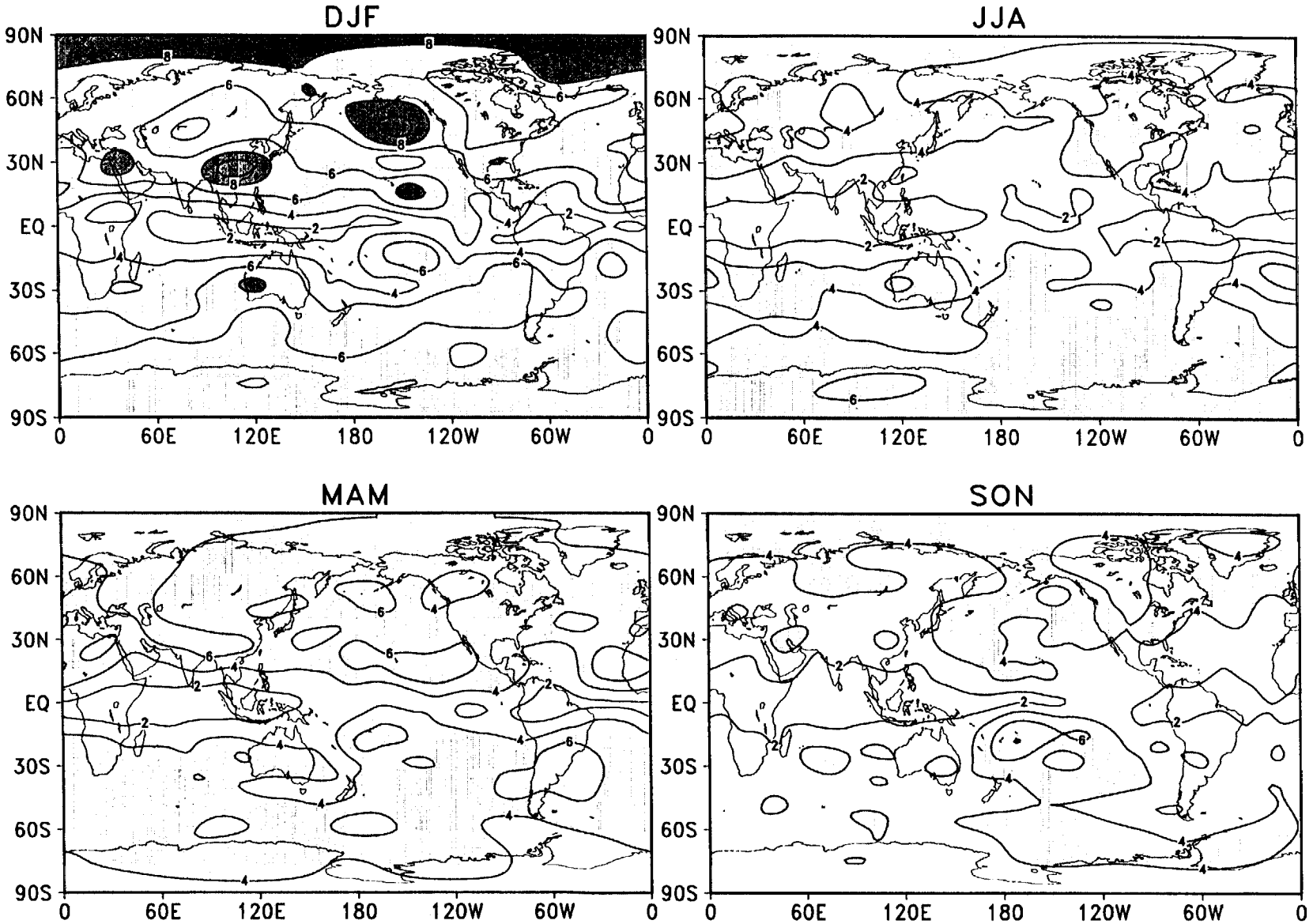

Figure 86: Standard deviations of seasonal mean 200 hPa eddy streamfunction for NCEP/NCAR reanalysis during 1980–1995. The contour interval is $2 \times 10^{10} m^2 s^{-1}$. Values larger than $4 \times 10^{10} m^2 s^{-1}$ are shaded.

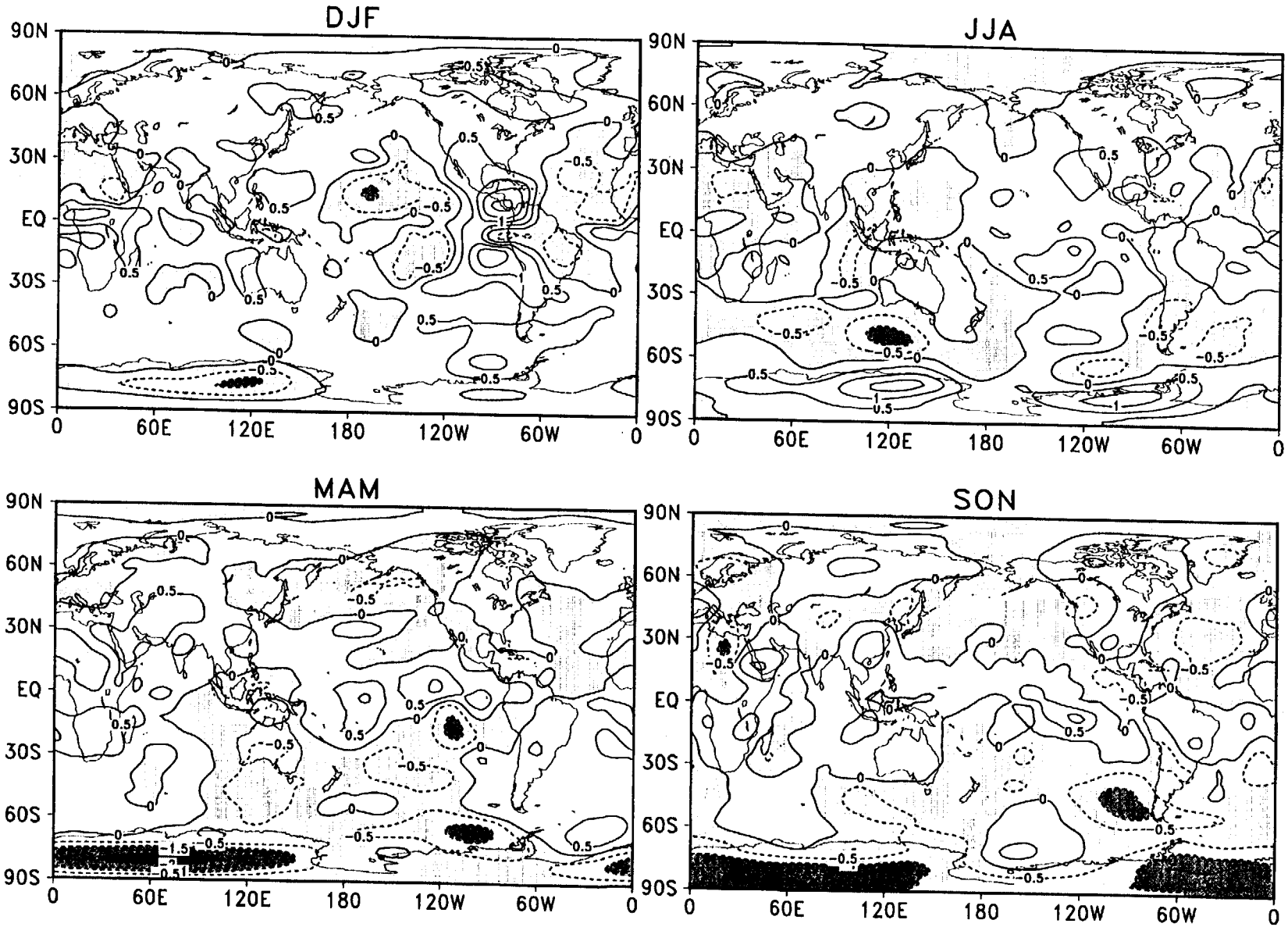

Figure 87: Difference of the standard deviations of seasonal mean 200 hPa eddy streamfunction during 1980–1995 (NCEP/NCAR minus DAO). The contour interval is 0.5 $\times 10^{10} m^2 s^{-1}$. Negative values are shaded.

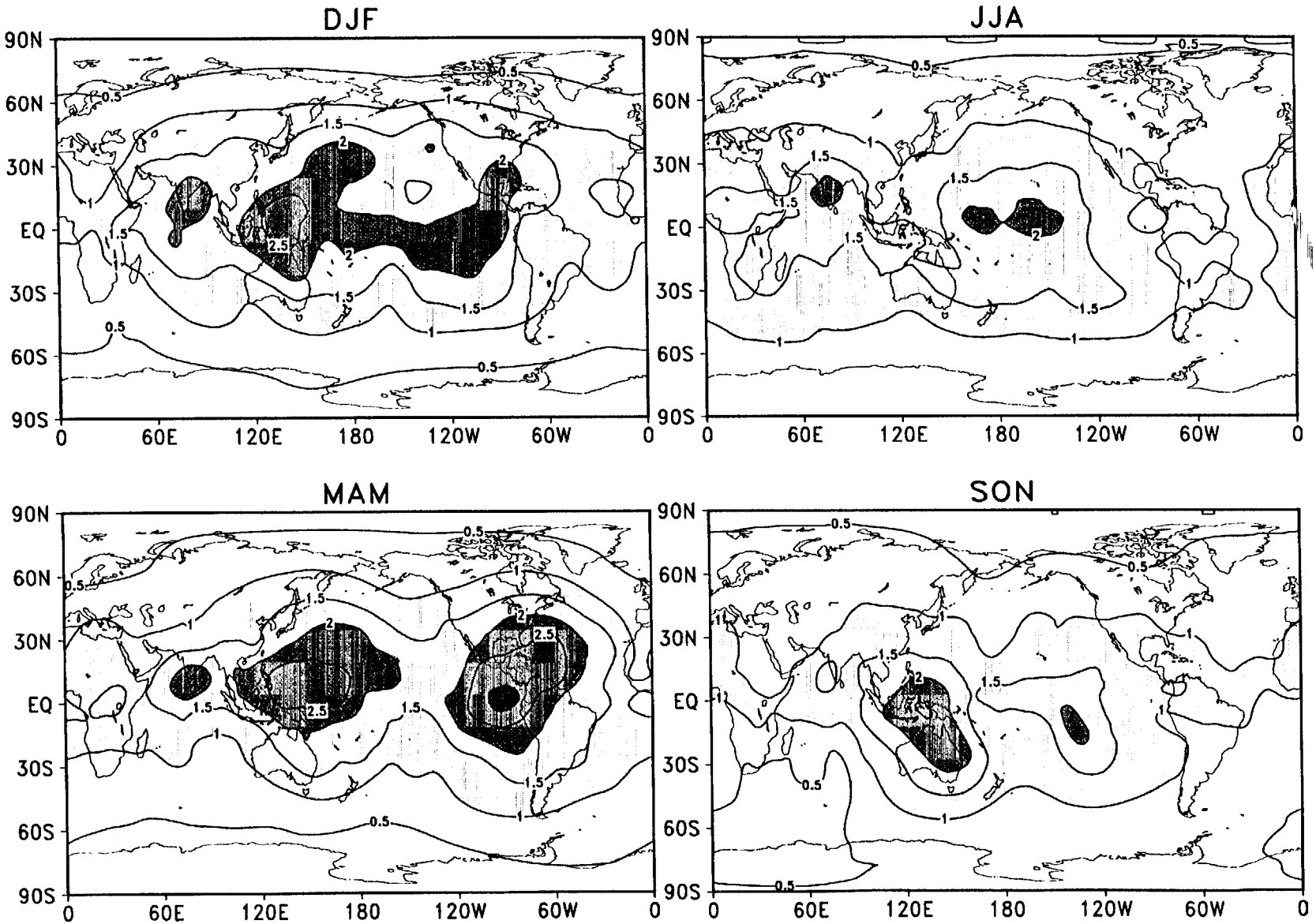

Figure 88: Standard deviations of seasonal mean 200 hPa velocity potential for DAO reanalysis during 1980–1995. The contour interval is 0.5 $\times 10^{10} m^2 s^{-1}$. Values larger than 1 $\times 10^{10} m^2 s^{-1}$ are shaded.

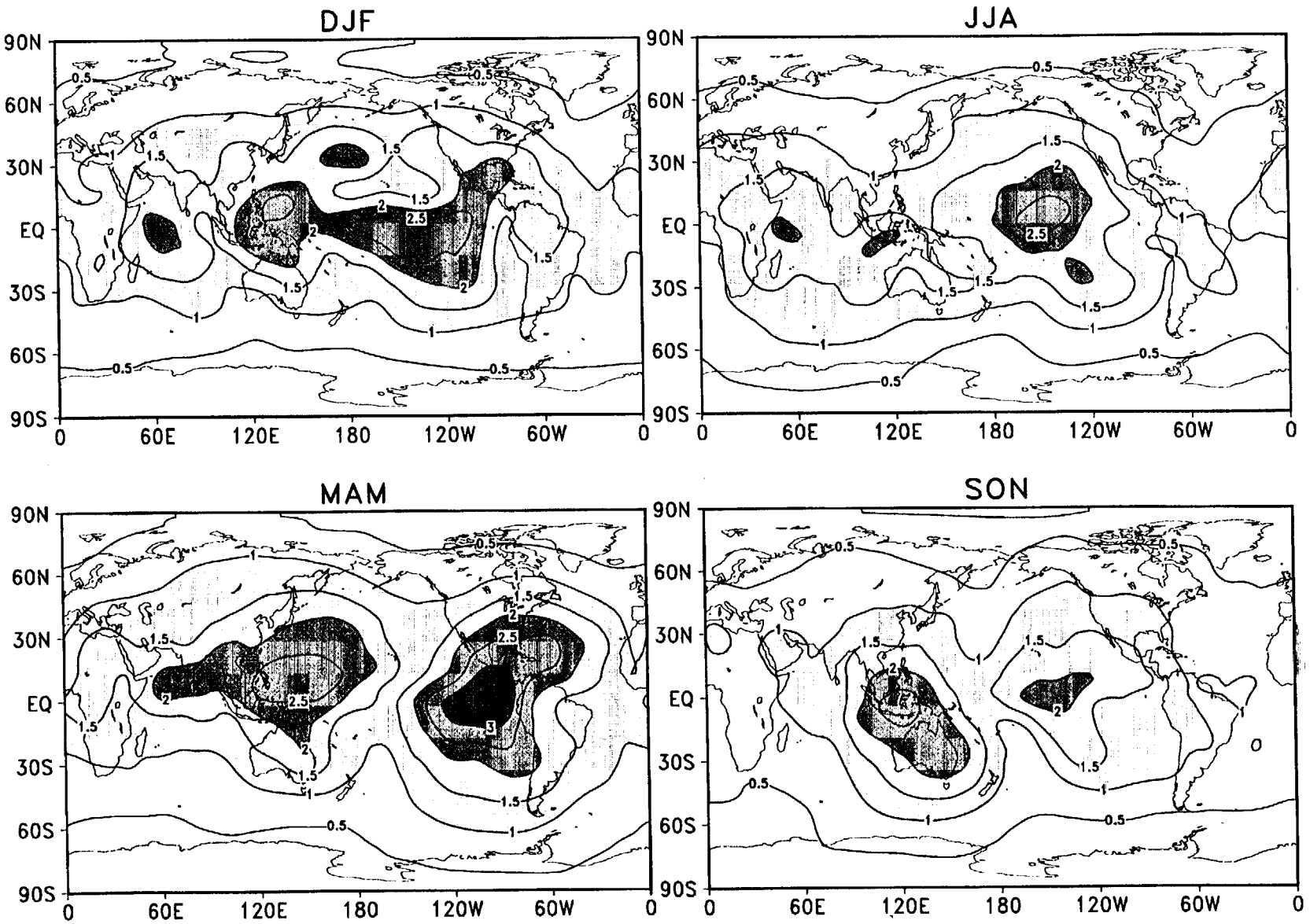

Figure 89: Standard deviations of seasonal mean 200 hPa velocity potential for NCEP/NCAR reanalysis during 1980–1995. The contour interval is 0.5 $\times 10^{10} m^2 s^{-1}$. Values larger than 1 $\times 10^{10} m^2 s^{-1}$ are shaded.

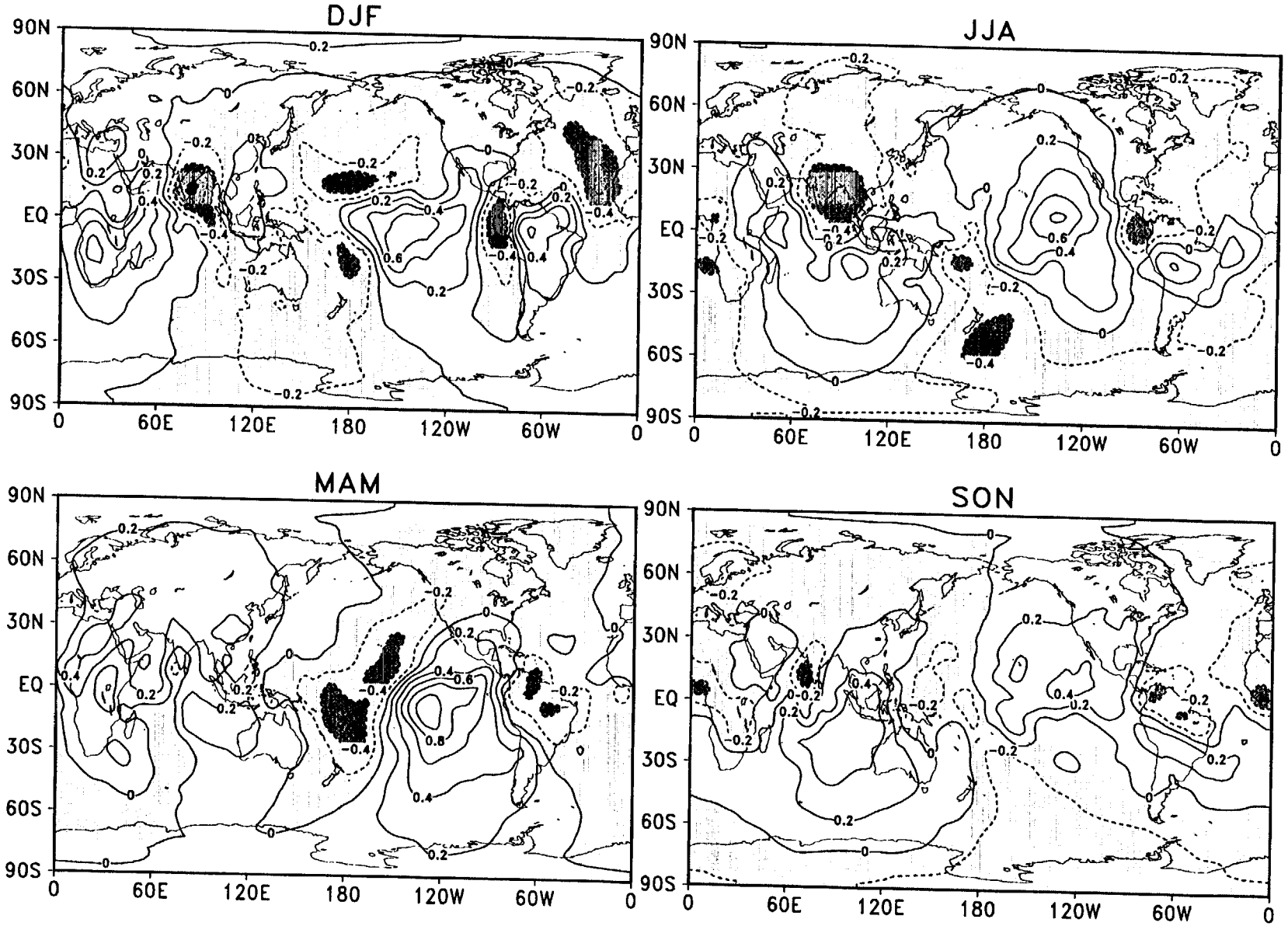

Figure 90: Difference of the standard deviations of seasonal mean 200 hPa velocity potential during 1980–1995 (NCEP/NCAR minus DAO). The contour interval is 0.2 $\times 10^{10} m^2 s^{-1}$. Negative values are shaded.

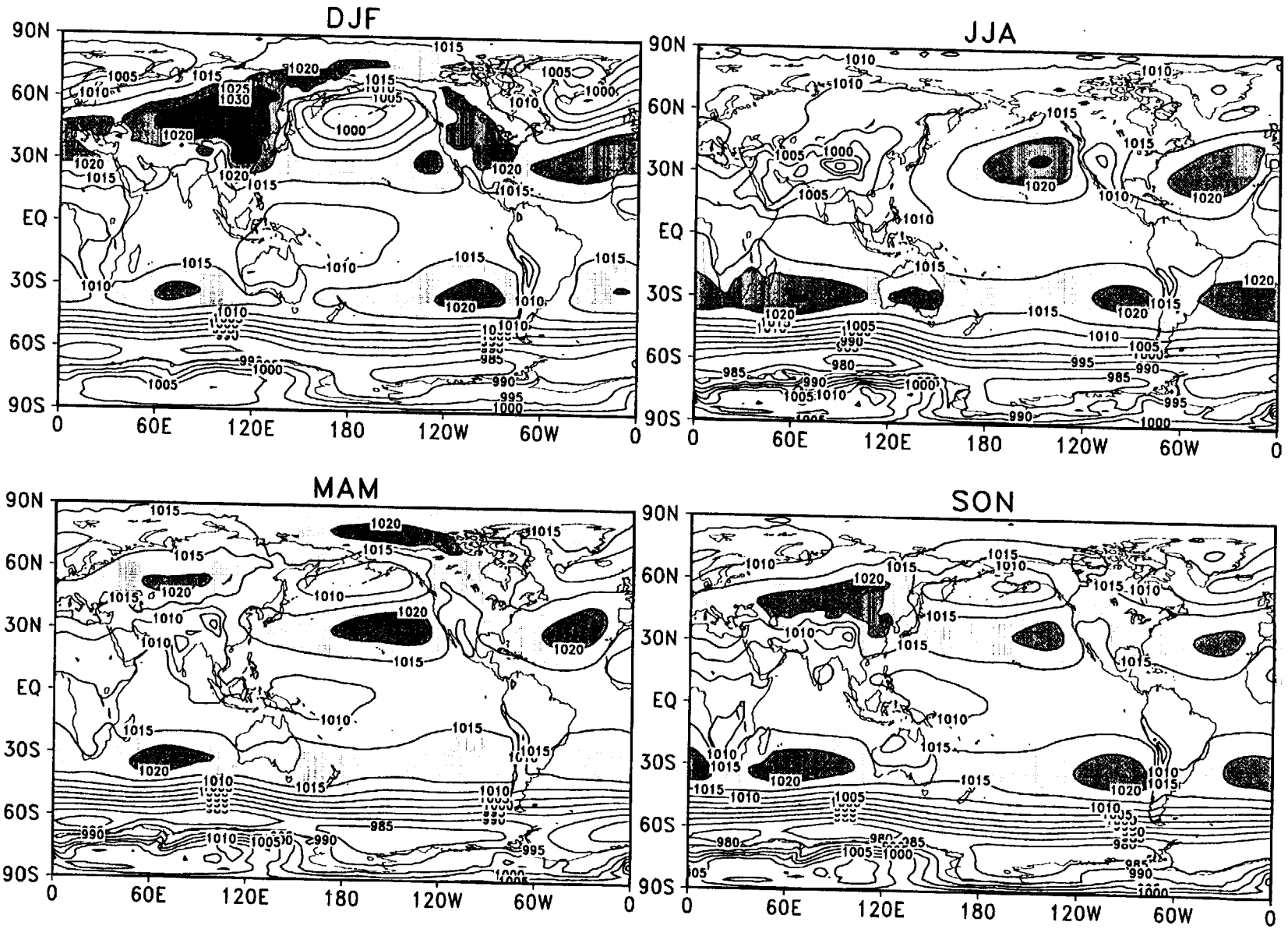

Figure 91: Seasonal means of mean sea level pressure for DAO reanalysis during 1980–1995. The contour interval is 5 hPa. Values larger than 1015 hPa are shaded.

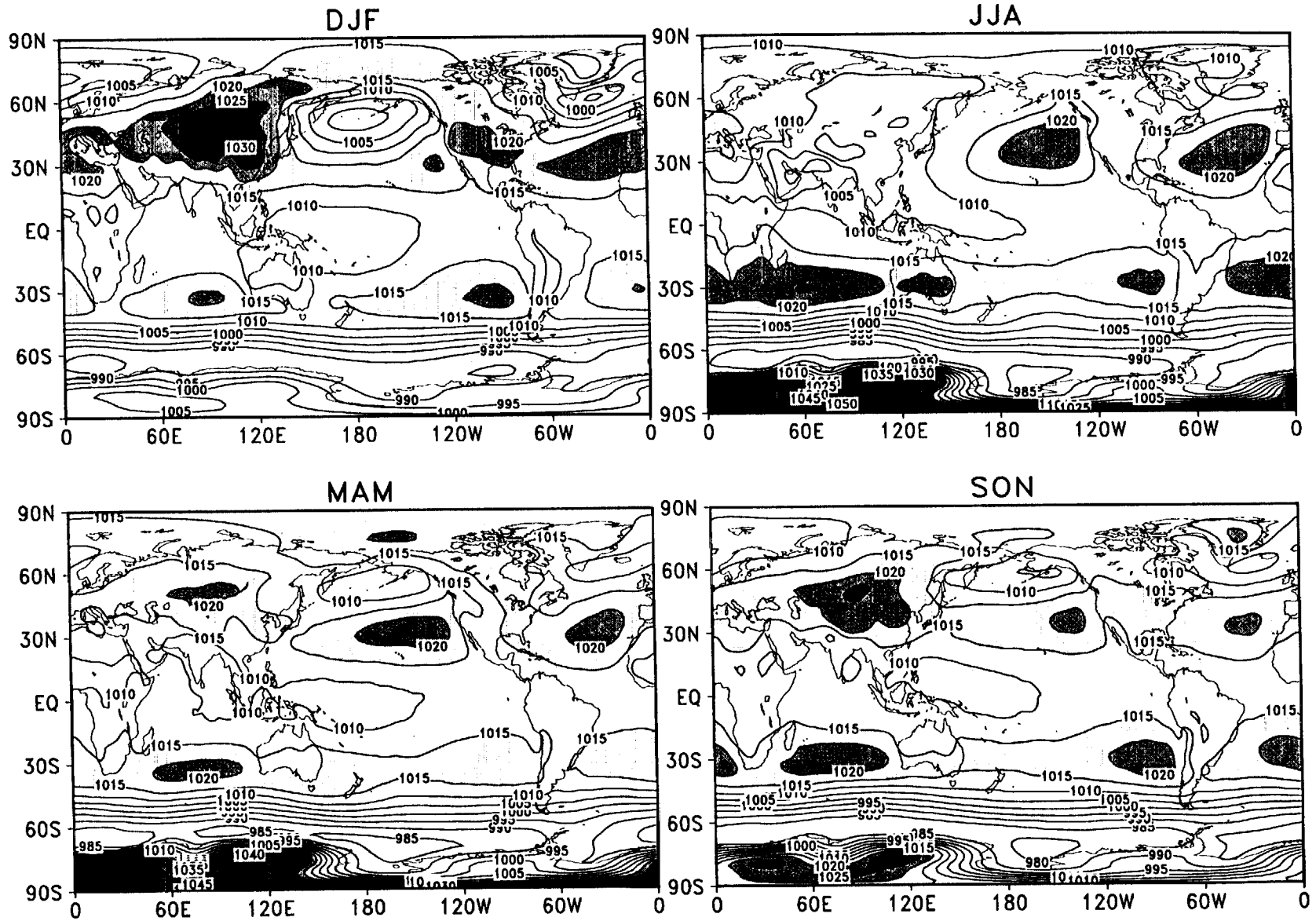

Figure 92: Seasonal means of mean sea level pressure for NCEP/NCAR reanalysis during 1980–1995. The contour interval is 5 hPa. Values larger than 1015 hPa are shaded.

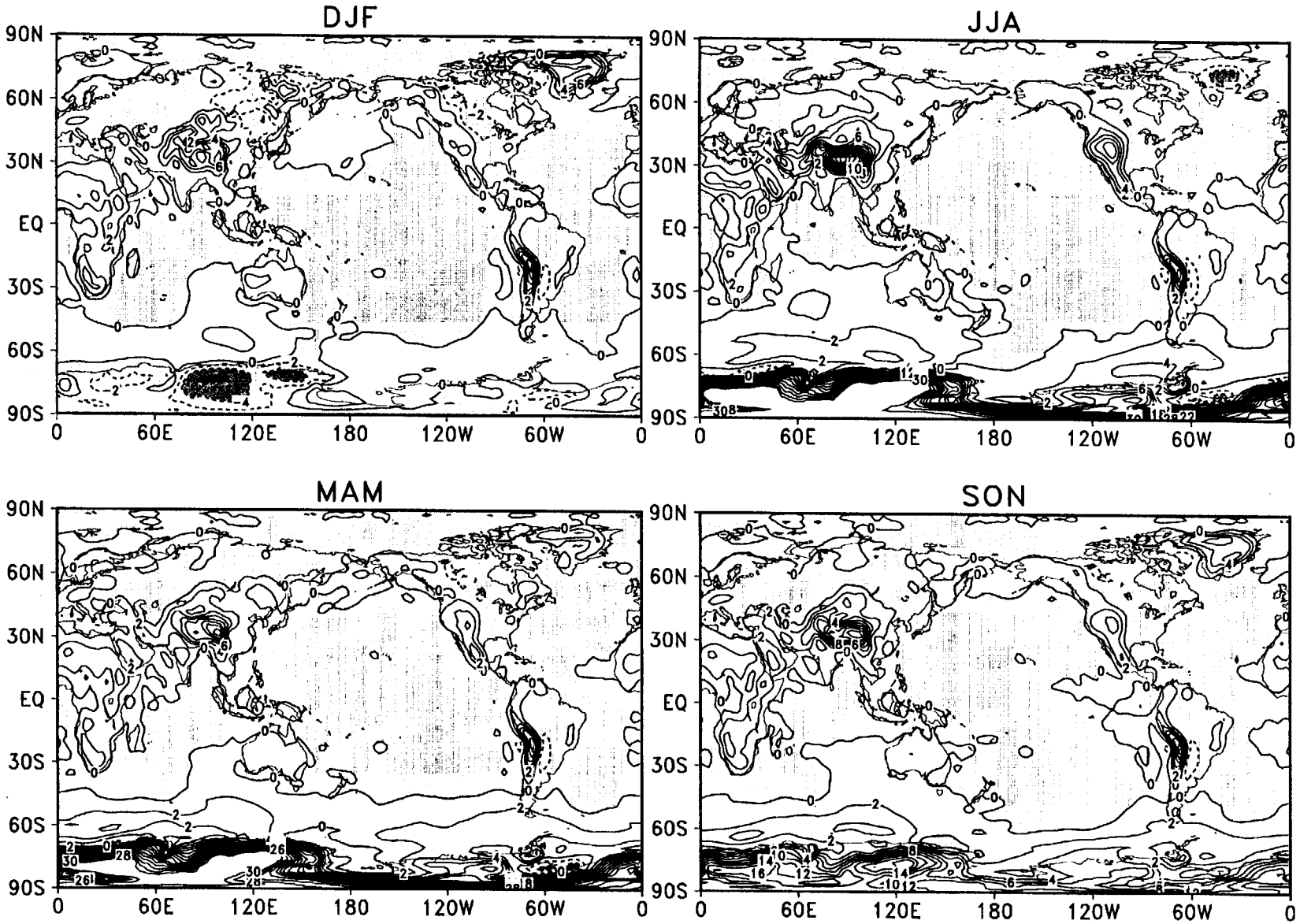

Figure 93: Difference of the seasonal means of mean sea level pressure during 1980–1995 (NCEP/NCAR minus DAO). The contour interval is 2 hPa. Negative values are shaded.

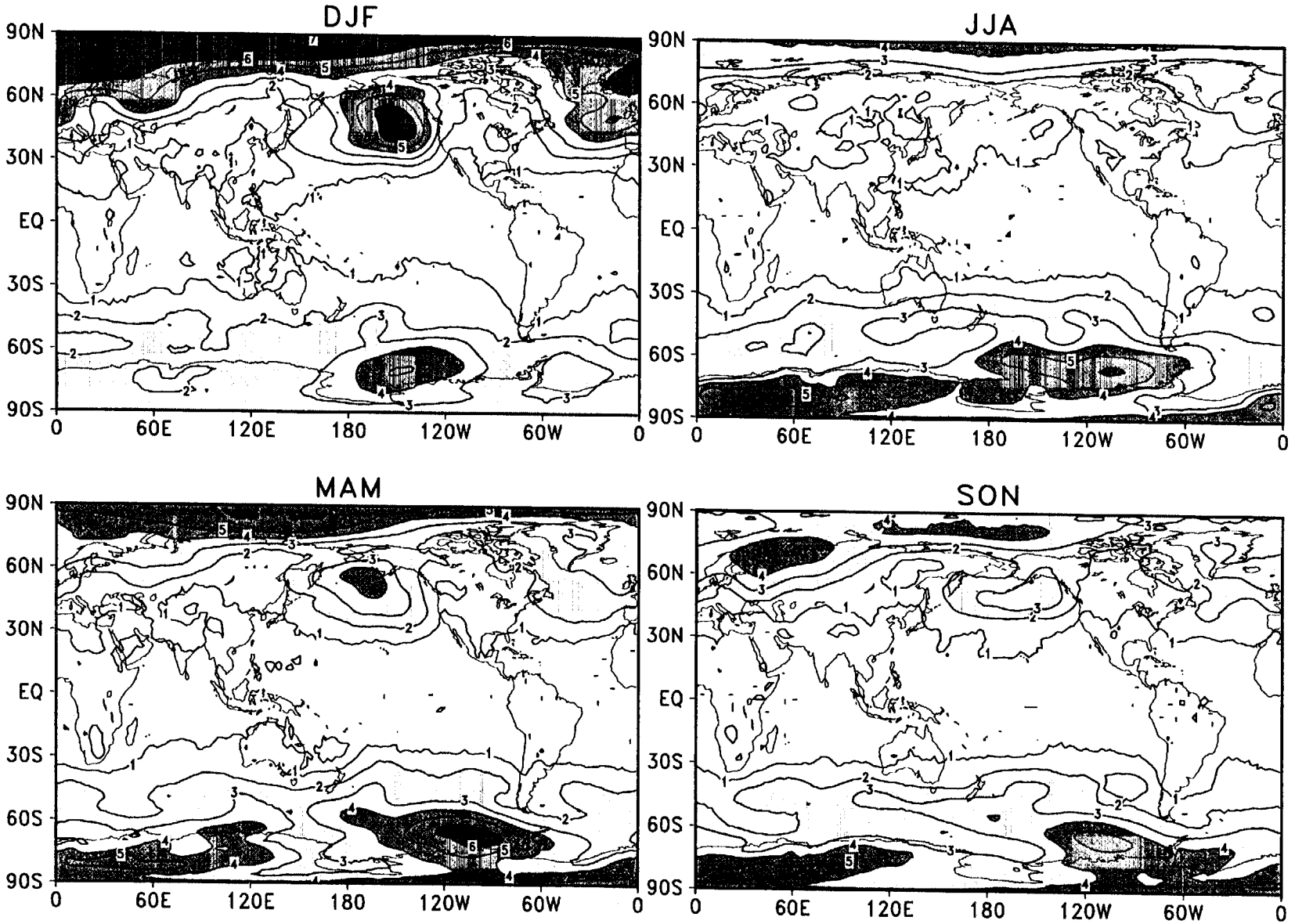

Figure 94: Standard deviations of seasonal mean sea level pressure for DAO reanalysis during 1980–1995. The contour interval is 1 hPa. Values larger than 2 hPa are shaded.

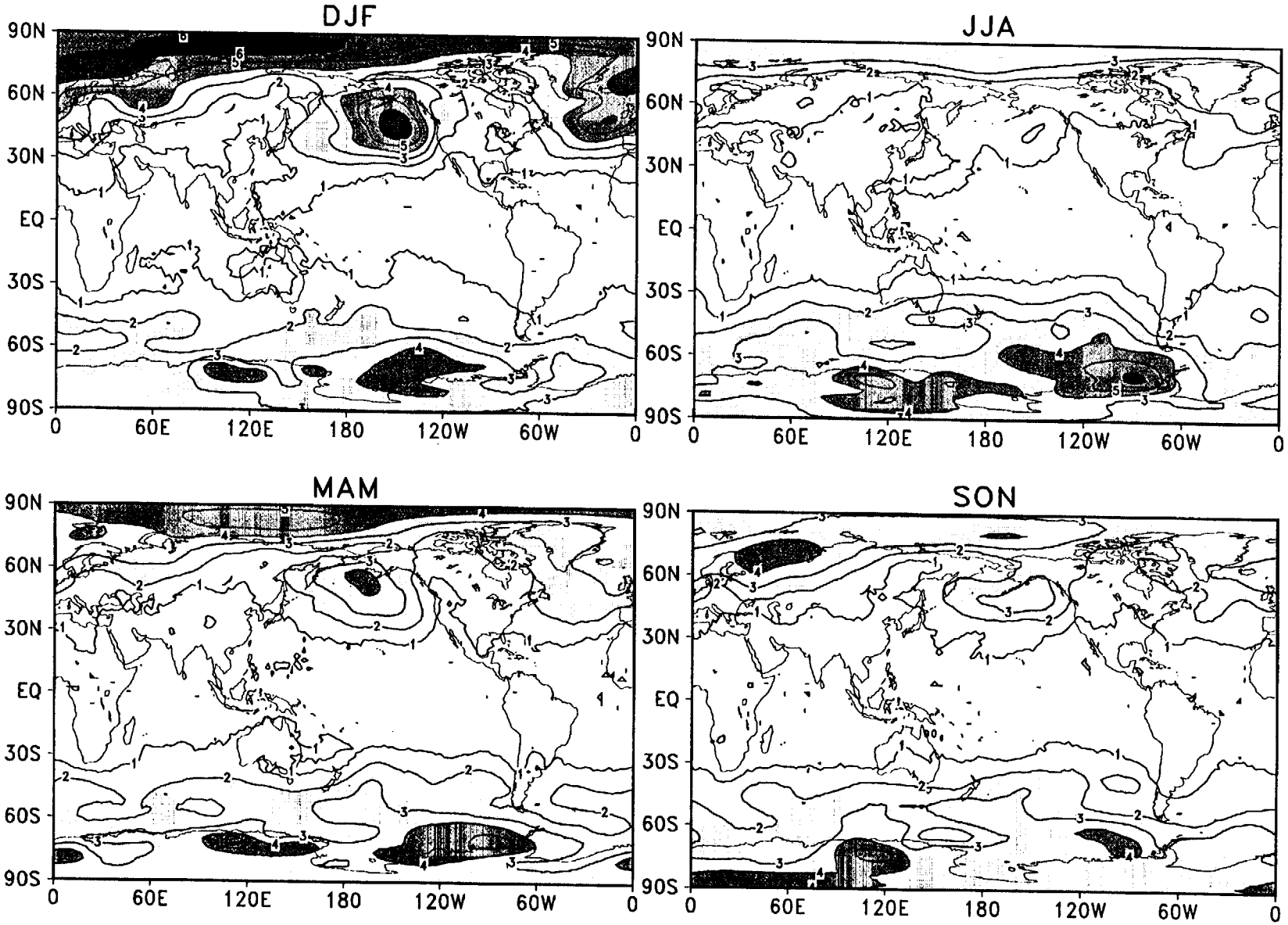

Figure 95: Standard deviations of seasonal mean sea level pressure for NCEP/NCAR reanalysis during 1980–1995. The contour interval is 1 hPa. Values larger than 2 hPa are shaded.

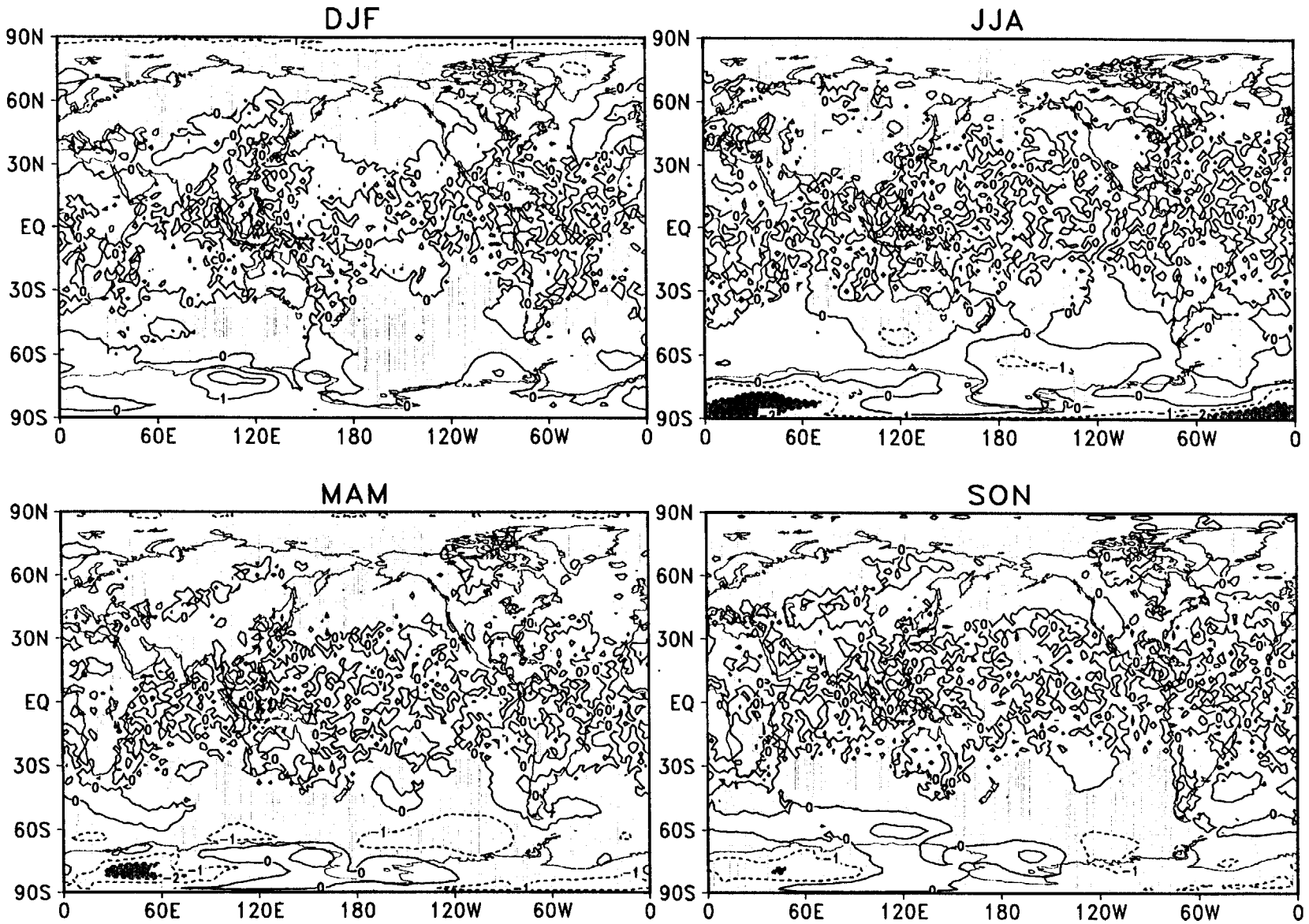

Figure 96: Difference of the standard deviations of seasonal mean sea level pressure during 1980–1995 (NCEP/NCAR minus DAO). The contour interval is 1 hPa. Negative values are shaded.

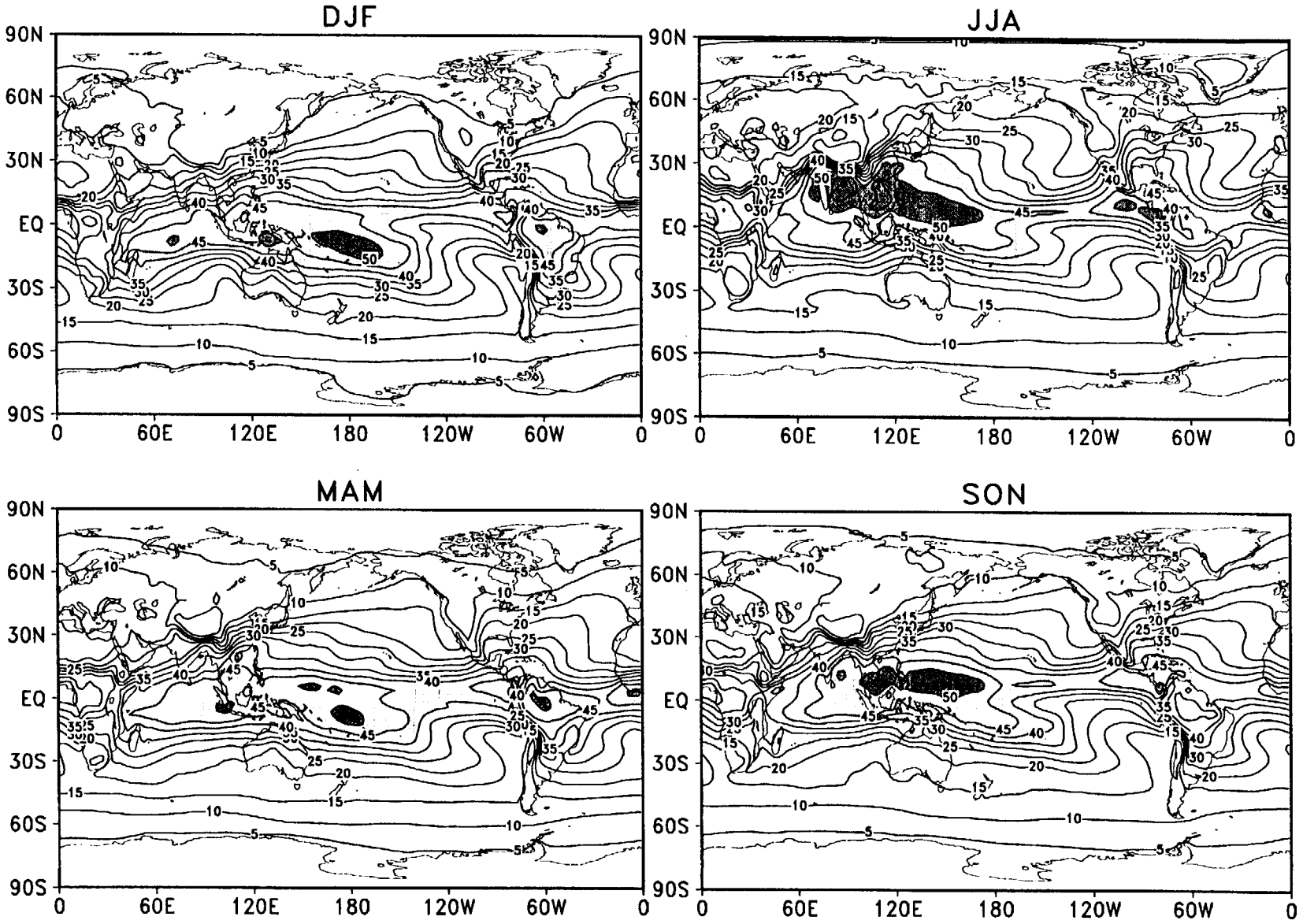

Figure 97: Seasonal means of total precipitable water for DAO reanalysis during 1980–1995. The contour interval is 5 Kg m^{-2}. Values larger than 40 Kg m^{-2} are shaded.

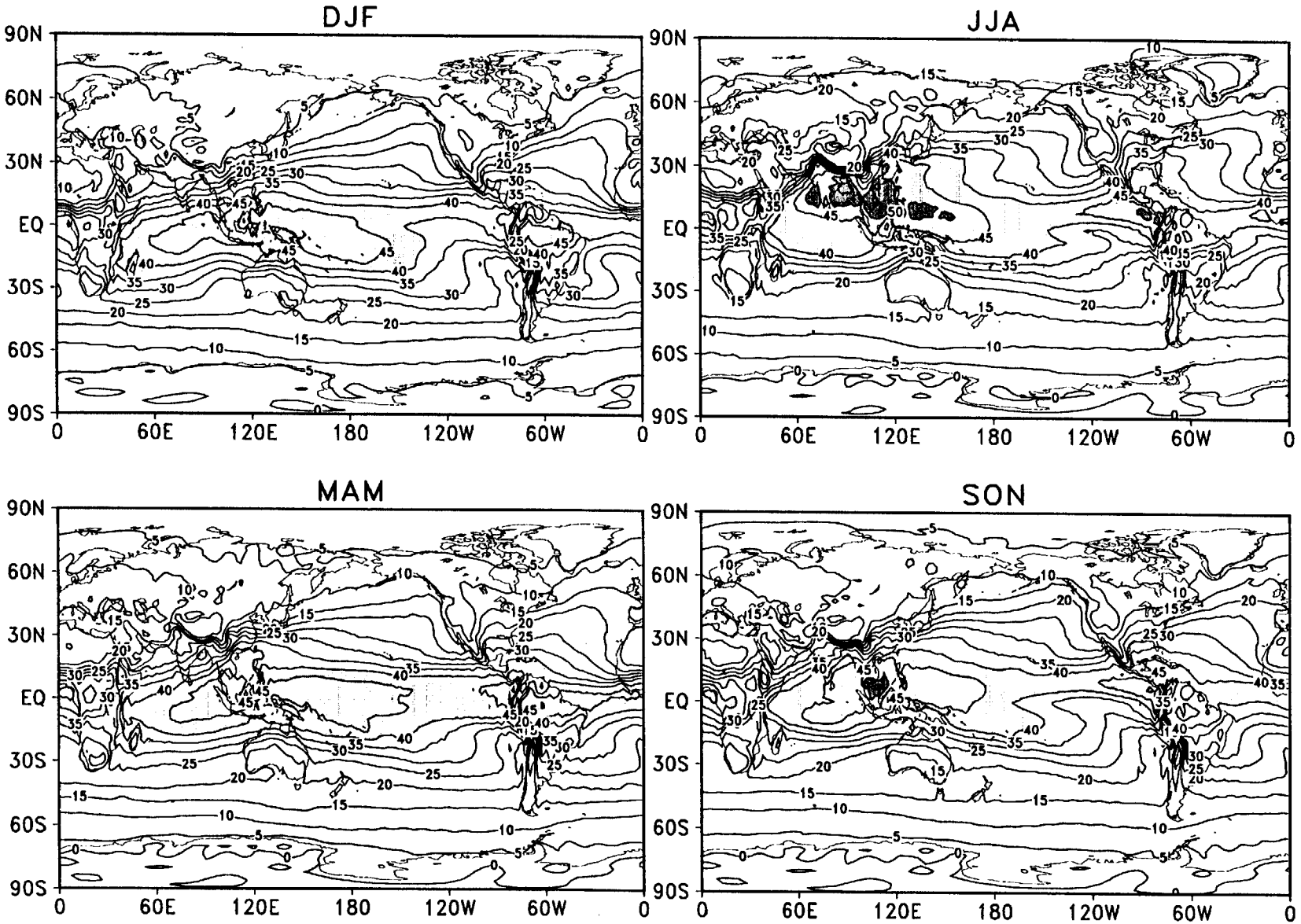

Figure 98: Seasonal means of total precipitable water for NCEP/NCAR reanalysis during 1980–1995. The contour interval is 5 Kg m^{-2}. Values larger than 40 Kg m^{-2} are shaded.

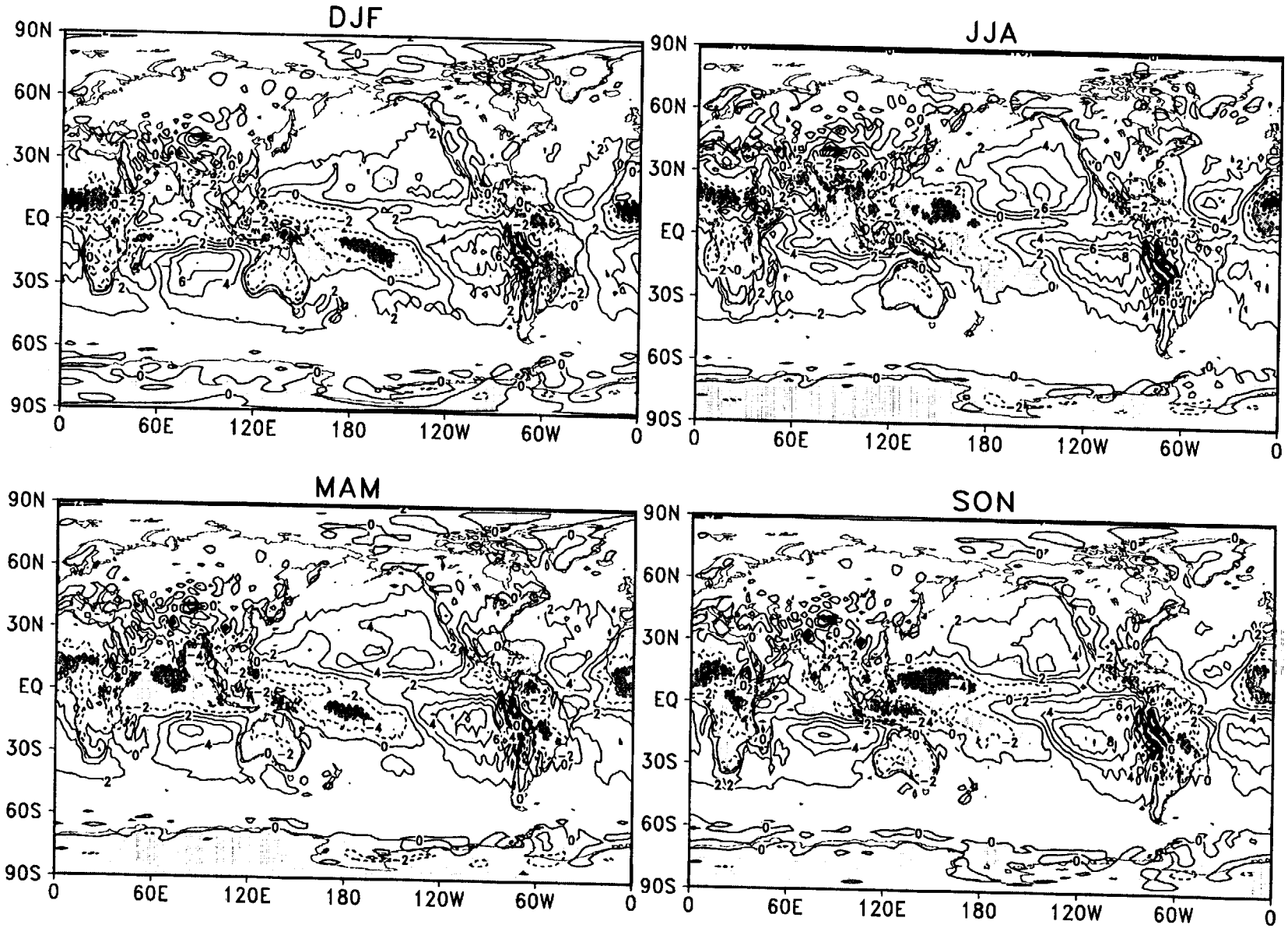

Figure 99: Difference of the seasonal means of total precipitable water during 1980–1995 (NCEP/NCAR minus DAO). The contour interval is 2 Kg m^{-2}. Negative values are shaded.

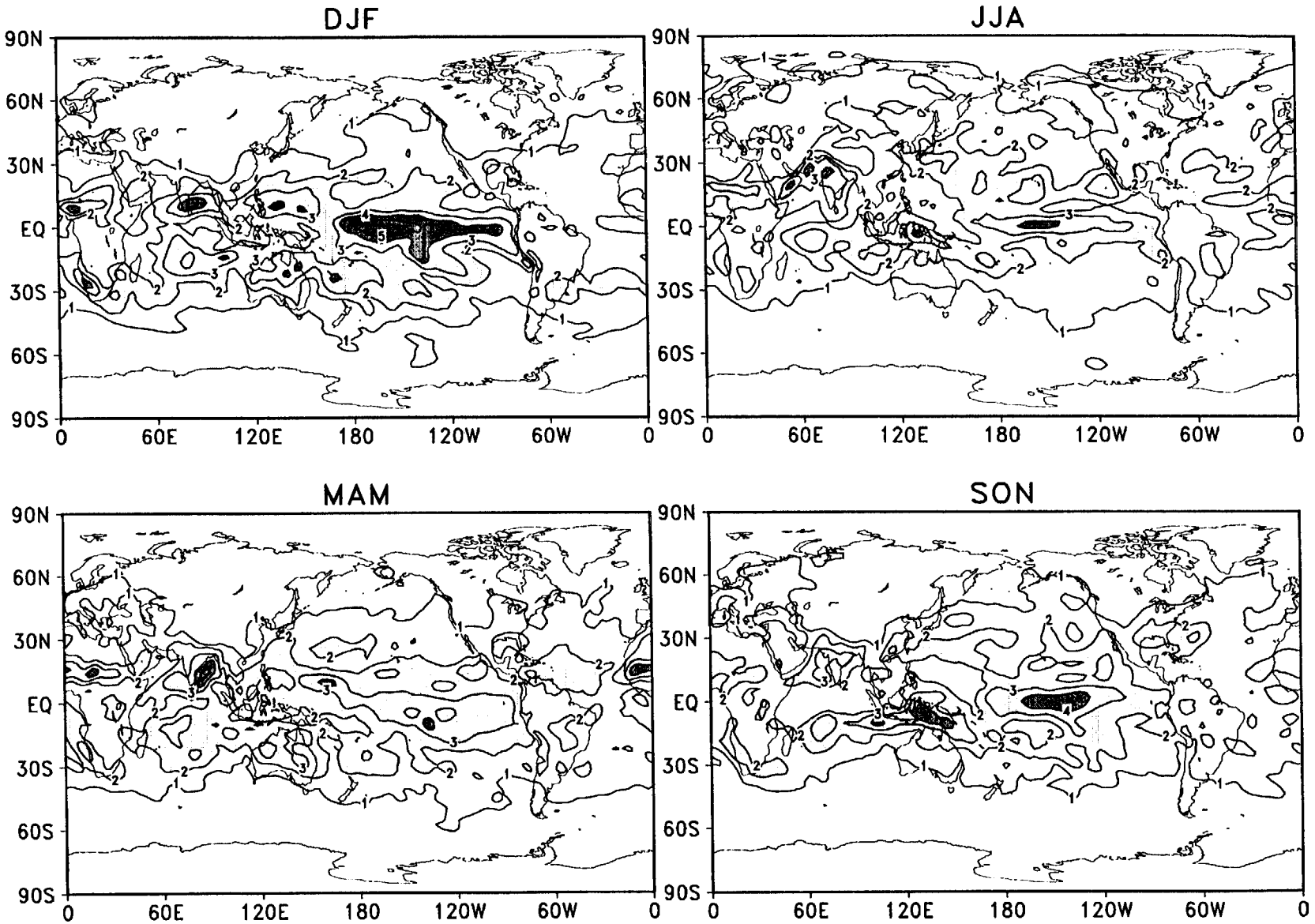

Figure 100: Standard deviations of seasonal mean total precipitable water for DAO reanalysis during 1980–1995. The contour interval is 1 Kg m^{-2}. Values larger than 2 Kg m^{-2} are shaded.

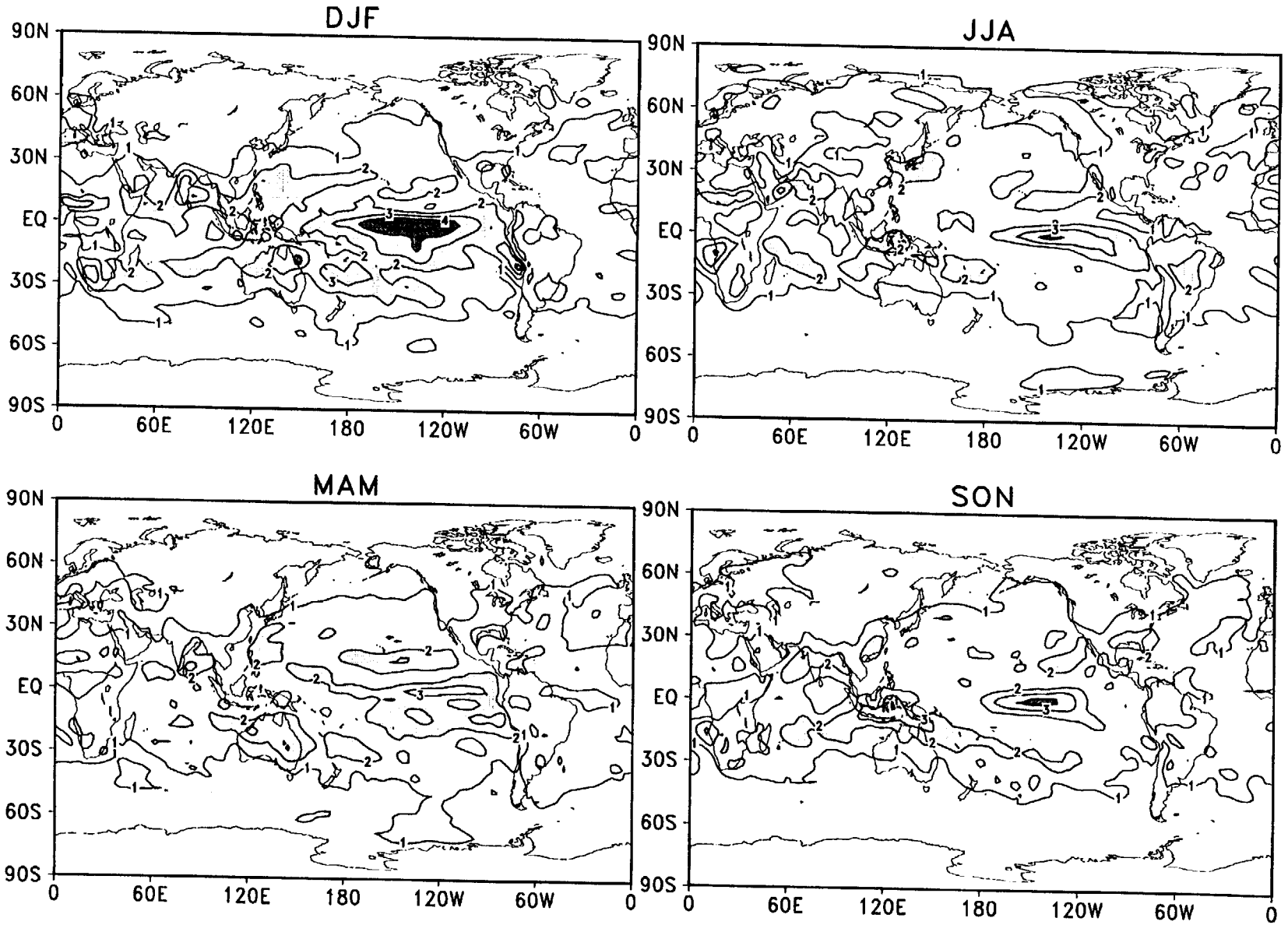

Figure 101: Standard deviations of seasonal mean total precipitable water for NCEP/NCAR reanalysis during 1980–1995. The contour interval is 1 Kg m^{-2}. Values larger than 2 Kg m^{-2} are shaded.

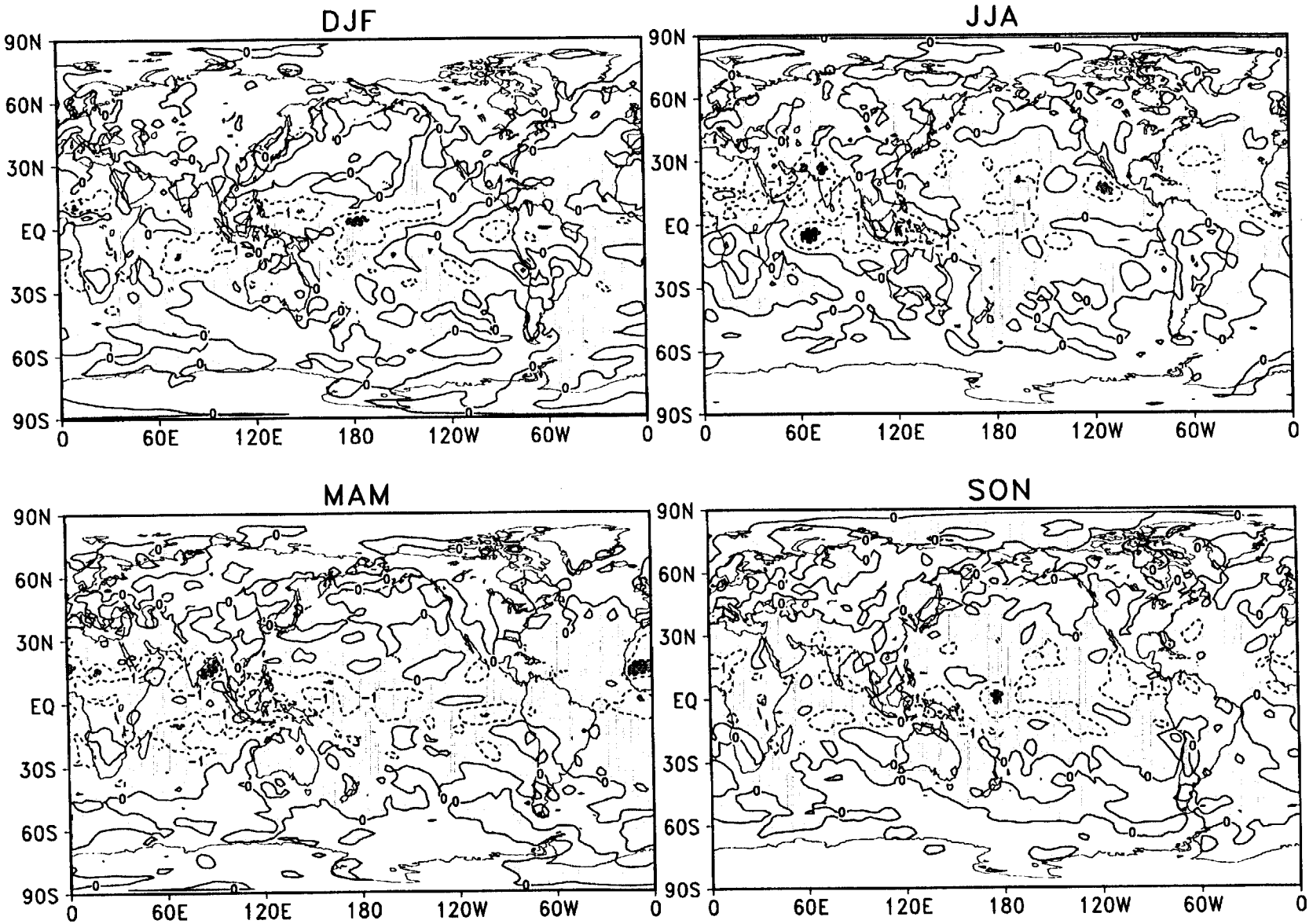

Figure 102: Difference of the standard deviations of seasonal mean total precipitable water during 1980–1995 (NCEP/NCAR minus DAO). The contour interval is 1 Kg m^{-2}. Negative values are shaded.

3.2.2 Stratosphere

We look in this section in more detail at the differences between the two reanalysis in the lower stratosphere. Neither system has a highly resolved stratosphere. This is particularly true for this version of the DAO assimilation system (GEOS-1) which has 20 model levels and a top at 10 hPa. We note that the new version of the DAO system does have a well resolved stratosphere with 70 model levels and a top at 0.01 hPa. We have already shown that the zonal mean fields in both wind and temperature (Figs.3 and 9) have substantial systematic differences between the DAO and the NCEP products in the lower stratosphere. In the following, we will examine the global distributions of the zonal wind and temperature at 50 hPa.

The seasonal mean zonal wind at 50 hPa shows distinct seasonal variations (Fig.103–104). Westerlies prevail in the northern hemisphere during DJF while strong easterlies occur in the subtropics of the southern hemisphere. This structure is reversed in JJA with the corresponding westerlies considerably stronger in the southern hemisphere high latitudes. The transition seasons show a more symmetrical structure with respect to the equator, with easterlies in the tropics and westerlies in the extratropics. The differences between MAM and SON are largest in the southern hemisphere extratropics which show considerably stronger westerlies during SON. The differences between the reanalyses (Fig.105), in general, show positive values in the subtropical region of the northern hemisphere and negative values in the subtropical and polar regions of the southern hemisphere. The interannual standard deviation of 50 hPa u-wind shows large seasonal variations in the middle and high latitudes (Figs.106 and 107). Large variability is observed in the tropics with maximum over the western Pacific, which is likely associated with the Quasibiennial Oscillation (QBO). The difference between the two reanalyses shows that the DAO has larger variability than the NCEP except for the tropical western Pacific and the tropical Indian ocean. The largest differences are found in the tropical central and eastern Pacific.

The seasonal mean temperature at 50 hPa shows large seasonal variations with a warm pole in the summer hemisphere (Figs.109 and 110). There is evidence of noise near the pole in the DAO datasets for all seasons. NCEP shows consistently warmer temperature at 50 hPa over the entire globe (Fig.111). Generally, large interannual temperature variability is found in the high latitudes during the winter seasons. The transition seasons show some asymmetry with the largest variability occurring in the northern hemisphere during MAM, and in the southern hemisphere during SON. The differences in the variability between the two reanalyses are small (Figs.112–114).

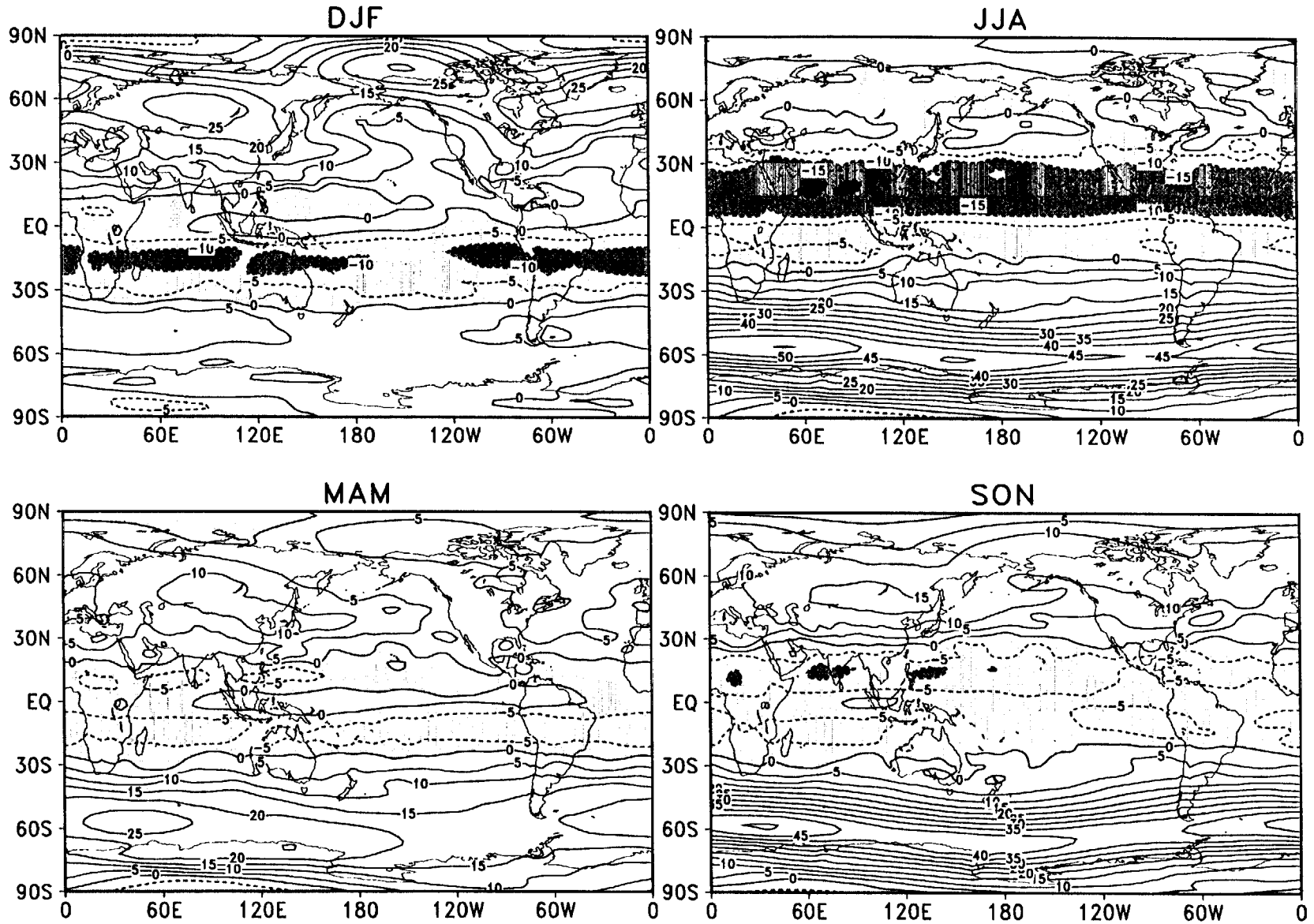

Figure 103: Seasonal means of 50 hPa u-wind for DAO reanalysis during 1980–1995. The contour interval is 5 m s^{-1}. Negative values are shaded.

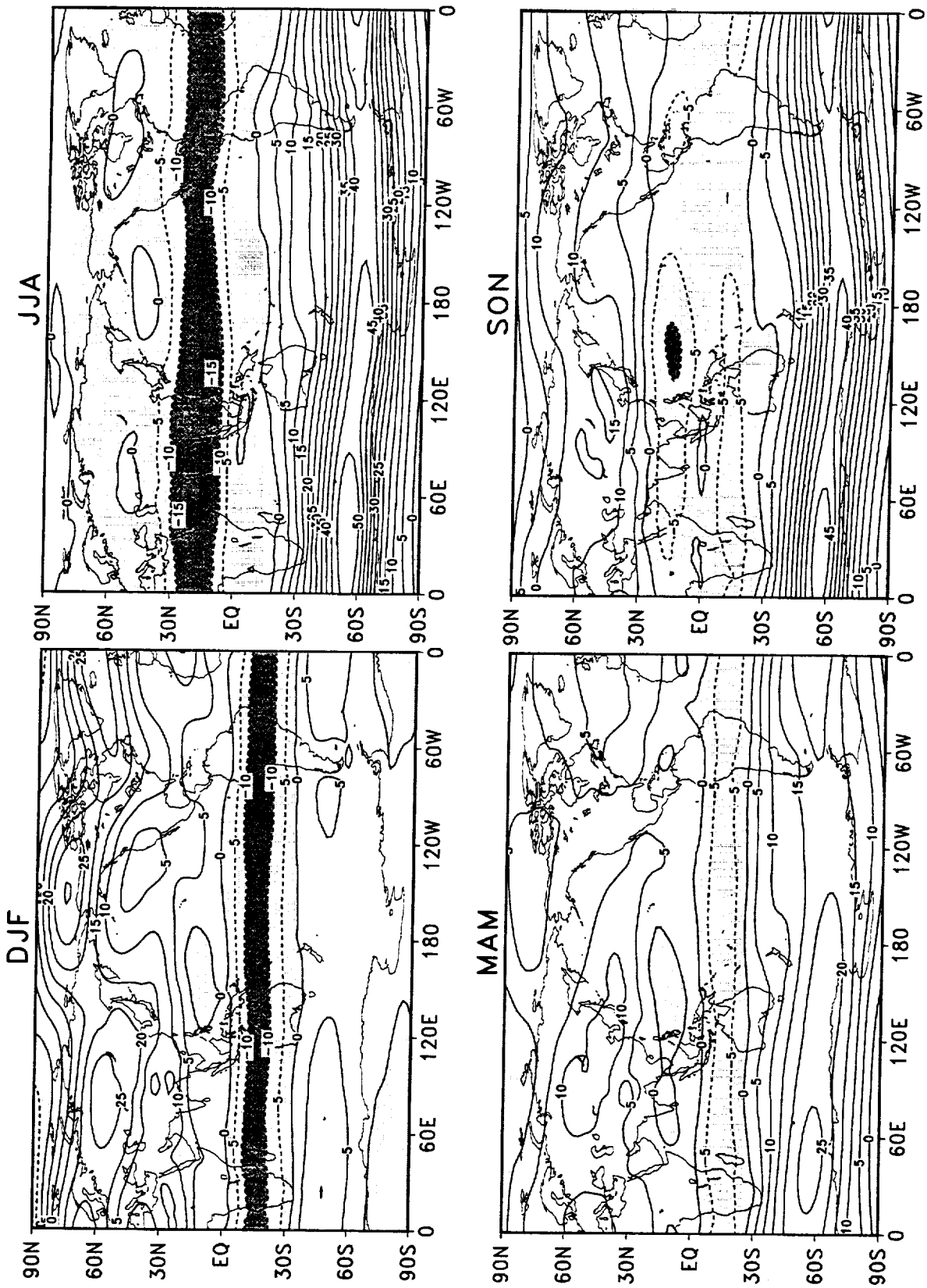

Figure 104: Seasonal means of 50 hPa u-wind for NCEP/NCAR reanalysis during 1980–1995. The contour interval is 5 m s^{-1}. Negative values are shaded.

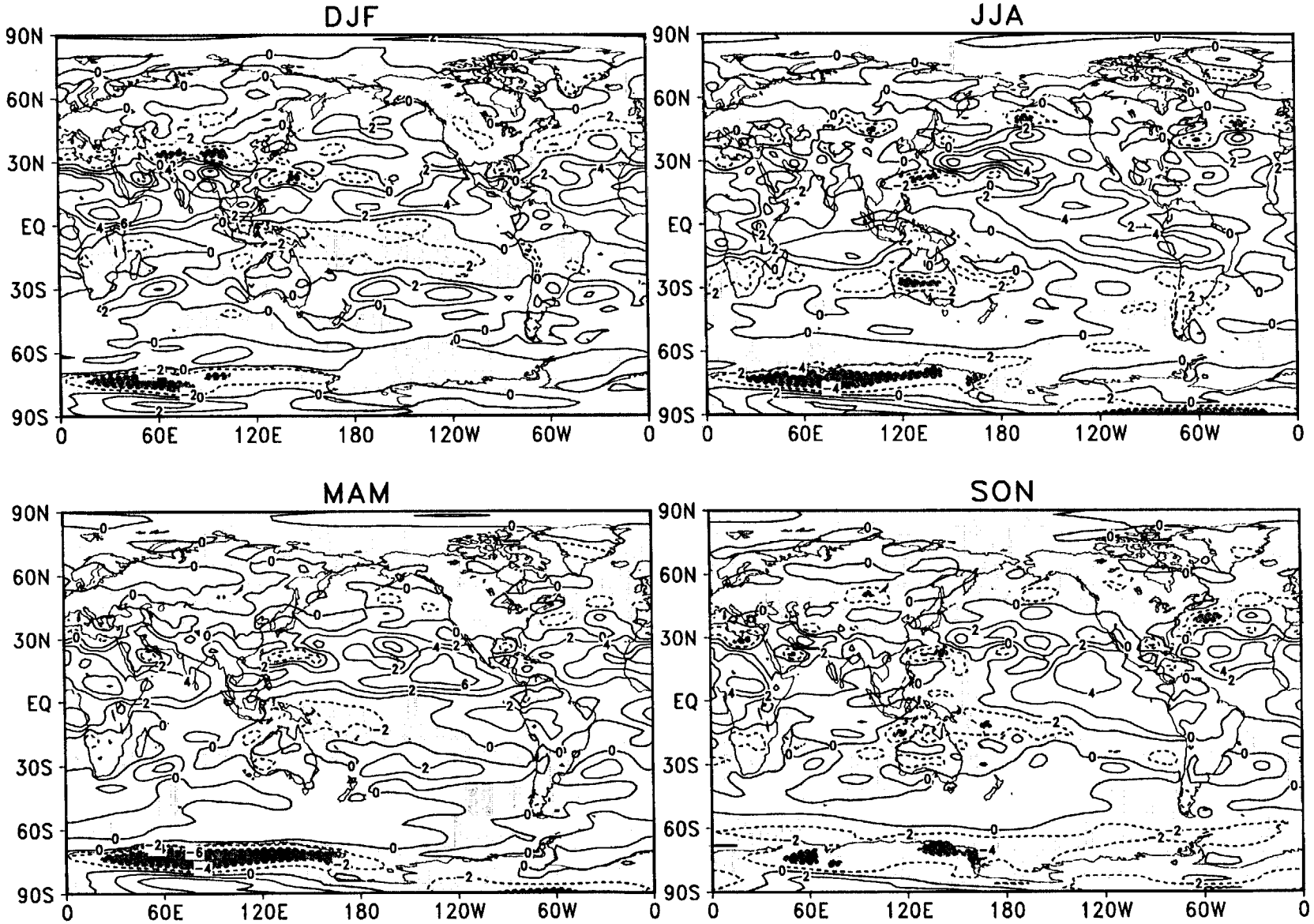

Figure 105: Difference of the seasonal means of 50 hPa u-wind during 1980–1995 (NCEP/NCAR minus DAO). The contour interval is 2 m s^{-1}. Negative values are shaded.

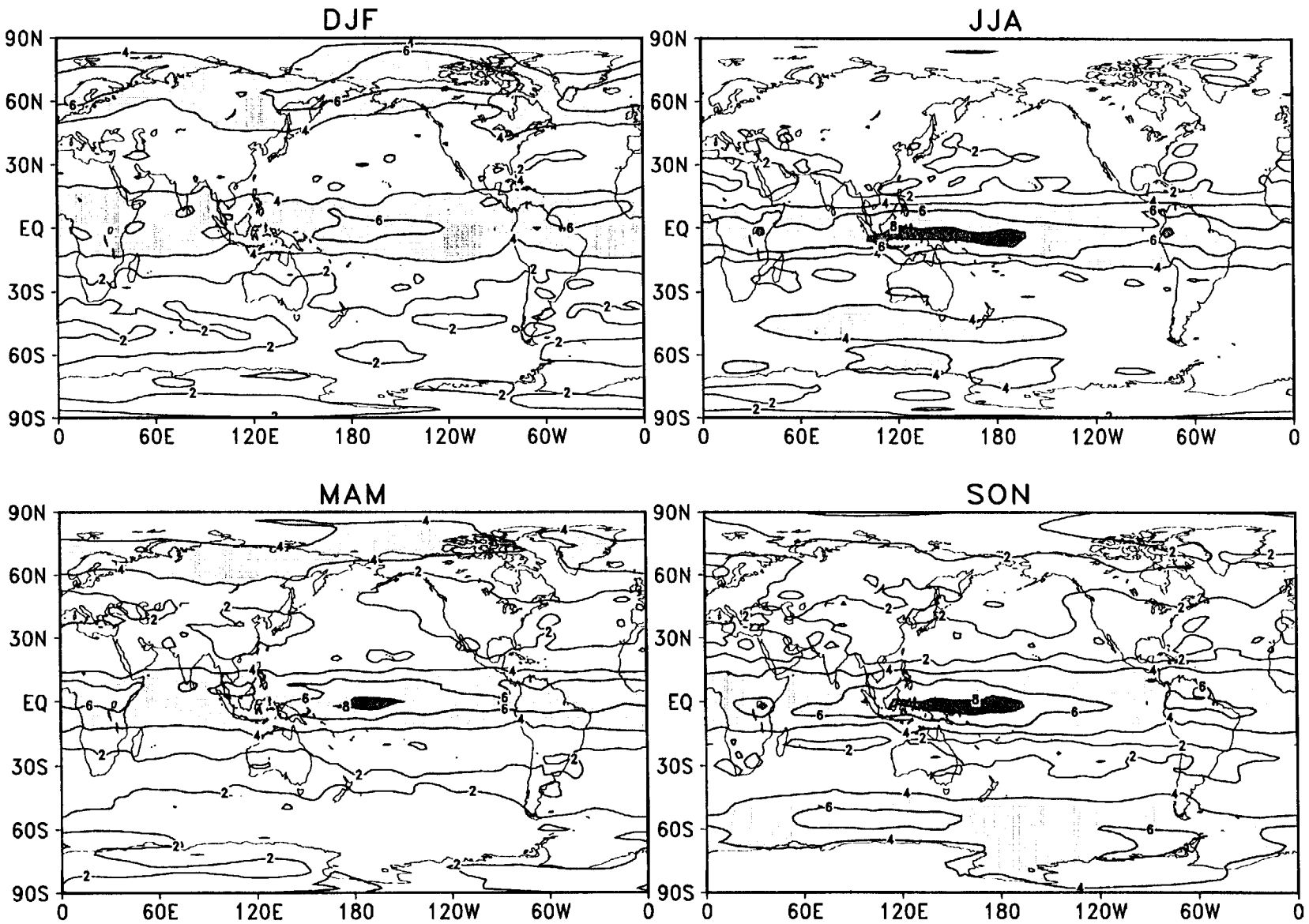

Figure 106: Standard deviations of seasonal mean 50 hPa u-wind for DAO reanalysis during 1980–1995. The contour interval is 2 m s^{-1}. Values larger than 4 m s^{-1} are shaded.

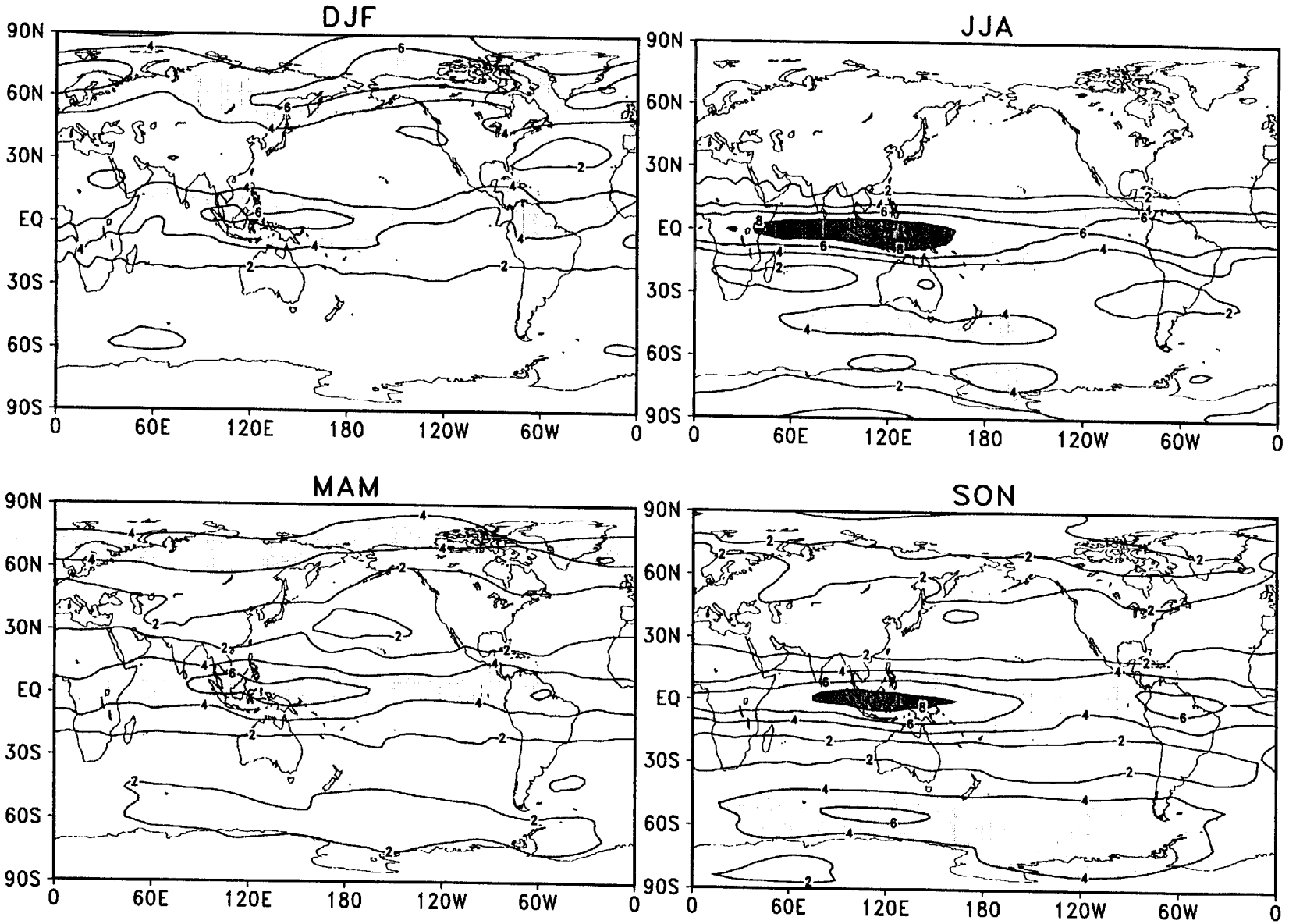

Figure 107: Standard deviations of seasonal mean 50 hPa u-wind for NCEP/NCAR reanalysis during 1980–1995. The contour interval is 2 m s^{-1}. Values larger than 4 m s^{-1} are shaded.

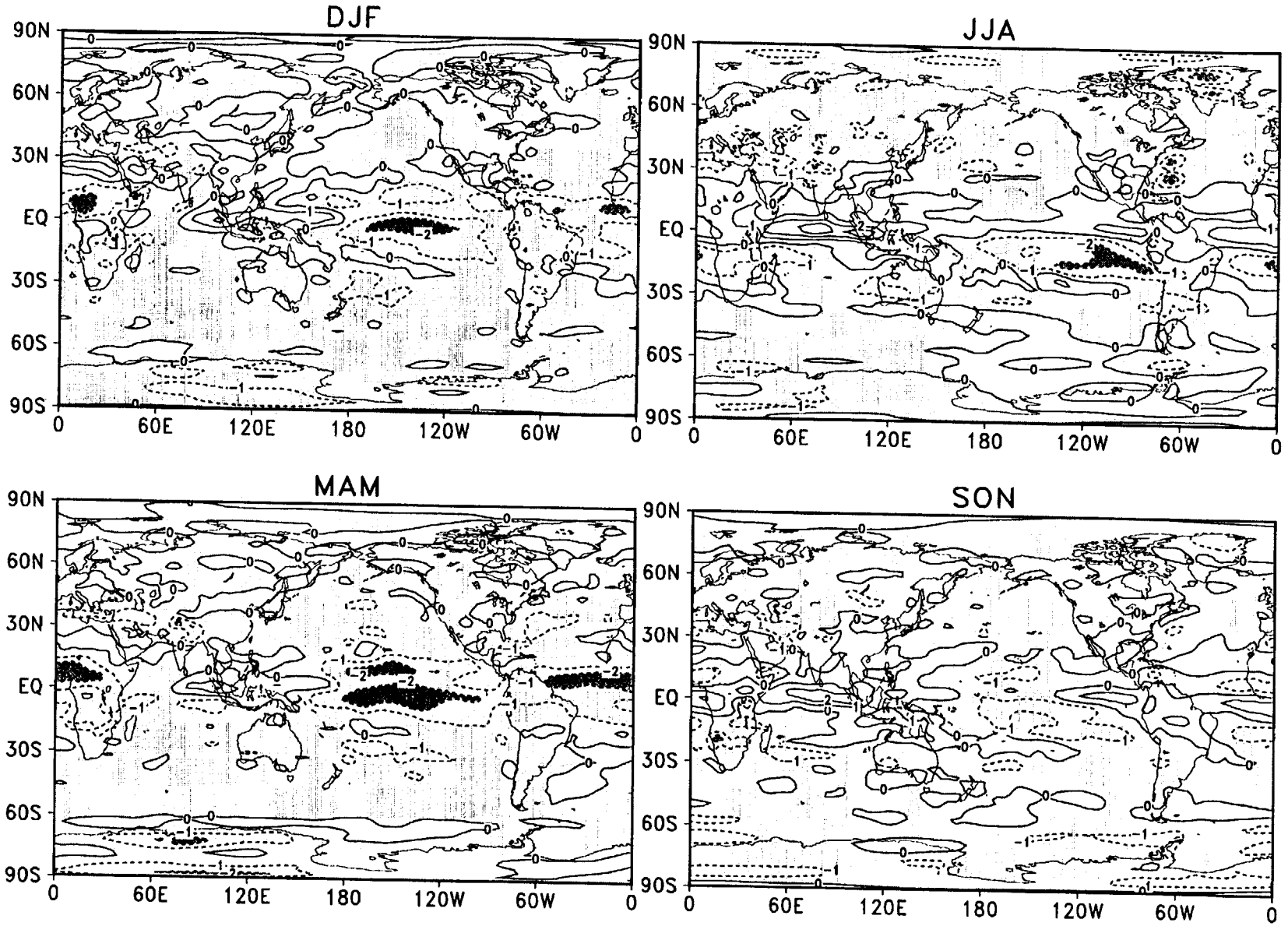

Figure 108: Difference of the standard deviations of seasonal mean 50 hPa u-wind during 1980–1995 (NCEP/NCAR minus DAO). The contour interval is 1 m s^{-1}. Negative values are shaded.

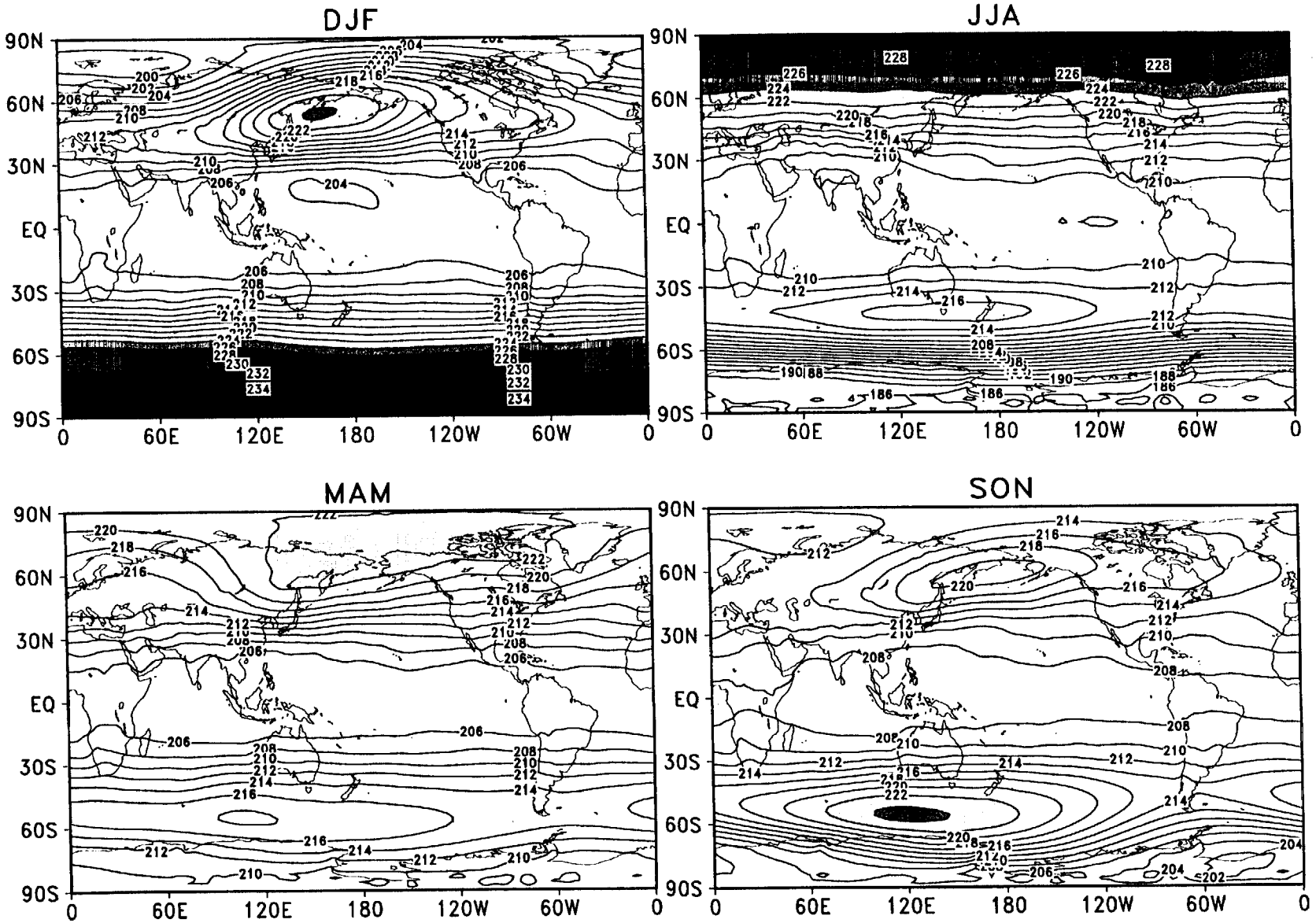

Figure 109: Seasonal means of 50 hPa temperature for DAO reanalysis during 1980–1995. The contour interval is 2°K. Values less than 222°K are shaded.

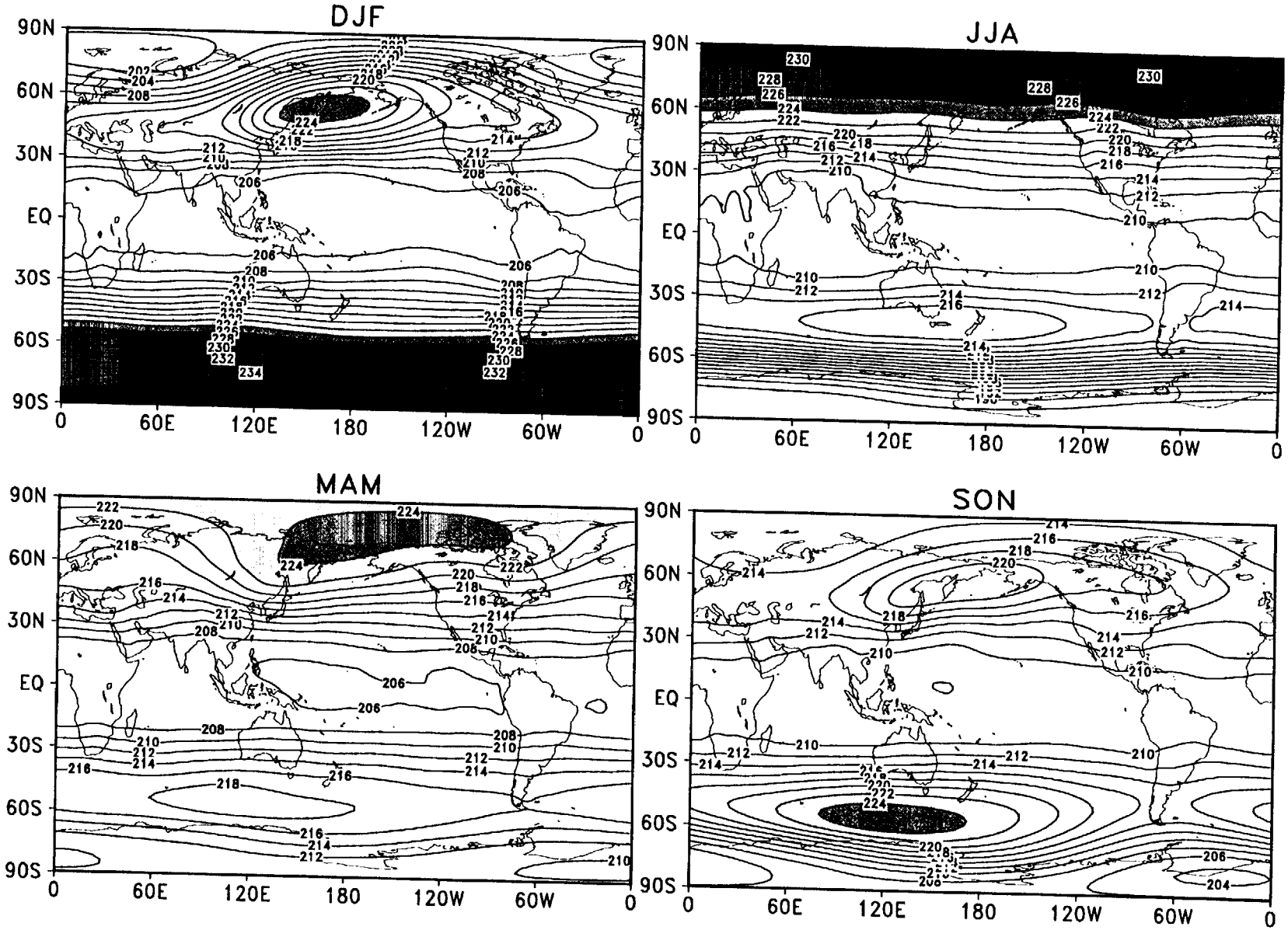

Figure 110: Seasonal means of 50 hPa temperature for NCEP/NCAR reanalysis during 1980–1995. The contour interval is 2°K. Values less than 222°K are shaded.

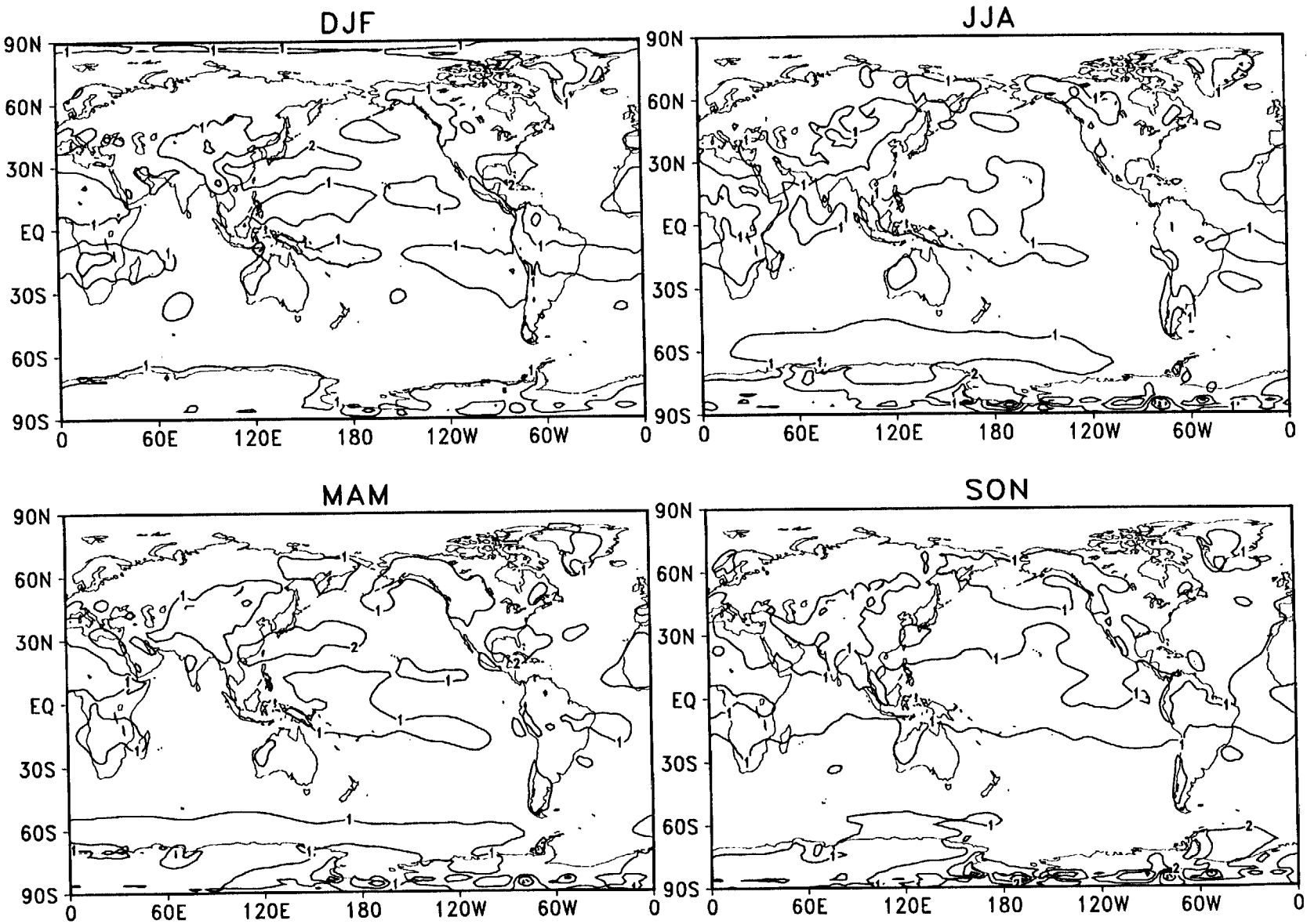

Figure 111: Difference of the seasonal means of 50 hPa temperature during 1980–1995 (NCEP/NCAR minus DAO). The contour interval is 1°K. Negative values are shaded.

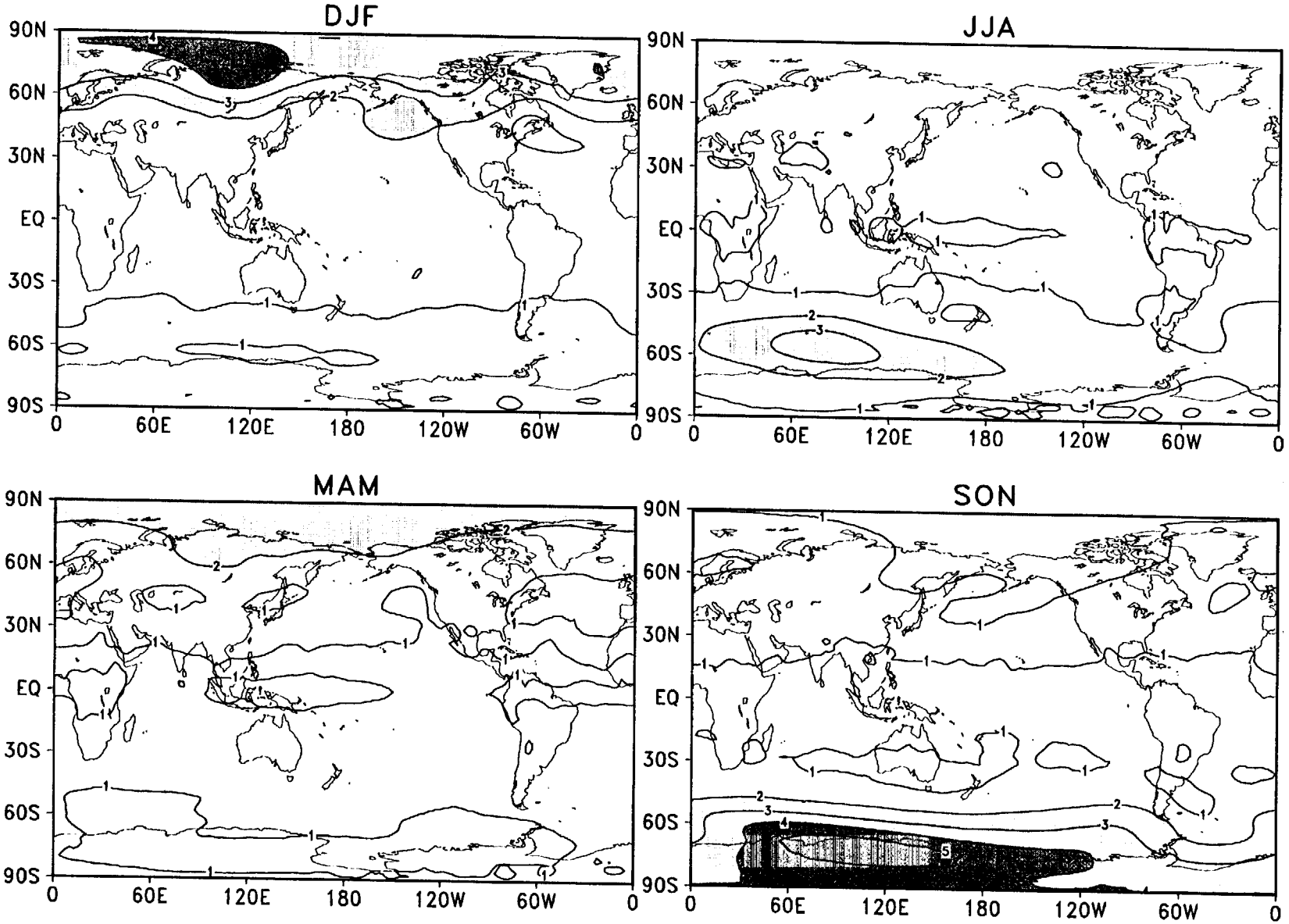

Figure 112: Standard deviations of seasonal mean 50 hPa temperature for DAO reanalysis during 1980–1995. The contour interval is 1°K. Values larger than 2°K are shaded.

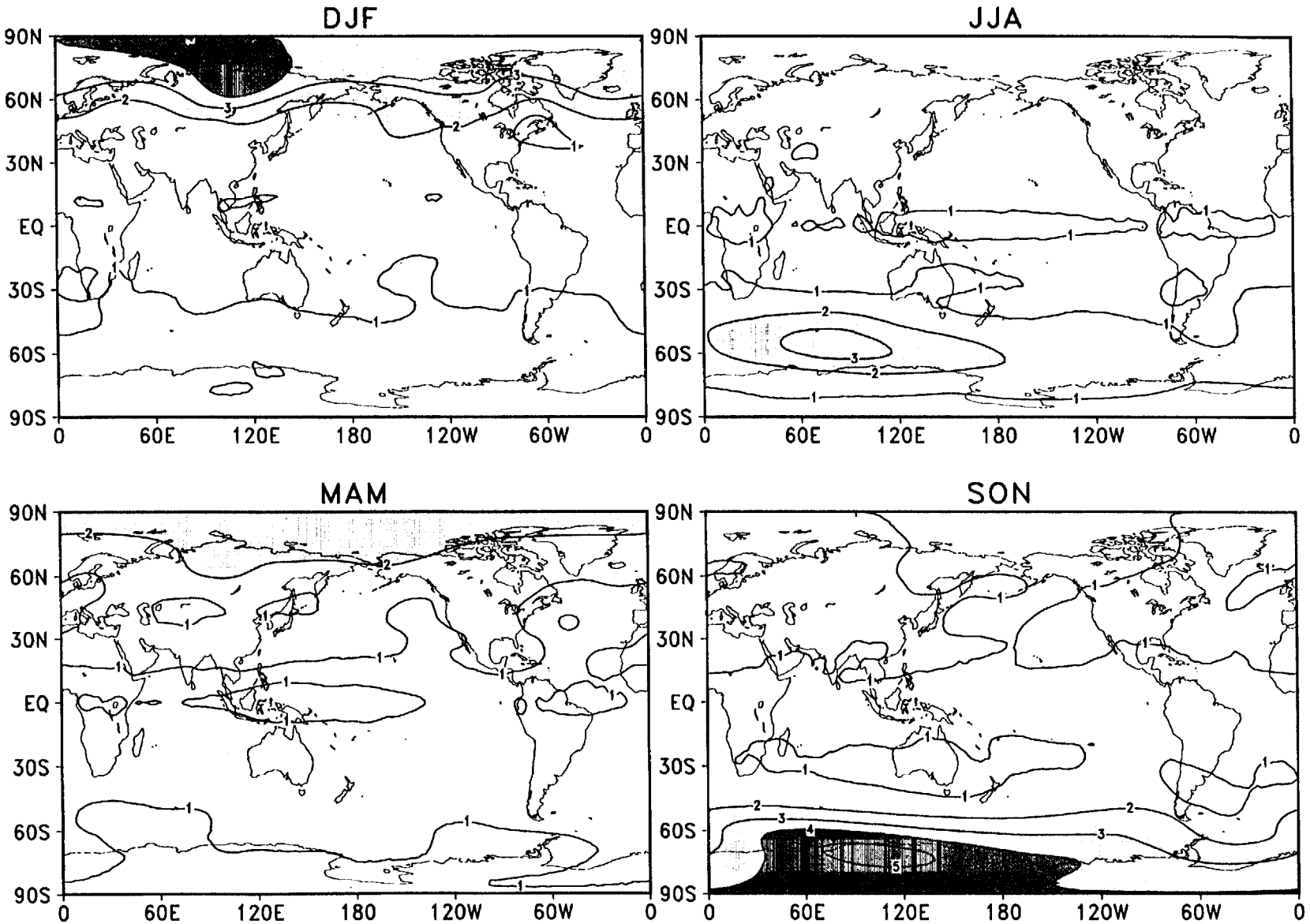

Figure 113: Standard deviations of seasonal mean 50 hPa temperature for NCEP/NCAR reanalysis during 1980–1995. The contour interval is 1°K. Values larger than 2°K are shaded.

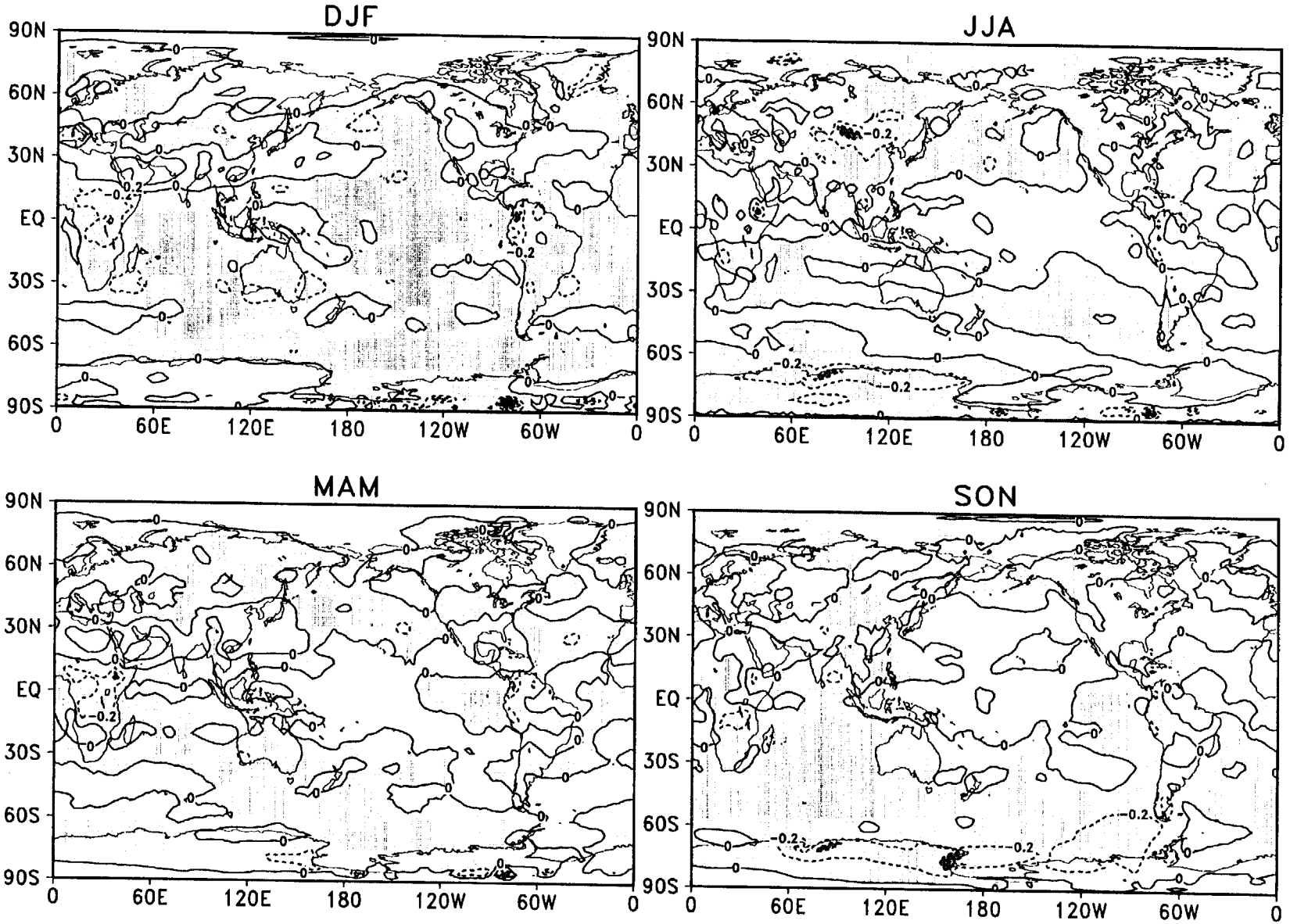

Figure 114: Difference of the standard deviations of seasonal mean 50 hPa temperature during 1980–1995 (NCEP/NCAR minus DAO). The contour interval is 0.2°K. Negative values are shaded.

3.3 Global diagnostic fields

In this subsection, we will compare the seasonal means and the interannual variability of the seasonal means for selected diagnostic quantities.

The precipitation shows a clear seasonal evolution in the tropics as well as in the subtropics (Figs.115 and 116). Key features include the boreal winter precipitation in the storm track regions, the Indian summer monsoon rainfall, and the enhancement of summer rainfall over land. The largest differences between the two reanalyses are in the vicinity of heavy tropical rainfall where the DAO product generally has more rainfall than NCEP. The NCEP system generates more precipitation over the storm tracks. There is also considerable small scale noise in the NCEP product at high latitudes. The largest interannual variability is found in the normally heavy rainfall regions of the tropics and the subtropics. Large interannual variability is also observed over the northern Europe, eastern Asia and the eastern coast of the United States during JJA. The difference field (Fig.120) shows that the DAO rainfall has larger interannual variability than NCEP in the regions of heaviest tropical rainfall.

Figures 121–126 show the seasonal mean and interannual variability of the outgoing longwave radiation (OLR) of the two reanalyses. The differences in the seasonal means (Fig.123) again suggests that in the tropics and subtropics the DAO system generates stronger convection (and higher clouds) than the NCEP system. The extratropical differences are largely negative. This is especially evident over the storm tracks, consistent with the generally greater rainfall in the NCEP product in these regions. The largest variability occurs in the tropics and subtropics with a maximum in the western Pacific regions. Again, the NCEP product shows less variable than the DAO throughout the year.

The evaporation depends on the magnitude of the surface wind, the vertical moisture gradient near the surface and the surface layer stability. Since the techniques used in determining evaporation are very similar in the two reanalyses, the differences in the evaporation reflects differences in the surface wind or the vertical moisture gradient near the surface. In general, the DAO product shows less evaporation over most of the ocean area and more evaporation over land (Fig.129). The interannual variability is generally small and spotty (Figs.130 and 131). The largest differences in the variability occur over land, where the DAO product shows consistently larger values.

The sensible heat flux is determined by the magnitude of the surface wind, the vertical temperature gradient near the surface and the surface roughness. In general, the sensible heat flux is from the surface to the atmosphere except for regions covered with snow or ice (Figs.133 and 134). The main differences between the two reanalyses occur over land, and over ocean where SST gradients are the largest (Fig.135). The DAO has larger sensible heat flux over land and less over the Gulf Stream and the Kuroshio current. The differences of the sensible heat flux over the ocean may reflect in part the differences in the sea surface

temperature (SST) between the two reanalyses. The SST data set used in the DAO incorporates the monthly mean blended SST analyses of Renolds and Marsico (1993) while the NCEP uses the the improved weekly global optimum interpolated SST analyses of Renolds and Smith (1994). The major differences between the two SST data sets are in regions of large SST gradients, such as the Gulf Stream and the Kuroshio. The largest interannual variability in the sensible heat flux occurs over land, and in the regions with large SST gradients and the ocean area near the south pole where the variability is associated with the migration of the sea ice concentration (Figs.136 and 137). Figure 138 shows that the DAO sensible heat flux has generally larger variability than NCEP–exceptions include the Gulf Stream and Europe during DJF and MAM.

Figures 139–144 show the seasonal means and the interannual standard deviations of temperature at 2 meters. The seasonal means are similar in the two reanalyses. However, large differences are observed over the cold season middle and high latitude continents of both hemispheres (Fig.141), with considerably colder temperatures in the DAO product. Both reanalyses show a large seasonal cycle in the regions of maximum variability. Note also that there is a local maximum of interannual variability over the tropical eastern Pacific. This is likely linked to the ENSO phenomenon. The differences map shows that the DAO two meter temperature generally has larger variability than NCEP.

The seasonal means of the 10 meter zonal wind show similar patterns in the two reanalyses with the largest differences occurring near the polar regions. the coastal regions and the central tropical Pacific (Figs.145–147). The main features in the seasonal means of the 10 meter wind are the prevailing easterlies in the tropics and subtropics with maxima off the equator, and the westerlies in the midlatitudes. Large interannual variations are observed in the storm track regions, such as the North Pacific, the North Atlantic and the east of New Zealand. Large variability is also found in the central and western Pacific which may be linked to ENSO variability. The difference map, while noisy, shows a tendency for the DAO winds to have larger variability over the tropics and subtropics, while the NCEP winds have greater variability over the extratropics.

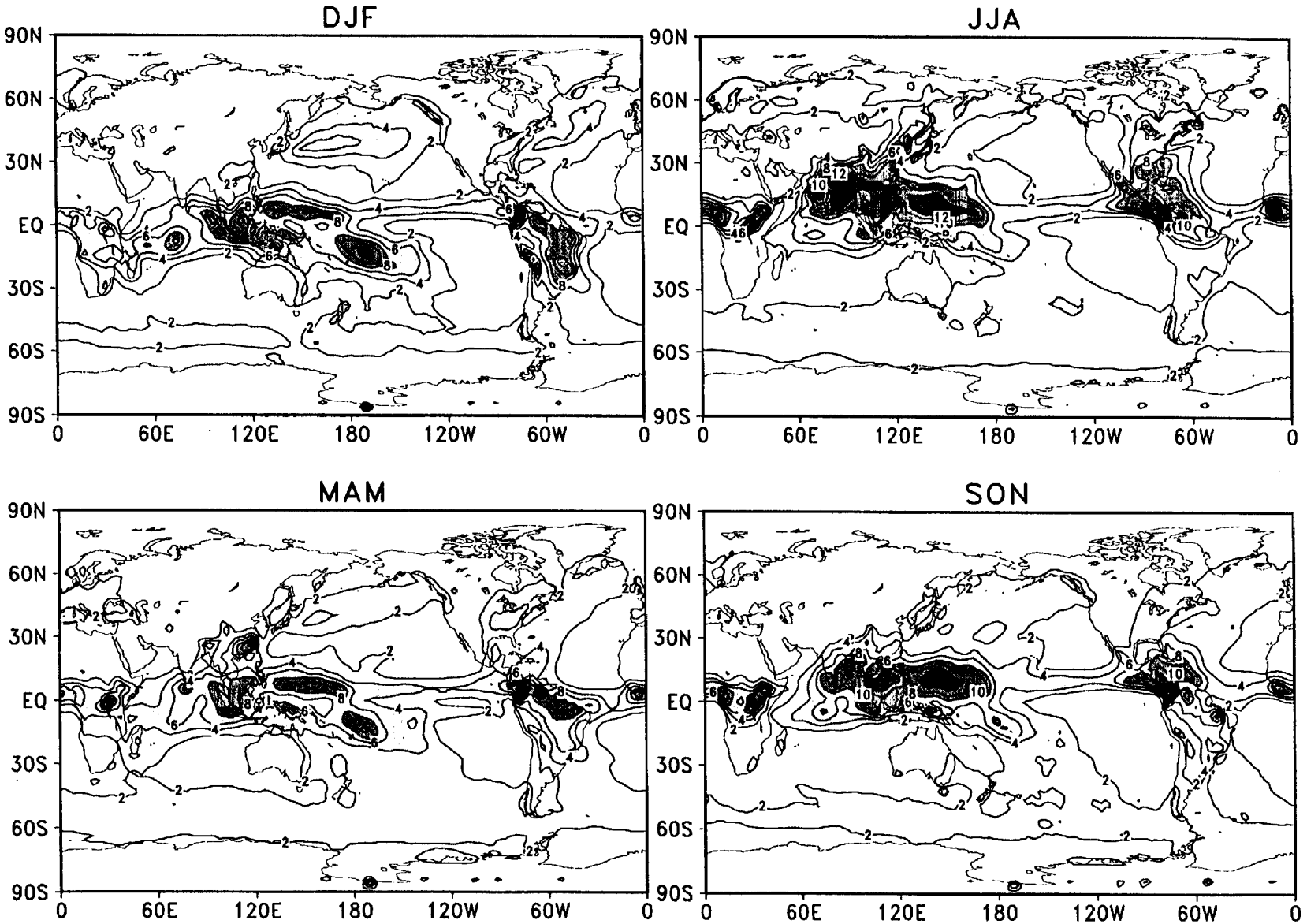

Figure 115: Seasonal means of precipitation for DAO reanalysis during 1980–1995. The contour interval is 2 mm day^{-1}. Values larger than 4 mm day^{-1} are shaded.

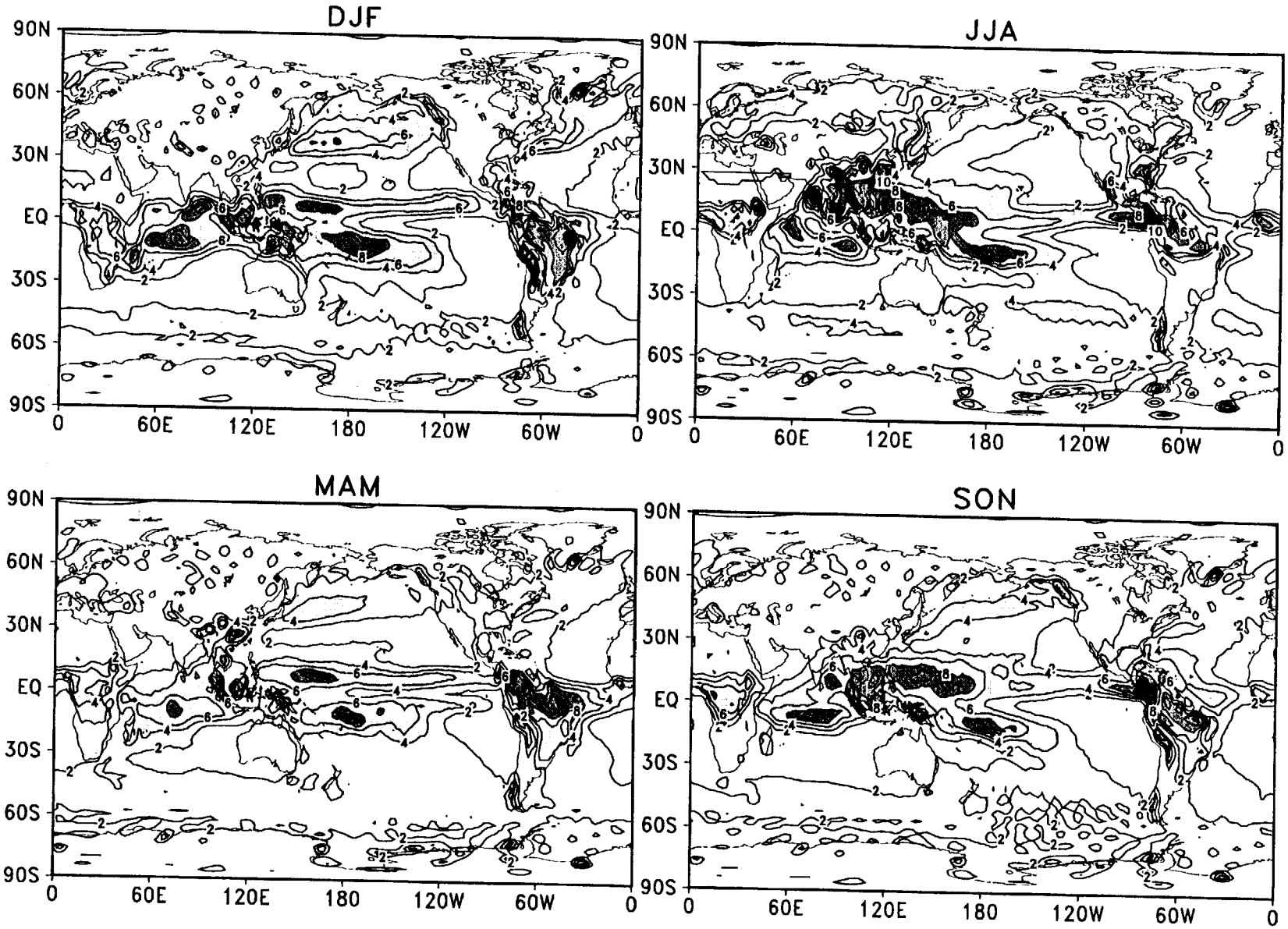

Figure 116: Seasonal means of precipitation for NCEP/NCAR reanalysis during 1980–1995. The contour interval is 2 mm day^{-1}. Values larger than 4 mm day^{-1} are shaded.

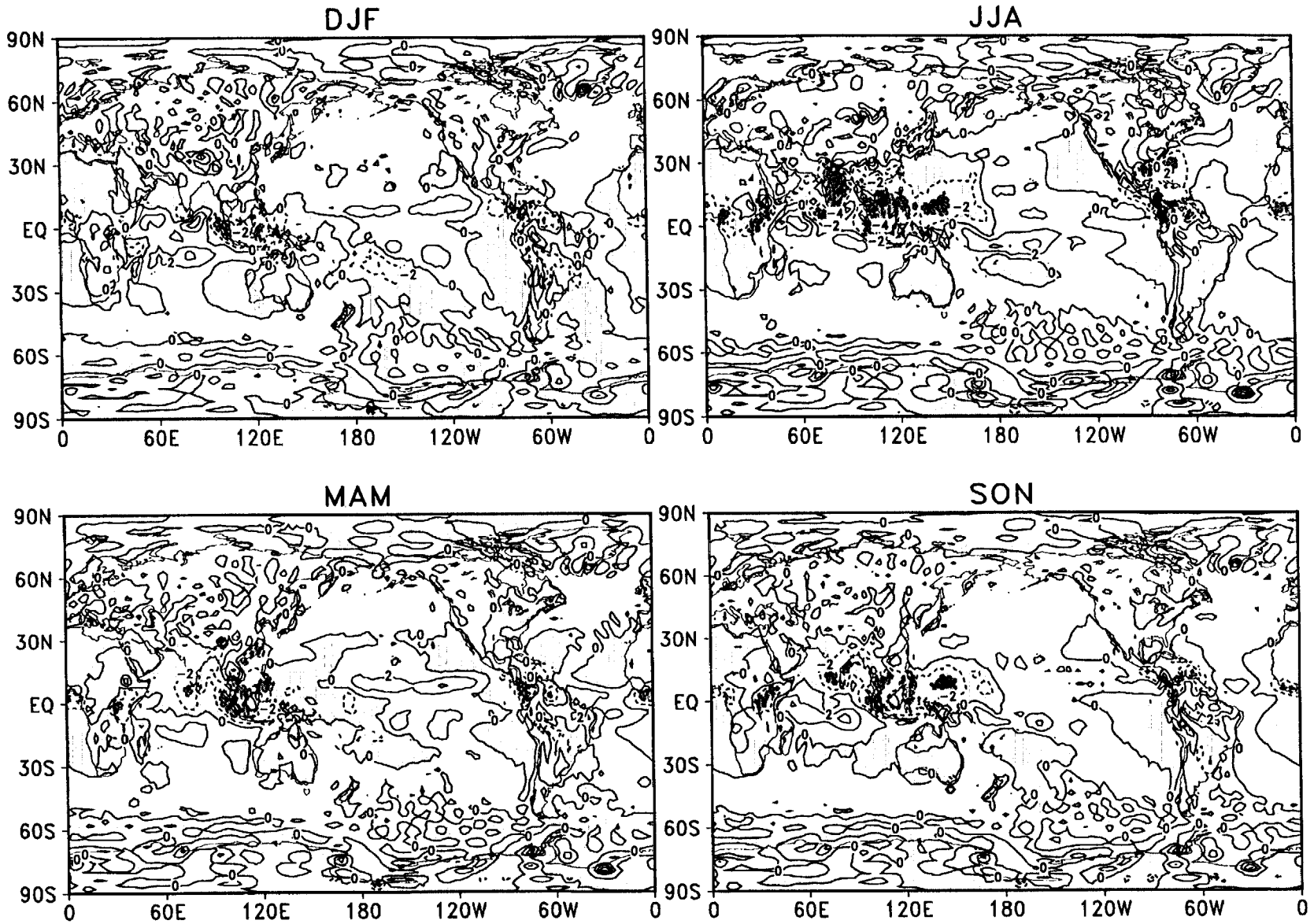

Figure 117: Difference of the seasonal means of precipitation during 1980–1995 (NCEP/NCAR minus DAO). The contour interval is 2 mm day^{-1}. Negative values are shaded.

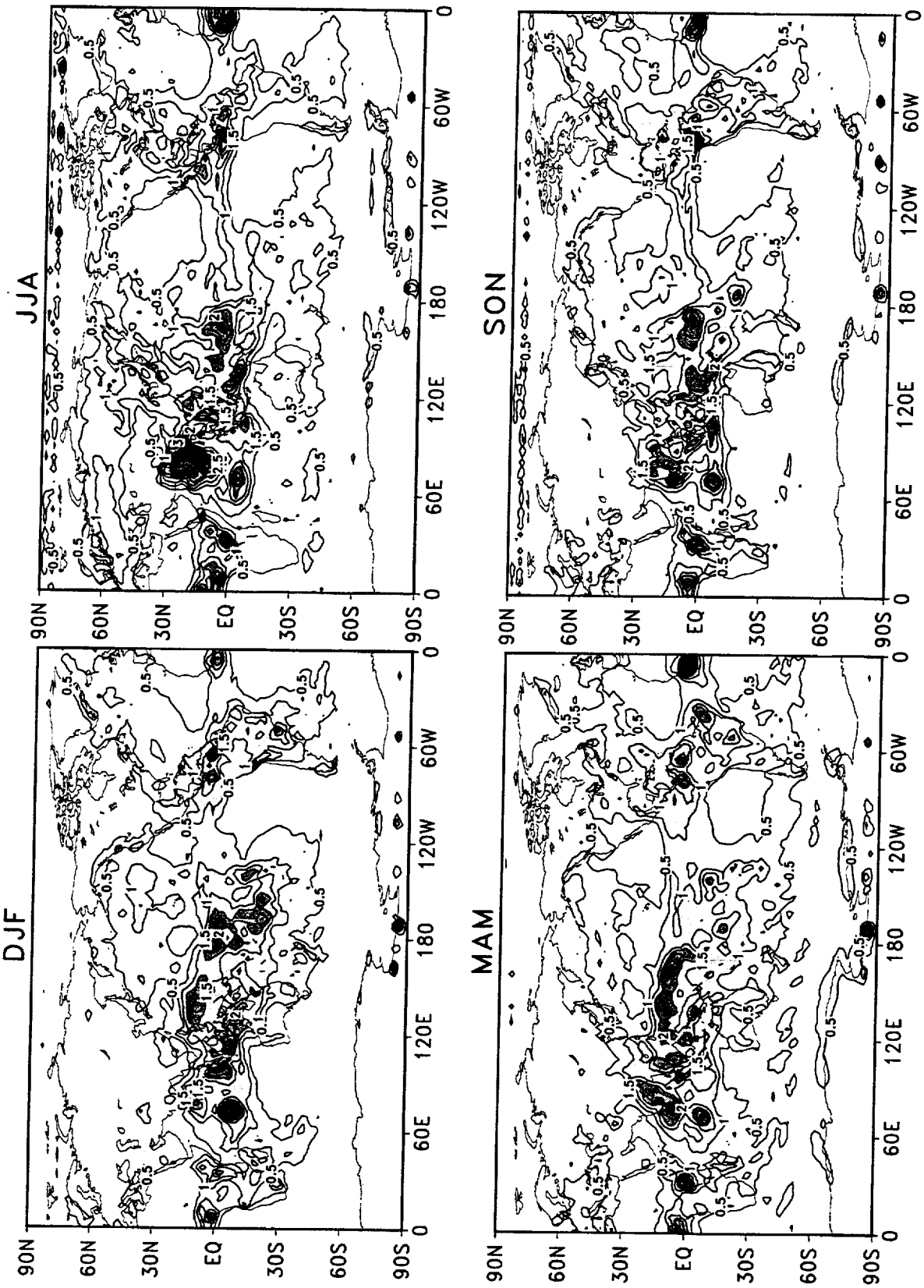

Figure 118: Standard deviations of seasonal mean precipitation for DAO reanalysis during 1980–1995. The contour interval is 0.5 mm day^{-1}. Values larger than 1 mm day^{-1} are shaded.

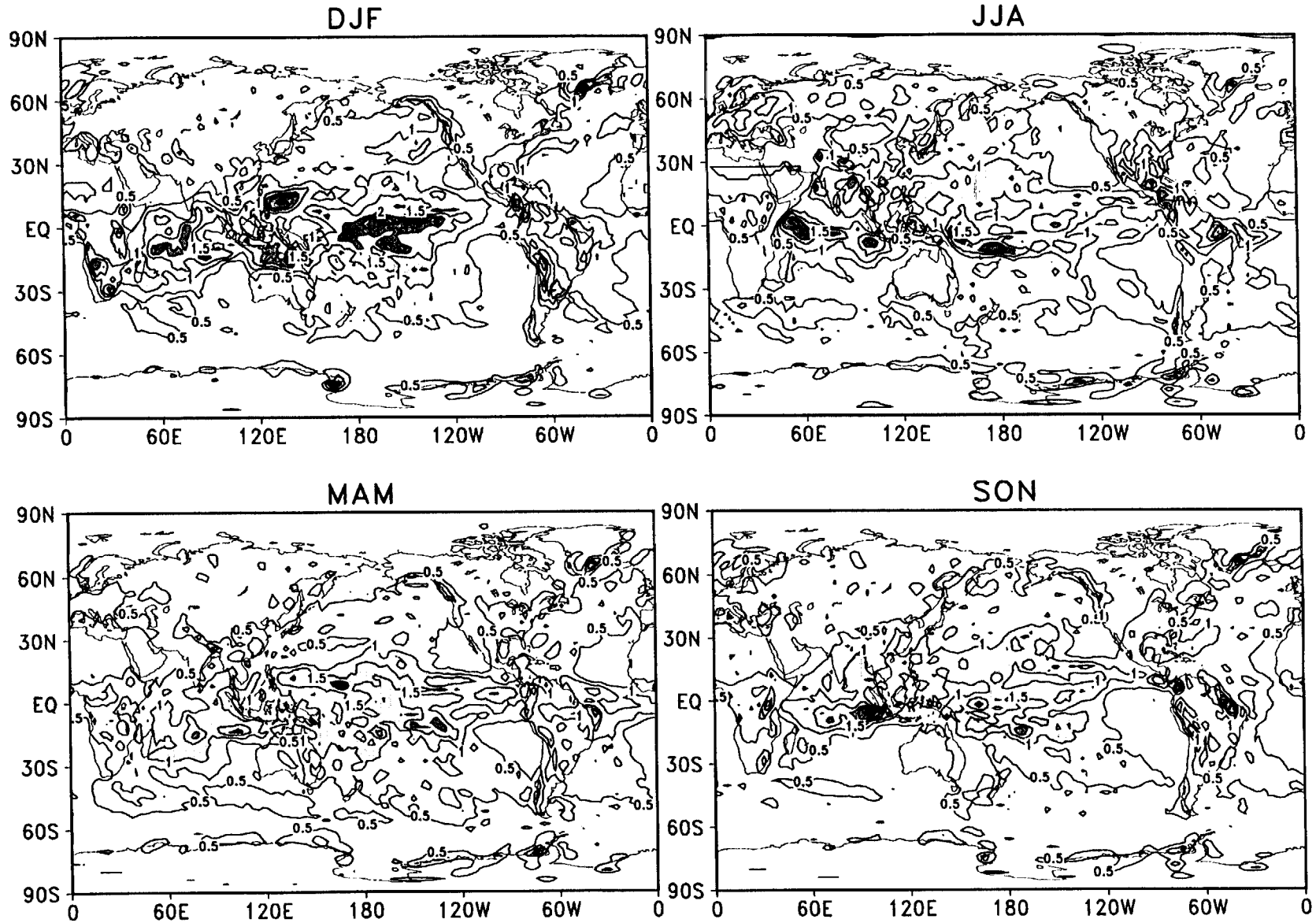

Figure 119: Standard deviations of seasonal mean precipitation for NCEP/NCAR reanalysis during 1980–1995. The contour interval is 0.5 mm day^{-1}. Values larger than 1 mm day^{-1} are shaded.

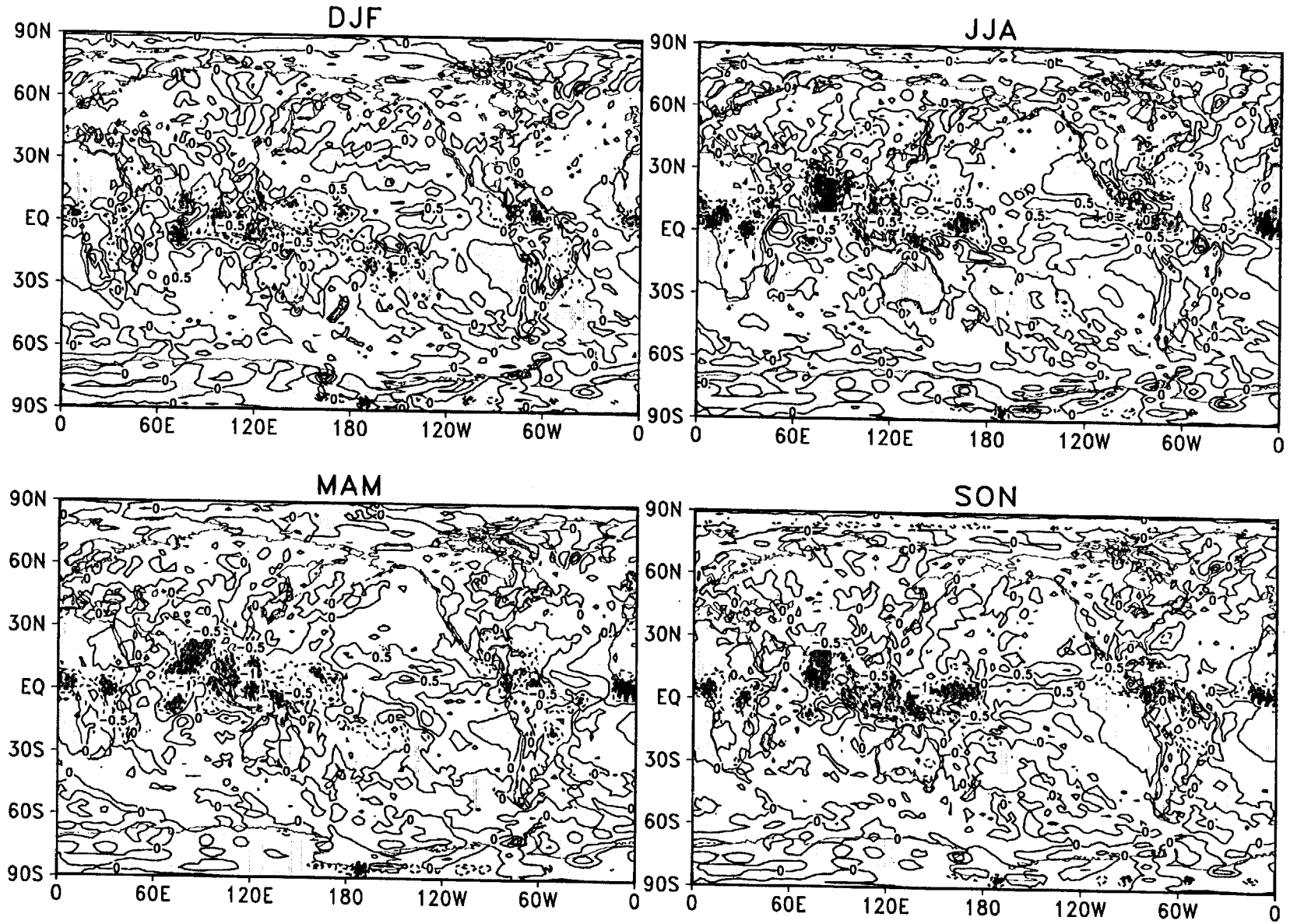

Figure 120: Difference of the standard deviations of seasonal mean precipitation during 1980–1995 (NCEP/NCAR minus DAO). The contour interval is 0.5 mm day^{-1}. Negative values are shaded.

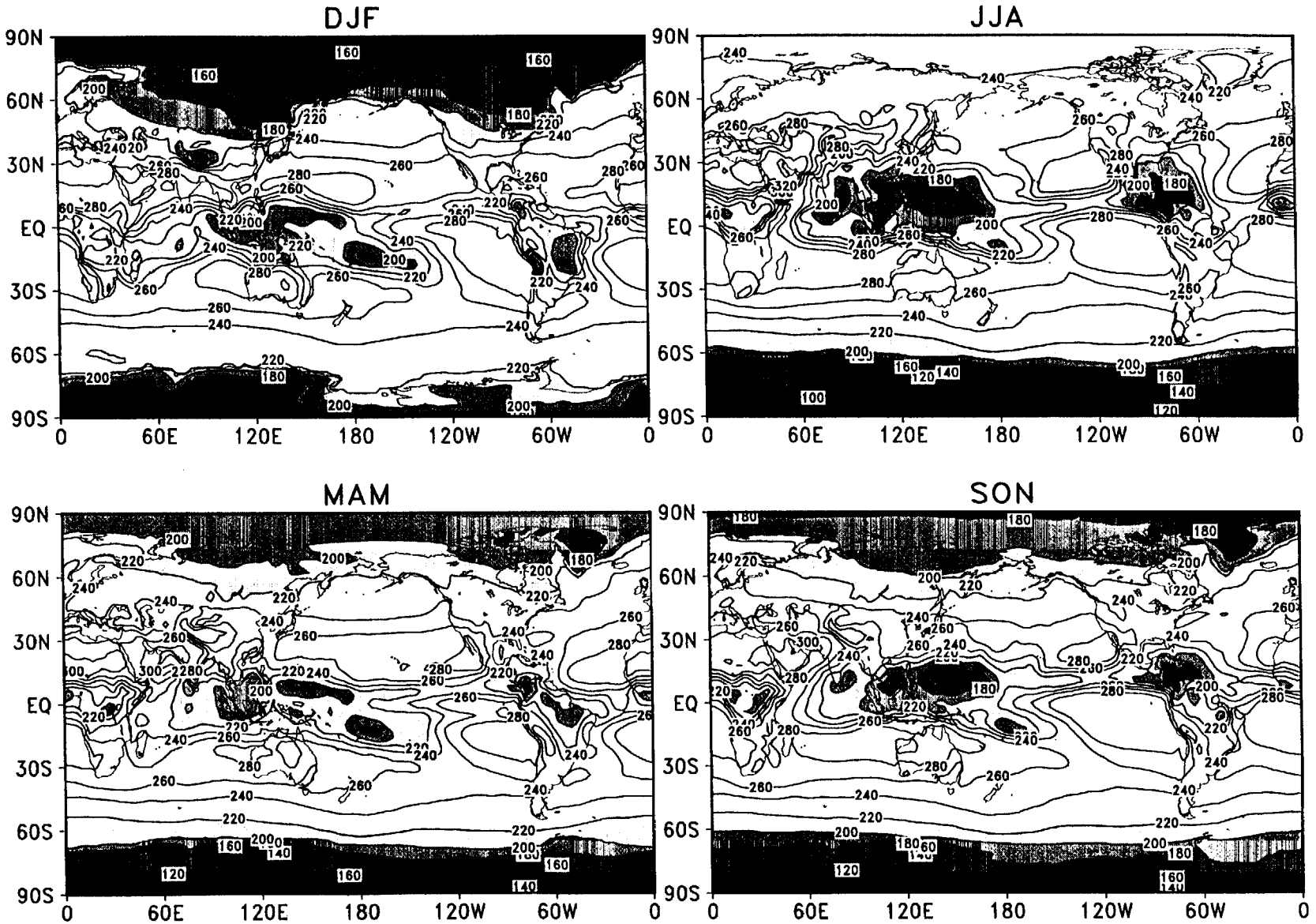

Figure 121: Seasonal means of outgoing longwave radiation for DAO reanalysis during 1980–1995. The contour interval is 20 W m^{-2}. Values less than 220 W m^{-2} are shaded.

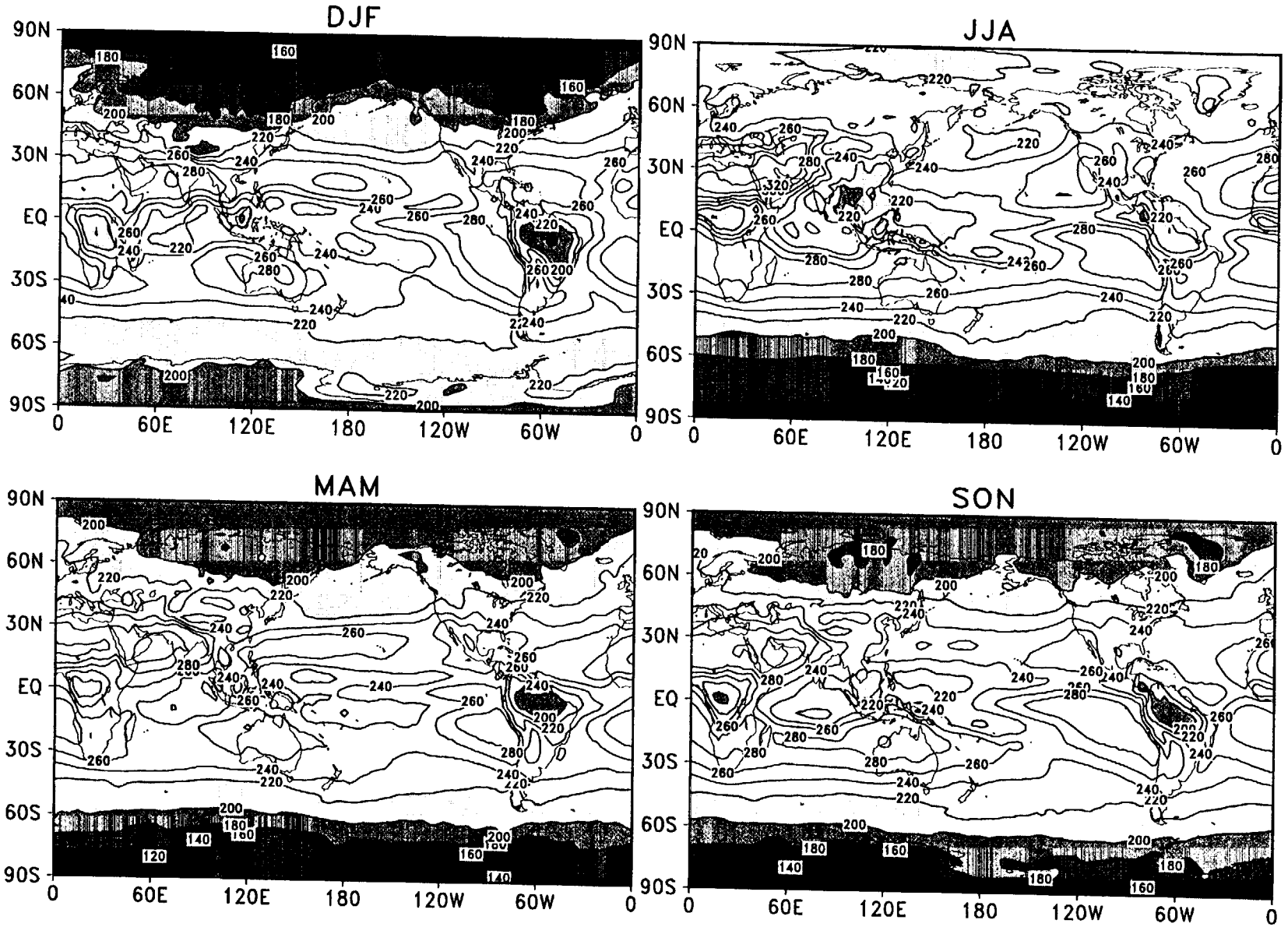

Figure 122: Seasonal means of outgoing longwave radiation for NCEP/NCAR reanalysis during 1980–1995. The contour interval is 20 W m^{-2}. Values less than 220 W m^{-2} are shaded.

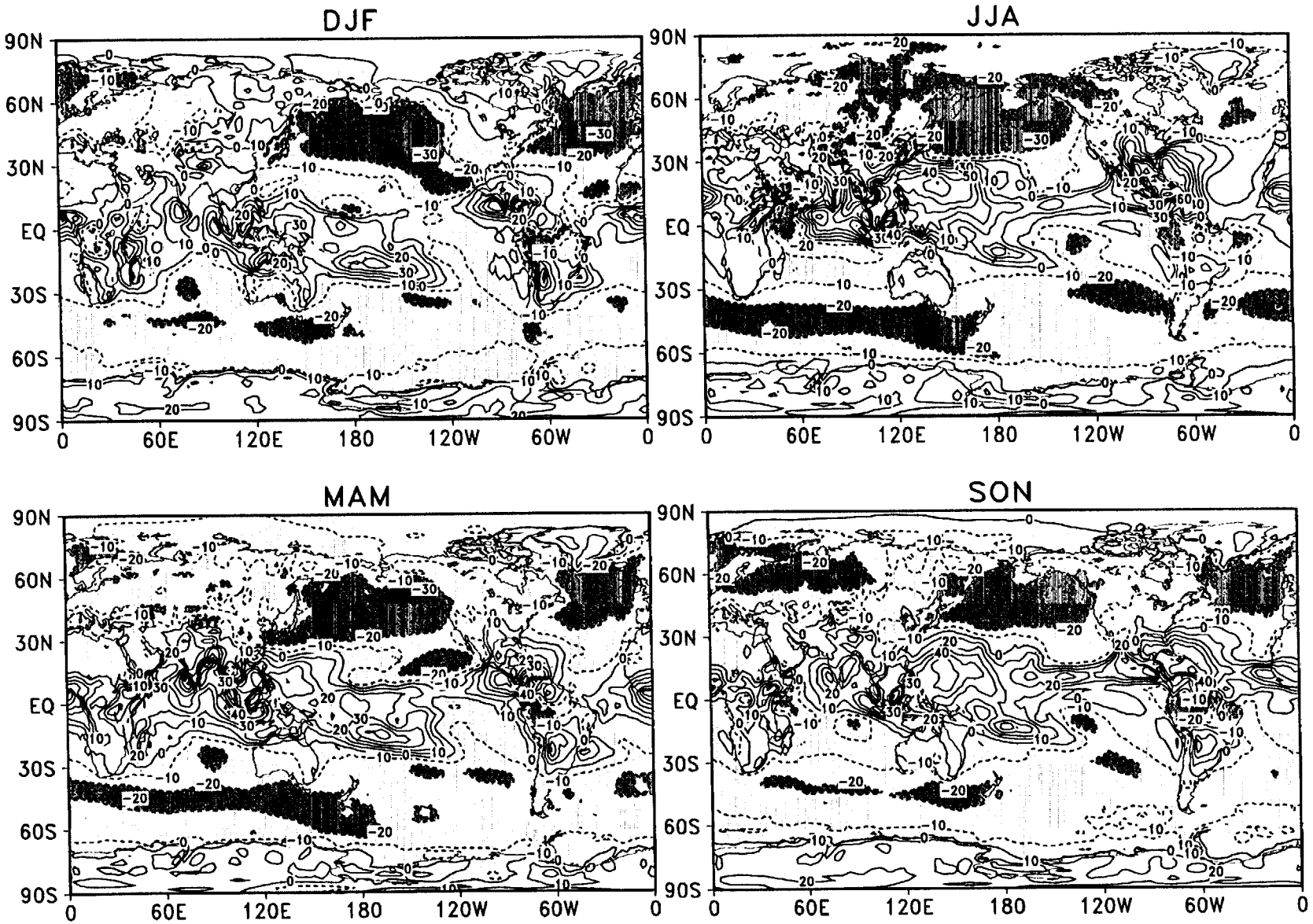

Figure 123: Difference of the seasonal means of outgoing longwave radiation during 1980–1995 (NCEP/NCAR minus DAO). The contour interval is 10 W m^{-2}. Negative values are shaded.

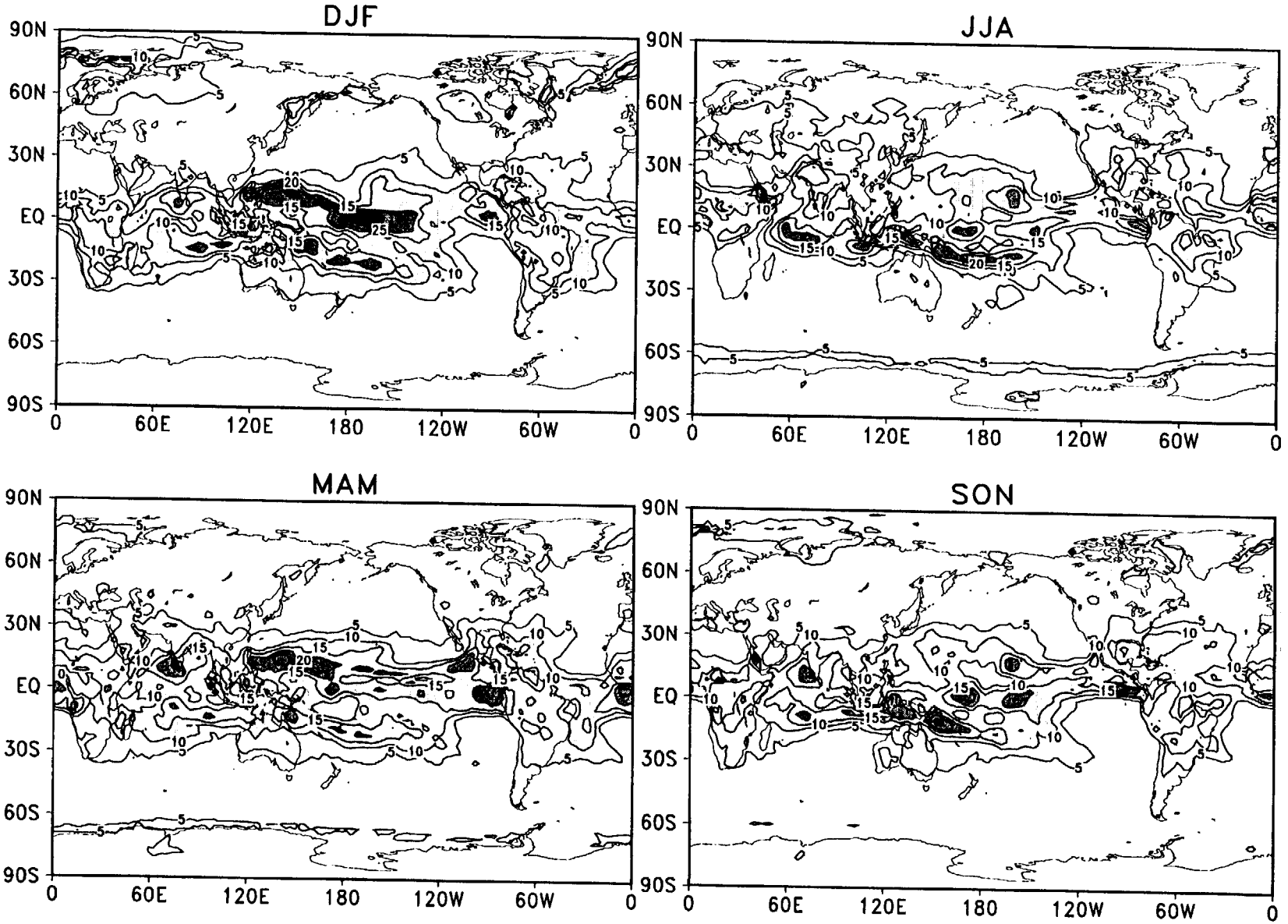

Figure 124: Standard deviations of seasonal mean outgoing longwave radiation for DAO reanalysis during 1980–1995. The contour interval is 5 W m^{-2}. Values larger than 10 W m^{-2} are shaded.

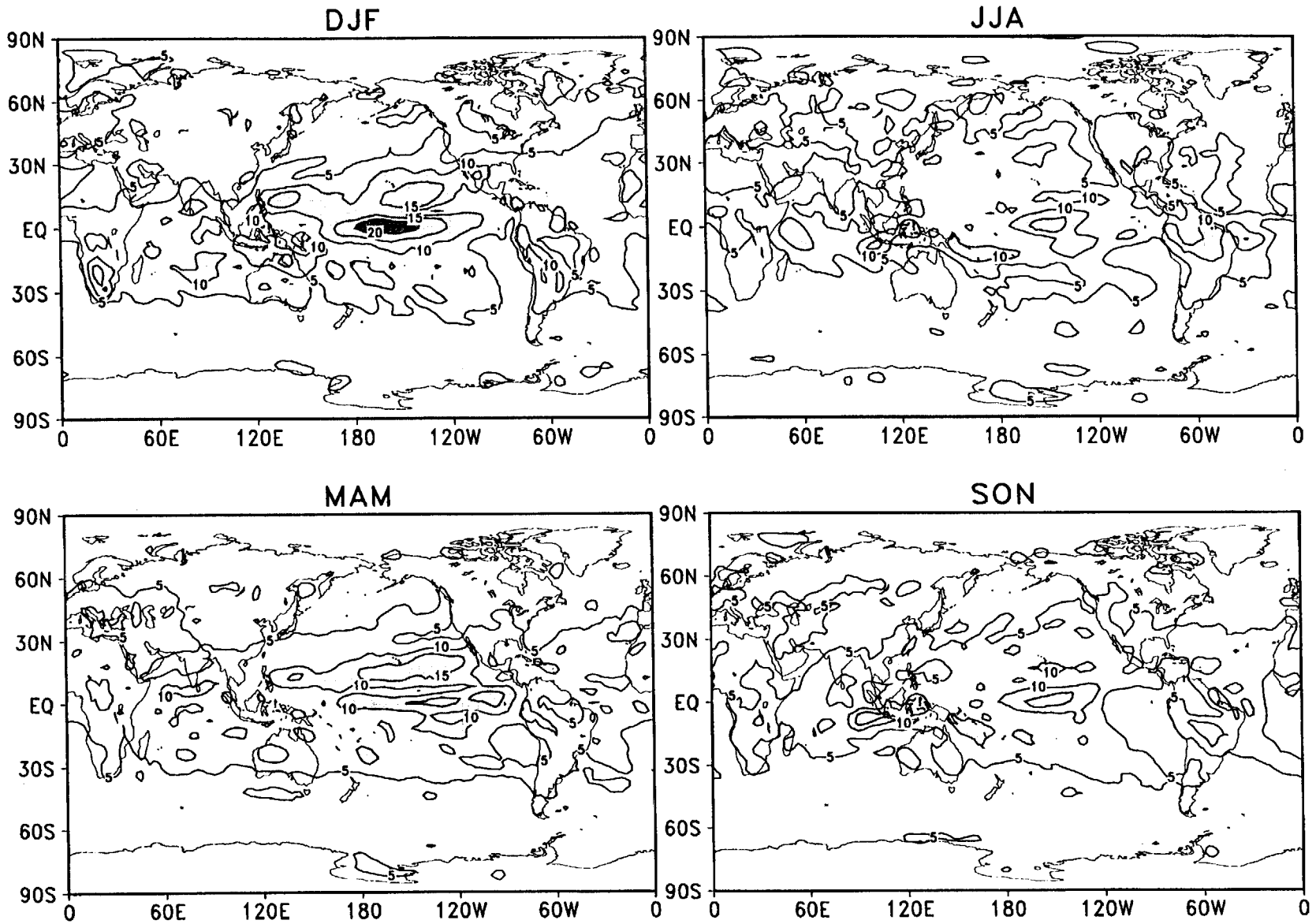

Figure 125: Standard deviations of seasonal mean outgoing longwave radiation for NCEP/NCAR reanalysis during 1980–1995. The contour interval is 5 W m^{-2}. Values larger than 10 W m^{-2} are shaded.

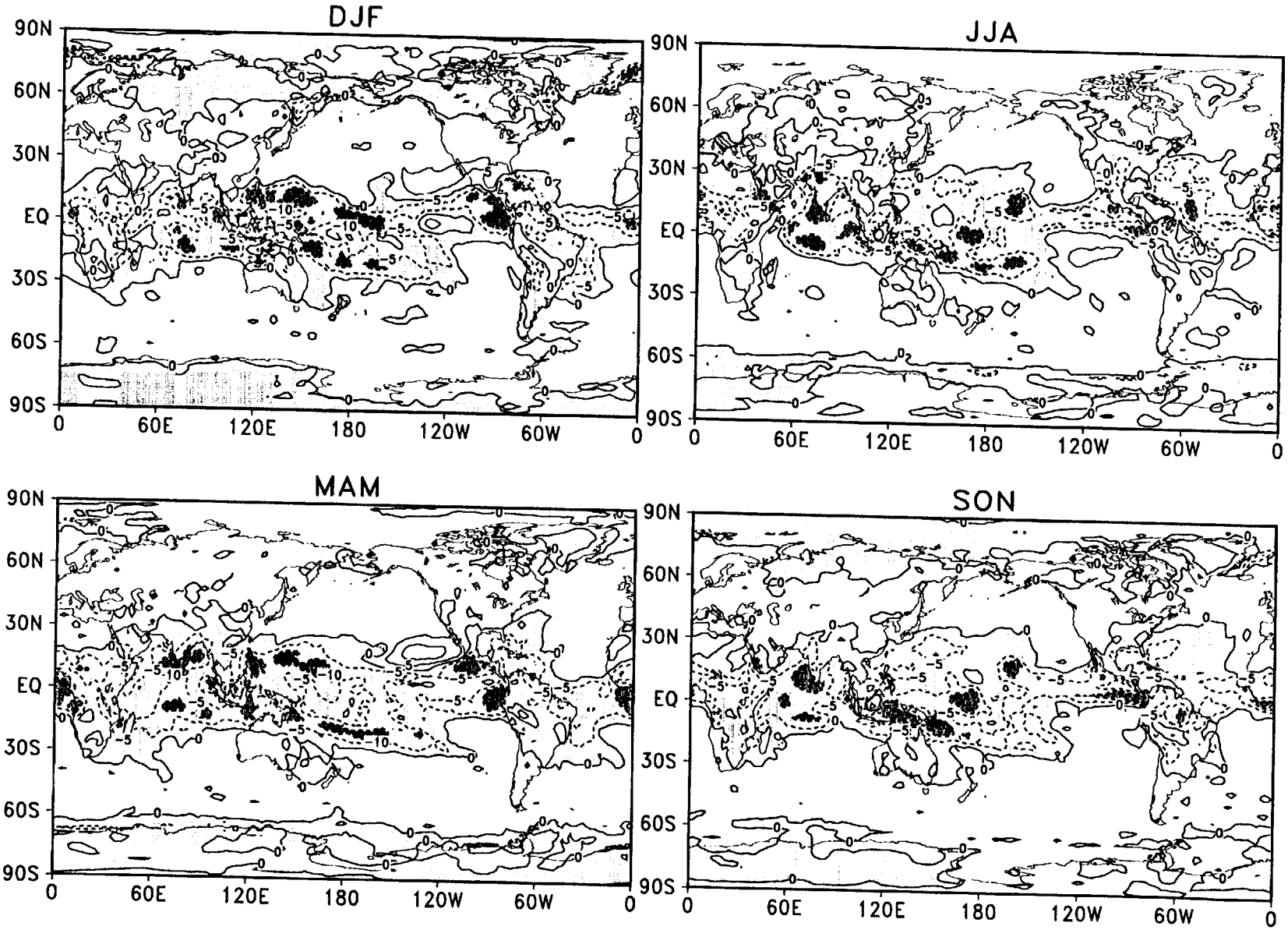

Figure 126: Difference of the standard deviations of seasonal mean outgoing longwave radiation during 1980–1995 (NCEP/NCAR minus DAO). The contour interval is 5 W m^{-2}. Negative values are shaded.

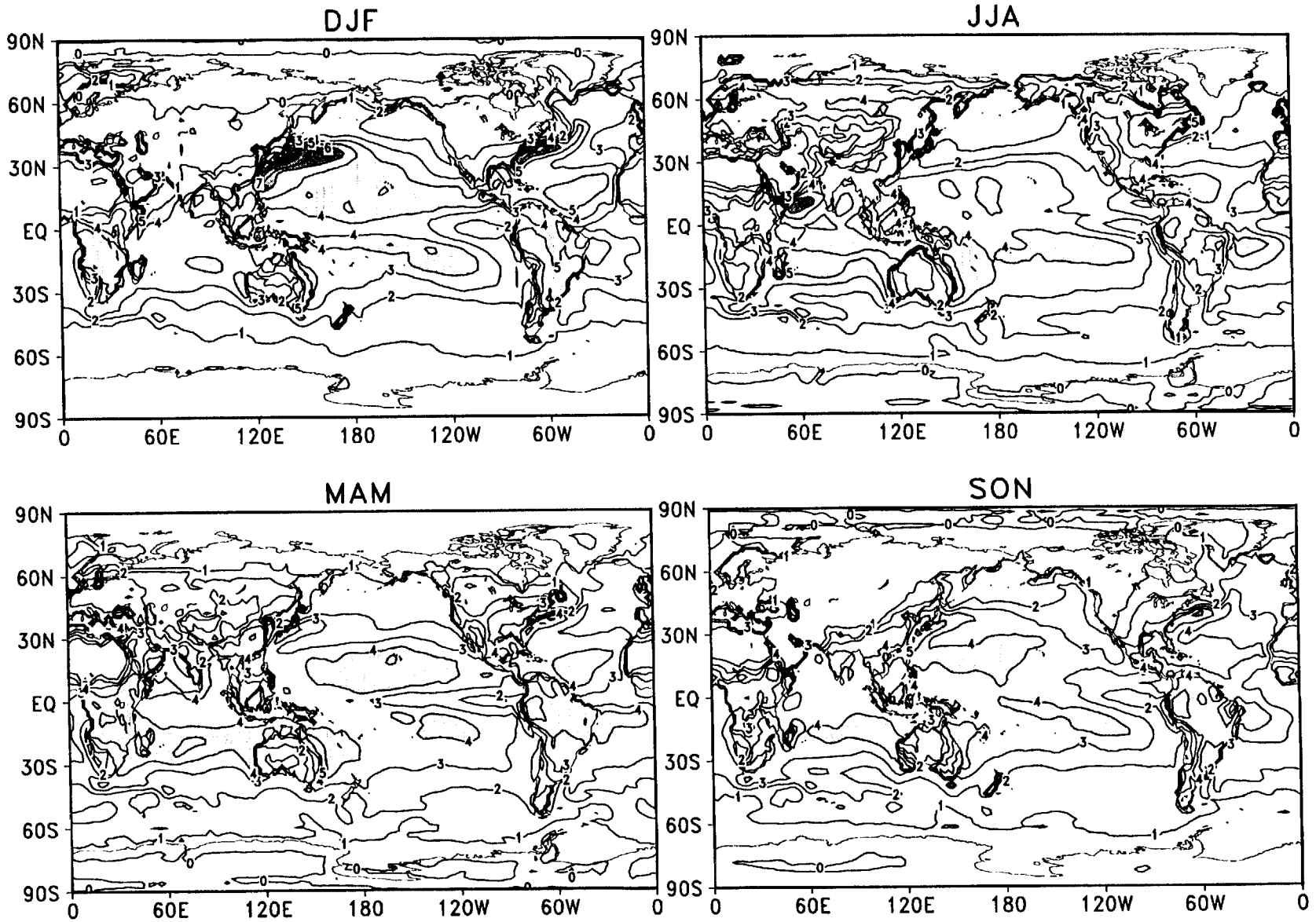

Figure 127: Seasonal means of evaporation for DAO reanalysis during 1980–1995. The contour interval is 1 mm day^{-1}. Values larger than 4 mm day^{-1} are shaded.

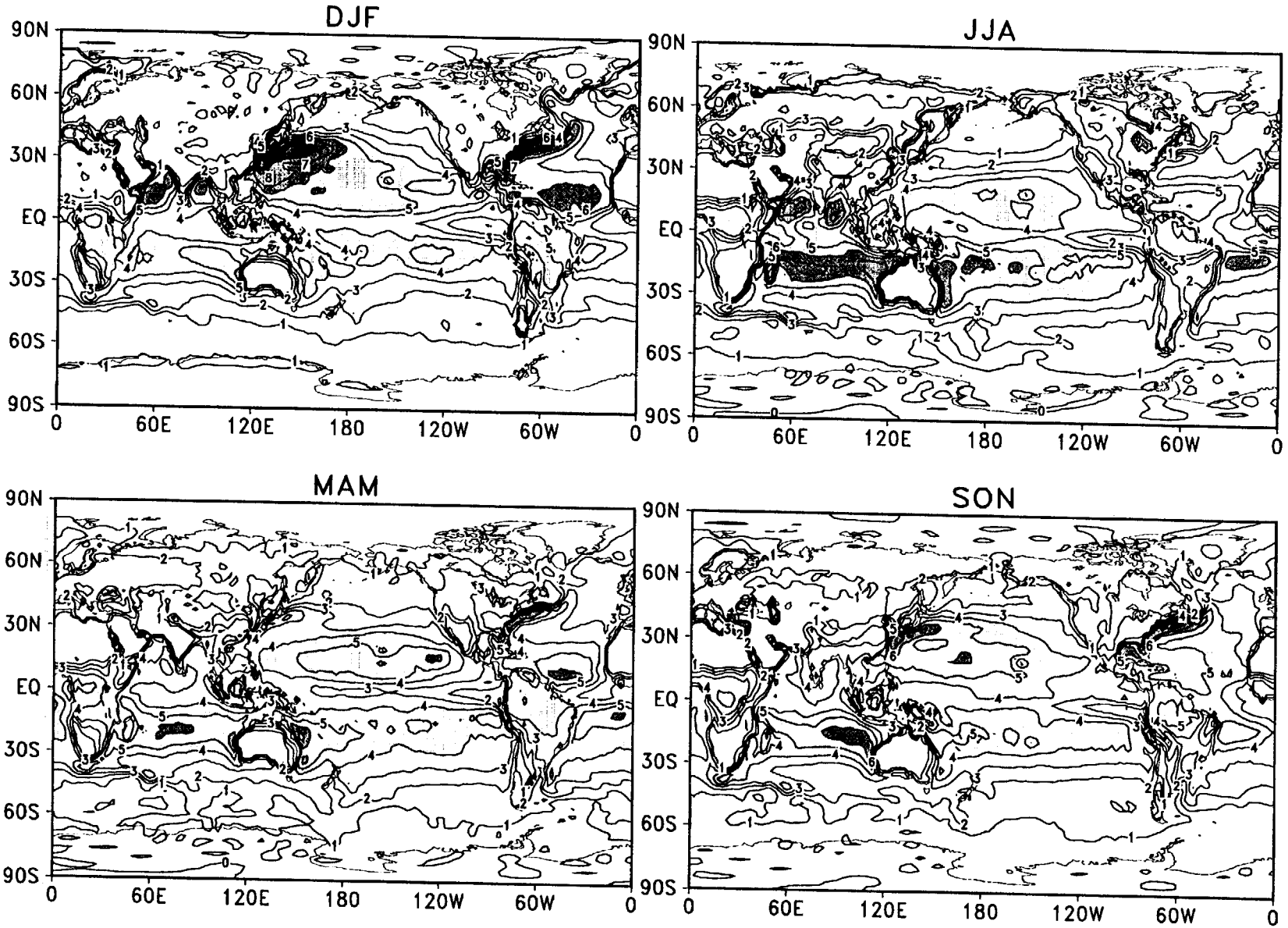

Figure 128: Seasonal means of evaporation for NCEP/NCAR reanalysis during 1980–1995. The contour interval is 1 mm day^{-1}. Values larger than 4 mm day^{-1} are shaded.

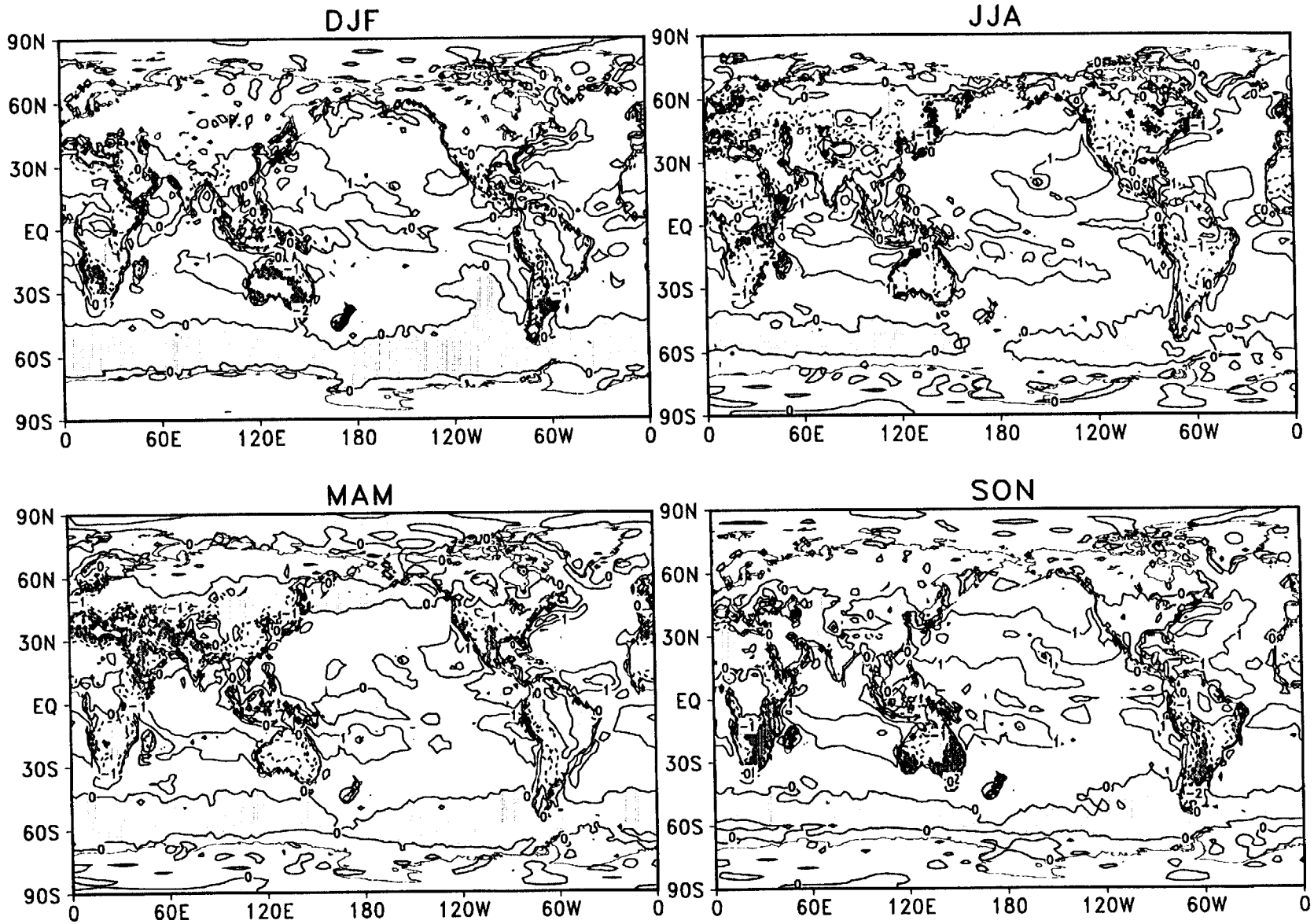

Figure 129: Difference of the seasonal means of evaporation during 1980–1995 (NCEP/NCAR minus DAO). The contour interval is 1 mm day^{-1}. Negative values are shaded.

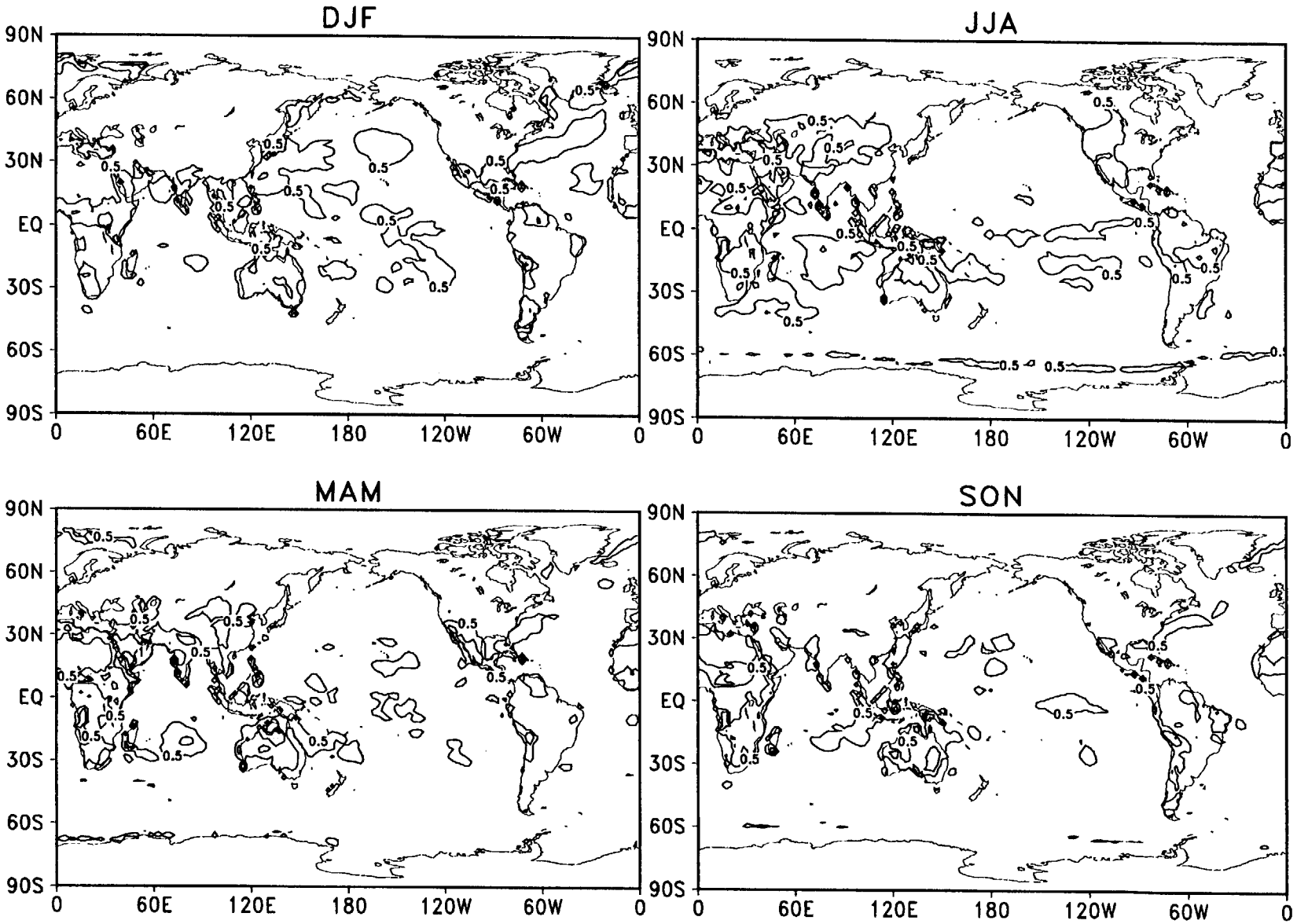

Figure 130: Standard deviations of seasonal mean evaporation for DAO reanalysis during 1980–1995. The contour interval is 0.5 mm day^{-1}. Values larger than 1 mm day^{-1} are shaded.

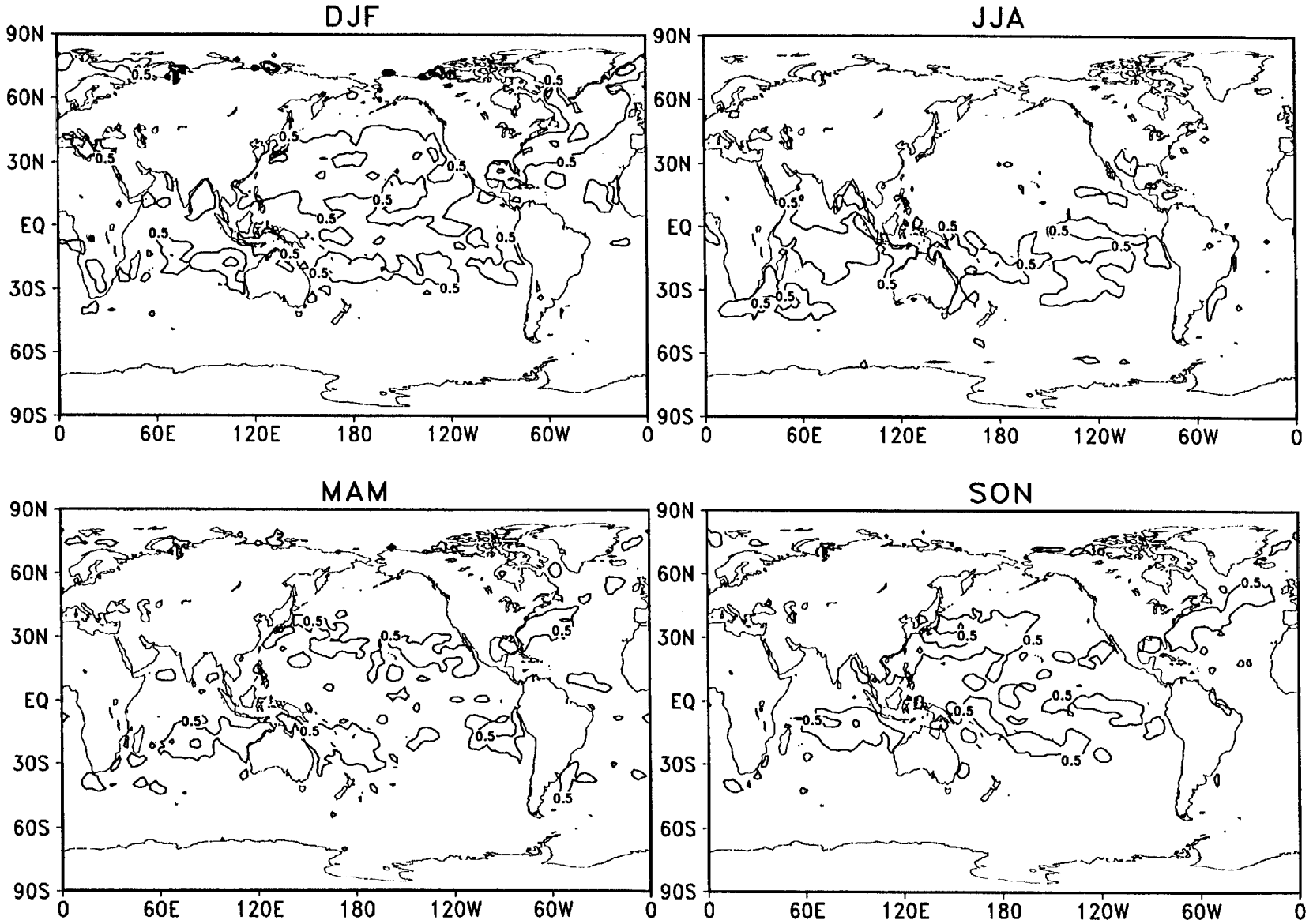

Figure 131: Standard deviations of seasonal mean evaporation for NCEP/NCAR reanalysis during 1980–1995. The contour interval is 0.5 mm day^{-1}. Values larger than 1 mm day^{-1} are shaded.

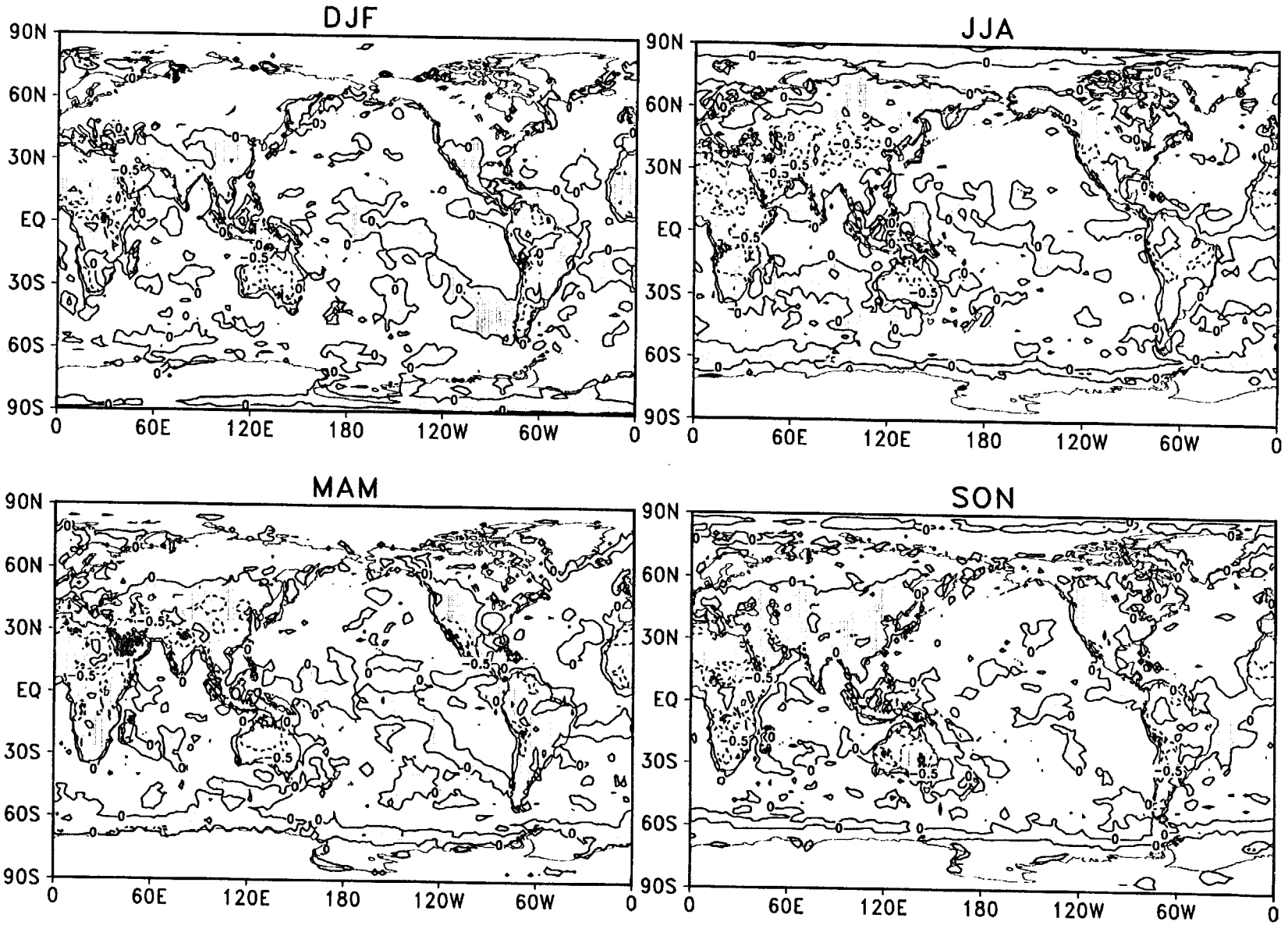

Figure 132: Difference of the standard deviations of seasonal mean evaporation during 1980–1995 (NCEP/NCAR minus DAO). The contour interval is 0.5 mm day^{-1}. Negative values are shaded.

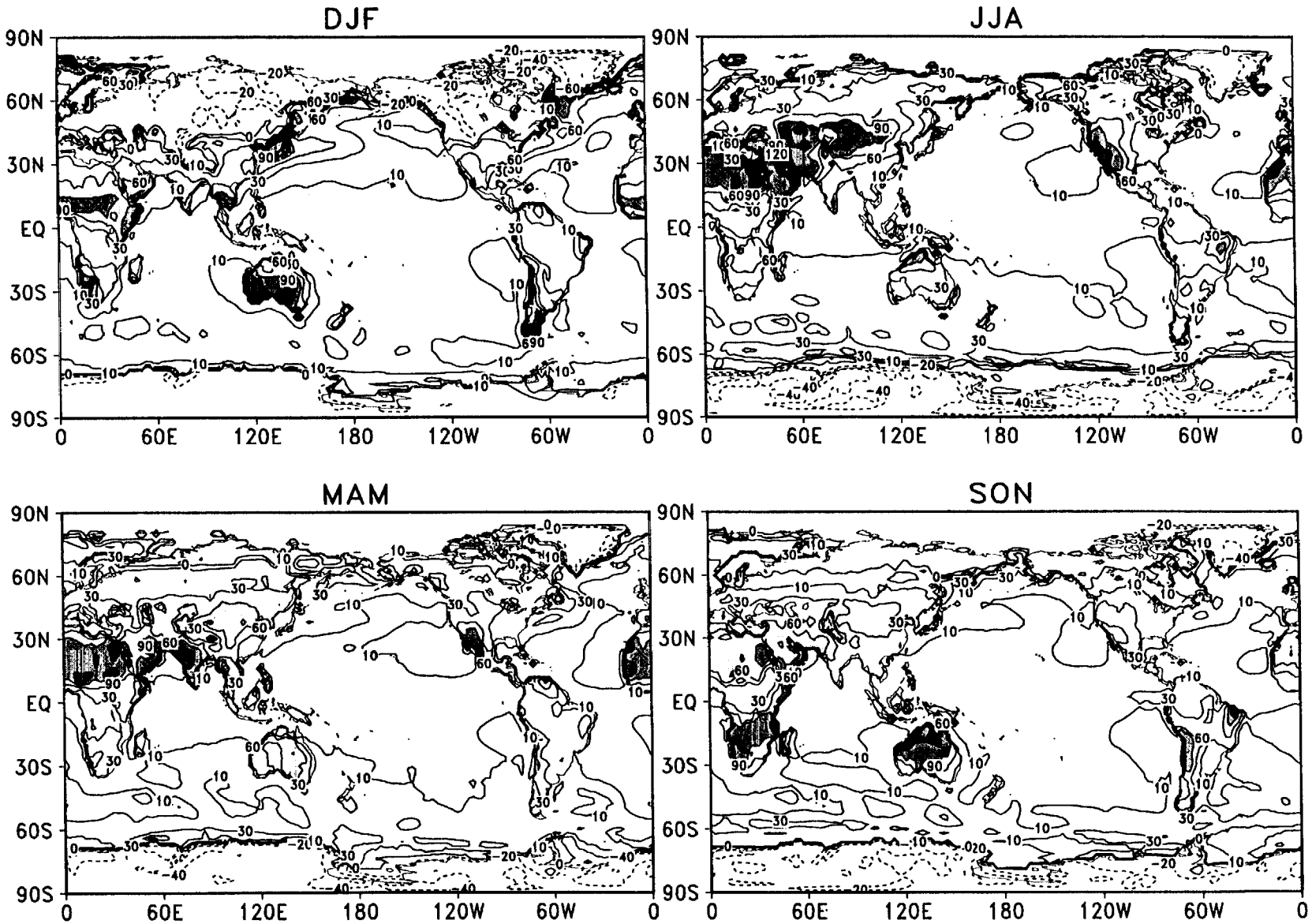

Figure 133: Seasonal means of sensible heat flux for DAO reanalysis during 1980–1995. The contour intervals are -60, -40, -20, 0, 10, 30, 60, 90, 120, 150 W m^{-2}. Values larger than 60 W m^{-2} are shaded.

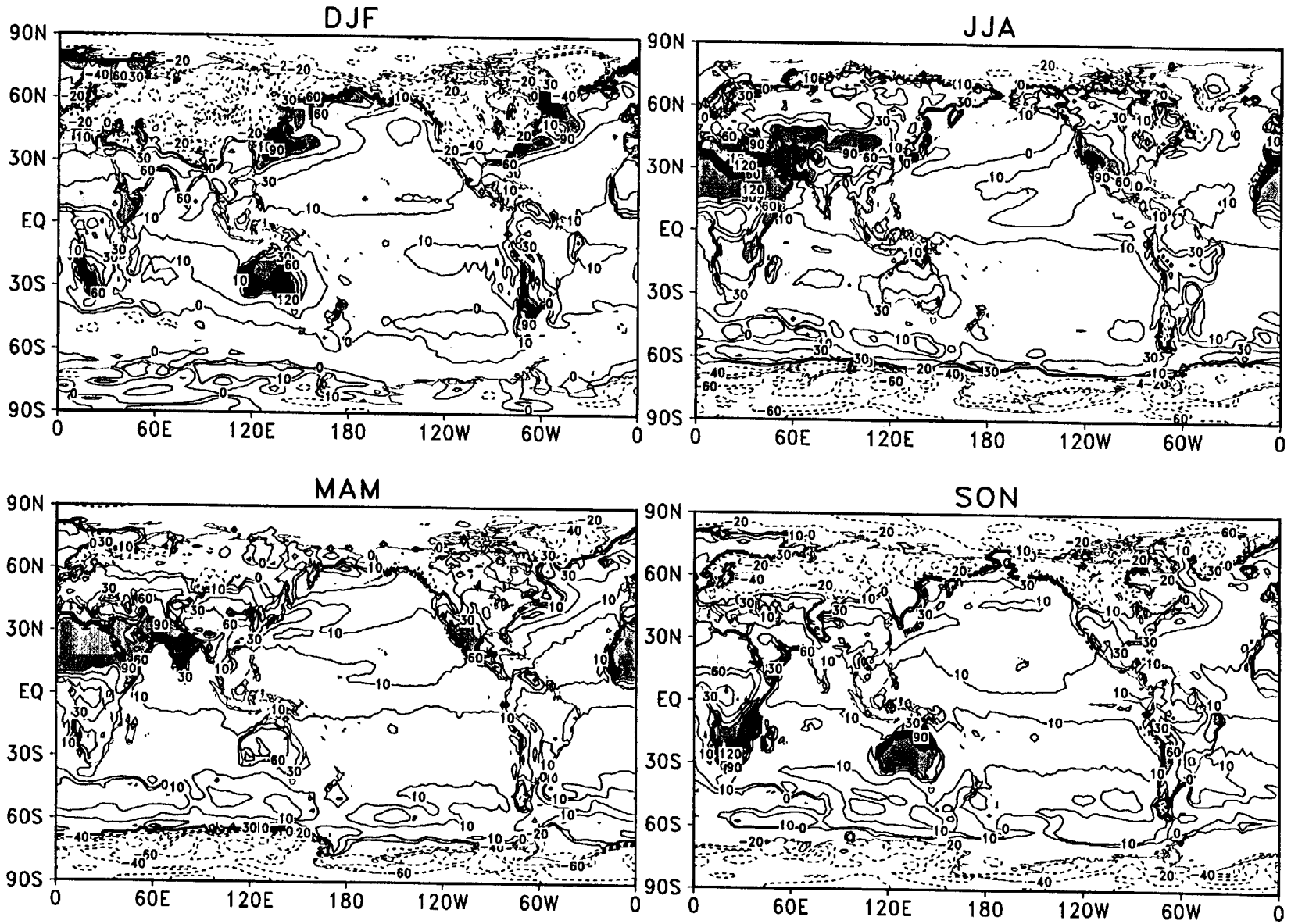

Figure 134: Seasonal means of sensible heat flux for NCEP/NCAR reanalysis during 1980–1995. The contour intervals are -60, -40, -20, 0, 10, 30, 60, 90, 120, 150 W m^{-2}. Values larger than 60 W m^{-2} are shaded.

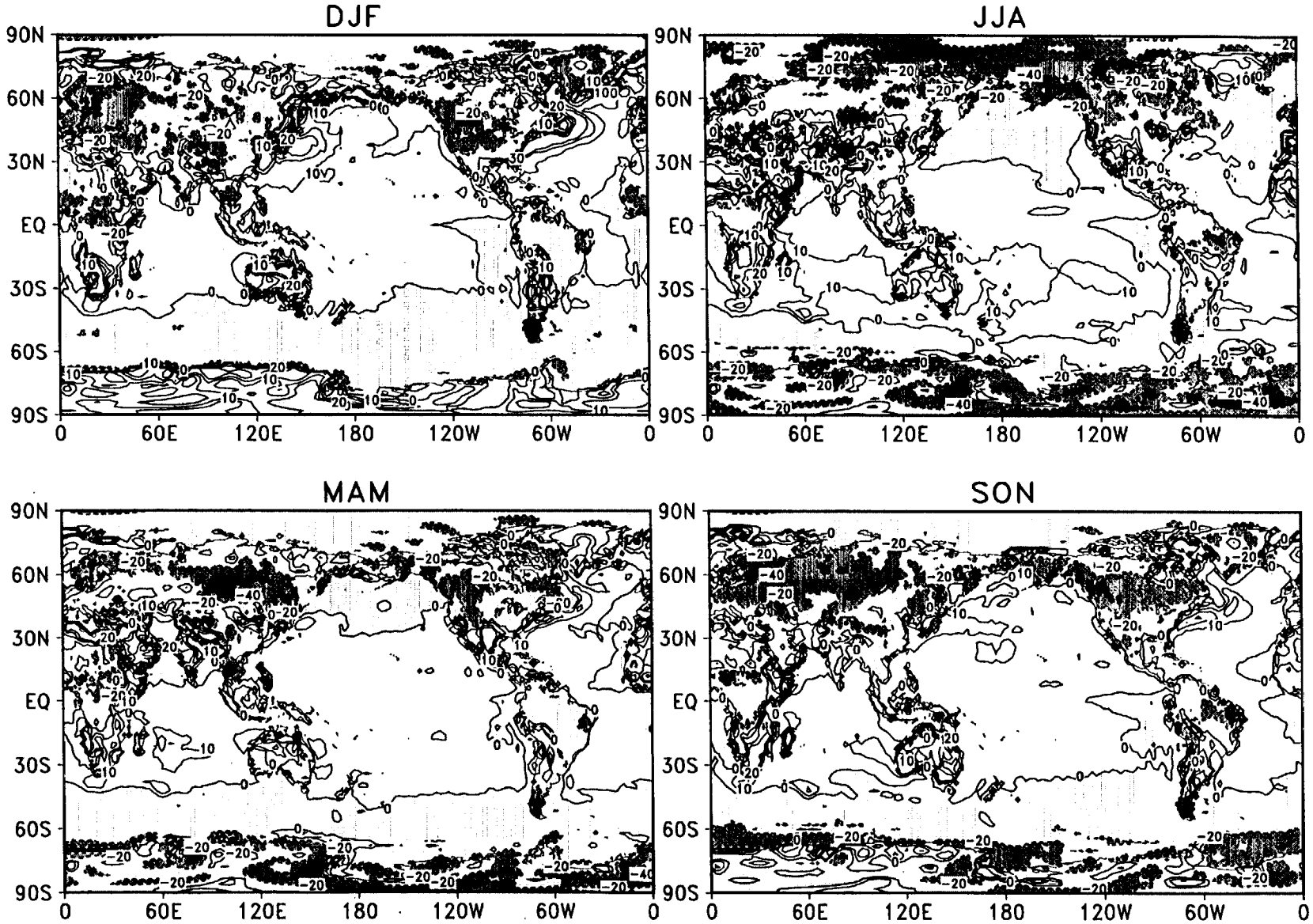

Figure 135: Difference of the seasonal means of sensible heat flux during 1980–1995 (NCEP/NCAR minus DAO). The contour intervals are -60, -40, -20, 0, 10, 20, 30 W m^{-2}. Negative values are shaded.

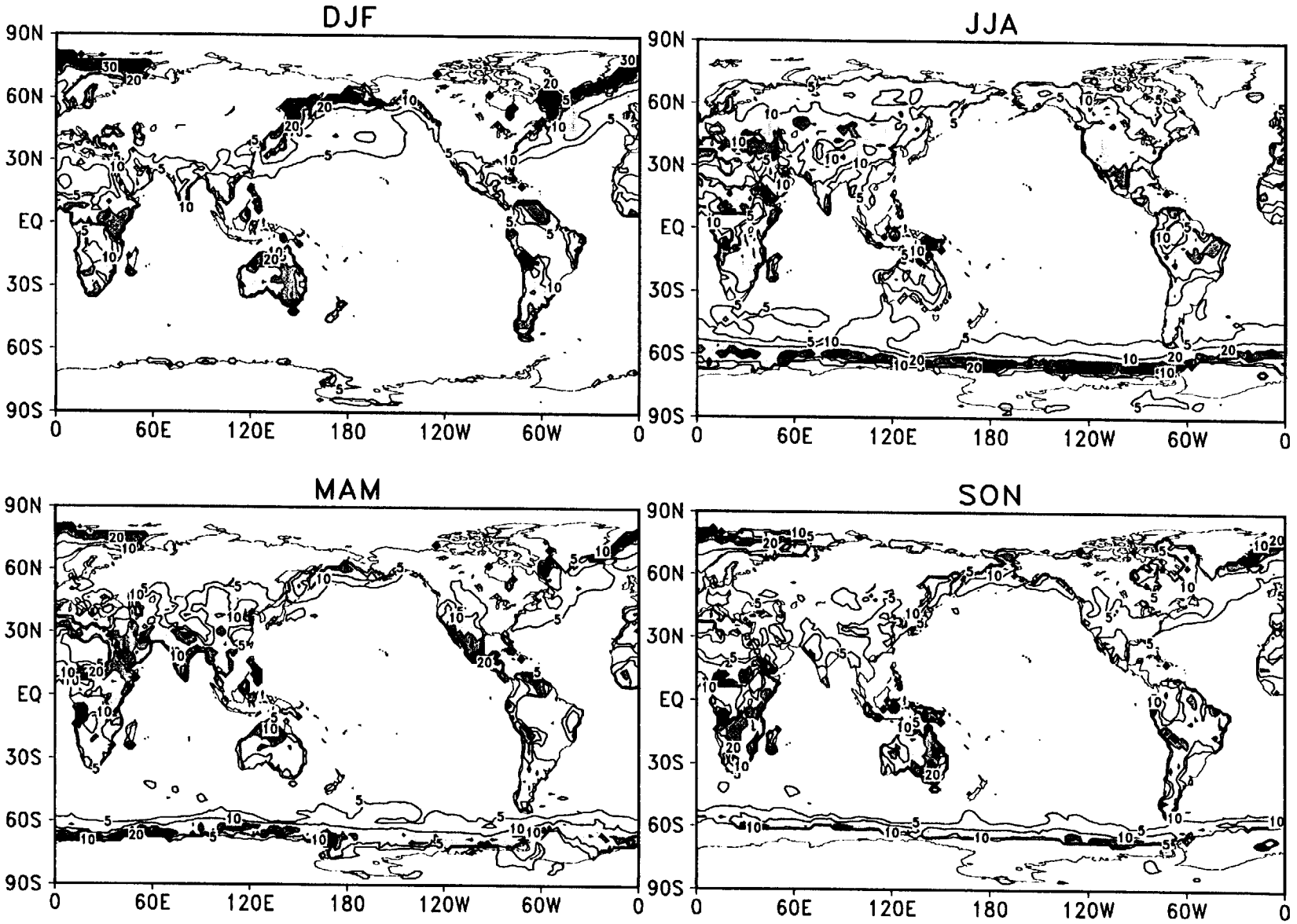

Figure 136: Standard deviations of seasonal mean sensible heat flux for DAO reanalysis during 1980–1995. The contour intervals are 5, 10, 20, 30, 40, 50, 60 W m^{-2}. Values larger than 10 W m^{-2} are shaded.

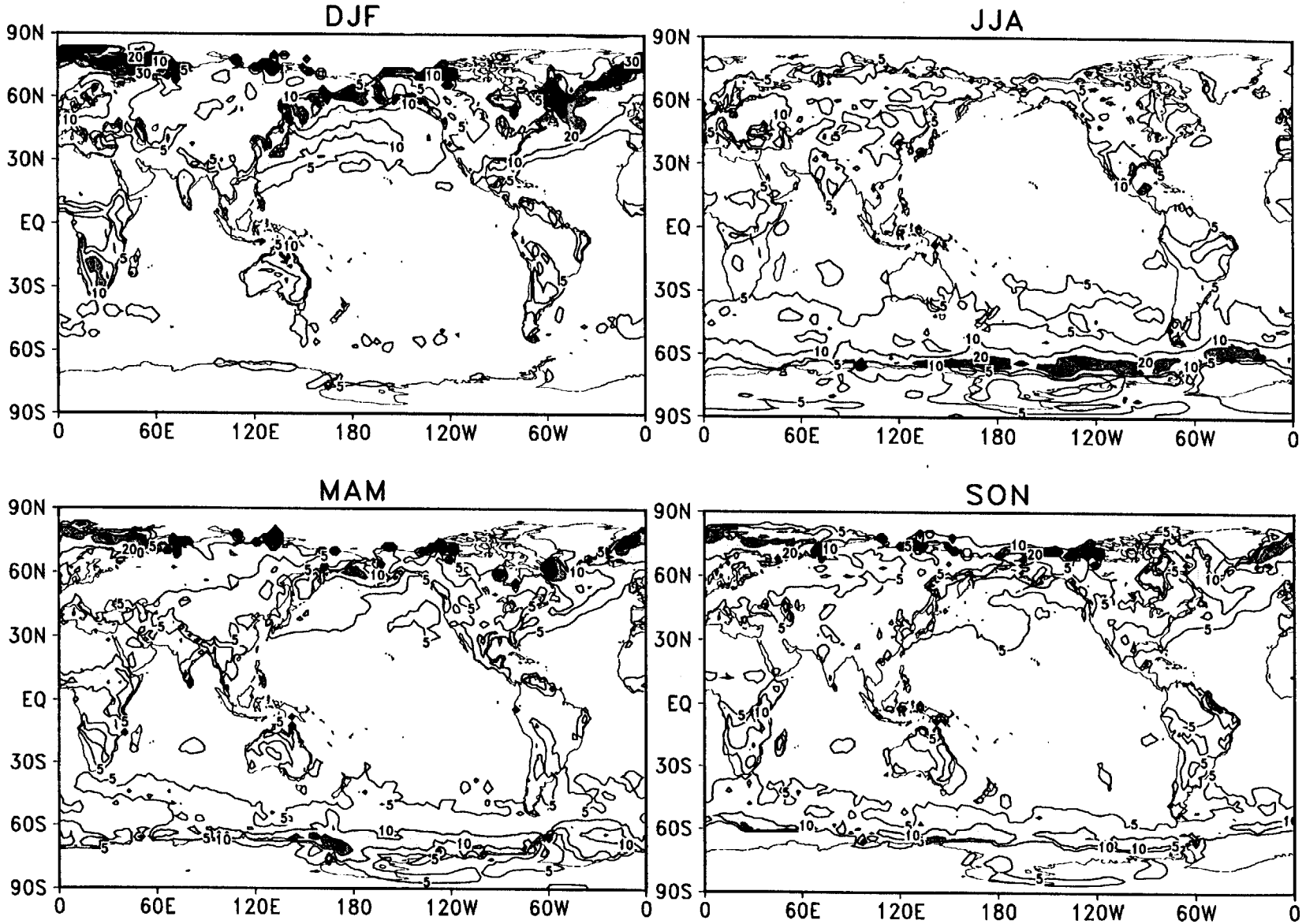

Figure 137: Standard deviations of seasonal mean sensible heat flux for NCEP/NCAR reanalysis during 1980–1995. The contour intervals are 5, 10, 20, 30, 40, 50, 60 W m^{-2}. Values larger than 10 W m^{-2} are shaded.

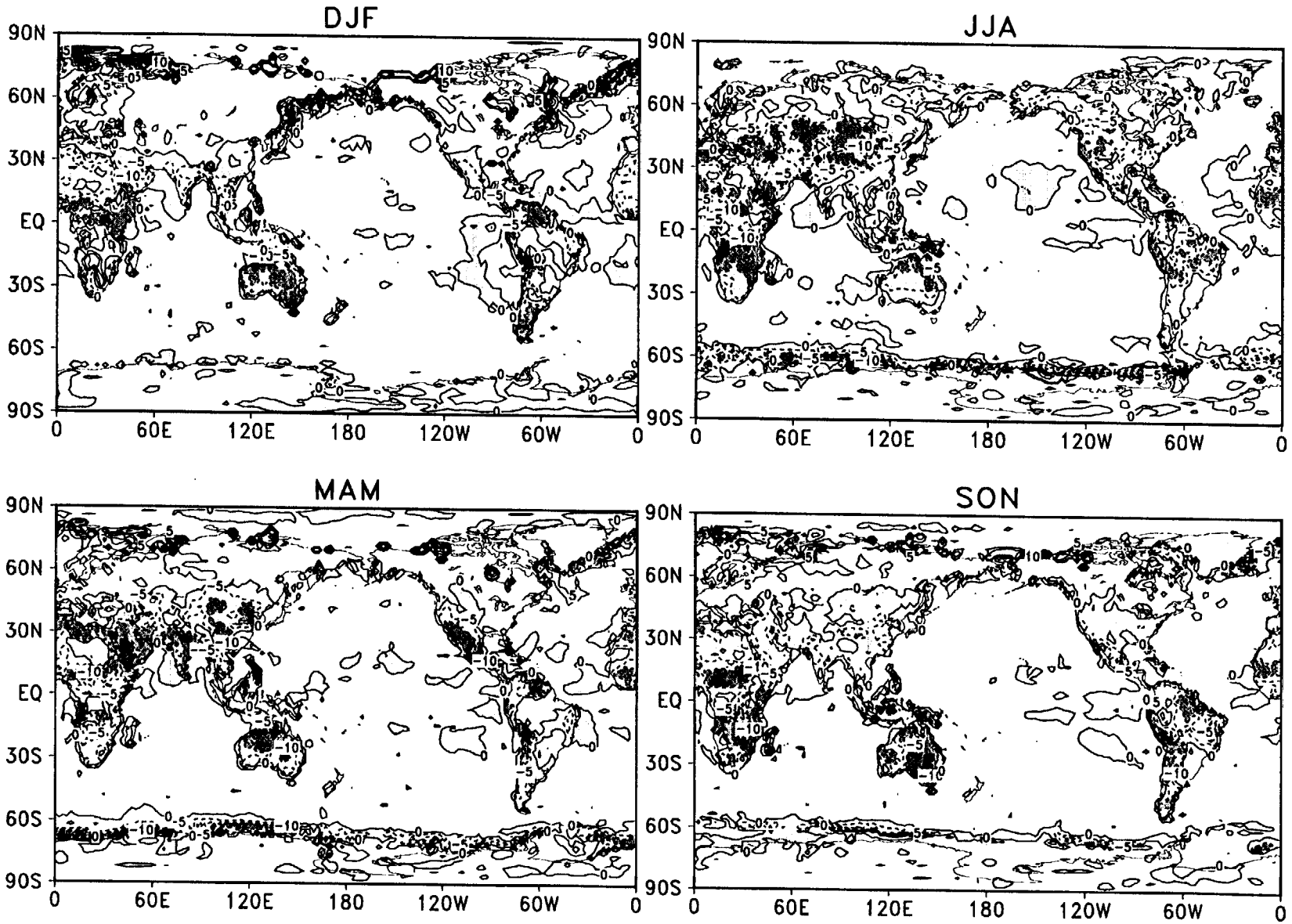

Figure 138: Difference of the standard deviations of seasonal mean sensible heat flux during 1980–1995 (NCEP/NCAR minus DAO). The contour intervals are -40, -30, -10, -5, 0, 5, 10 W m^{-2}. Negative values are shaded.

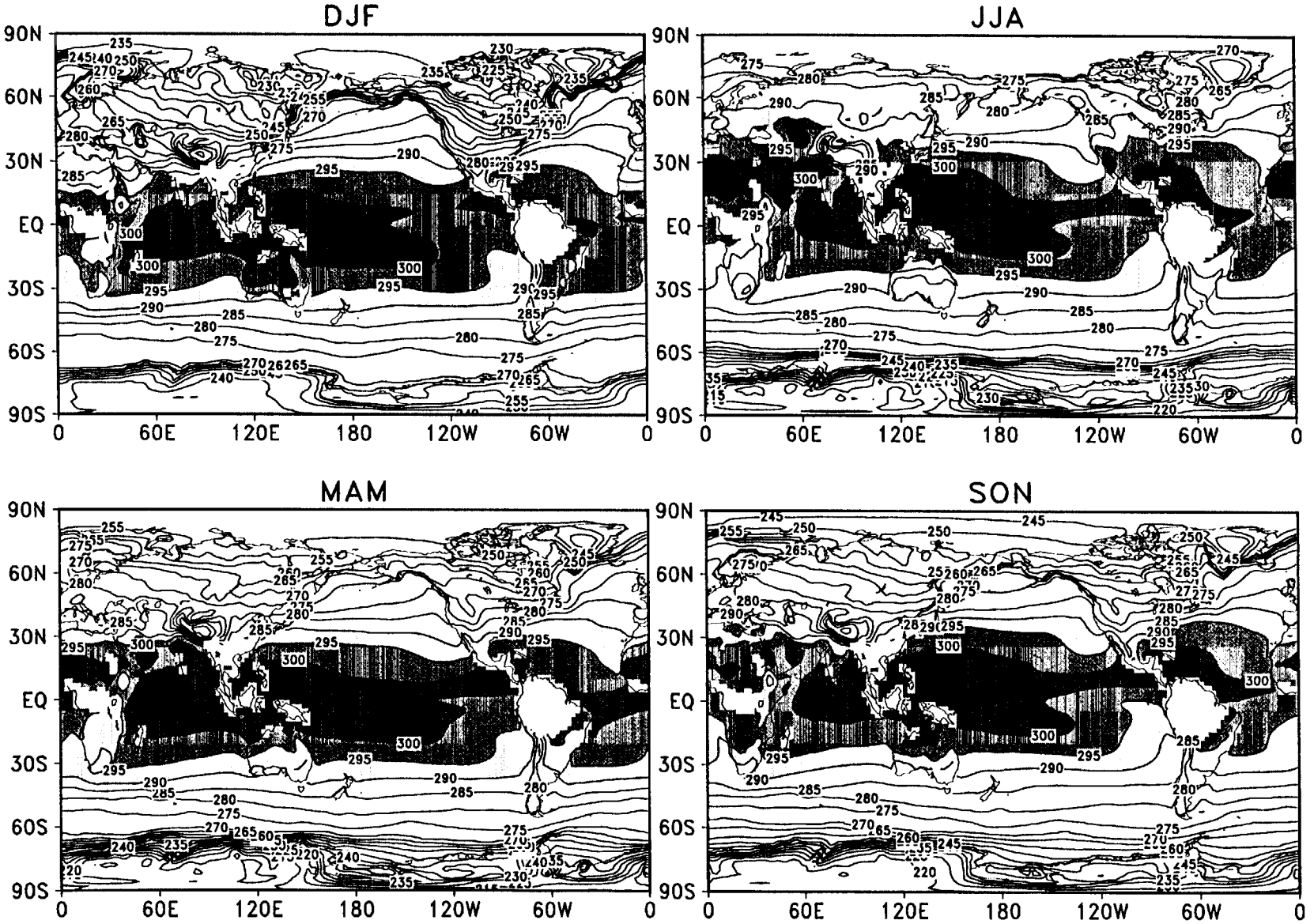

Figure 139: Seasonal means of temperature at 2 meters for DAO reanalysis during 1980–1995. The contour interval is 5°K. Values larger than 290°K are shaded.

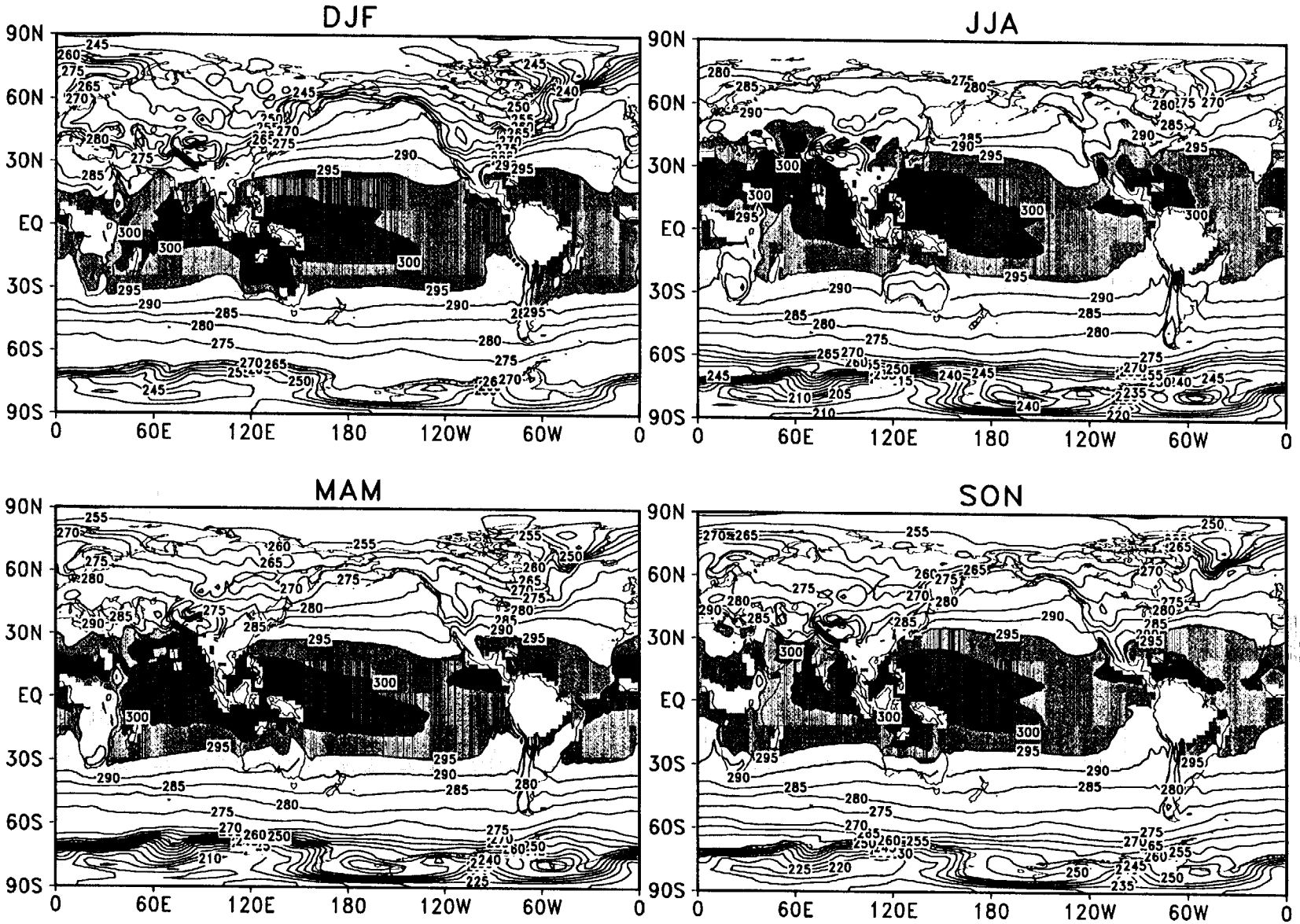

Figure 140: Seasonal means of temperature at 2 meters for NCEP/NCAR reanalysis during 1980–1995. The contour interval is 5°K. Values larger than 290°K are shaded.

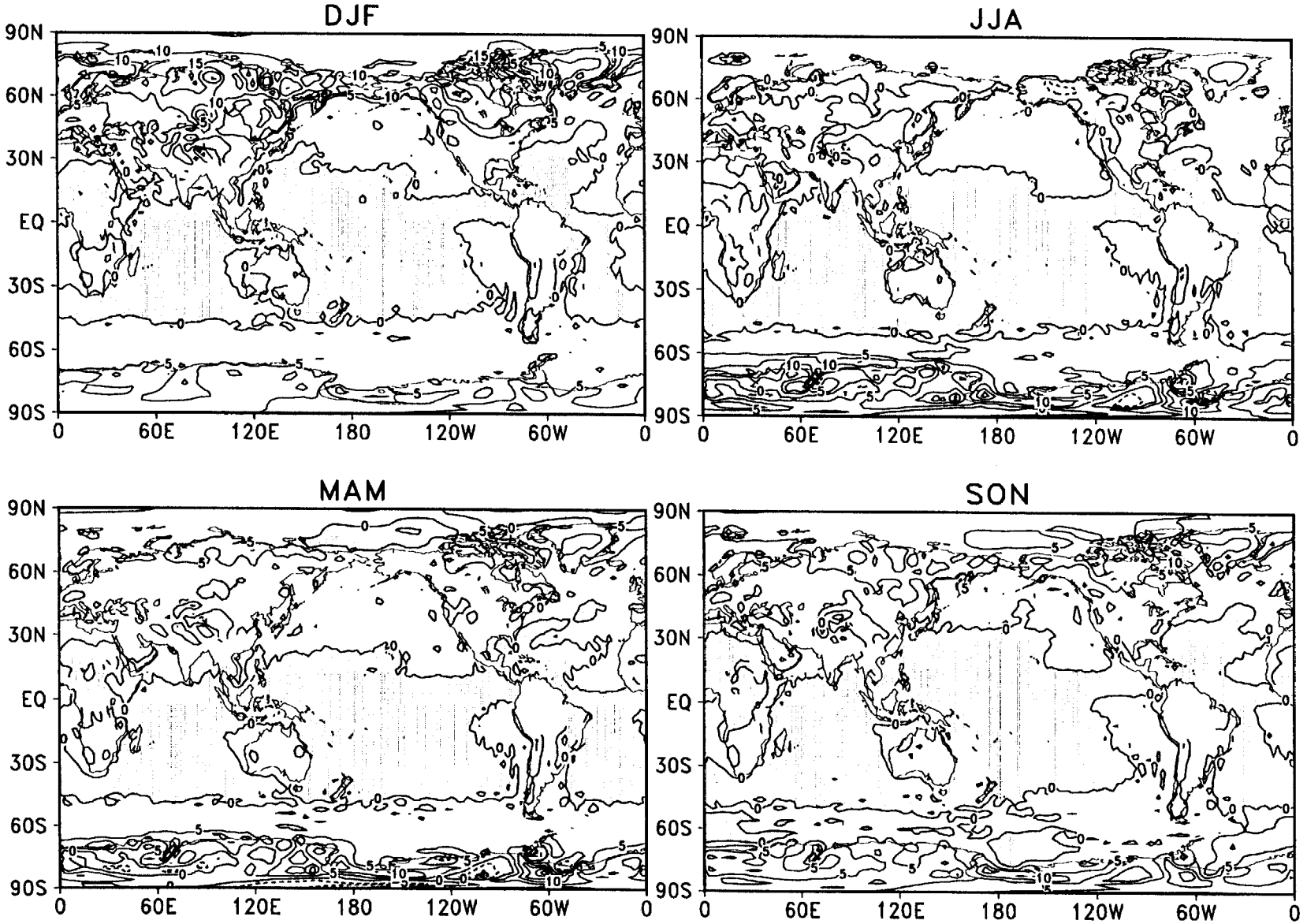

Figure 141: Difference of the seasonal means of temperature at 2 meters during 1980–1995 (NCEP/NCAR minus DAO). The contour interval is 5°K. Negative values are shaded.

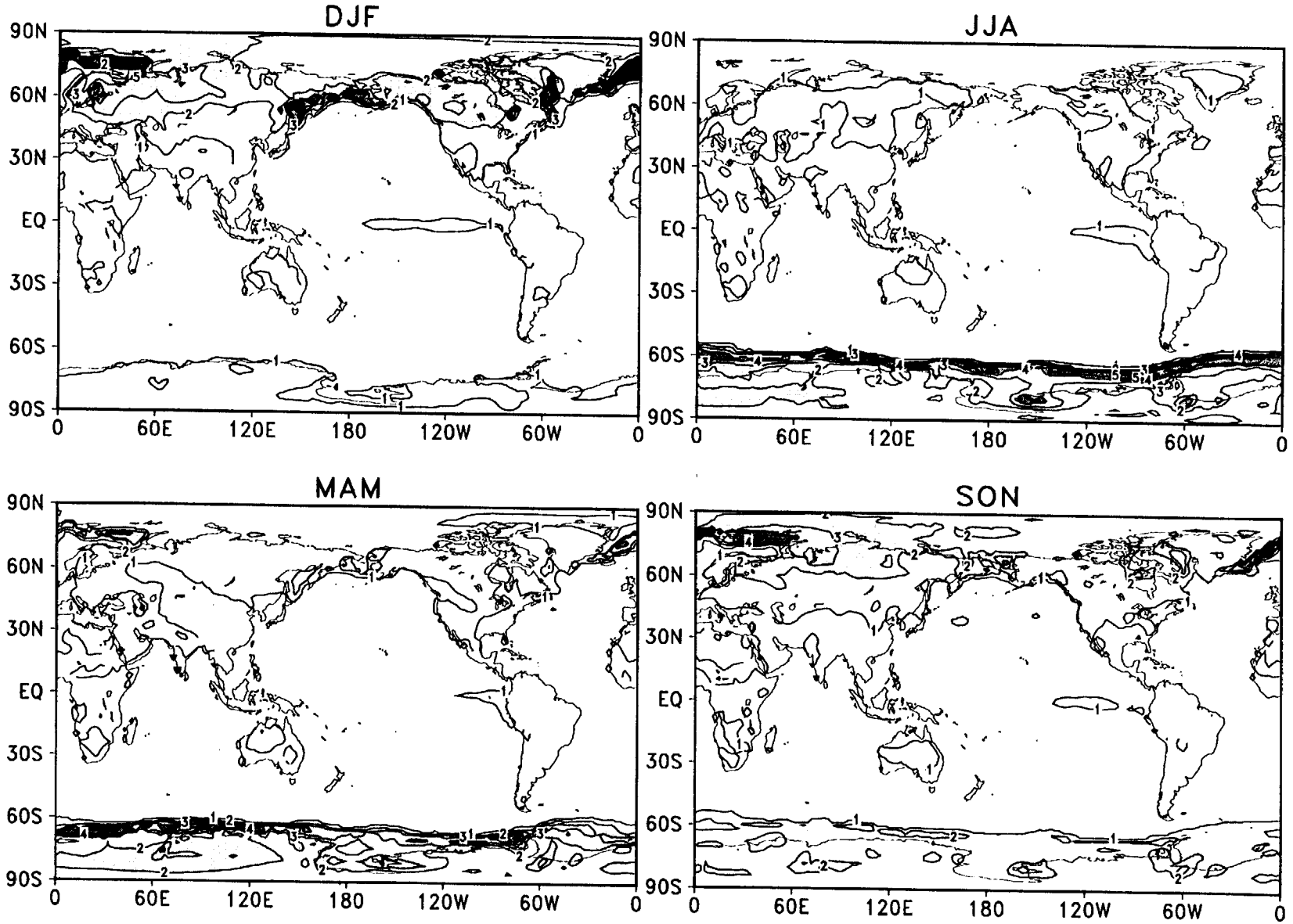

Figure 142: Standard deviations of seasonal mean temperature at 2 meters for DAO reanalysis during 1980–1995. The contour interval is 1°K. Values larger than 2°K are shaded.

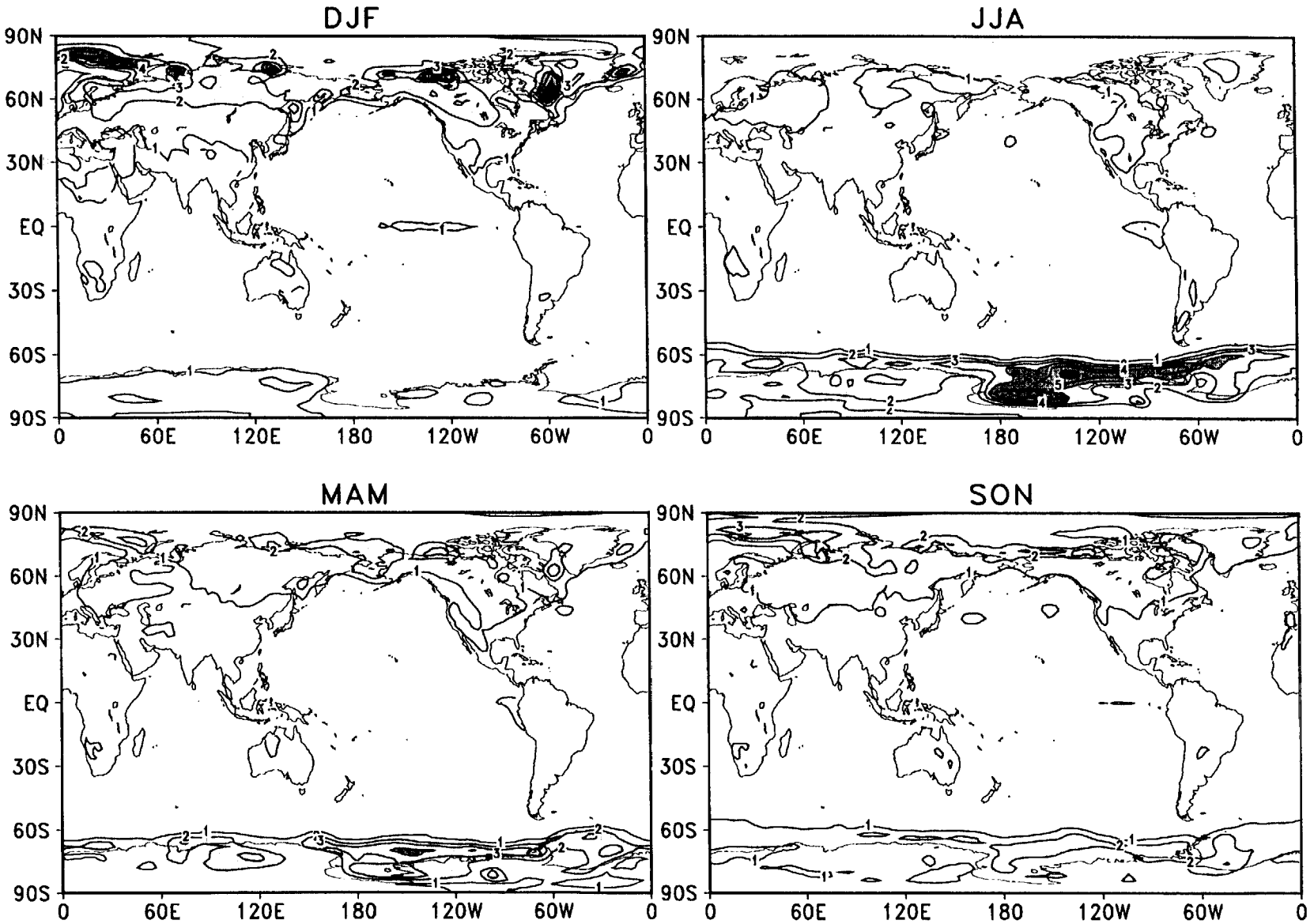

Figure 143: Standard deviations of seasonal mean temperature at 2 meters for NCEP/NCAR reanalysis during 1980–1995. The contour interval is 1°K. Values larger than 2°K are shaded.

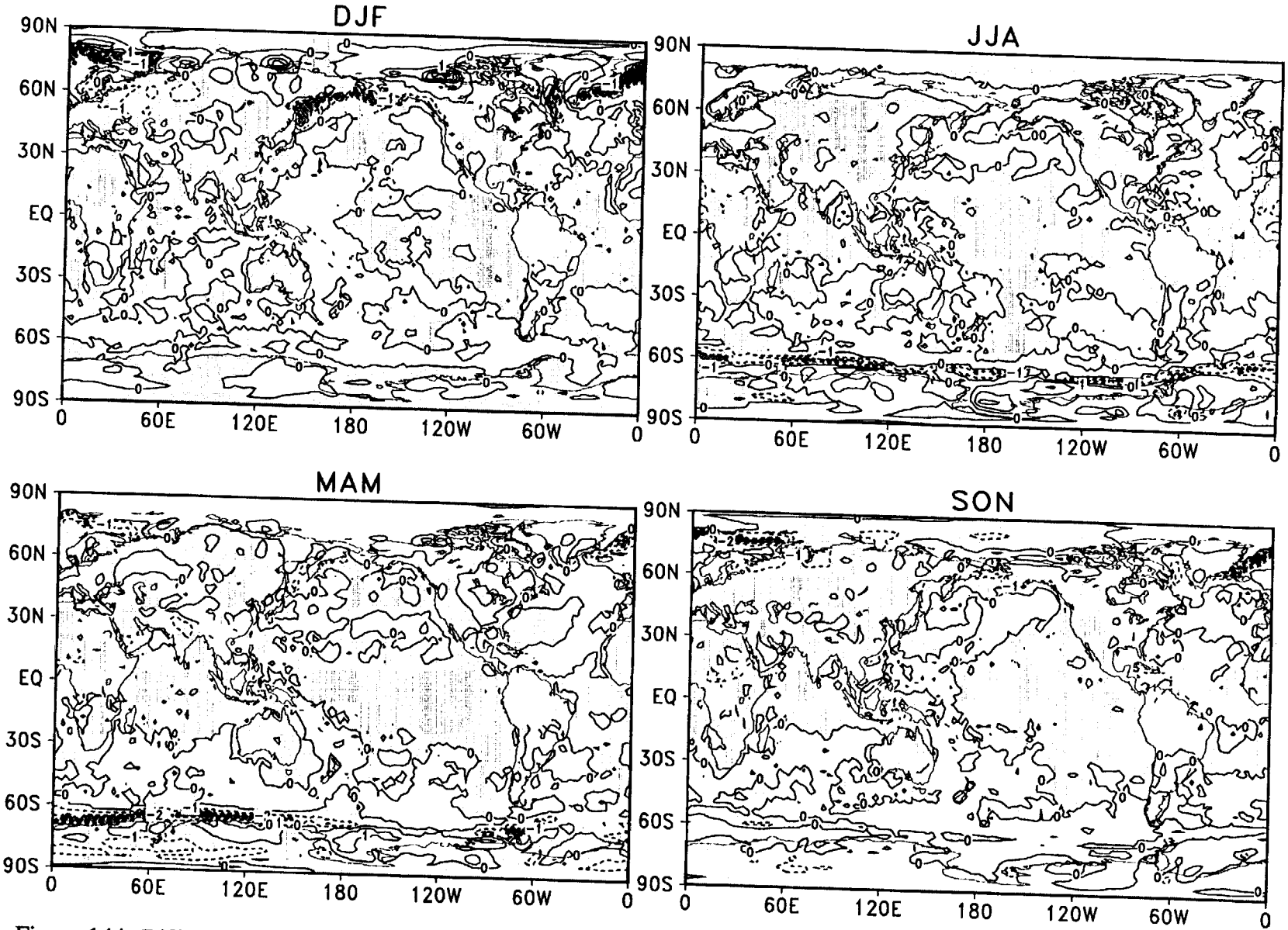

Figure 144: Difference of the standard deviations of seasonal mean temperature at 2 meters during 1980–1995 (NCEP/NCAR minus DAO). The contour interval is 1°K. Negative values are shaded.

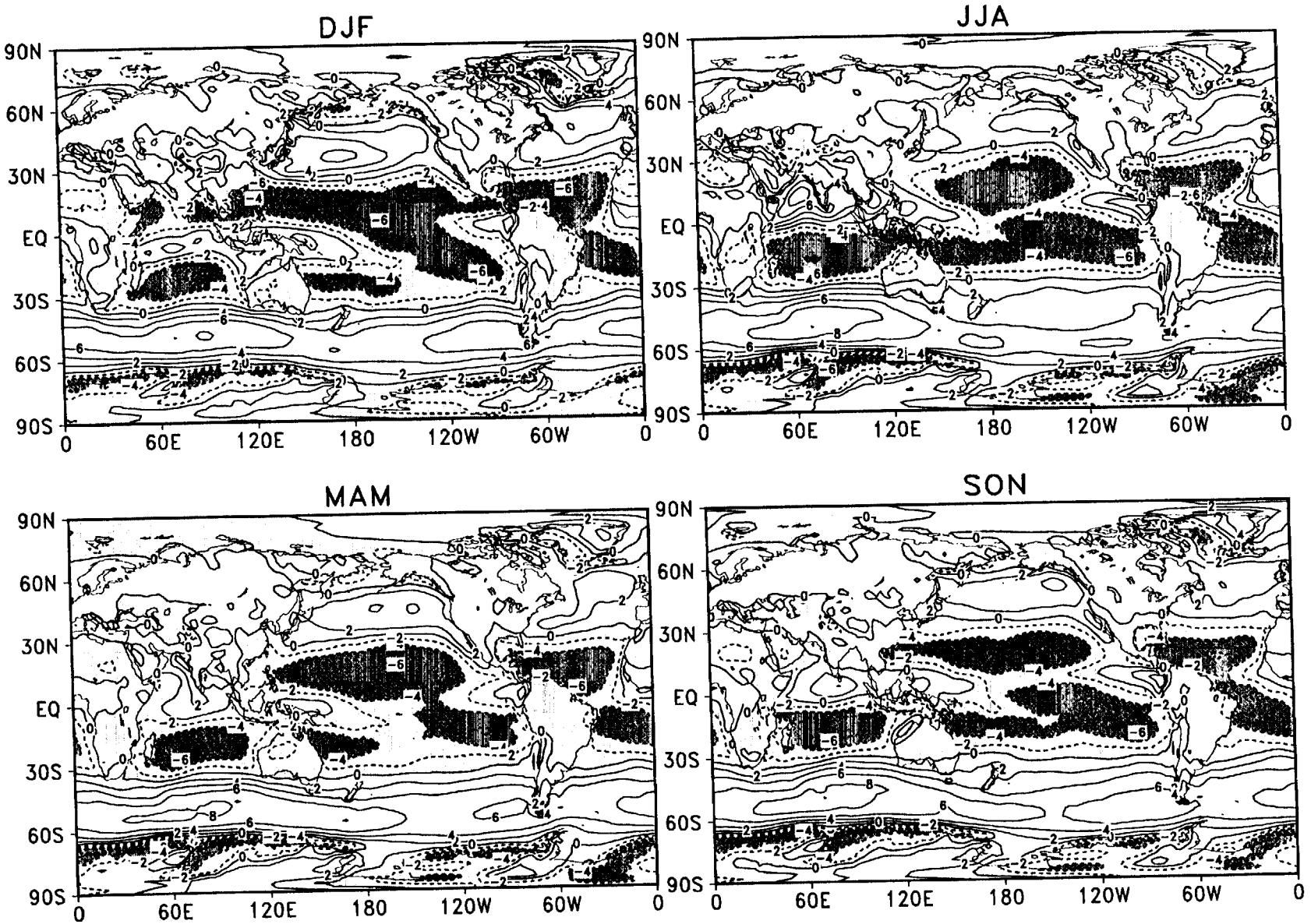

Figure 145: Seasonal means of u-wind at 10 meters for DAO reanalysis during 1980–1995. The contour interval is 2 m s^{-1}. Negative values are shaded.

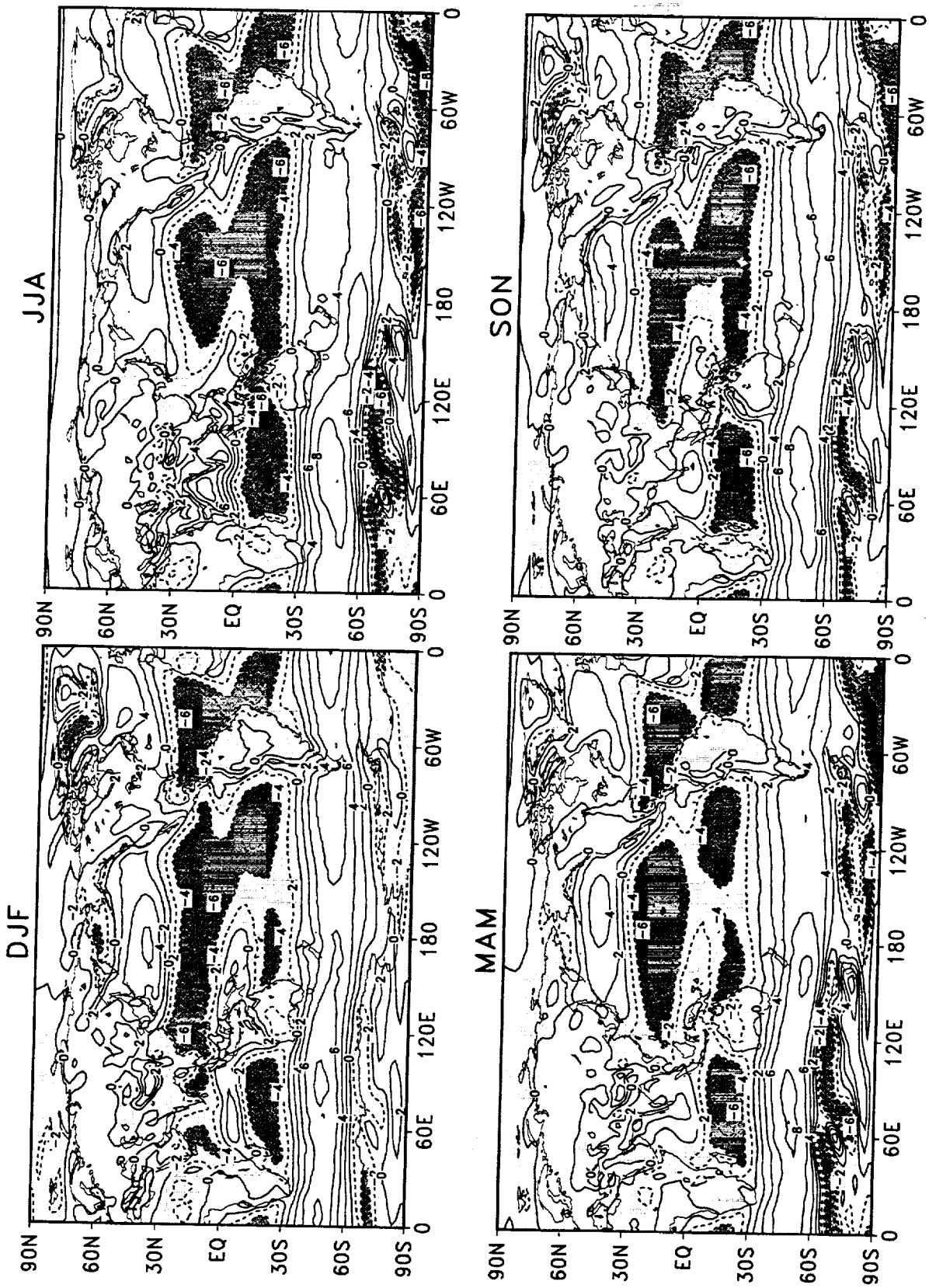

Figure 146: Seasonal means of u-wind at 10 meters for NCEP/NCAR reanalysis during 1980–1995. The contour interval is 2 m s^{-1}. Negative values are shaded.

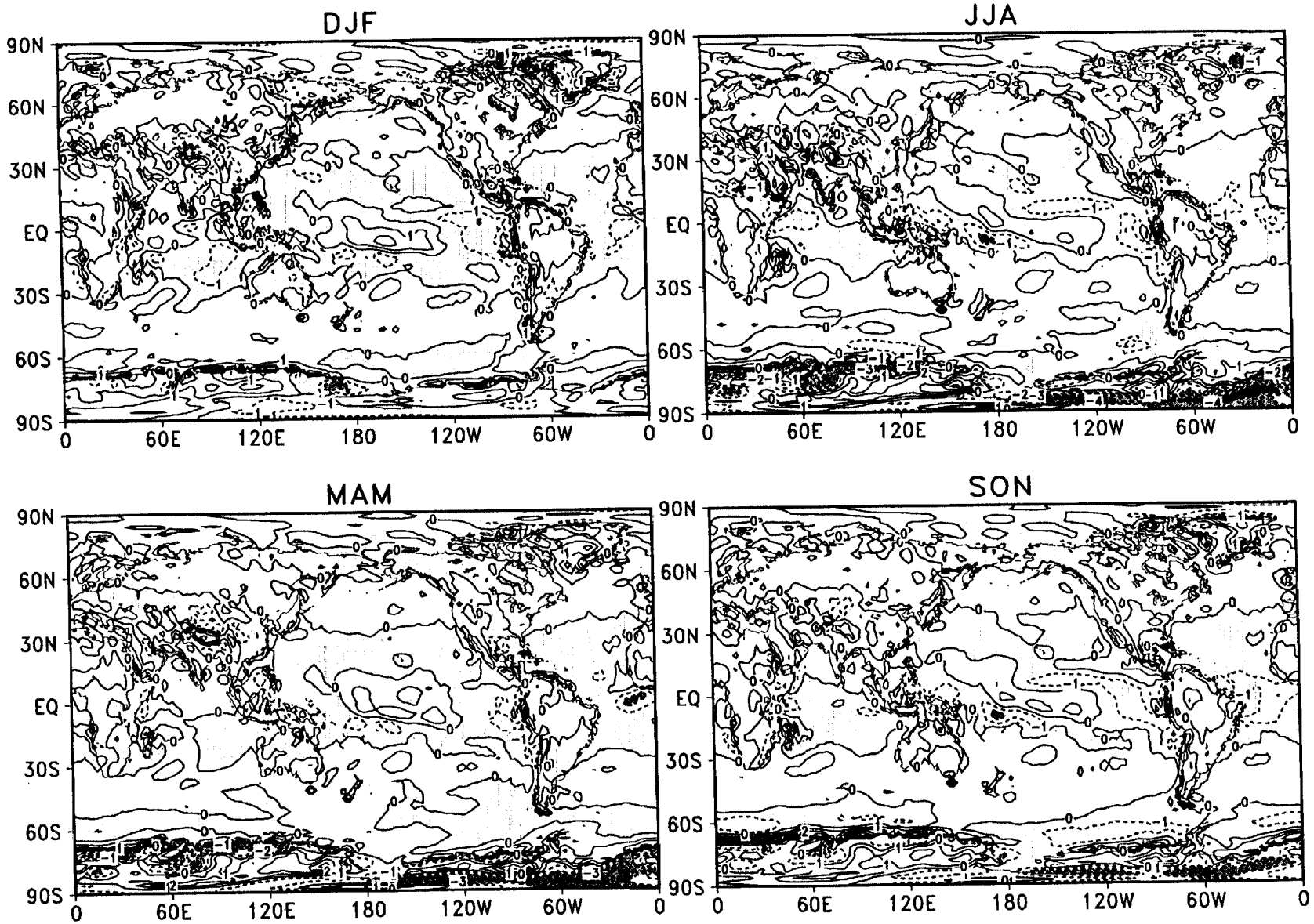

Figure 147: Difference of the seasonal means of u-wind at 10 meters during 1980–1995 (NCEP/NCAR minus DAO). The contour interval is 1 m s^{-1}. Negative values are shaded.

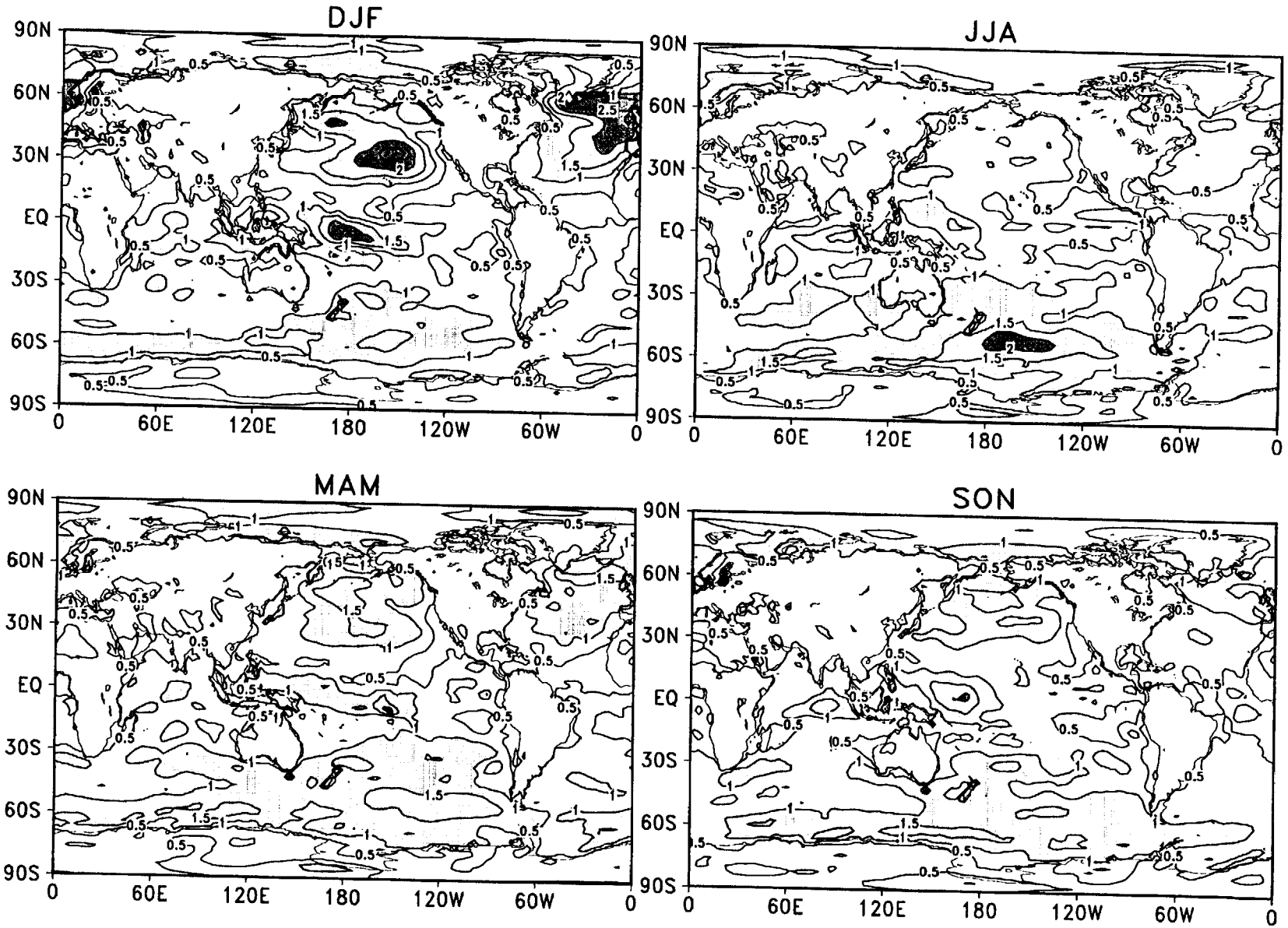

Figure 148: Standard deviations of seasonal mean u-wind at 10 meters for DAO reanalysis during 1980–1995. The contour interval is 0.5 m s^{-1}. Values larger than 1 m s^{-1} are shaded.

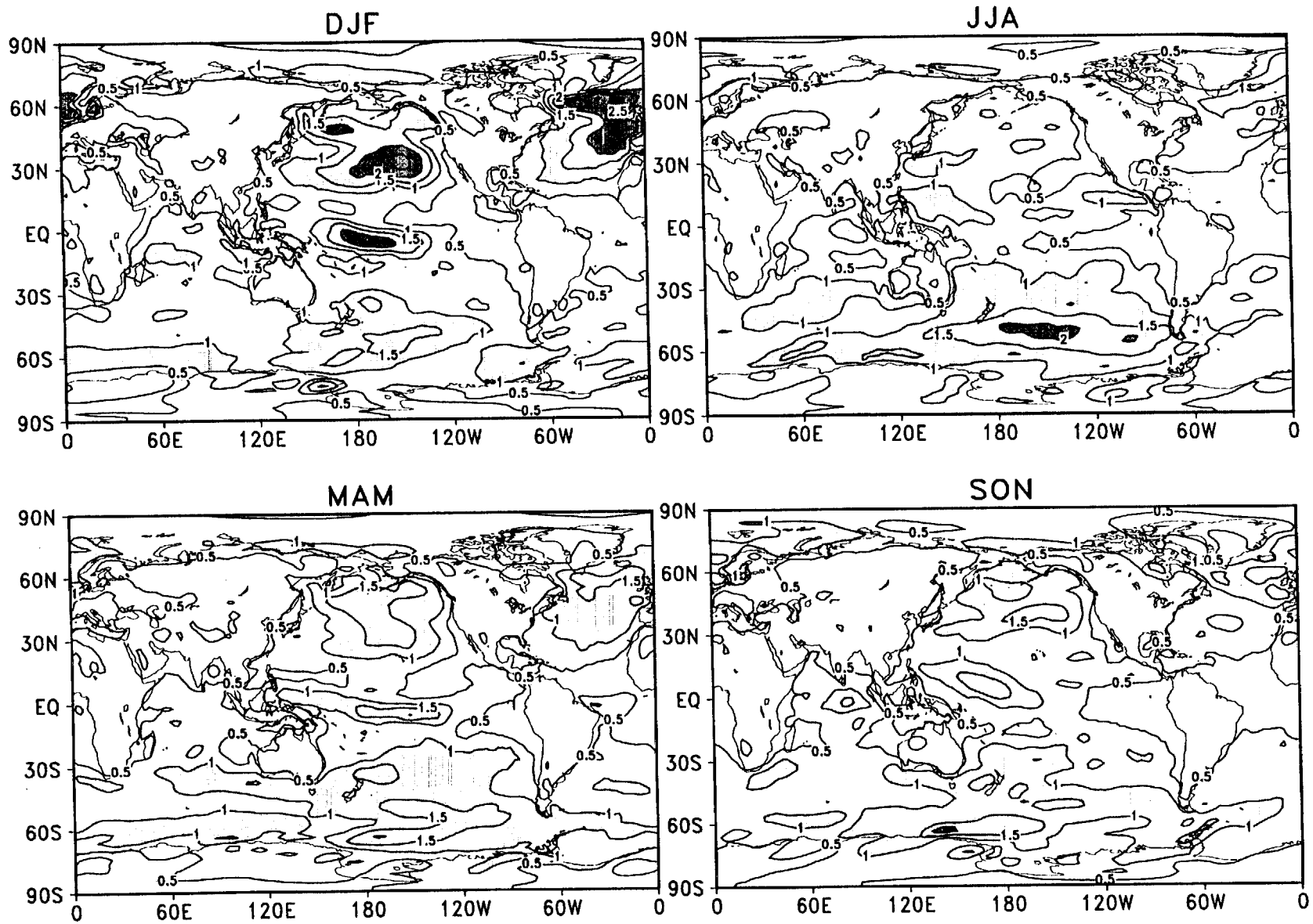

Figure 149: Standard deviations of seasonal mean u-wind at 10 meters for NCEP/NCAR reanalysis during 1980–1995. The contour interval is 0.5 m s^{-1}. Values larger than 1 m s^{-1} are shaded.

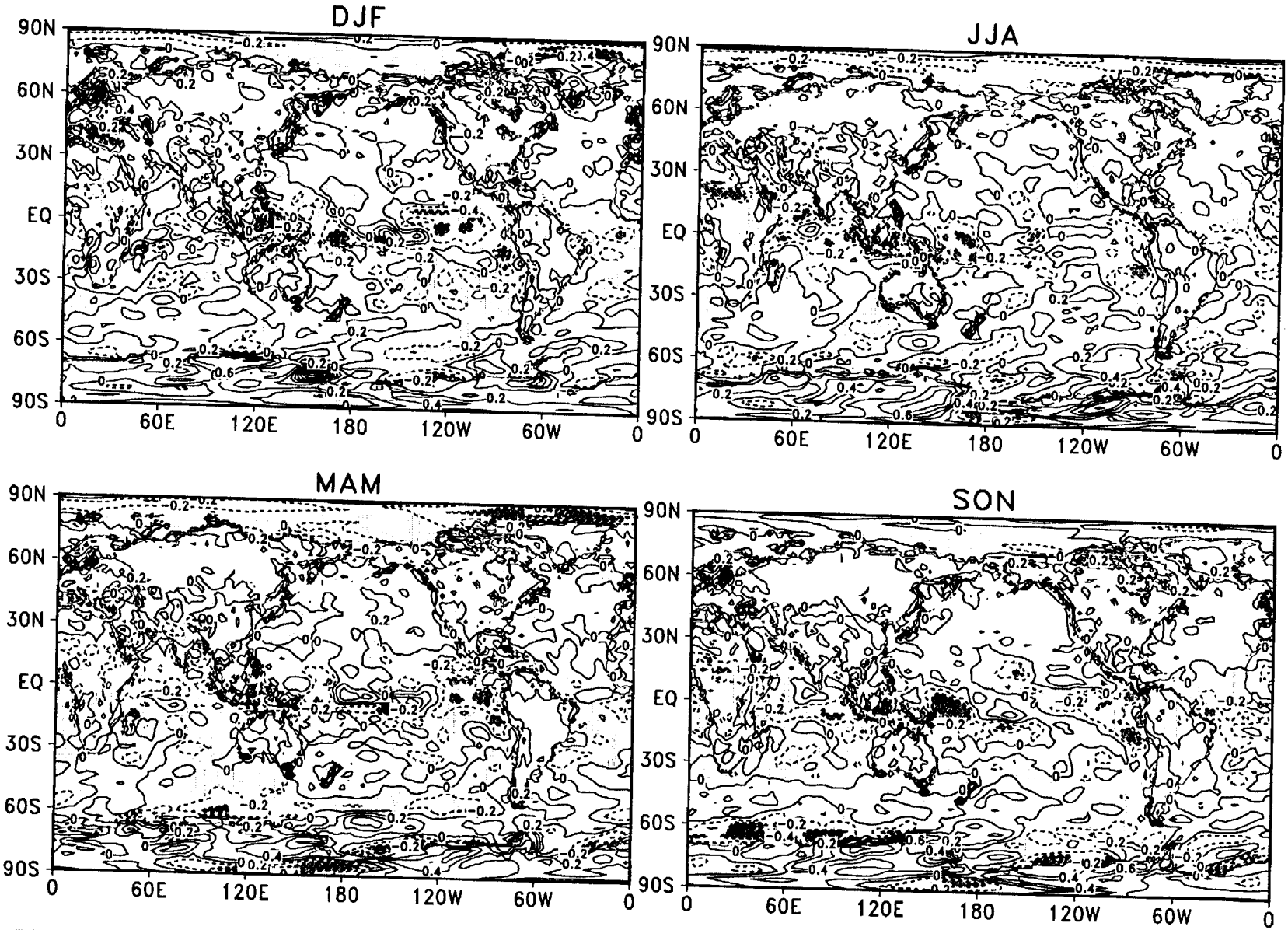

Figure 150: Difference of the standard deviations of seasonal mean u-wind at 10 meters during 1980–1995 (NCEP/NCAR minus DAO). The contour interval is 0.2 m s^{-1}. Negative values are shaded.

4 Potential Predictability

Leith (1973) conceptualized the problem of climate predictability by analyzing the signal-to-noise ratio in the time averages and stated that the noise in the climate means is closely dependent on the persistence in the daily weather fluctuations. Madden (1976) pioneered the study of potential predictability of the atmosphere by examining the mean sea level pressure in the Northern Hemisphere using a 74-year dataset. He concluded that there is little potential predictability between 40°N and 60°N in all seasons and that potential predictability increases to the north and south of this mid-latitude band. In a similar study, Madden and Shea (1978) showed that there is fairly strong evidence for potential predictability in surface temperature over the United States in the winter season but less in other seasons. Shukla and Gutzler (1983), using 15 years of NMC analyzed 500 hPa height in the northern hemisphere, showed stronger evidence for potential predictability in January and July, though the distribution of the ratio of interannual to intraseasonal variability has the same characteristics as that in Madden (1976). These differences illustrate the sensitivity of the results to the methods employed for estimating potential predictability (Zwiers 1987). Further aspects of the sensitivity will be examined below.

In this section, we document the interannual variability and seasonal potential predictability in the DAO reanalysis products. The approach basically follows the formulation given in Trenberth (1985b). The current study, however, employs a fit to an autoregressive process to estimate the autocorrelation which, in turn, is used to determine the characteristic time scales. The data and a brief description of the methodology are given in subsection 4.1. The results are presented in subsection 4.2.

4.1 Data and data processing

a. Data

The data consist of the daily averages of mean sea level pressure (SLP), 500 hPa geopotential height, 200 hPa stream function and 200 hPa velocity potential generated from the DAO multiyear reanalysis for the 15 year period of March 1980–February 1995 (Schubert et al. 1995). The daily mean values were computed from the 6-hourly fields sampled at a resolution of 2° lat $\times 2.5^{\circ}$ lon.

b. Annual cycle

The 15-year mean annual cycle of the daily data is represented by a truncated Fourier expansion (Madden 1976; Madden and Shea 1978). The full amplitudes of the first four harmonics were included and harmonics five through seven were weighted by 0.75, 0.50, and 0.25 respectively. The smoothed annual cycle was then used to generate the anomalies

by removing the annual cycle from the daily data. Note that these anomalies retain any interannual variations. Figure 151 gives an example of the original and truncated Fourier representation of the mean annual cycle of the 500 hPa geopotential height at 60°N and 150°W.

Conventional seasons were used for the northern spring (March, April and May : MAM), summer (June, July and August : JJA), fall (September, October and November : SON) and winter (December, January and February : DJF).

c. Estimating the autocorrelation

For the anomaly time series, $\{x_{i,j}\}$, the autocovariance for a particular season at lag L for the jth year is estimated by

$$C_j(L) = \frac{1}{N}\sum_{i=1}^{N-L}(x_{i,j} - \bar{x}_j)(x_{i+L,j} - \bar{x}_j), \tag{1}$$

where

$$\bar{x}_j = \frac{1}{N}\sum_{i=1}^{N} x_{i,j},$$

and N is the sample size (number of days in the season). Then mean autocovariance and autocorrelation over J years are given by

$$C(L) = \frac{1}{J}\sum_{j=1}^{J} C_j(L), \tag{2}$$

and

$$\rho(L) = \frac{C(L)}{C(0)}, \tag{3}$$

respectively. Jones (1975) and Trenberth (1985) note that the $\rho(L)$ estimate from (1)–(3) is unreliable at large lags for small sample sizes. In this study, we employ an autoregressive process to fit the autocorrelation (e.g. Jones 1975). Figure 152 shows an example of the autocorrelation calculated from (3) and the first and second order AR fits. In general, the second order AR model fits the time series better than a red noise approximation (first order AR process).

d. Definition of potential predictability

There are generally two approaches to estimating potential predictability: one in the time domain (e.g., Trenberth 1985b) and another in frequency domain (e.g., Madden 1976; Madden and Shea 1978; Zwiers 1986). Th two approaches are essentially similar. The method used in this study is described in detail in Trenberth (1985b) and outlined below.

For each season of year j, there are N daily values, $x_{i,j}$, with the mean annual cycle removed. An unbiased estimate of the interannual variance is

$$\sigma_m^2 = \frac{1}{J-1}\sum_{j=1}^{J}\bar{x}_j^2 = \frac{J}{J-1}s_m^2, \tag{4}$$

where

$$s_m^2 = \frac{1}{J}\sum_{j=1}^{J}\bar{x}_j^2. \tag{5}$$

This is a measure of the climatic signals. In order to test whether there is a significant contribution from potentially predictable sources, we need to estimate independently the variance due to the noise in the time averages. The noise is the high frequency variability of the daily mean values.

The variance of the seasonal means due to climate noise, σ_N^2 , is given

$$\sigma_N^2 = \frac{\sigma^2}{N_{eff}} = \frac{\sigma^2 T_0}{N}, \tag{6}$$

where σ^2 is the unbiased estimate of total variance, N_{eff} is the effective number of independent observations, and T_0 the characteristic time between independent samples as defined in Leith (1973)as

$$T_0 = 1 + 2\sum_{L=1}^{N}(1-\frac{L}{N})\rho(L). \tag{7}$$

The estimate of T_0 is sensitive to the estimate of autocorrelation at lag L, as it is shown in Fig.153. Different estimates of the autocorrelation result in very different T_0 values. For example, the T_0 values calculated from the first order AR model are very different from those based on the original sample estimates of the autocorrelation.

An unbiased estimate of σ^2 based on intraseasonal variances is given by

$$\sigma^2 = \frac{N}{N-T_0}s^2, \tag{8}$$

where s^2 is the mean intraseasonal variance and is given by

$$s^2 = \frac{1}{J}\sum_{j=1}^{J}s_j^2, \tag{9}$$

and where

$$s_j^2 = \frac{1}{N}\sum_{i=1}^{N}(x_{i,j} - \bar{x}_j)^2. \tag{10}$$

The variance due to climatic noise is

$$\sigma_N^2 = \frac{T_0}{N - T_0}s^2. \tag{11}$$

Under the null hypothesis that there is no potentially predictable signal, the ratio,

$$F = \frac{\sigma_m^2}{\sigma_N^2}, \tag{12}$$

will approximately follow an F distribution with J-1 and $J(N_{eff}$-$1)$ degrees of freedom. The null hypothesis will be rejected if $F > F_c$ where F_c is the critical value of F at an appropriate significant level.

4.2 Results

a. Intraseasonal variances

Figures 154 – 157 show the intraseasonal variances of the 500 hPa height, sea level pressure, 200 hPa stream function and 200 hPa velocity potential for the four seasons. The seasonal variations of the variances of the 500 hPa height, SLP and 200 hPa stream function are larger in the northern hemisphere than in the southern hemisphere. In the northern hemisphere, the winter (DJF) has the largest variability while the summer (JJA) has the least variability. The height field (Fig. 154) shows three centers of large variability over the North Pacific/Gulf of Alaska, the North Atlantic extending over Europe, and the Arctic. This is consistent with previous studies using the NMC analysis (e.g., Blackmon 1976; Blackmon et al. 1986; Min and Kung 1997). The transition seasons show similar variability patterns, with somewhat larger variability over Europe and eastern Asia during SON. For the southern hemisphere, the seasonal variation is weaker with maximum variability occurring during JJA over the South Pacific. The regions of large variability are consistent with those found in Trenberth (1985b). That study was based on about 8 years of 0000 UTC analyses from Australian World Meteorology Center. The pattern of the intraseasonal variance is, however, more zonally symmetric than in the Northern Hemisphere, with the maximum variability occurring at about 60°S.

The regions of high SLP variability (Fig. 155) are similar to those of the height field, though the location of the maxima tend to be displaced somewhat to the east with respect to the height variance maxima. The regions of high stream function variability (Fig. 156) tend

to be displaced equatorward of the height variances, and are more closely identified with fluctuations in the major subtropical and midlatitude jet streams. The 200 hPa velocity potential shows large variability in the tropics with large seasonal variations (Fig.157). For DJF, the maximum is located over the tropical Indian Ocean. In contrast, JJA shows substantially weaker variability over the Indian Ocean and somewhat stronger variability over central America, and just east of Australia. There is a large difference in the variance for the transition seasons, with a broad tropical maximum in variability for MAM and much weaker tropical variability during SON with the maximum over the Indian Ocean. In general, the MAM variability is more like DJF, while the SON variability is more like JJA. It is likely that a substantial fraction of the intraseasonal variances in 200 hPa velocity potential comes from the 40–50 day oscillation (Madden and Julian 1972). We note that this variance is treated as climatic noise in the estimate of potential predictability in this study.

b. Interannual variances

The interannual variability is shown in Figs.158–161. The maxima in the height and SLP variance occur over the North Pacific, the North Atlantic, the Arctic, and the South Pacific near 120°S. The Northern Hemisphere has a large seasonal variation with relatively large variability occurring during DJF and very weak summer time variability. The Southern Hemisphere shows less season variation in the variance with, however, the weakest variance again occurring during the summer. These results are consistent with earlier studies (e.g., Madden 1976; Trenberth 1985b) for both the winter and summer seasons. In the northern hemisphere, interannual variance maxima tend to be displaced equatorward of the maxima in the intraseasonal variances, while in the southern hemisphere they are displaced to the south. The interannual variance is about 1/4 of the intraseasonal variance.

The interannual variance of the 200 hPa stream function is largest during DJF. During both DJF and MAM the meridional sequence of variance maxima in the central/eastern Pacific suggest a coupling between the tropics and extratropics. Maxima in variance also occur over the Gulf of Alaska, Southeast Asia, the Arctic, the North Atlantic, and the South Pacific (southeast of New Zealand). During JJA, the interannual variability is substantially reduced with the largest variability apparently tied to fluctuations in the subtropical jets. The variability is also weak during SON, except for a local maximum which occurs east of Australia in the region of the South Pacific Convergence Zone (SPCZ).

The interannual variance of the 200 hPa velocity potential is primarily concentrated in the tropics. Surprisingly, the transition seasons (MAM and SON) show the largest variability. The major maxima in variance during MAM occur over the western Pacific and the Americas, while during SON the primary maximum is located over Indonesia and Australia, with a secondary maximum located over the central Pacific. During DJF there is a broad maxi-

mum across the tropical Pacific which extends into middle latitudes over both the western Pacific and Mexico. The variability is substantially reduced during JJA, with weak maxima over India, southern Africa, and the central tropical Pacific.

c. Characteristic time scales

Previous studies have presented T_0 values for sea level pressure (Madden 1976), surface temperature (Madden and Shea 1978), and geopotential height (Shukla and Gutzler 1983) in the northern hemisphere. Trenberth (1985a) provided T_0 values for 500 hPa and 1000 hPa height in the southern hemisphere. Stefanick (1981) presented global distributions of an "integral time scale" ($\approx \frac{1}{2}T_0$) for wind, temperature and geopotential height at different levels for DJF. In view of the sensitive of the characteristic time scale to the estimate of autocorrelation we have examined several different estimates and found that a second order AR process provides in many cases an improved estimate (see section 4.1c and references cited therein).

Figures 162–165 show the characteristic time scales obtained by fitting the data with an AR(2) process. The results are generally consistent with previous studies for the 500 hPa height and SLP for DJF and JJA seasons (e.g., Madden 1976; Stefanick 1981; Shukla and Gutzler 1983; Trenberth 1985a). In general, T_0 ranges from 2 days to more than one week with minima in the midlatitudes in both hemisphere and maxima in the tropics and polar regions. During the northern winter (DJF), the T_0 values for 500 hPa height and SLP are larger than 6 days over the eastern North Pacific and North Atlantic regions. These are the preferred regions of winter blocking. Regions with relatively smaller T_0 correspond to regions of frequent cyclogenesis. Also during DJF, the tropical height field is characterized by a very narrow band (centered on the equator) of long time scales (greater than 5 days) extending eastward from eastern Africa across South America. In view of the small fluctuations of the height field in the deep tropics, these estimates may not be very reliable. For the SLP, the long tropical time scales cover a broader band with the longest time scales (greater than 7 days) occurring over Indonesia and the western Pacific. During JJA and SON the largest tropical time scales in the SLP are over the Indian Ocean and the western Pacific, while during MAM the region of long tropical time scales moves east, extending from Indonesia across the Pacific.

The T_0 values of the 200 hPa stream function show characteristics similar to the 500 hPa geopotential height and the sea level pressure in the middle and high latitudes for all seasons, though the values tend to be larger (e.g. about 2 weeks over Antarctic during DJF). The major differences are in the subtropical and the tropical regions. The T_0 values show a narrow band of minimum T_0 along the equator with maxima in the subtropics of both hemispheres for all seasons but JJA. The 200 hPa velocity potential generally shows time scales of one to two weeks throughout much of the tropical and subtropical eastern hemi-

sphere for all season except JJA. DJF and MAM patterns are quite similar with long time scales extending from the tropics poleward to +/-60° in some regions. During the northern summer, the longest time scales are found off the east coasts of Asia and North America, and over tropical South America.

d. Signal–to–Noise Ratios

Figures 166–169 present the F-ratios (signal–to–noise ratios) computed from (12) for the 500 hPa geopotential height, SLP, 200 hPa stream function and velocity potential for all seasons. Following Jones (1975), we make the null hypothesis that there is no potentially predictable signal in the data. The ratio (12) then has an F distribution. Regions where the ratio is larger than the critical value for a given significant level are considered potentially predictable. For convenience, we take everywhere values of the F-ratio less than 2 to indicate regions with no potential predictability. This is based on the fact that at the 97.5% confidence level, F_c is approximately 2.0 for the 200 hPa stream function in DJF over Antarctica: this represents the worst case from a statistical sampling point of view, since it has the longest time scales and therefore has the smallest number of effective samples.

For the 500 hPa geopotential height (Fig.166), the largest values of F-ratio are found in the tropical regions (20°S–20°N), highlighting the importance of SST forcing of the tropical atmosphere. This region of large signal–to–noise ratios is consistent with the findings of Schubert et al. (1997). That study found substantial coherence extending well into the upper troposphere between the tropical temperature from the reanalysis and the temperature from a simulation employing the observed SSTs as boundary conditions. In the extratropics, the small signal-to-noise ratios are generally consistent with Shukla and Gutzler (1983) for the northern hemisphere, and with Trenberth (1985b) for the southern hemisphere. We note, however, the F-values do exceed 2 throughout much of the northern extratropical oceans for all seasons except JJA, at which point the values greater than 2 tend to shift to the summer continents. In the Southern Hemisphere, signal–to–noise ratios exceeding 4 are found extending eastward from Australia into the central South Pacific. These signals, which may be related to the Southern Oscillation (Trenberth 1976; Nicholls 1981; van Loon 1984), were not evident in the Trenberth (1985b) study. For the northern hemisphere winter season, the major differences between the current results and those of Shukla and Gutzler (1983) are over the central and eastern United States and over the North Atlantic (see Fig.2 in Shukla and Gutzler 1983). The large F values over the central and eastern United States in Shukla and Gutzler are not found in the current study, while Shukla and Gutzler do not obtain the large F values over the North Atlantic where persistent anomalies or blocking events tend to occur.

The sea level pressure (SLP) depicts similar patterns of F values as the 500 hPa geopotential height in the middle and high latitudes of both hemisphere (Fig.167). In the subtropical and

tropical regions, however, local maxima are observed. For example, during the northern winter (DJF) large F values are found over the southeastern Pacific, the western Pacific region, the Indian ocean, and the southern Atlantic ocean. During the northern summer (JJA), large F values are observed over Africa, the central Pacific, and just off the coast of Peru. Large values over southern Asia and the southwestern United States are likely associated with the summer monsoons.

Figures 168 and 169 show the F values of the 200 hPa streamfunction and velocity potential. For the 200 hPa streamfunction, two regions of locally enhanced F values straddle the tropical central Pacific for all seasons. These regions of enhanced signal–to–noise move east/west and change strength with the seasons. During DJF they are located just east of the dateline. During MAM, the patterns are slightly to the east of th DJF position and have weaker signal-to-noise ratios. During JJA the signal–to–noise ratios are smallest and located in the western and central Pacific. During SON the regions have the largest signal–to–noise ratio and are located in the central Pacific. Large F values also occur over the tropical/subtropical Atlantic during DJF, MAM and JJA. Surprisingly large F values also occur over much of the Southern Hemisphere middle latitudes during DJF.

The velocity potential exhibits large seasonal variations of the F values. During DJF the largest F values are located over the eastern Pacific extending across North America, and over Antarctica. During MAM the high F values have switched from the Antarctica to the North Polar region, and the eastern Pacific region of high F values has moved further east to cover most of the Americas. During JJA the highest signal–to–noise ratios are located over the central Pacific and the high latitudes of both hemispheres. The largest F values during SON are located over Australia.

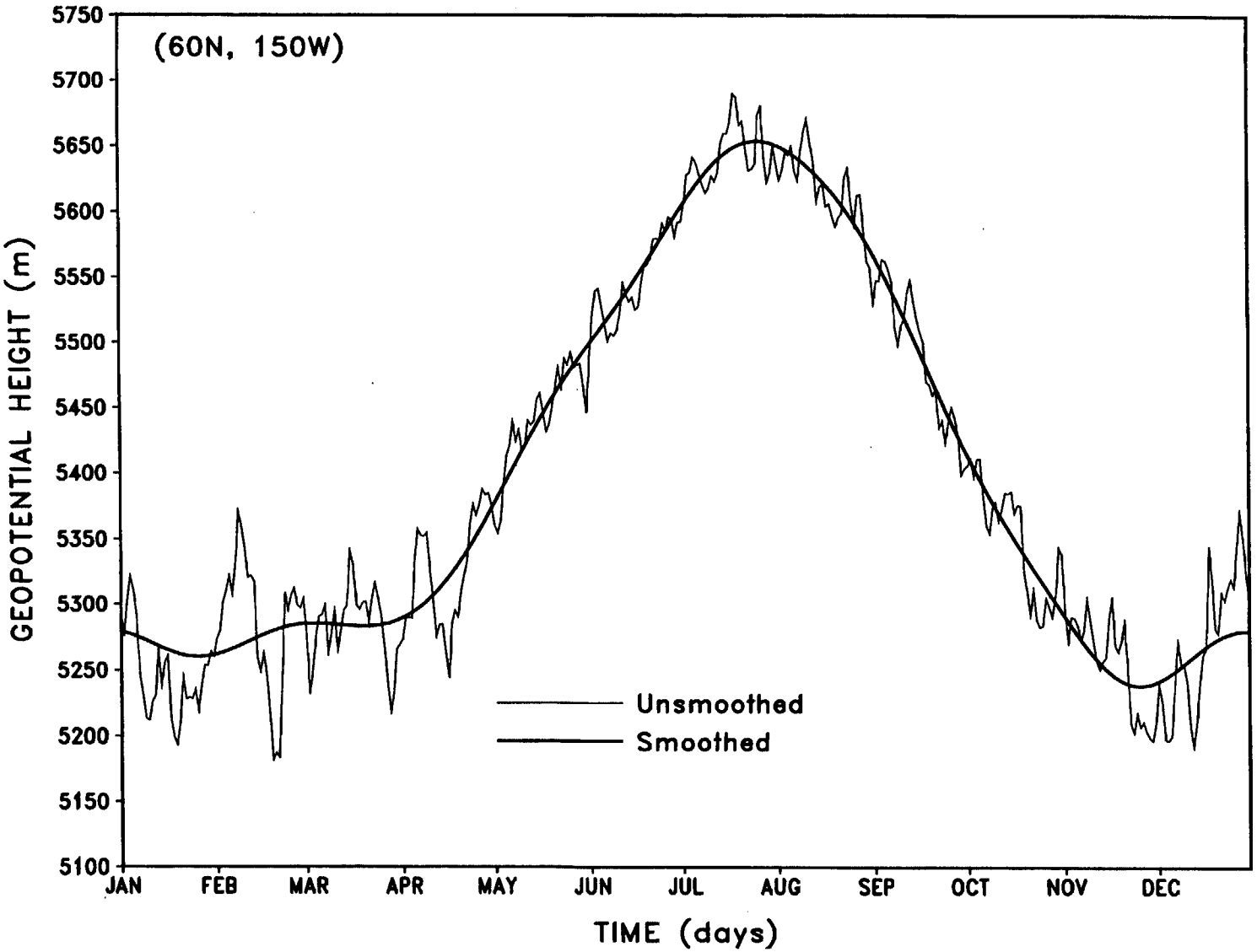

Figure 151: Annual variation of the 15-year mean annual cycle of 500 hPa height at 60°N, 150°W. The thick line represent the smoothed seasonal cycle fitted with truncated Fourier harmonics and the thin line denotes the unsmoothed values.

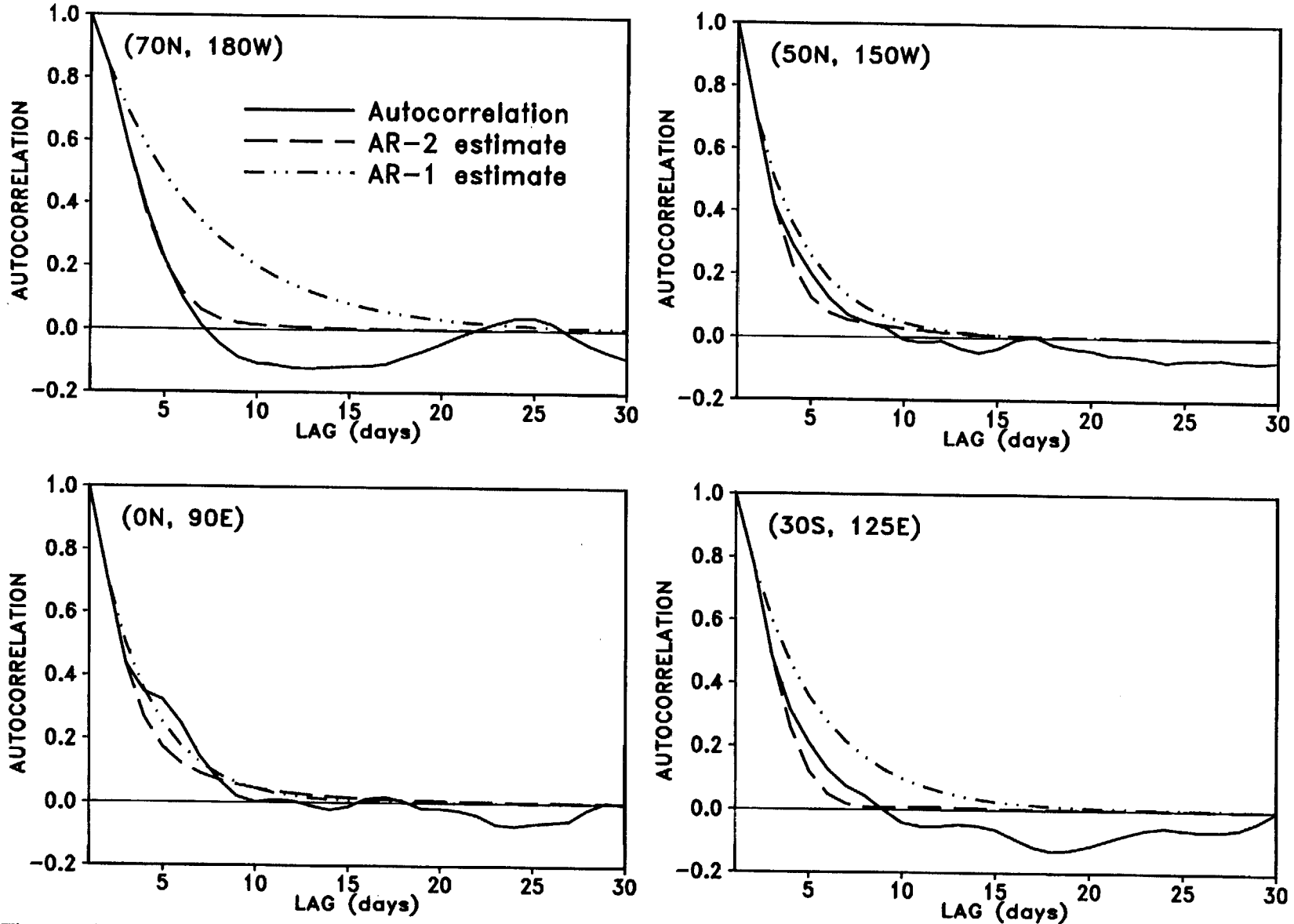

Figure 152: Lag correlations of 500 hPa height at selected grid points. Solid line is the autocorrelation estimated directly from the data, the broken line denotes the estimate of the autocorrelation by fitting a first order autoregressive (AR) model, and the dash-dotted line is the estimate of the autocorrelation by fitting a second order AR model.

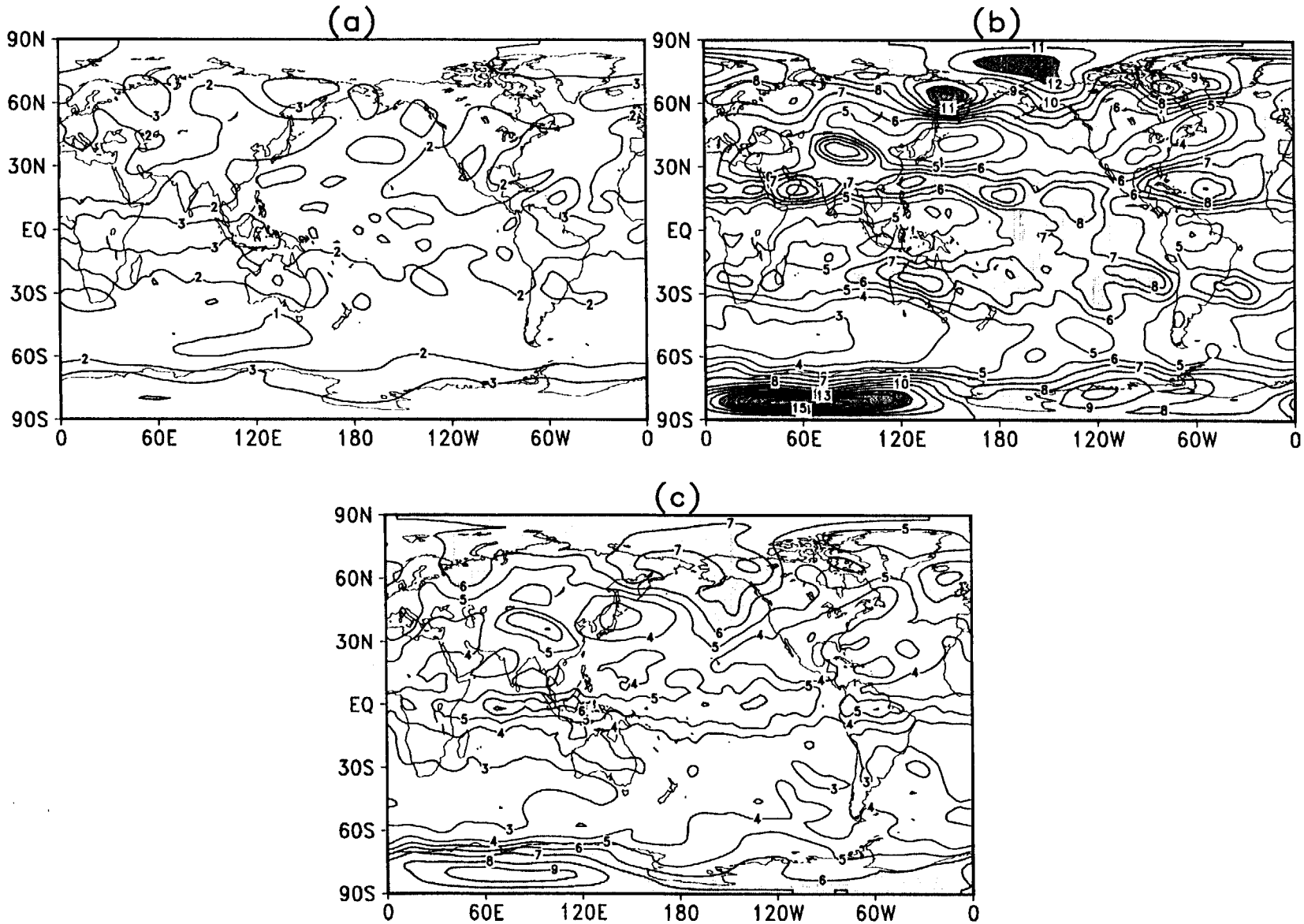

Figure 153: Characteristic time scales for 500 hPa height in winter season. (a) Direct estimate; (b) First order AR model fit; (c) Second order AR model fit. Unit : days.

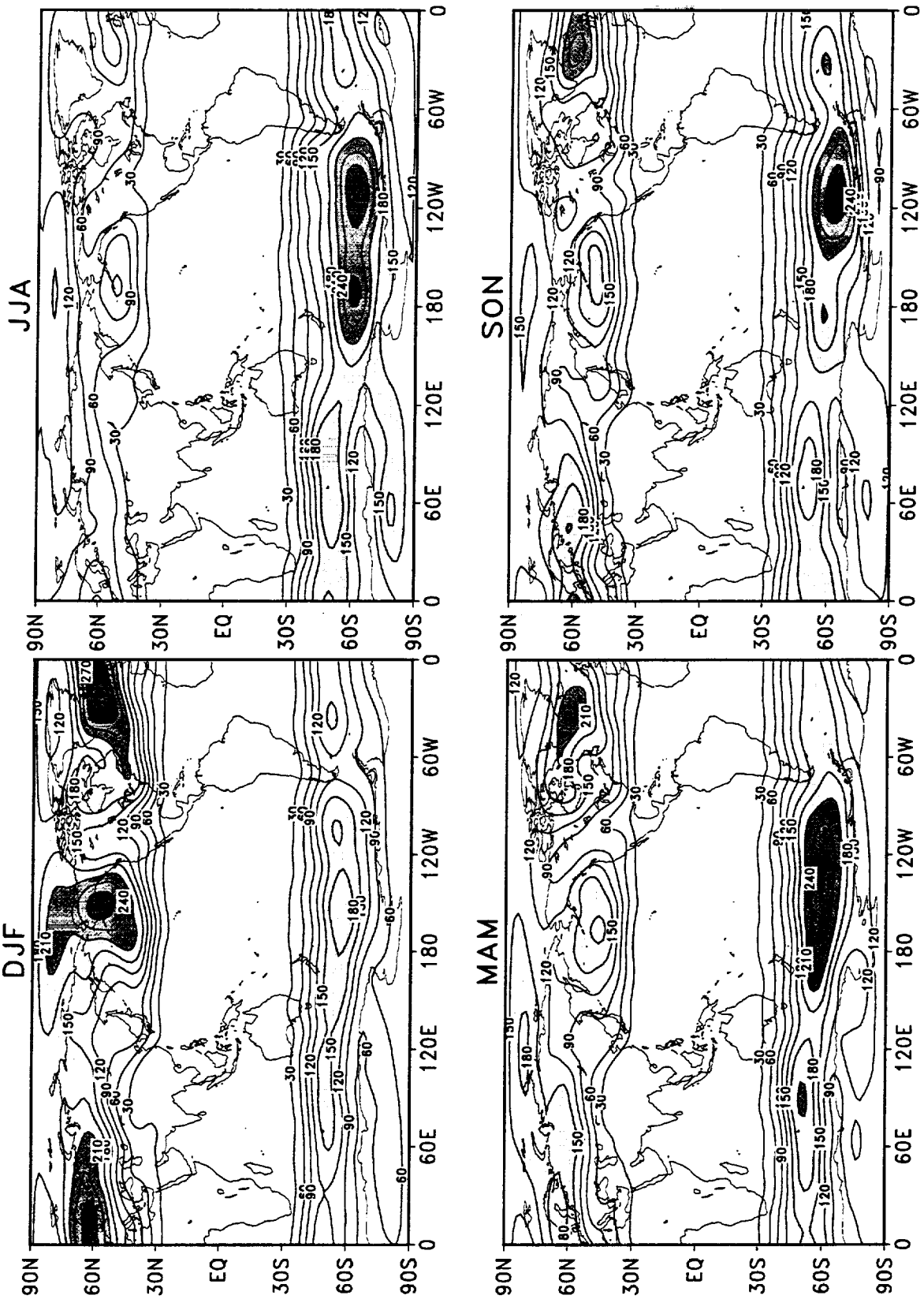

Figure 154: Intraseasonal variances of 500 hPa height from the DAO reanalysis during 1980–1995. The contour interval is $30\times10^4\mathrm{m}^2$. Values larger than $150\times10^4\mathrm{m}^2$ are shaded.

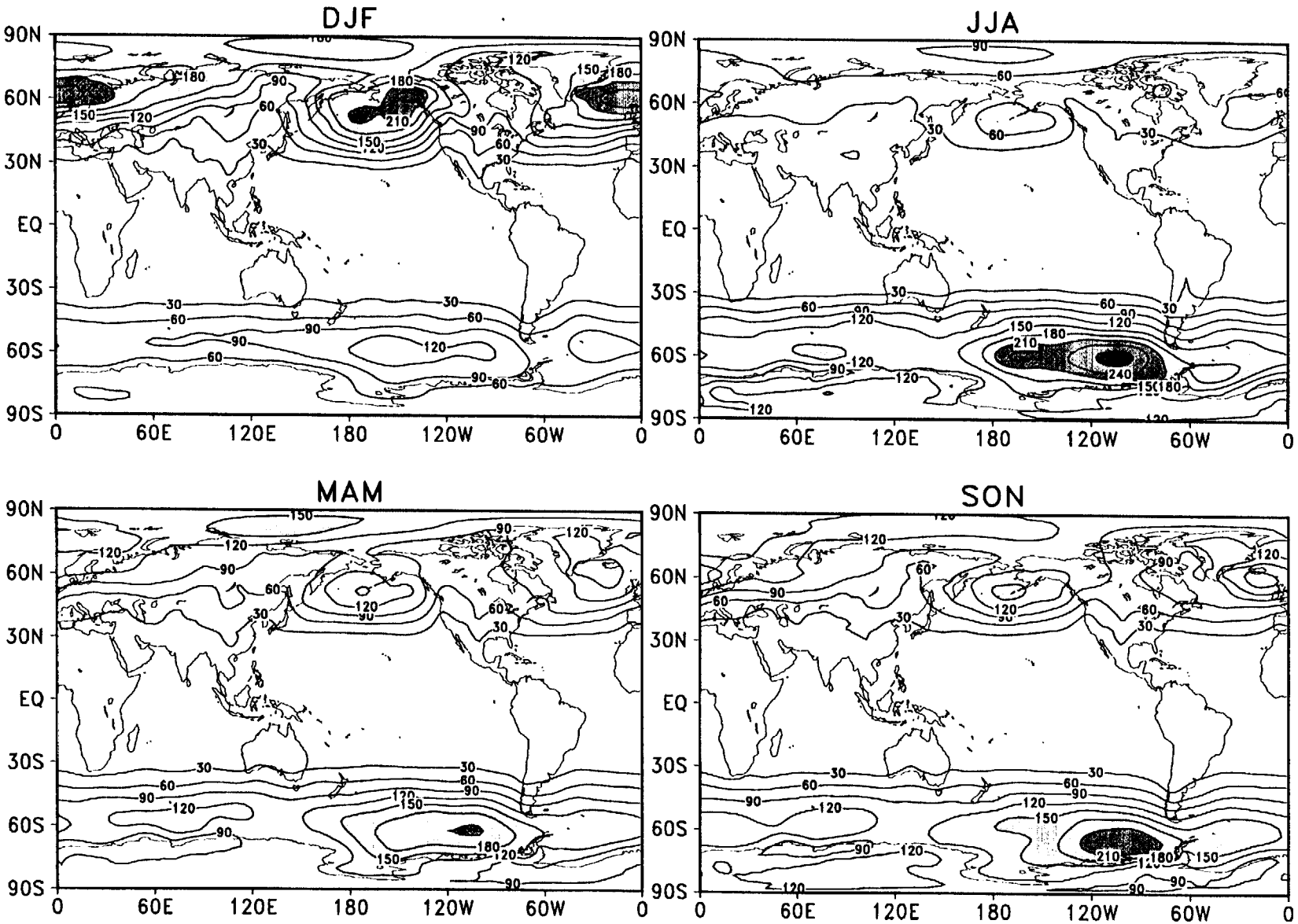

Figure 155: Intraseasonal variances of sea level pressure from the DAO reanalysis during 1980–1995. The contour interval is 30 $(\text{hPa})^2$. Values larger than 150 $(\text{hPa})^2$ are shaded.

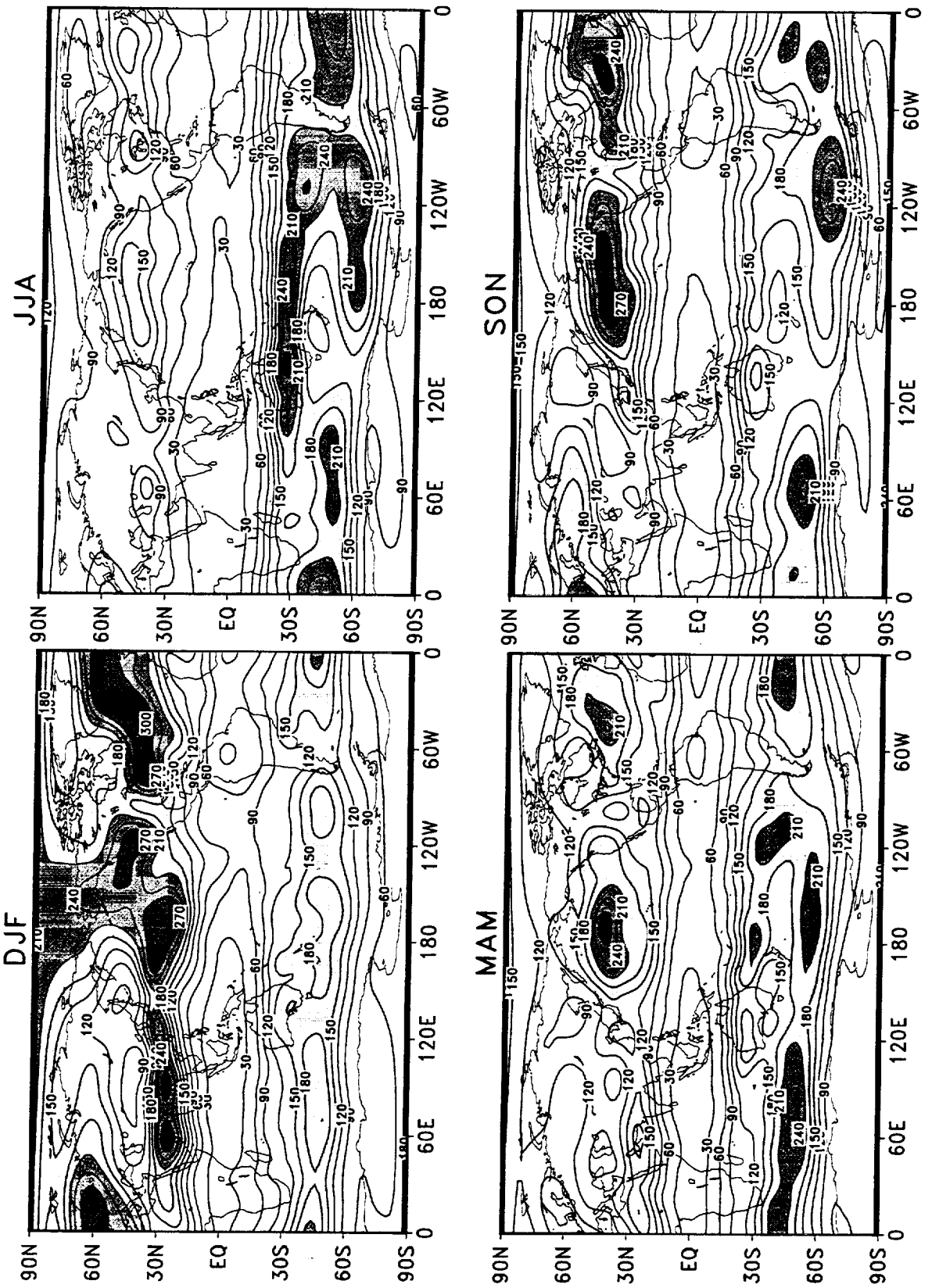

Figure 156: Intraseasonal variances of 200 hPa streamfunction from the DAO reanalysis during 1980–1995. The contour interval is $30 \times 10^{12} \mathrm{m}^4 \mathrm{s}^{-2}$. Values larger than $150 \times 10^{12} \mathrm{m}^4 \mathrm{s}^{-2}$ are shaded.

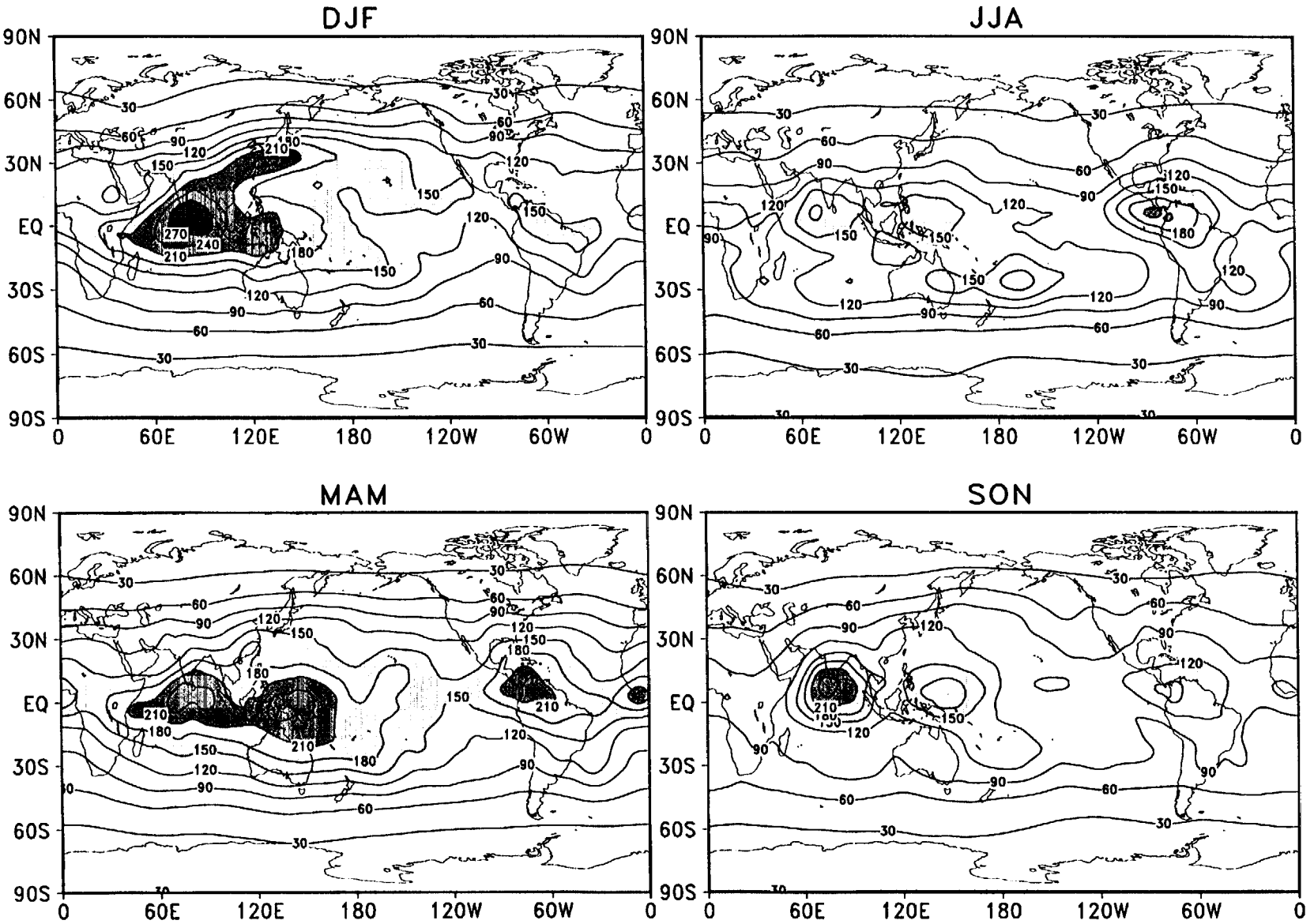

Figure 157: Intraseasonal variances of 200 hPa velocity potential from the DAO reanalysis during 1980–1995. The contour interval is $30\times10^{11}\mathrm{m}^4\mathrm{s}^{-2}$. Values larger than $150\times10^{11}\mathrm{m}^4\mathrm{s}^{-2}$ are shaded.

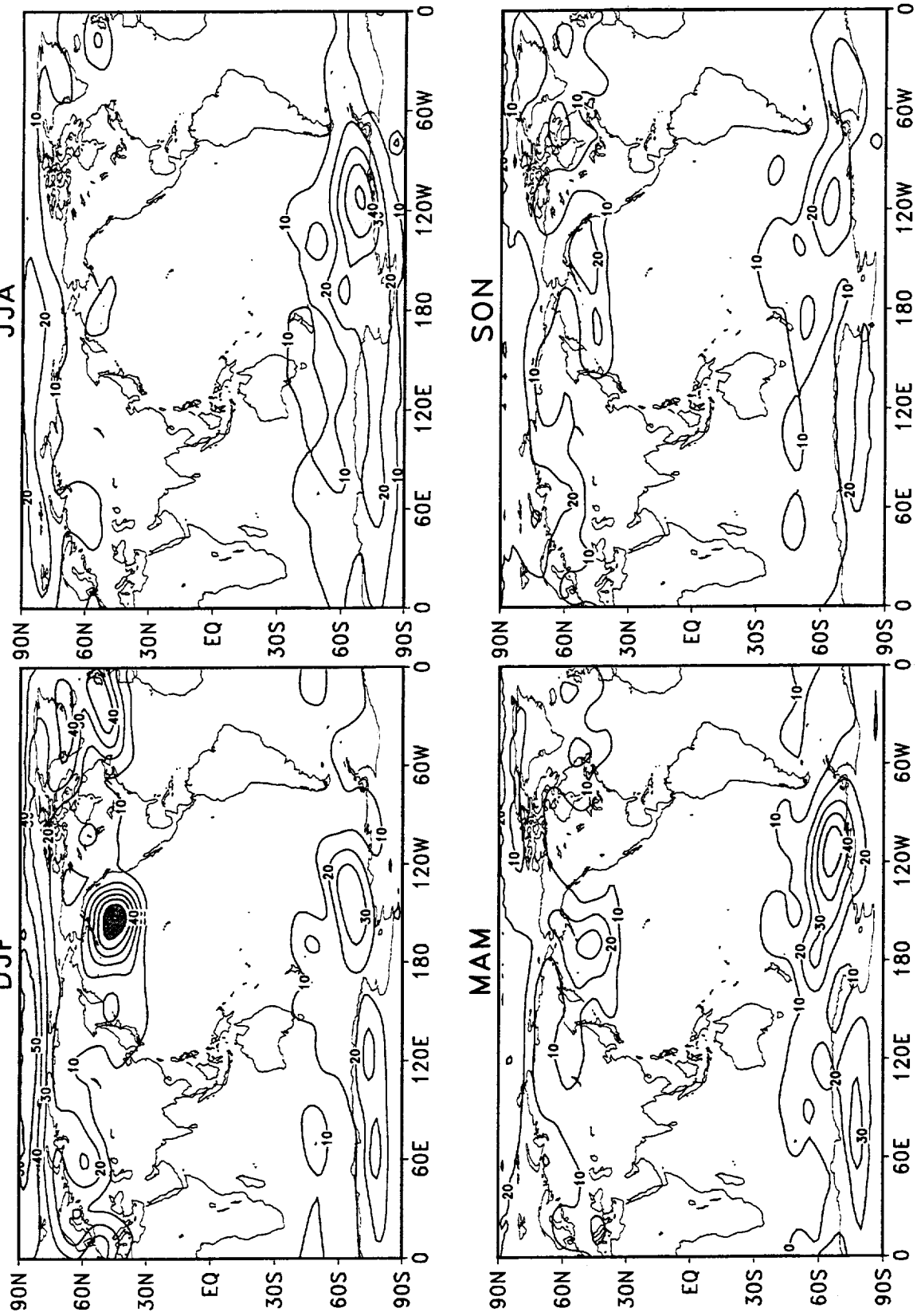

Figure 158: Interannual variances of 500 hPa height from the DAO reanalysis during 1980–1995. The contour interval is $10\times10^4 m^2$. Values larger than $40\times10^4 m^2$ are shaded.

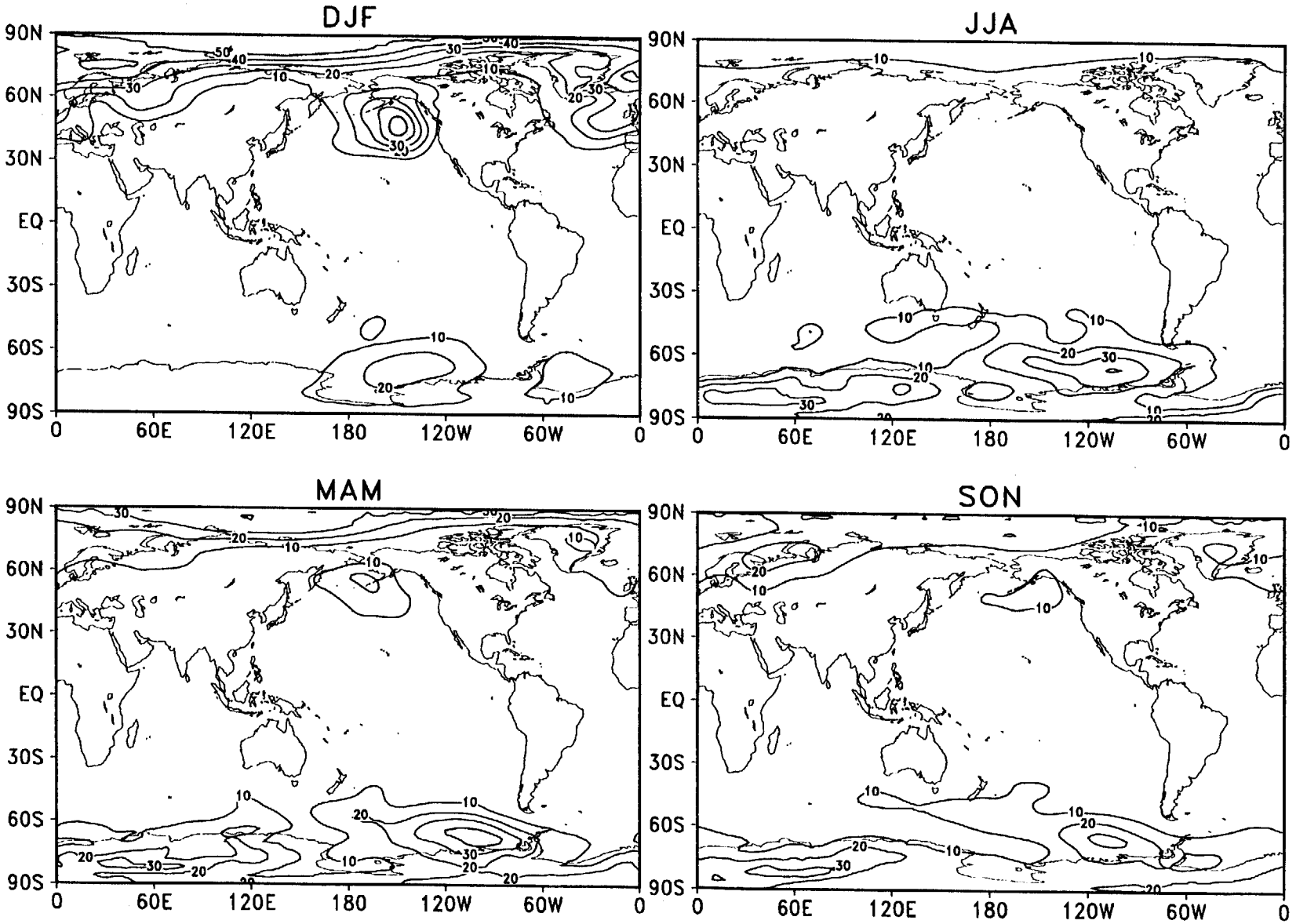

Figure 159: Interannual variances of sea level pressure from the DAO reanalysis during 1980–1995. The contour interval is 10 $(\text{hPa})^2$. Values larger than 40 $(\text{hPa})^2$ are shaded.

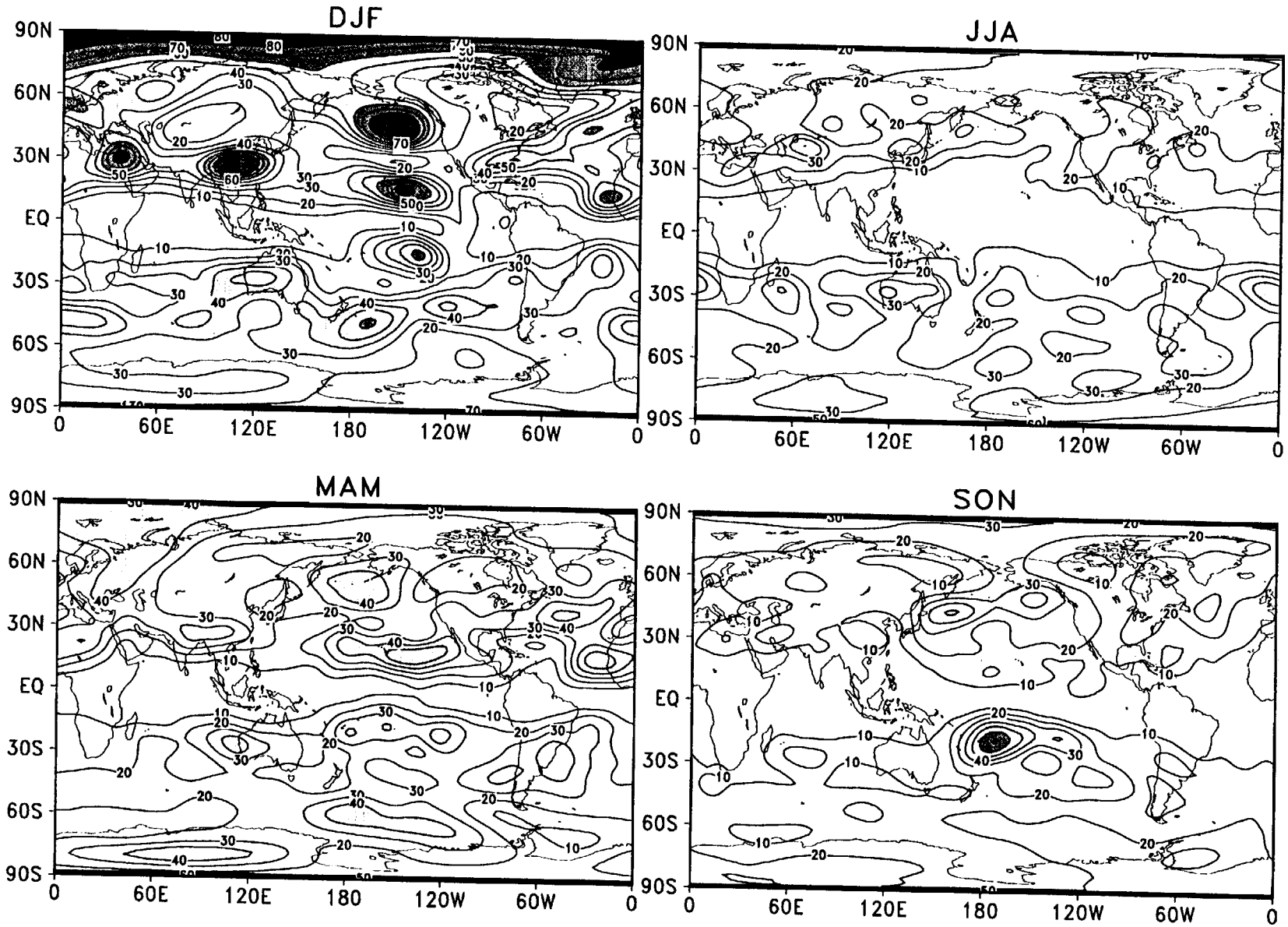

Figure 160: Interannual variances of 200 hPa streamfunction from the DAO reanalysis during 1980–1995. The contour interval is $10\times10^{12}\mathrm{m}^4\mathrm{s}^{-2}$. Values larger than $40\times10^{12}\mathrm{m}^4\mathrm{s}^{-2}$ are shaded.

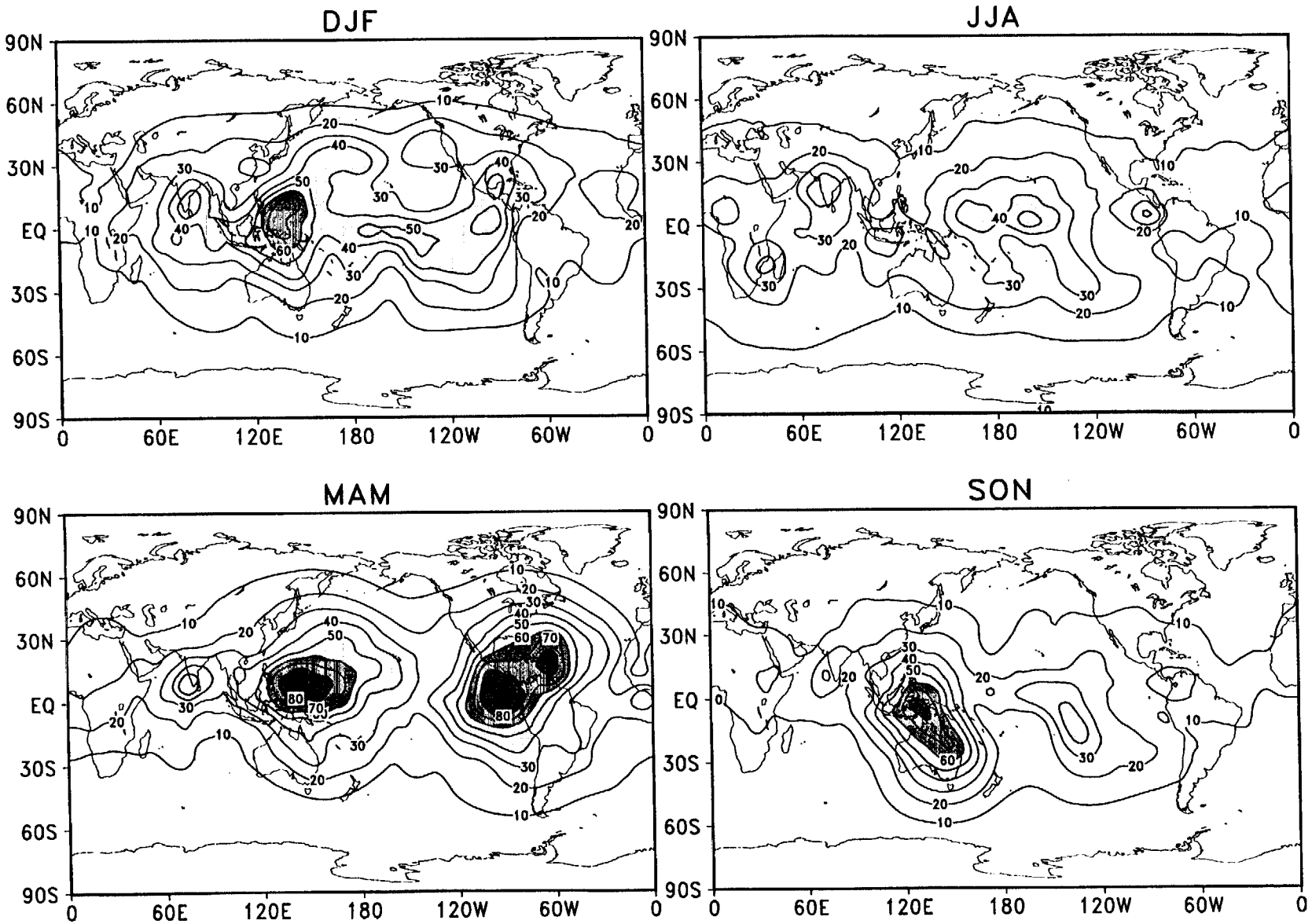

Figure 161: Interannual variances of 200 hPa velocity potential from the DAO reanalysis during 1980–1995. The contour interval is $10\times10^{11}\mathrm{m}^4\mathrm{s}^{-2}$. Values larger than $40\times10^{11}\mathrm{m}^4\mathrm{s}^{-2}$ are shaded.

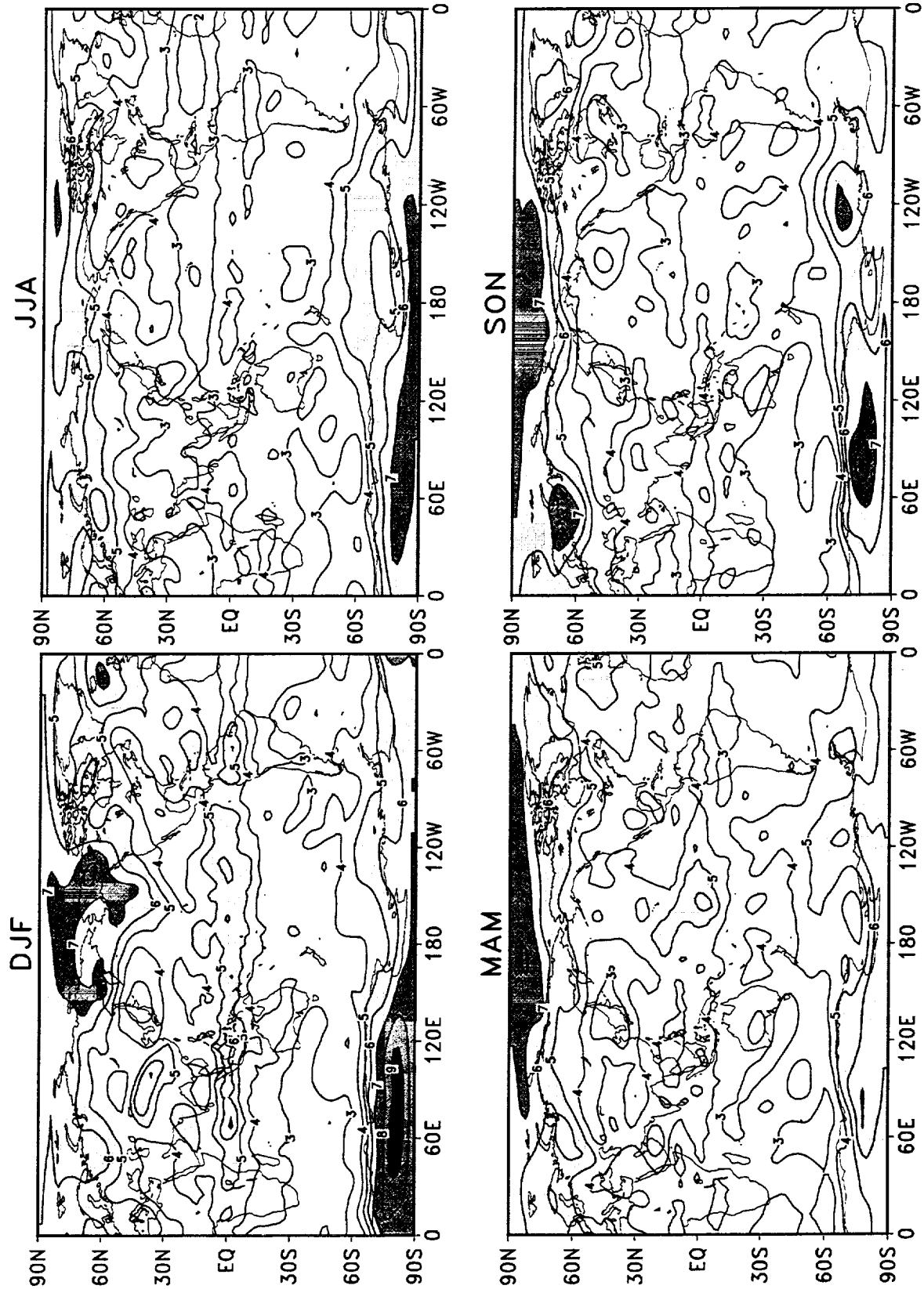

Figure 162: Characteristic time scales of 500 hPa height from the DAO reanalysis during 1980–1995. The contour interval is 1 day. Values larger than 5 days are shaded.

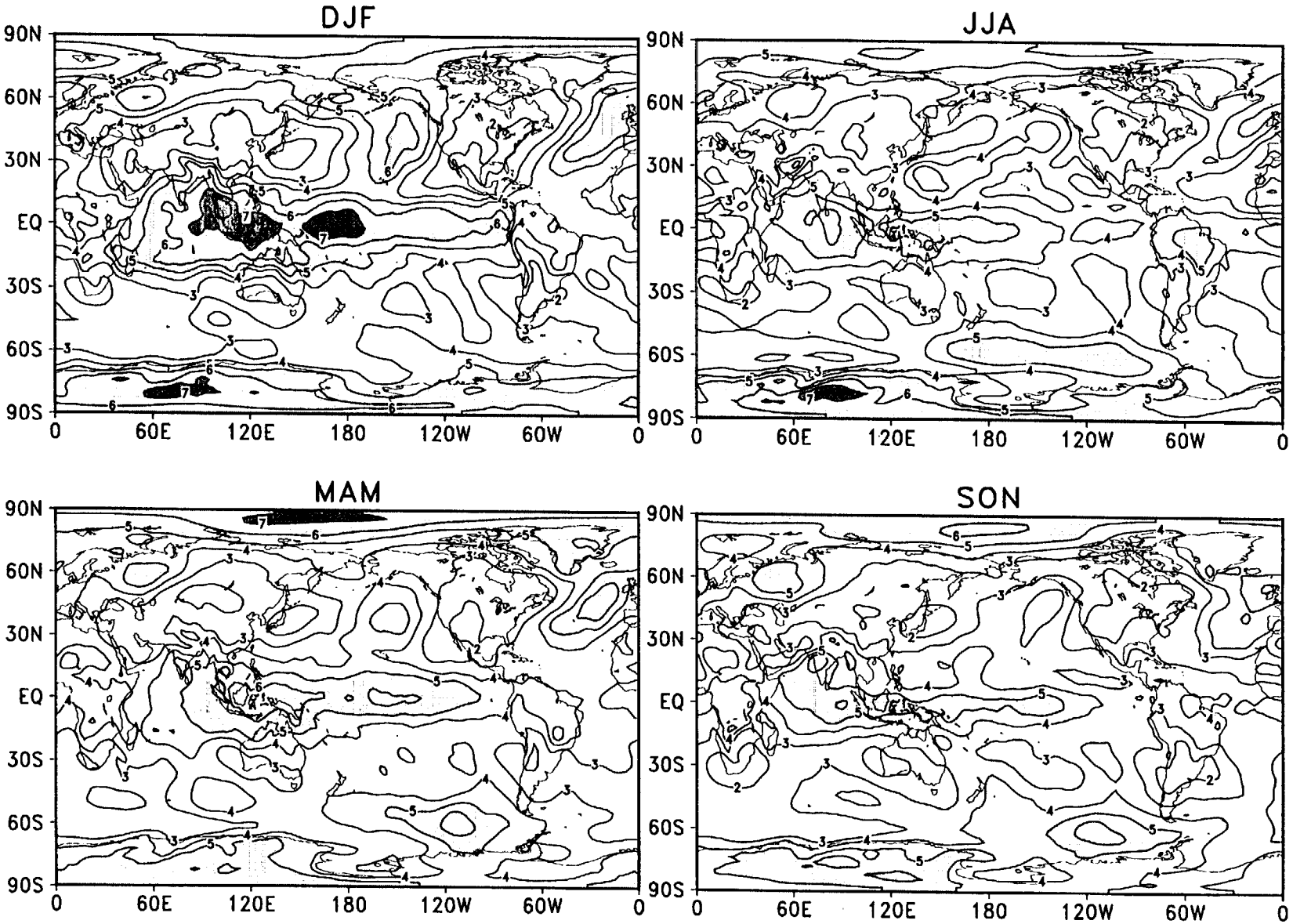

Figure 163: Characteristic time scales of sea level pressure from the DAO reanalysis during 1980–1995. The contour interval is 1 day. Values larger than 5 days are shaded.

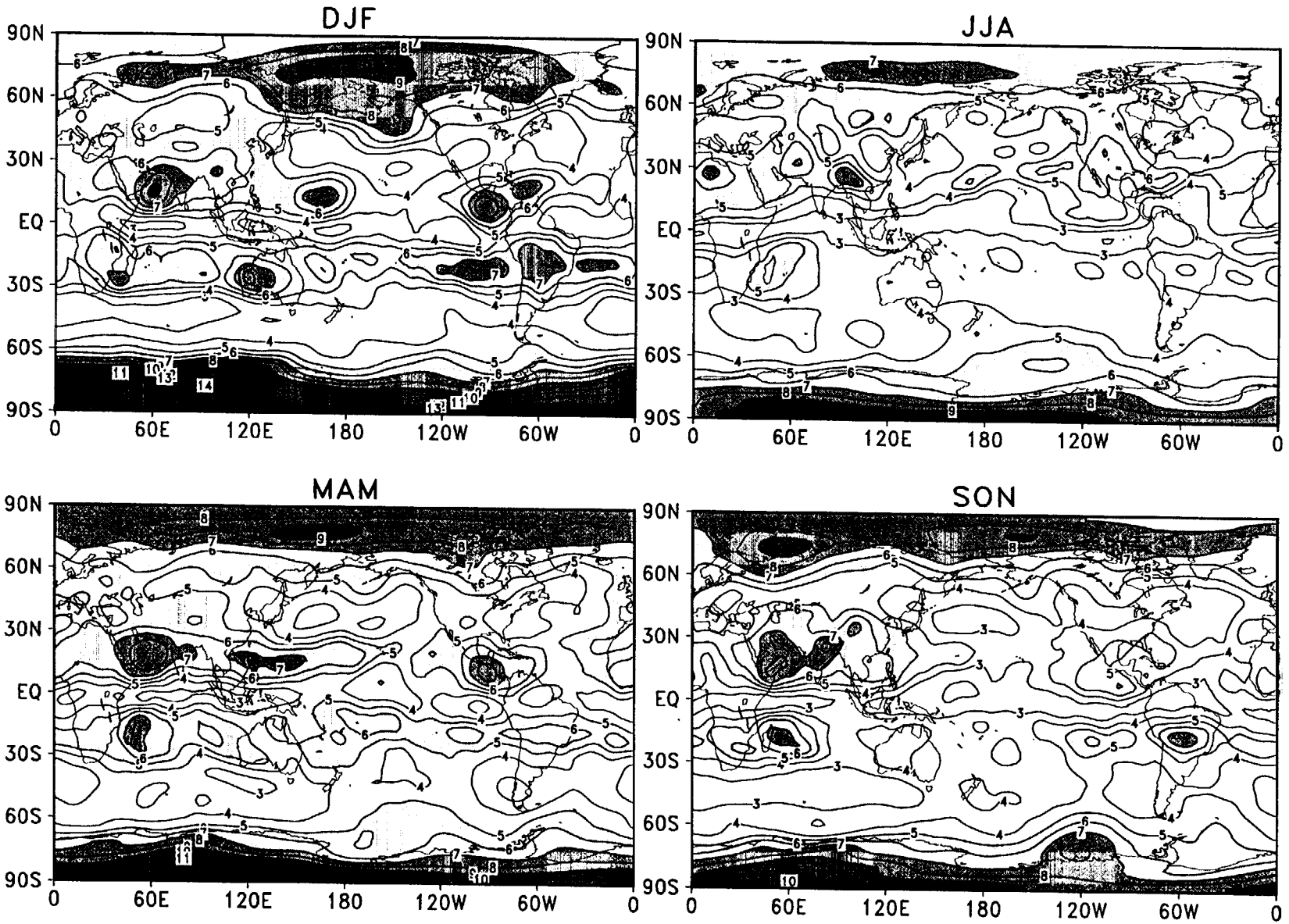

Figure 164: Characteristic time scales of 200 hPa streamfunction from the DAO reanalysis during 1980–1995. The contour interval is 1 day. Values larger than 5 days are shaded.

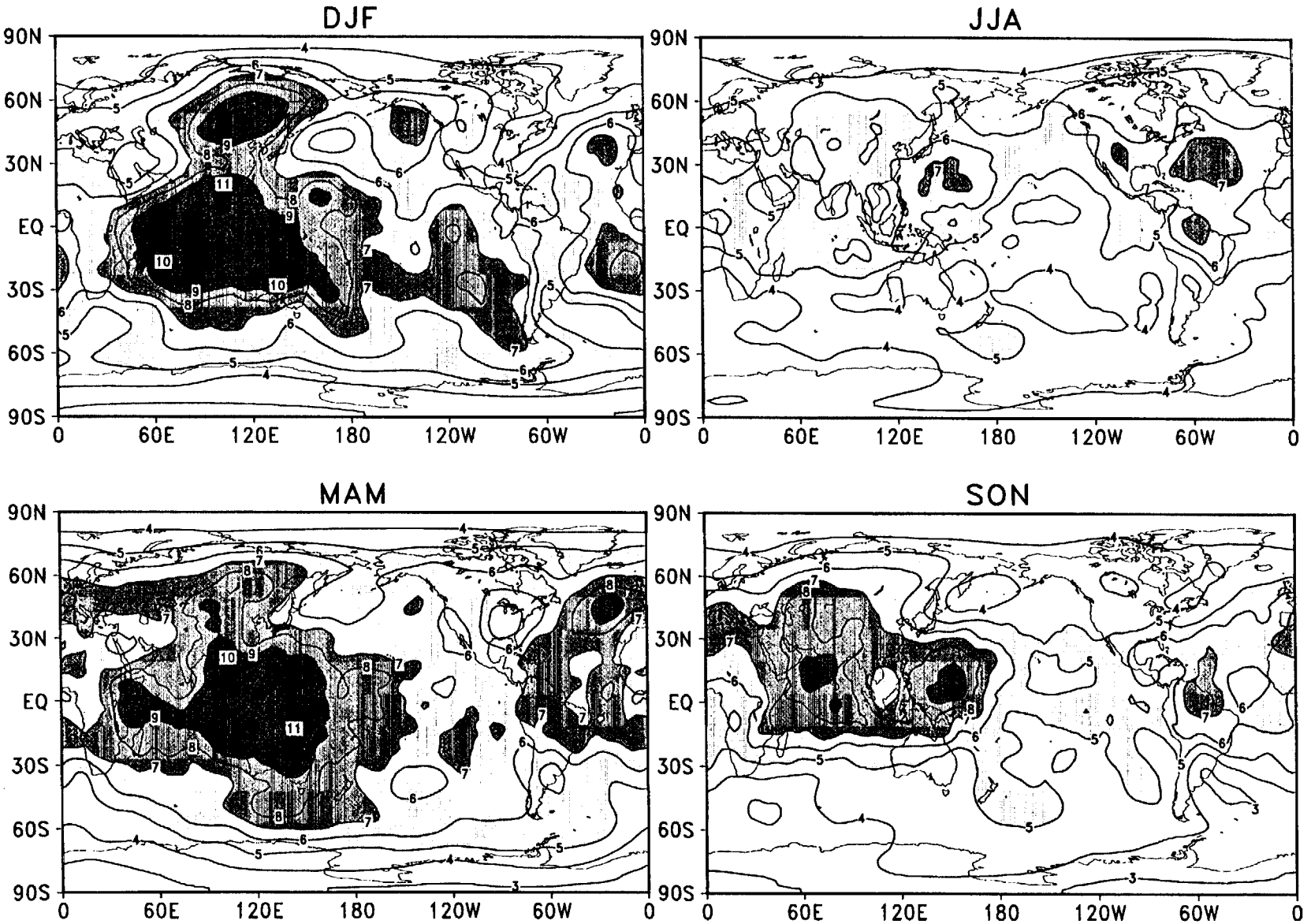

Figure 165: Characteristic time scales of 200 hPa velocity potential from the DAO reanalysis during 1980–1995. The contour interval is 1 day. Values larger than 5 days are shaded.

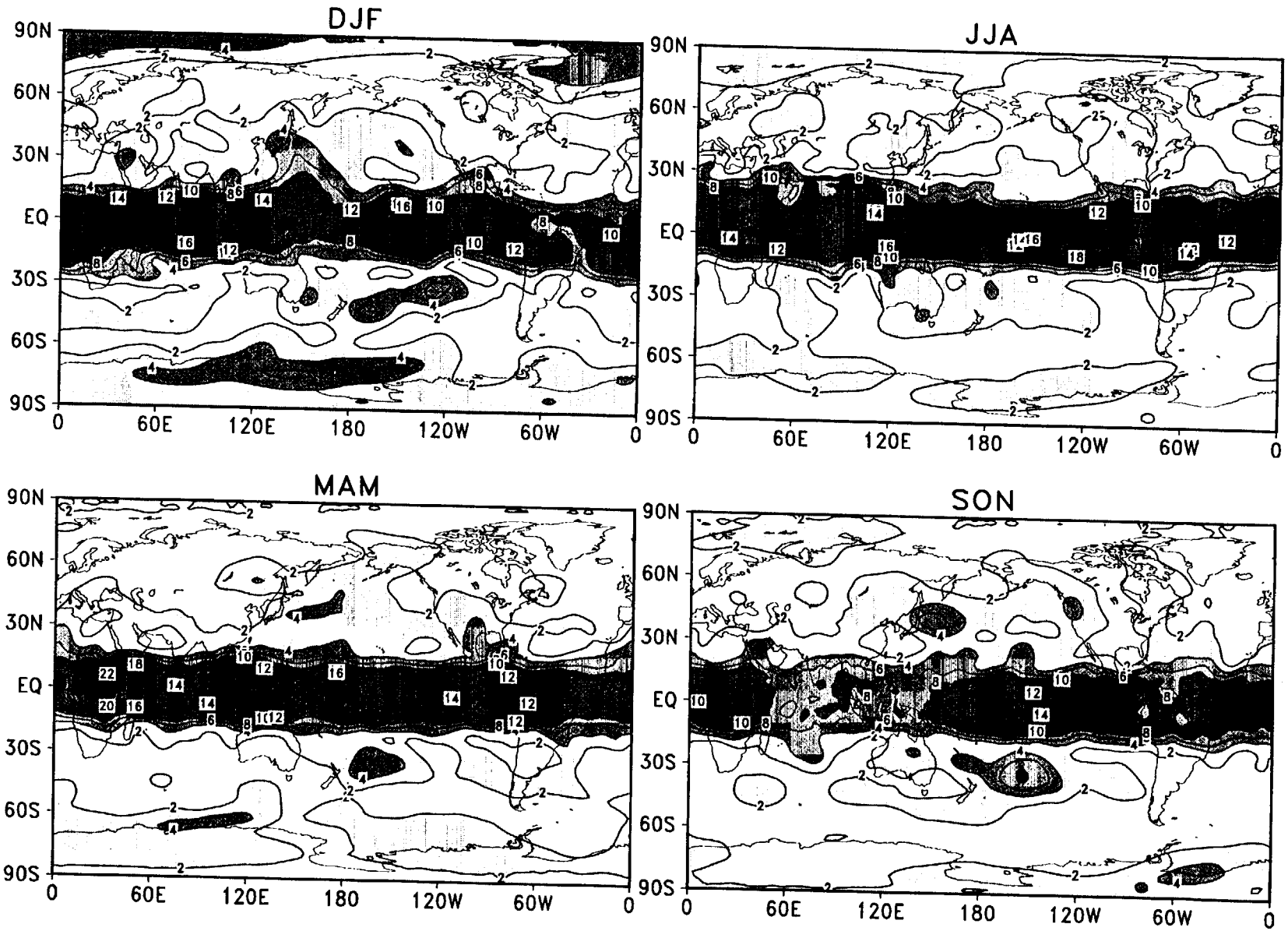

Figure 166: The F ratio of 500 hPa height from the DAO reanalysis during 1980–1995. The contour interval is 2. Light, intermediate and dark shadings denote values larger than 2, 4, and 6, respectively.

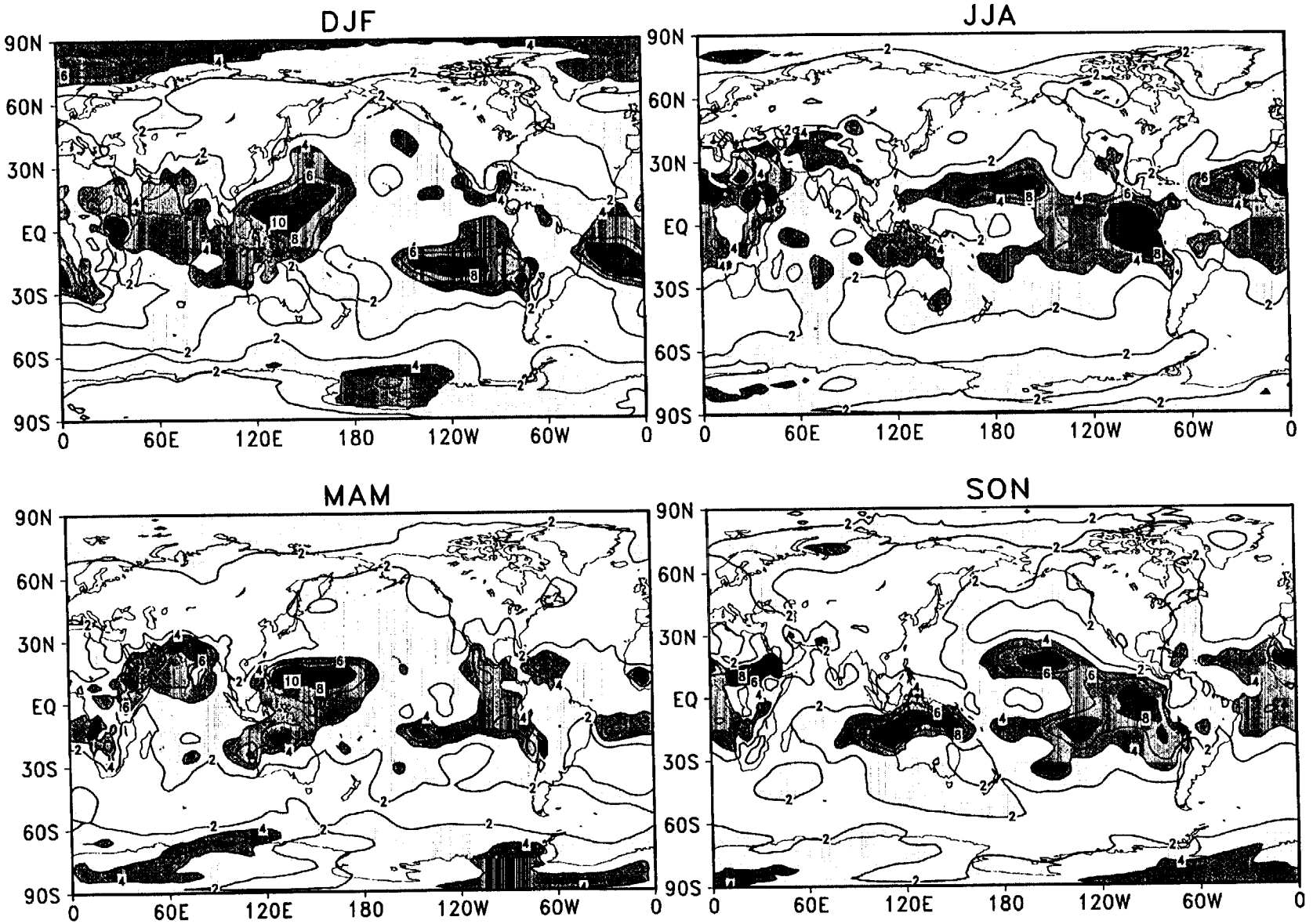

Figure 167: The F ratio of sea level pressure from the DAO reanalysis during 1980–1995. The contour interval is 2. Light, intermediate and dark shadings denote values larger than 2, 4, and 6, respectively.

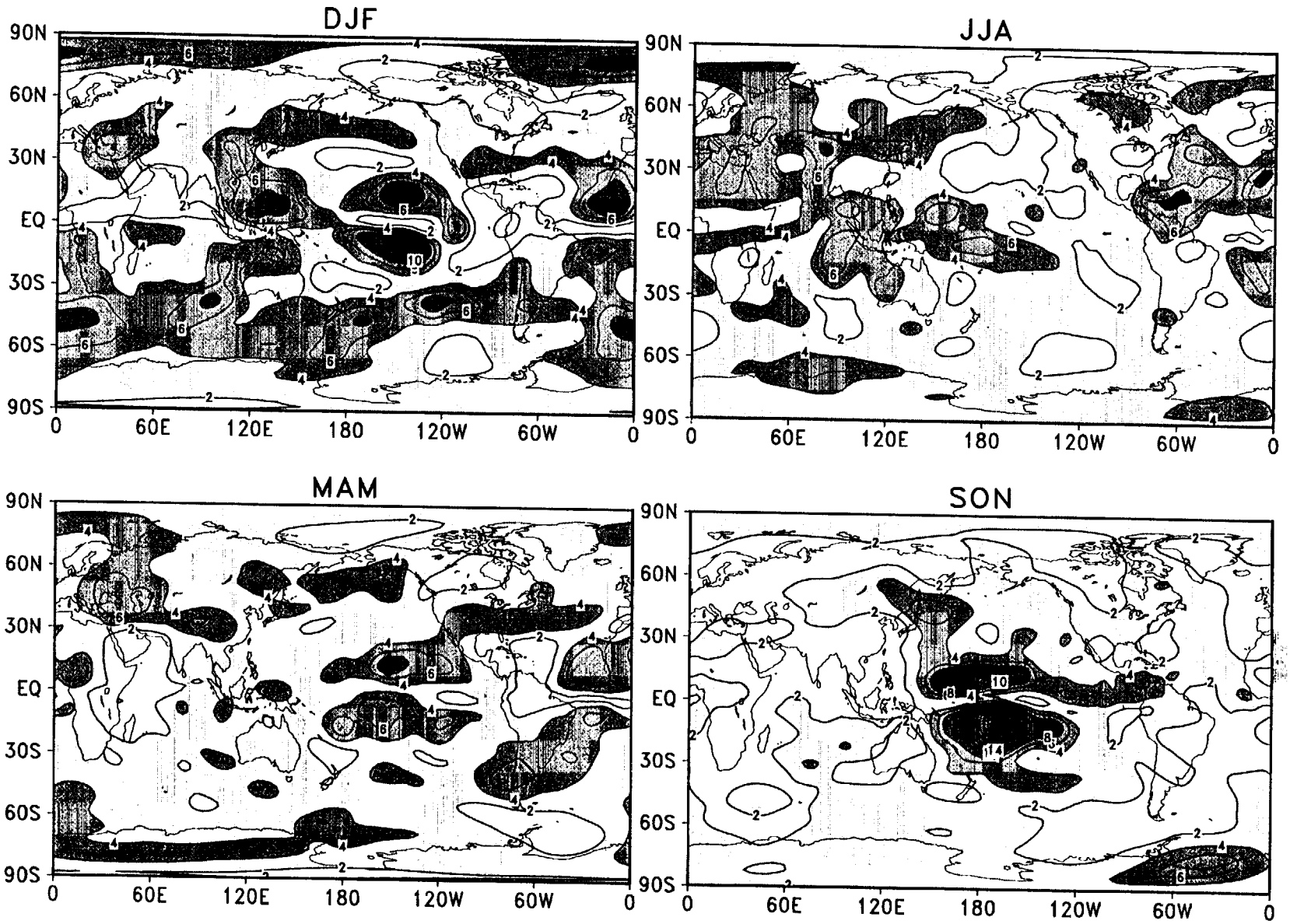

Figure 168: The F ratio of 200 hPa streamfunction from the DAO reanalysis during 1980–1995. The contour interval is 2. Light, intermediate and dark shadings denote values larger than 2, 4, and 6, respectively.

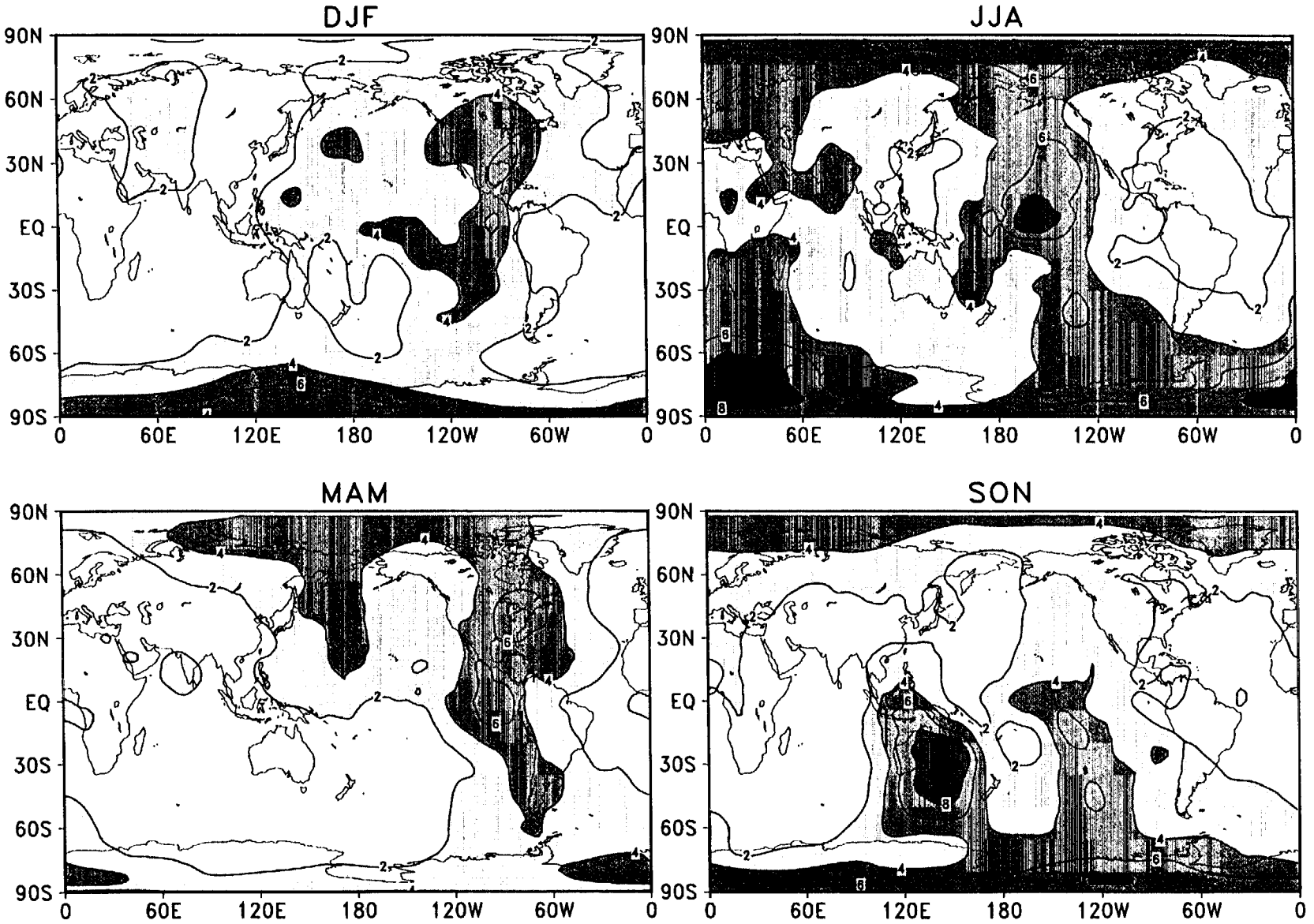

Figure 169: The F ratio of 200 hPa velocity potential from the DAO reanalysis during 1980–1995. The contour interval is 2. Light, intermediate and dark shadings denote values larger than 2, 4, and 6, respectively.

5 Summary

The results presented in this document are intended as an updated atlas of seasonal and interannual variability. The results are based on a 15-year period from March 1980 to February 1995 employing assimilated data (the NASA/DAO and NCEP/NCAR reanalyses) which do not suffer from artificial climate signals introduced by system changes typical of operational analyses. The comparisons between the two reanalyses serve to assess the quality and consistency of the various quantities at seasonal and longer time scales.

The results show that, in general, the seasonal means of the prognostic fields are consistent in the two reanalyses. However, systematic differences do occur even in the zonal wind and temperature fields. For example, the DAO product shows a consistently colder lower stratosphere than the NCEP product. The largest differences tend to occur over regions where observations are sparse, though it is not clear how many of these differences are associated with model bias, the input observations, or the analysis techniques. In particular, differences in the weighting of conventional and satellite observations may play an important role. Systematic differences in the moisture are found throughout the troposphere with the largest occurring in the lower levels which contribute substantially to the differences in the hydrological cycle. These differences also occur largely over data sparse regions, such as the tropical oceans and South America. Since the current analyses only use radiosonde moisture observations it is expected that the incorporation of alternative high quality sources of moisture observations will have a major positive impact on future reanalyses.

The differences tend to be largest for the diagnostic quantities (especially those involving the hydrological cycle) and those quantities involving the divergent wind. For example, the mass streamfunction in the DAO system is stronger than in the NCEP system during the northern summer (JJA) while the opposite is true during the northern winter (DJF). The key moisture source terms also show substantial differences. For example, the tropical precipitation is consistently larger in the DAO product, especially over the Pacific warm pool. The NCEP/NCAR evaporation is larger over the oceans compared to the DAO and less than the DAO over land during the warm seasons.

While it is clear there are still substantial bias' in the reanalysis fields, the most promising products of the reanalysis are the estimates of interannual variability. This is potentially the major improvement over the operational products, though it must be pointed out that the inhomogeneities in the observations can still induce spurious signals. The comparisons show that, in general, the differences in the wind and temperature variability tend to be small, except in the lower stratosphere and the high latitudes of the Southern Hemisphere. On the other hand, the variability of the Hadley Cell is quite different in the two reanalyses with the DAO product showing consistently stronger interannual variability. The variability of the moisture also shows substantial differences with consistently greater variability in the

DAO moisture field. Similarly, various near surface quantities and surface fluxes examined here show substantial differences in variability. These quantities are only indirectly constrained by the observations, and depend strongly on the physical parameterizations of the assimilating general circulation models. While in most cases the patterns of variability are similar, the DAO products show a tendency for larger variability than the NCEP products in both the tropics and the midlatitudes. These results suggests substantial uncertainty still exists in the estimates of seasonal variability, especially in the diagnostic quantities. We note that other studies (e.g. Schubert et. al. 1995; Min and Schubert 1997) suggest greater agreement and/or more accurate estimates of variability on monthly time scales, and of variability associated with extreme events.

Finally, we have re-examined atmospheric potential predictability with selected variables from the DAO reanalysis products. The results are generally consistent with previous studies in that potential predictability is smallest in the midlatitudes (40°–60°) of both hemispheres and increases both to the north and south. On the other hand, the use of the reanalysis data, and careful fitting of the autocorrelation, appear to have provided improved estimates of the signal–to–noise ratio, which are more consistent with known climate signals. For example, we find enhance potential predictability over Australia and the South Pacific, apparently linked to the Southern Oscillation. We have also seen a strong seasonal cycle in the potential predictability of most quantities examined here. For example, the seasonal evolution of patterns of strong signal–to–noise ratios tied to the tropical SSTs can be tracked across the Pacific during the course of the annual cycle. These estimates appear to be sufficiently reliable to now provide a basis for assessing the veracity of signal–to–noise ratios generated with general circulation models.

Acknowledgments. This work was supported by NASA's Earth Observing Systems (EOS) projects on 4D data Assimilation and Computing.

References

Arpe, K., 1990: Impacts of changes in the ECMWF analysis-forecasting scheme on the systematic error of the model. *Ten years of medium-range weather forecasting*, **Volume I**, 4-8 September, 1989. European Center for Medium Range Weather Forecasts, Shinfield Park, Reading/Berks., RG2 9AX, England.

Bengtsson, L. and J. Shukla, 1988: Integration of space and in situ observations to study global climate change. *Bull. Am. Meteor. Soc.*, **69**, 1130-1143.

Blackmon, M.L., 1976: A climatological spectral study of the 500 mb geopotential height of the Northern Hemisphere. *J. Atmos. Sci.*, **33**, 1607-1623.

Blackmon, M.L., S.L. Mullen, and G.T. Bates, 1986: The climatology of blocking events in a perpetual January simulation of a spectral general circulation model. *J. Atmos. Sci.*, **43**, 1379-1405.

Bloom, S. C., L. L. Takacs, A. M. DaSilva and D. Ledvina, 1996: Data assimilation using incremental analysis updates. *To appear in Mon. Wea. Rev.*

Campana, K.A., Y.-T. Hou, K.E. Mitchell, S.-K. Yang and R. Cullather, 1994: Improved diagnostic cloud parameterization in NMC's global model. Preprints, *10th Conf. on Numerical Weather Prediction*, Portland, OR, Amer. Meteor. Soc, 324-325.

Gibson, R., P. Kallberg and S. Uppsala, 1996: The ECMWF reanalysis (ERA) project. *ECMWF Newsletter*, **73**, 7-16.

Higgins, R. W., K. C. Mo and S. D. Schubert, 1996: The moisture budget of the central United States in spring as evaluated in the NMC/NCAR and the NASA/DAO reanalyses. *Mon. Wea. Rev.*, **124**, 939-963.

Higgins, R. W., Y.-P. Yao, M. Chelliah, W. Ebisuzaki, J. E. Janowiak, and C. F. Ropelewski, 1997: Intercomparison of the NCEP/NCAR and the NASA/DAO Reanalyses (1985-1993). NCEP/Climate Prediction Center ATLAS No.2, 169pp.

Jones, R. H., 1975: Estimating the variance of time averages. *J. Appl. Meteor.*, **14**, 159-163.

Kalnay, E., M. Kanamitsu, R. Kistler, W. Collins, D. Deaven, J. Derber, L. Gandin, S. Sara, G. White, J. Woollen, Y. Zhu, M. Chelliah, W. Ebisuzaki, W. Higgins, J. Janowiak, K. C. Mo, C. Ropelewski, J. Wang, A Leetma, R. Reynolds, R Jenne, 1995: The NMC/NCAR Reanalysis Project. *Bull. Amer. Meteor. Soc.*, **77**, 437-471.

Kanamitsu, M., 1989: Description of the NMC global data assimilation and forecast system. *Weather Forecasting*, **4**, 334-342.

Leith, C. E., 1973: The standard error of time-average estimates of climatic means. *J. Appl. Meteor.* **12**, 1066-1069.

Leith, C. E., 1978: Objective methods for weather prediction. *Ann. Rev. Fluid Mech.*, **10**, 107-128.

Lorenz, E. N., 1982: Atmospheric predictability experiments with a large numerical model. *Tellus*, **34**, 505-513.

Madden, R. A., 1976: Estimates of the natural variability of time-averaged sea level pressure. *Mon. Wea. Rev.*, **104**, 942-952.

Madden, R.A. and P. Julian, 1972: Description of global-scale circulation cells in the tropics with a 40–50 day period. *J. Atmos. Sci.*, **29**, 1109-1123.

Madden, R.A. and D.J. Shea, 1978: Estimates of the natural variability of time-averaged temperature over the United States. *Mon. Wea. Rev.*, **106**, 1695-1703.

Min, W. and E. C. Kung, 1997: A spectral analysis of wave activities and blocking in the northern hemisphere winter. *Terr. Atmos. Ocean Sci.*, **8**, 69-94.

Min, W. and S.D. Schubert, 1997: The climate signal in regional moisture budgets: A comparison of three global data assimilation products. *J. Climate*, **10**, 2623-2642.

Mo, K. C. and R. W. Higgins, 1996: Large scale atmospheric water vapor transport as evaluated from the NMC/NCAR and the NASA/DAO reanalyses. *J. Climate*, **9**, 1531-1545.

Moorthi, S. and M. J. Suarez, 1992: Relaxed Arakawa-Schubert: A parameterization of moist convection for general circulation models. *Mon. Wea. Rev.*, **120**, 978-1002.

Nicholls, N., 1981: Air-sea interaction and the possibility of long-range weather prediction in the Indonesian Archipelago. *Mon. Wea. Rev.*, **100**, 2435-2443.

Pan, H.-L. and L. Mahrt, 1987: Interaction between soil hydrology and boundary-layer development. *Bound.-Layer Meteor.*, **38**, 185-220.

Pan, H.-L. and W.-S. Wu, 1994: Implementing a mass flux convection parameterization package for the NMC medium-range forecast model. Proceedings of the Tenth Conference on Numerical Weather Prediction, Portland, Oregon, 96-98.

Parrish, D. F. and J. C. Derber, 1992: The National Meteorological Center's spectral statistical interpolation analysis system. *Mon. Wea. Rev.*, **120**, 1747-1763.

Reynolds, R. W. and D. S. Marsico, 1993: An improved real time global sea surface temperature analysis. *J. Climate*, **6**, 114-119.

Reynolds, R. W. and T. M. Smith, 1994: Improved global sea surface temperature analyses using optimum interpolation. *J. Climate*, **7**, 929-948.

Schubert, S. D., J. Pfaendtner and R. Rood, 1993: An assimilated data set for Earth Science applications. *Bull. Am. Meteor. Soc.*, **74**, 2331-2342.

Schubert, S. D., C.-K, Park, C.-Y. Wu, W. Higgins, Y. Kondratyeva, A. Molod, L. Takacs, M. Seablom. R. Rood, 1995: A multiyear assimilation with the GEOS-1 system: overview and results. *NASA Tech. Memo. No.* 104606, Volume **6**, 183pp. [available from Goddard Space Flight Center, Greenbelt, MD 20771.]

Schubert, S. D., W. Min, L. Takacs, and J. Joiner, 1997: Reanalysis of historical observations and its role in the development of the Goddard EOS climate data assimilation system. *Adv. Space. Res.*, **19**, 491-501.

Schemm, J.-K., S. Schubert, J. Terry and S. Bloom, 1992: Estimates of monthly mean soil moisture for 1979-89, *NASA Tech. Memo.* 104571, pp 252, Oct. 1992. [Available from Goddard Space Flight Center, Greenbelt, MD 20771.]

Shukla, J. , 1983: On natural variability and predictability. *Mon. Wea. Rev.*, **111**, 581-585.

Shukla, J. and D. Gutzler, 1983: Interannual variability and predictability of 500 mb geopotential heights over the Northern Hemisphere. *Mon. Wea. Rev.*, **111**, 1273-1279.

Stefanick, M., 1981: Space and time scales of atmospheric variability. *J. Atmos. Sci.*, **38**, 988-1002.

Suarez, M. J. and L. L. Takacs, 1995: Documentation of the Aries-GEOS Dynamical Core:Version 2. *NASA Tech. Memo. No.* 104606, Volume **5**, 58pp. [Available from Goddard Space Flight Center, Greenbelt, MD 20771.]

Takacs, L. L., A. Molod and T. Wang, 1994: Goddard Earth Observing System (GEOS) General Circulation Model (GCM) Version 1. *NASA Tech. Memo. No.* 104606, Volume **1**, 100pp. Goddard Space Flight Center, Greenbelt, MD 20771., Technical Memorandum 104606. [Available from Goddard Space Flight Center, Greenbelt, MD 20771.]

Trenberth, K.E., 1976: Spatial and temporal variations of the Southern Oscillation. *Quart. J. Roy. Meteor. Soc.*, **102**, 639-653.

Trenberth, K. E. 1985a: Persistence of daily geopotential heights over the Southern Hemisphere. *Mon. Wea. Rev.*, **113**, 38-53.

Trenberth, K. E. 1985b: Potential predictability of geopotential heights over the Southern Hemisphere. *Mon. Wea. Rev.*, **113**, 54-64.

Wang, M. and J. N. Paegle, 1996: Impact of analysis uncertainty upon regional atmospheric moisture flux. *J. Geophys. Res.*, **101**, 7291-7303.

Zwiers, F. W., 1987: A potential predictability study conducted with an atmospheric general circulation model. *Mon. Wea. Rev.*, **115**, 2957-2974.

Previous Volumes in This Series

Volume 1 *September 1994*	Documentation of the Goddard Earth Observing System (GEOS) general circulation model - Version 1 **L.L. Takacs, A. Molod, and T. Wang**
Volume 2 *October 1994*	Direct solution of the implicit formulation of fourth order horizontal diffusion for gridpoint models on the sphere **Y. Li, S. Moorthi, and J.R. Bates**
Volume 3 *December 1994*	An efficient thermal infrared radiation parameterization for use in general circulation models **M.-D. Chou and M.J. Suarez**
Volume 4 *January 1995*	Documentation of the Goddard Earth Observing System (GEOS) Data Assimilation System - Version 1 **James Pfaendtner, Stephen Bloom, David Lamich, Michael Seablom, Meta Sienkiewicz, James Stobie, and Arlindo da Silva**
Volume 5 *April 1995*	Documentation of the Aries-GEOS dynamical core: Version 2 **Max J. Suarez and Lawrence L. Takacs**
Volume 6 *April 1995*	A Multiyear Assimilation with the GEOS-1 System: Overview and Results **Siegfried Schubert, Chung-Kyu Park, Chung-Yu Wu, Wayne Higgins, Yelena Kondratyeva, Andrea Molod, Lawrence Takacs, Michael Seablom, and Richard Rood**
Volume 7 *September 1995*	Proceedings of the Workshop on the GEOS-1 Five-Year Assimilation **Siegfried D. Schubert and Richard B. Rood**

Volume 8
March 1996

Documentation of the Tangent Linear Model and Its Adjoint of the Adiabatic Version of the NASA GEOS-1 C-Grid GCM: Version 5.2

Weiyu Yang and I. Michael Navon

Volume 9
March 1996

Energy and Water Balance Calculations in the Mosaic LSM

Randal D. Koster and Max J. Suarez

Volume 10
April 1996

Dynamical Aspects of Climate Simulations Using the GEOS General Circulation Model

Lawrence L. Takacs and Max J. Suarez

Volume 11
May 1997

Documentation of the Tangent Linear and its Adjoint Models of the Relaxed Arakawa-Schubert Moisture Parameterization Package of the NASA GEOS-1 GCM (Version 5.2)

Weiyu Yang I. Michael Navon, and Ricardo Todling

Volume 12
August 1997

Comparison of Satellite Global Rainfall Algorithms

Alfred T.C. Chang and Long S. Chiu

REPORT DOCUMENTATION PAGE

Form Approved
OMB No. 0704-0188

1. AGENCY USE ONLY *(Leave blank)*	2. REPORT DATE	3. REPORT TYPE AND DATES COVERED
	December 1997	Technical Memorandum

4. TITLE AND SUBTITLE
Technical Report Series on Global Modeling and Data Assimilation
Volume 13—Interannual Variability and Potential Predictability in Reanalysis Products

5. FUNDING NUMBERS
Code 910.3/913

6. AUTHOR(S)
Wei Min and Siegfried D. Schubert
Max Suarez, Editor

7. PERFORMING ORGANIZATION NAME(S) AND ADDRESS (ES)
Data Assimilation Office
Climate and Radiation Branch
Goddard Space Flight Center
Greenbelt, Maryland

8. PEFORMING ORGANIZATION REPORT NUMBER
97A00357

9. SPONSORING / MONITORING AGENCY NAME(S) AND ADDRESS (ES)
National Aeronautics and Space Administration
Washington, DC 20546-0001

10. SPONSORING / MONITORING AGENCY REPORT NUMBER
TM–97–104606, Vol. 13

11. SUPPLEMENTARY NOTES
Wei Min: General Sciences Corporation, Laurel, Maryland

12a. DISTRIBUTION / AVAILABILITY STATEMENT
Unclassified–Unlimited
Subject Category: 46

Availability: NASA CASI (301) 621-0390.

12b. DISTRIBUTION CODE

13. ABSTRACT *(Maximum 200 words)*

The Data Assimilation Office (DAO) at Goddard Space Flight Center and the National Center for Environmental Prediction and National Center for Atmospheric Research (NCEP/NCAR) have produced multi-year global assimilations of historical data employing fixed analysis systems. These "reanalysis" products are ideally suited for studying short-term climatic variations. The availability of multiple reanalysis products also provides the opportunity to examine the uncertainty in the reanalysis data. The purpose of this document is to provide an updated estimate of seasonal and interannual variability based on the DAO and NCEP/NCAR reanalyses for the 15-year period 1980–1995. Intercomparisons of the seasonal means and their interannual variations are presented for a variety of prognostic and diagnostic fields. In addition, atmospheric potential predictability is re-examined employing selected DAO reanalysis variables.

14. SUBJECT TERMS
DAO, NCEP/NCAR, reanalysis products, seasonal variability, interannual variability

15. NUMBER OF PAGES
218

16. PRICE CODE

17. SECURITY CLASSIFICATION OF REPORT	18. SECURITY CLASSIFICATION OF THIS PAGE	19. SECURITY CLASSIFICATION OF ABSTRACT	20. LIMITATION OF ABSTRACT
Unclassified	Unclassified	Unclassified	UL